Supramolecular networks and on-surface chemical reactions studied by STM under UHV conditions

Ali Hamadeh

THESE DE DOCTORAT DE L'ETABLISSEMENT UNIVERSITE BOURGOGNE FRANCHE-COMTE

PREPAREE Al'UNIVERSITE DE FRANCHE-COMTE

Ecole doctorale no 37

Sciences pour l'ingénieur et microtechniques

Doctorat en physique

Par

Mr. HAMADEH Ali

Réseaux supramoléculaires et réactions chimiques sur surface étudiés par STM sous ultra-haut vide

Thèse présentée et soutenue à Montbéliard le 24 septembre 2024

Composition du Jury :

Mr. LAGOUTE Jérôme	Directeur de recherche, CNRS	Président
Mr. CLAIR Sylvain	Directeur de recherche, CNRS	Rapporteur
Mr. CORAUX Johann	Directeur de recherche, CNRS	Rapporteur
Mr. DAZZI Alexandre	Professeur, Université de Paris-Saclay	Invité
Mr. PALMINO Frank	Professeur, Université de Franche-Comté	Directeur de thèse
Mr. CHERIOUX Frédéric	Directeur de recherche, CNRS	Co-directeur de thèse

THESIS TO OBTAIN THE DEGREE OF

DOCTOR OF PHILOSOPHY FROM THE UNIVERSITY OF BOURGOGNE FRANCHE-COMTE

PREPARED AT THE UNIVERSITY OF FRANCHE-COMTE

Doctoral school no 37

Physical Sciences for Engineers and Microtechnology

PhD in Physics

By

Mr. HAMADEH Ali

Supramolecular networks and on-surface chemical reactions studied by STM under UHV conditions

Thesis presented and defended in Montbéliard, September 24, 2024

Composition of the Jury:

Mr. LAGOUTE Jérôme	Senior researcher at CNRS	Chairman
Mr. CLAIR Sylvain	Senior researcher at CNRS	Reviewer
Mr. CORAUX Johann	Senior researcher at CNRS	Reviewer
Mr. DAZZI Alexandre	Professor at Paris-Saclay University	Guest
Mr. PALMINO Frank	Professor at Université de Franche-Comté	Supervisor
Mr. CHERIOUX Frédéric	Senior researcher at CNRS	Co-supervisor

Acknowledgments

I want to extend my heartfelt thanks to my supervisors Prof. Frank PALMINO and Dr. Frédéric CHERIOUX, for welcoming me into their team and granting me access to the laboratory and research resources. I am grateful to them for introducing me to the realm of science and research, and for generously imparting their experience, knowledge, and engaging in scientific discussions. These insights will undoubtedly shape my journey in the long term. Their confidence and support throughout the last three years have inspired me to strive for excellence in this research project.

I extend my heartfelt gratitude to Mr. Judicaël JEANNOUTOT for his assistance and support, both within and beyond the laboratory. Mr. JEANNOUTOT, responsible for maintaining and managing the STM and UHV systems, has been a pleasure to work with on a daily basis.

I am grateful to the jury members for devoting their time to reading and evaluating the thesis dissertation. My sincere gratitude goes to Mr. Johann CORAUX and Mr. Sylvain CLAIR for agreeing to be reviewers of my manuscript, as well as Mr. Jérôme LAGOUTE for agreeing to be an examiner and a Charmain for my thesis defense jury.

I convey my deepest gratitude to my collaborators, Prof. Alexandre Dazzi from the University of Paris Saclay, Prof. Carmelo PIRRI, Dr. Samar HAJJAR from the University of Haute Alsace, and Prof. Alain ROCHEFORT from the University of Polytechnique Montréal, for their irreplaceable contributions to my work and pleasant personal interactions paired with a high degree of professionalism.

I want to express my deep appreciation to my friend for the unforgettable moments we shared and for their constant support throughout my three-year tenure. In particular, I am grateful to Elie GEAGEA, whom I initially met as a colleague in the group but who quickly became a cherished lifelong friend.

Finally, I want to extend my deepest gratitude to my family. I am profoundly thankful to my parents, siblings, and relatives for their unwavering support and affection. Your boundless love, understanding, and encouragement have been instrumental in helping me realize my aspirations and ambitions in life. You are the foundation of my being, and my love for you surpasses all else.

Table of contents

Chapter I: A brief overview of supramolecular self-assemblies and on-surface synthesis:

Molecular self-assembly has been studied on surfaces for almost three decades now. Even though this research may already be regarded as the first correlation between organic chemistry and surface science, the relationship became stronger in 2007–2008 after two major investigations on Ullmann coupling and boronic acid condensation by Grill et al. and Porte et al. suggested that solid surfaces might also be a favorable location for coupling reactions involving relatively large organic molecules [1, 2]. At least two deductions flowed from this: On the one hand, the full suite of microscopic and spectroscopic surface science tools became accessible to study the course, intermediates, and end products of reactional processes. On the other hand, the notion of using "flatlands" for the synthesis of extended 2D networks or, eventually, the manufacturing of new 2D materials has been sparked by the apparent templating effect of surfaces caused by the confinement of the reacting species in two dimensions.

The remarkable potential of on-surface synthesis as a technique for creating new functional structures at surfaces has attracted a lot of interest in recent years. The capacity to create covalently bonded, thermally stable structures—which may find use even in harsh environments outside of ultra-high vacuum conditions is a crucial component of on-surface synthesis. Moreover, conjugated structures with improved electron transport properties may be created by covalent bonding. This is particularly true for the field of molecular electronics of the future, where the construction of functional devices requires the creation of unique molecule structures like cables and switches. Methods for separating the molecular network's electrical structure from the underlying substrate are needed to fulfill these purposes.

In the initial part of this chapter, the focus will be placed on providing an overview of the current advancements in assembling functional molecular structures within the constraints of two-dimensional surfaces, highlighting the transition in the field from primarily 2D (monolayers) to 3D structure (bilayers and multilayered systems). Following this, the second section of this chapter will be concerned with introducing 'on-surface' synthesis as a powerful tool for the highly precise fabrication of functional nanoarchitectures, where we represent the main key factors and parameters that help to trigger and manipulate chemical reactions in a controlled manner at the molecular scale. Finally, the last section will explore the future directions and perspectives for this domain of research. AFM (noncontact atomic force microscopy) and STM (scanning tunneling microscopy) in ultra-high vacuum (UHV) are used to illustrate concepts in select instances from the literature.

I.1 Self-assembled nanostructures

One possible path toward the main goals of nanotechnology, especially molecular electronics, is the assembly of functional molecular building blocks on a surface, which may enable the development of electronic circuits based on the functions of individual molecular species [3,4]. The bottom-up on-surface assembly of molecular building blocks into massive and extended structures can be achieved using many approaches. If extremely weak non-covalent intermolecular interactions support these nanostructures, they are categorized as supramolecular chemistry [5]. Noncovalent intermolecular forces that commonly occur within molecular assemblies confined to two-dimensional structures can be categorized into various types. These include hydrogen bonding, van der Waals forces, dipole-dipole interactions, π-π stacking, metal-organic coordination, and halogen-halogen interactions, among

others. Additionally, effectively manipulating molecular units on surfaces largely relies on factors such as the atomic composition of the substrate, the chemical reactivity of surface atoms or adatoms, adsorption energies, and the symmetry of the surface. Achieving complex self-assembled arrangements requires a delicate balance between intermolecular forces and molecule-surface interactions.

Noncovalent interactions	Energy (eV)	Distance (nm)	Reference
Van der Waals	E ≃0.02-0.1 eV	<1nm	6
Interaction π-π	E ≃0.1eV	0.33-0.38 nm	7
Hydrogen bond	E ≃0.05- 0.7 eV	0.15-0.35 nm	8
Halogen bond	E ≃0.05- 1.86 eV	0.26-0.36 nm	9
Metal-organic	E ≃0.5- 2eV	0.15-0.25 nm	10

Figure I.1: Category of noncovalent interactions.

I will focus on π-π interactions, halogen bonds interactions, and van der Waals forces as these are the primary areas of interest in my thesis, particularly in the research presented in Chapter V.

I.1.1 π-π interactions

Interaction forces between aromatic groups often referred as π-π interactions, are dedicated to the attraction and repulsion interactions that occur between molecules that possess π-electron system. These interactions are caused due to the electron deficient plan of H atoms and the π electrons which often refers as interaction between two neighboring aromatic rings. According to the relative orientations of the aromatic rings, three conformations were distinguished, the face to-face orientation where two benzene cycles are face-to-face aligned (Figure I.2 a), the T-shaped orientation where the extremity of one cycle points perpendicularly towards the center of another cycle (Figure I.2 b) and the parallel displaced orientation where two cycles are parallel but with an offset (Figure I.2 c).[11] π-π interactions are shown as one of the notable interactions for engineering self-assembly especially with molecular building block that possess π-conjugated moieties and in that way by π-π stacking stabilize two dimensional and three-dimensional growth of organic supramolecular nanostructures on surfaces.

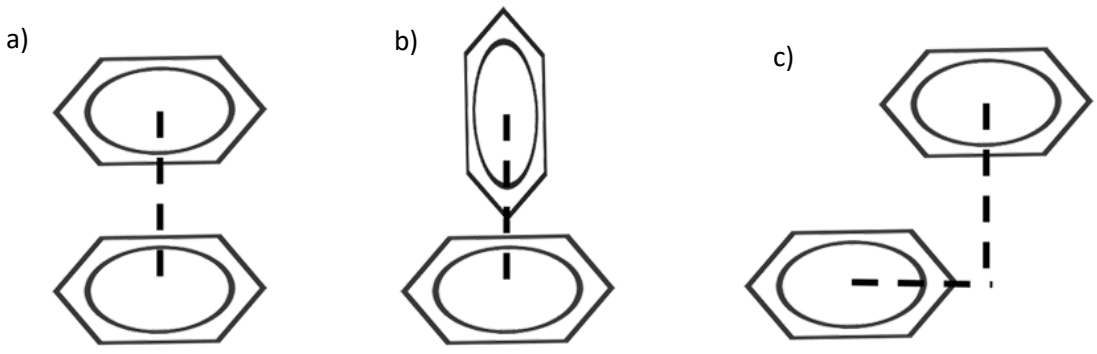

Figure I.2: Three orientations of the aromatic–aromatic interactions: a) Face-to-face b) T shaped and c) Parallel displaced conformations.[11]

I.1.2 Halogen bonds

Supramolecular networks are often built using weak interactions such as van der Waals forces, π–π stacking, and hydrogen bonding. However, increasing attention has been drawn to utilizing stronger interactions, like halogen bonds and metal-organic interactions, due to their capacity to form more

stable systems. A halogen bond is characterized by a net attractive interaction between an electrophilic region (electron-deficient area) associated with a halogen atom in one molecular entity and a nucleophilic region (electron-rich area) in another, or even the same, molecular entity. XB exhibits a high directionality, because the electron density in halogen atoms is anisotropically distributed.[12,13] A structural scheme for XB is shown in Figure I.3.a. The directionality of XB refers to the angle between the R-X covalent bond and the X--X or X--Y noncovalent bonds. The different directionality of such XB is attributed to the bond formation. The type-I interaction is of van der Waals type that arises from close-packing requirements, where the angles between two groups R-X are identical ($\theta_1 = \theta_2$) as presented in Figure I.3.b. The type-II interaction is an attractive interaction between the electro-deficient area and electron-rich areas of halogen atoms where the angels (θ_1 and θ_2) are different (Figure I.3.c). Many investigations reveal that the type-II interaction is most favored by the order of iodinated derivatives > brominated derivatives > chlorinated derivatives.

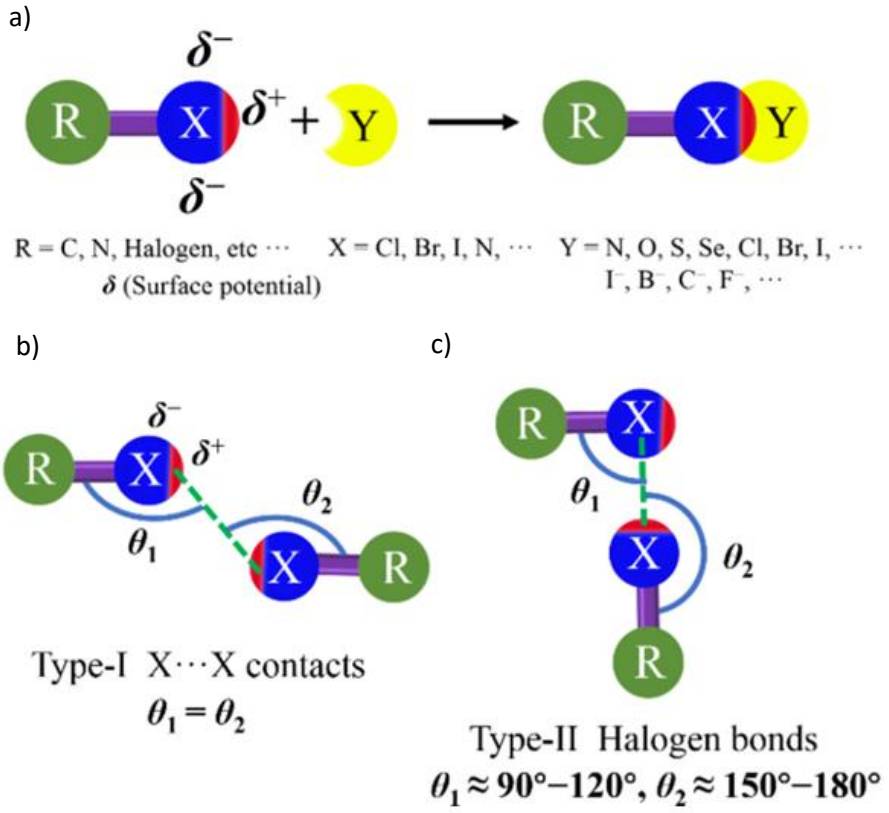

Figure I.3: a) Structural scheme for a halogen bond (XB). b) Structural scheme for type-I (left) and type-II (right) halogen interactions. X=halogen atom; R =C, N, O, halogen atom, etc.[12]

I.1.3 Van der Waals forces:

Van der Waals interactions are both attractive and repulsive electrical forces that arise from fluctuations in polarized charge between atoms, leading to non-specific and non-directive interactions. Despite being the weakest type of intermolecular interaction, they are the most prevalent non-covalent force in nature. These forces play a significant role as either the dominant or supporting intermolecular force in the self-assembly of supramolecular structures, especially in two-dimensional confinement on surfaces. According to the literature, 2D self-assemblies formed from organic molecular building blocks with lateral alkyl or alkoxy chains are stabilized by Van der Waals interactions. These chains tend to interlock, or interdigitate, with one another, resulting in densely packed two-dimensional nanostructures. Due to the high stability of these nanostructures, 2D self-assemblies on surfaces can be studied under ambient conditions rather than requiring ultra-high

vacuum environments. Under UHV conditions, a large variety of atomically flat metal surfaces are possible; however, many of them are unstable at ambient conditions or when exposed to a liquid solution. In those circumstances, more inert material is sought, such as highly oriented pyrolytic graphite (HOPG), MoS2, and MoSe2,[13] which have been the preferred substrates for physisorbed monolayers of organic molecules. The self-organization of normal alkane molecules on graphite surfaces has been widely investigated since the 1970s.[14,15] Zimmt and colleagues proposed a clever approach in which the stereochemical morphology of monolayers of prochiral molecules shifts from a two-dimensional racemate to a two-dimensional conglomerate, this was accomplished simply by elongating the alkyl chains with one methylene unit.[16] Two 1,5-bis-(3'-thiaalkyl)anthracene derivatives (Figure I.4 a) with linear alkyl chains containing either 11 or 12 carbon atoms were adsorbed at the interface of HOPG and 1-phenyloctane. The STM images of the monolayers formed by the two compounds revealed a striking difference in the organization. The anthracene moieties in the compound with the C_{11}-alkyl chains alternate from row to row, thereby leading to a racemic monolayer with pg plane-group symmetry (Figure I.4 b). In contrast, the orientation of the anthracene moieties in the compound with the C_{12}-alkyl chains is constant within a given domain, which reflects the formation of a two-dimensional conglomerate monolayer with p2 plane-group symmetry (Figure I.4 c). The organization of the molecules within the monolayer is governed by both molecule–molecule and molecule–substrate interactions. Alkyl chains tend to align along one of the main symmetry axes of HOPG and methylene groups of adjacent chains align in registry to maximize the intermolecular van der Waals interactions. Optimization of the van der Waals interactions between the chains, in combination with their favorable all-trans conformation, then leads to the difference in the orientation of the anthracene moieties in adjacent rows.

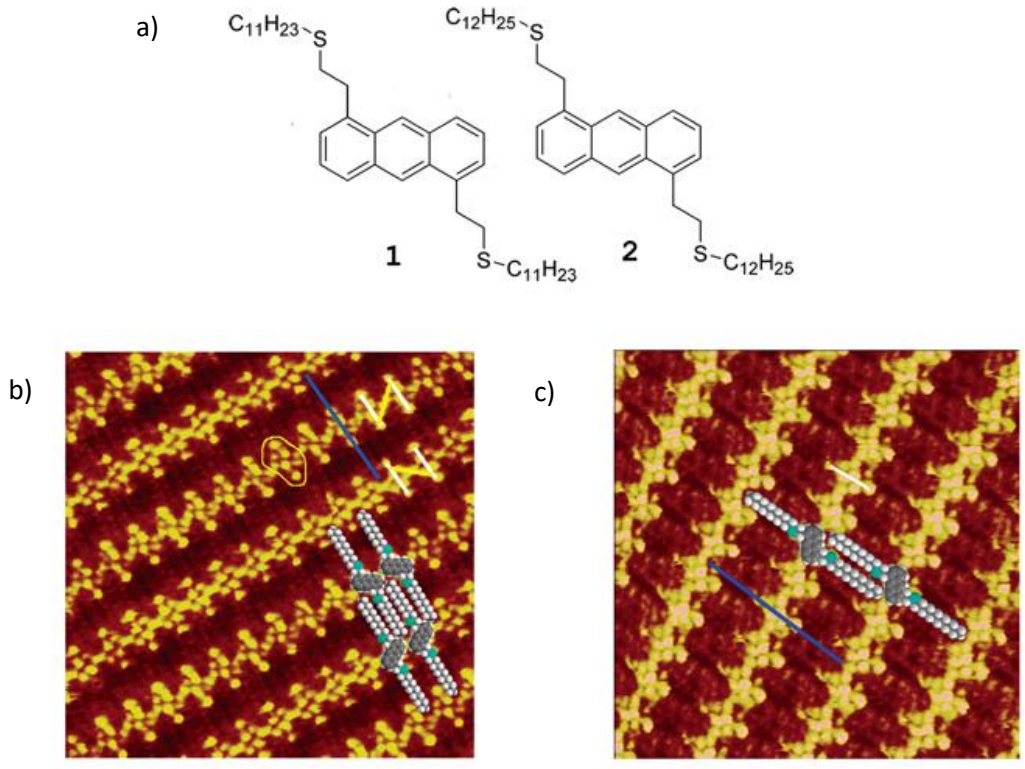

Figure I.4: a) Structures of 1,5-Bis-(3'-thia-tetradecyl) Anthracene (1) and 1,5-Bis-(3'-thia-pentadecyl) Anthracene (2) b) A 12x 12nm^2 constant current STM image of 1 adsorbed onto HOPG at-0.8 V (sample negative) and 280 pA. CPK models of 1 (sulfur atoms appear green) superimposed on adjacent rows of the image confirm adsorption via opposite enantiotopic faces. The blue bar indicates the length of one

molecule. White bars indicate the S-S distance in a single molecule. The overlapping white and yellow bars indicate the forward and backward N-shape referred to in the text. The circled region displays the eight-circle pattern c) An 11x11 nm^2 constant current STM image of 2 adsorbed onto HOPG at 0.8 V (sample negative) and 270 pA. CPK models of 2 (sulfur atoms appear green) superimposed on adjacent rows of the image confirm that all molecules in this region adsorb via the same enantiotopic face. The blue bar indicates the length of one molecule. The white bar indicates the S-S distance in a single molecule.

I.1.1 A paradigm shift from 2D to 3D self-assemblies:

A paradigm shift has developed in recent years, stretching the boundaries of our knowledge and potential uses of these assemblies. This transition focuses on the mechanics underpinning the change from primarily 2D structures to more intricate and adaptable 3D arrangements. The research is shifting from 2D to 3D supramolecular structures, namely from monolayers to bilayers and multilayers. The examination of the progression from 2D to 3D structures gives a new degree of control and utility. 3D supramolecular structures can be created in solution, on a solid surface, or at an interface. The transition to 3D assemblies enables the creation of more complicated and specialized materials with increased qualities that have the potential to change several technological sectors. Despite notable progress, the mastery of 3D self-organization remains incomplete, and less interest has been paid for bilayers and multilayers compared to monolayers and this could be attributed to several reasons:

- The more complicated mechanism behind these structural formations
- Difficulty in controlling the deposition procedure and repeating the resulting outcomes efficiently
- Controlling the interactions between the molecules in layers along the vertical direction to the underlying substrate surface

Scanning Probe Microscopies, such as scanning tunneling microscope (STM), and atomic force microscope (AFM), particularly in UHV conditions, provide the ideal toolset for delving deep into the structure-function relationship of surface supramolecular assemblies. UHV conditions eliminate the interference of contaminants and unwanted reactions, allowing precise control over the system under investigation. The nanoscale resolution and real-time imaging capabilities of SPMs enable us to visualize the dynamics of 2D to 3D transition at the molecular level, providing valuable insights into the processes governing this transformation. Addressing this paradigm shift Zeng and his colleagues reported bilayer formation of TPTC molecule over octanoic acid (OA)/highly oriented pyrolytic graphite (HOPG) interface, using a protocol that involves the mixture of two types of solutions that have different solubility, by which they have shown via STM that upon deposition, the vertical growth of TPTC on the bottom layer of self-assembled networks can take place gradually. The procedure involves the mixing of two kinds of solutions: Solution I is the saturated one, in which TPTCs were totally dissolved in OA and sonicated well while another solution II was prepared by placing some TPTC powders into the pure OA solution which then was shaken by hand, resulting in naked-eye-visible TPTCs (un-dissolved particles) in the solution. Then, both solutions I and II were mixed, and a droplet of this mixture was deposited onto the HOPG surface for preparing the sample as shown in figure I.5.b. Time is an important factor in the formation of bilayer structure. Solution II must be used within 30 min upon being prepared, or it does not work on forming a bilayer, because the un-dissolved TPTC powder will gradually dissolve into the solvent over time. In the utilized methodology, solution I ensure the formation of the monolayer (the bottom layer) on the surface, whereas the low solubility of solution II forces the occurrence of the vertical stacking of TPTCs on the surface forming bilayers.

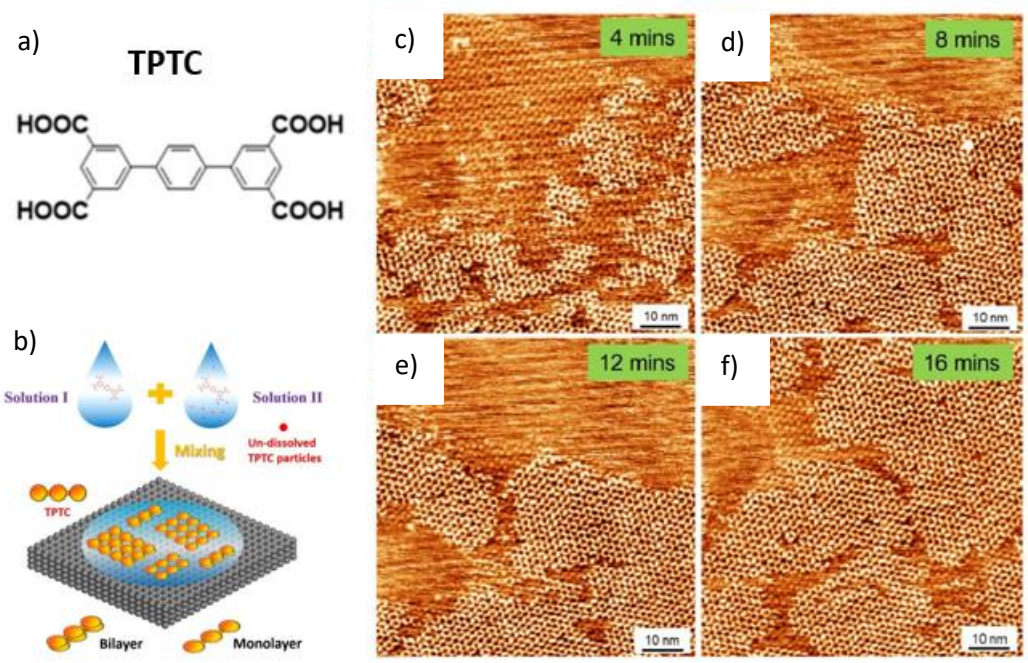

Figure I.5: a) Chemical structure of the TPTC used molecule. b) The schematic illustration representing the method developed in this work for forcing the vertical growth of TPTC. c-f) STM images showing the dynamics of bilayers function as a function of time. [17]

Supramolecular chemistry is defined as a three-way intersection of the natural sciences of chemistry, physics, and biology. Extending this issue from 2D to 3D entities necessitates a mix of scientific understanding and technical skills. Although the progression from monolayers to bilayers and multilayers has revealed previously unexplored territory, so-called "3D" structures remain surface structures. It may become an emergent issue shortly, namely, how to apply the information gained from this research to construct real-space 3D flawless structures, such as supramolecular single crystals. There is still a long way to go from constructed materials to practical applications, but the continued work in this direction will eventually enable new paths of investigation of the architectures and characteristics in 3D supramolecular materials for many organic electronics and optoelectronic devices, such as organic light-emitting diodes, and sandwich device where the electron transfer is from up to down, that is, vertical to the direction of the surface.[18,19]

I.2 On-Surface Synthesis

The exceptional electronic properties of molecule assemblies have raised enormous hopes for the capacity to fabricate novel electronics directly on surfaces. Despite the wide range of possibilities for creating extended 1D and 2D structures using a supramolecular self-assembly approach, the resulting nanoarchitectures are governed by weak noncovalent interactions, making them generally unsuitable for use in real-life functional devices. On-surface synthesis is a developing field of research that aims at making use of well-defined solid surfaces as confinement templates to initiate chemical reactions. On-surface polymerization is the formation of covalent bonds between molecular building blocks directly within the two-dimensional confinement of surfaces. Several figures of merit are presented by on-surface chemistry. First, the structures created acquire ideal stability, resulting in stable conformations and, as a result, temporal invariance with minimal heat loss of structural characteristics. As a result, they may be transported from the substrate where they were produced, making them more appropriate for applications. Another distinguishing property of covalent assemblies is excellent

electron transport across the generated links, which makes the networks suitable for molecular applications [20,21]. Third, these mechanisms may result in the formation of molecular species that cannot be synthesized using standard wet-chemistry protocols, as opposed to solution reactions, where molecules are confined in two-dimensional space. Finally, this method necessitates the application of surface science characterization techniques as well as highly controlled conditions decreasing the possibility of contamination leading to chemically pure structures.

On the whole, on-surface fabrication of covalently bonded structures belongs to the class of interfacial chemical reactions that occur on the solid surface and cannot be avoided due to the presence of interactions with the adsorbed precursors. As a result, the type and arrangement of both the solid surface and the molecular guest influence molecule-surface interactions, identifying precursor diffusion capacity and adsorption energy. Indeed, the surface's reactivity is an intrinsic characteristic, which might minimize energy barriers by opening up novel reaction pathways in which originally guested molecules react with surface atoms to generate certain intermediates. The process is described as catalytic if the reaction produces a final product that does not involve the surface atoms as reactants, i.e., the surface is regenerated at the end of the reaction. When the products stay adsorbed on the surface, the reaction is referred to as "on-surface polymerization," even if it involves a catalytic reaction phase. On surface reaction mechanisms, the balance between absorption energy and molecular diffusion is particularly critical, yet precise substrate selection is required to produce the desired effects. The surface material and its atom arrangement orientation are two aspects to consider when selecting a solid substrate. So far, the on-surface covalent coupling methodology has relied on a limited set of useful carbon-carbon bond-forming reactions: cyclodehydrogenation (CDH), dehydrogenative oligomerization or polymerization, radical dimerization (analogous to Ullmann coupling), carbene dimerization, and aryl halide-alkyne coupling. CDH (intramolecular oxidative C-C coupling) and dehydrogenative oligo- or polymerization (intermolecular oxidative C-C coupling) are two of the most appealing of these processes. Formally, the mechanisms correspond to the C-H activation of both precursors followed by (cross)coupling.[22]

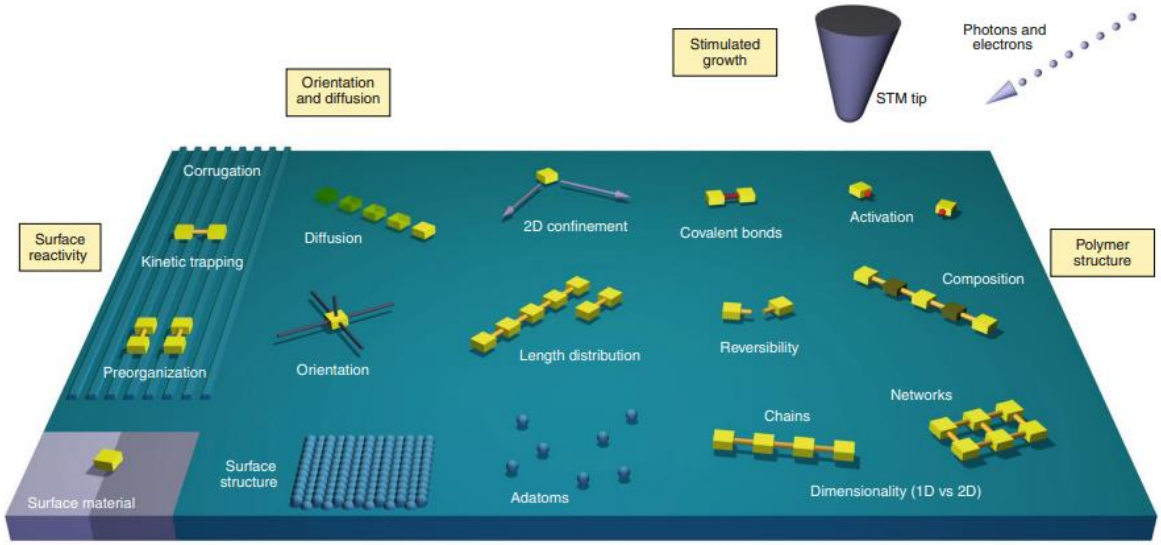

Figure I.6: Key aspects of on-surface polymerization. [23] It highlights the role of surface reactivity, including the surface material, structure, preorganization, kinetic trapping, and corrugation, which affect molecule adsorption and diffusion. The orientation and diffusion of precursor molecules, along with 2D confinement and length distribution, are crucial for polymer growth. External stimuli, such as photons, electrons, and the use of an STM tip, stimulate growth and activate the polymerization

process, leading to the formation of covalent bonds. The resulting polymer structures can vary in composition, reversibility, and dimensionality, forming either linear chains or complex networks.

In contrast to solution reactions, on surfaces molecules are confined in two-dimensional space, reducing their degrees of freedom as they diffuse by the underlying substrate, resulting in fundamentally different chemical reactions where many surface and molecule-related parameters can affect the reaction. The following points summarize the several elements that must be considered (Figure I.6) since they directly influence the on-surface responses in this concept:

I. The many on-surface chemical processes that can be used for bottom-up synthesis of covalently bound nanostructures.

II. The importance of developing molecular building blocks that allow the reaction to be carried out while keeping in mind the underlying surface and ensuring the development of a well-defined target structure and end-product composition. Diffusion of the activated monomers and intermediate oligomers is another key issue since it defines the rate of polymerization.

III. The role of the solid substrate surface as a reactive platform, composed of a highly ordered arrangement of atoms, surface structure plays an important role in the reactions. Not only because it lowers the energy barrier, but also because it brings together different adsorbed precursors through a diffusion mechanism. The first process is related to the energetics of the system, whereas the second is to kinetical aspects. Whether the reaction is driven by kinetics or thermodynamics depends on the diffusion/deposition-rate ratio.

The recently formed covalent bonds nature may be demonstrated not only by real space distances and orientations but also by spectroscopic detection of distinctive electronic states. A hierarchical growth scheme might be obtained when utilizing distinct halogen substituents because selective and sequential activation of the different substituents leads to programmed molecule reactivity. Based on the accumulated mechanistic knowledge and the capacity to guide reactivity by creating appropriate monomer building blocks and utilizing the surface as a template, 1D and 2D polymers with increasing structural and compositional complexity will emerge. Aside from the ongoing investigation of on-surface polymerization as a novel approach for producing specified nanostructures, the qualities and functionalities that arise will become increasingly relevant in the future. It is inconceivable to address all examples conducted in surface polymerization reactions in detail due to the multiple aspects that influence different phenomena occurrence. This portion will focus on the most important points to achieve a successful on-surface synthesis reaction. The upcoming sections will provide a detailed overview of the following crucial aspects that need to be considered when making choices to succeed in on-surface reactions:

I. Possible polymerization approaches: step-growth and chain-growth.

II. The importance of designing precursor molecules to control the reaction product.

III. Different types of solid substrates: metal, semiconductor, and insulator.

IV. Different possible stimuli that contribute to polymerization initiation, such as heat treatment, collisional dissociation, UV irradiation, and tunnel current.

I.2.1 On-surface different polymerization approaches:

Polymerization processes comprising an activated form of pre-absorbed molecular precursor are used to fabricate covalently bonded nanostructures on the surface. The nature of the reaction mechanism

used to link the monomers determines whether the polymerization proceeds step-wise to form oligomers, which dimerize into larger oligomers and subsequently assemble into polymers, as in typical step-growth polycondensation [24], or the possibility that the polymerization occurs exclusively at the growing polymer chain end, resulting in linear growth of the molecular weight with increasing monomer conversion, as in 'living' chain-growth polymerization [25]. Polymerization happens in a step-by-step process in which all monomers are activated simultaneously, then spread and collide to form bigger oligomers, as shown in Figure I.7a. Since all activated monomers are comparable, it may be assumed that they produce dimers at the same rate. Because most of the monomers have already interacted, when one end of the dimer begins to react again, it will most likely discover another dimer or oligomer. Considering the kinetics during the polymerization of a solid surface, the mobility and the reactivity of the (activated) monomers (and intermediate oligomers), and their molecular weights are crucial steps that dictate the polymerization outcome.

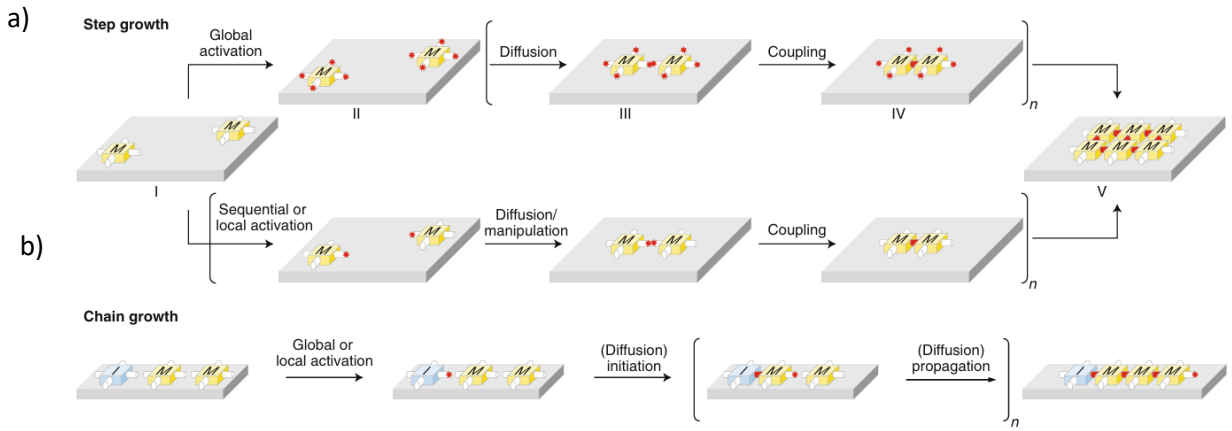

Figure I.7: A general mechanistic depiction of approaches to on-surface polymerization. a) Global, sequential, or local activation in phases, followed by diffusion/manipulation and coupling steps. b) Chain growth requires global or local activation, followed by initiation and propagation. [23]

Chain-growth polymerization primarily differs from step-growth polymerization through the introduction of initiation, propagation, and termination reactions. Local activation of the precursor is sufficient to form a reactive center known as an "initiator" in the chain-growth strategy. As illustrated in Figure I.7b, an initiator turns one monomer molecule into a reactive intermediate that may react with another monomer to generate a new reactive intermediate, and so on. In this situation, the polymerization process occurs at the end of the chain, resulting in linear development of the molecular weight as a function of monomer conversion. As a result, the pace of the reaction does not alter during the reaction since it relies on monomer diffusion to allow longer polymers to develop. Still, due to a lack of suitable precursors that are thermally stable during evaporation and the limited types of bonds that can be created on the substrate without interfering with or quenching chain propagation, on-surface polymerization studies based on the chain-growth approach are rarely performed. Most of the explored reactions on solid substrates are step-growth polycondensation reactions that involve the formation of small by-products at each activation-coupling sequence.

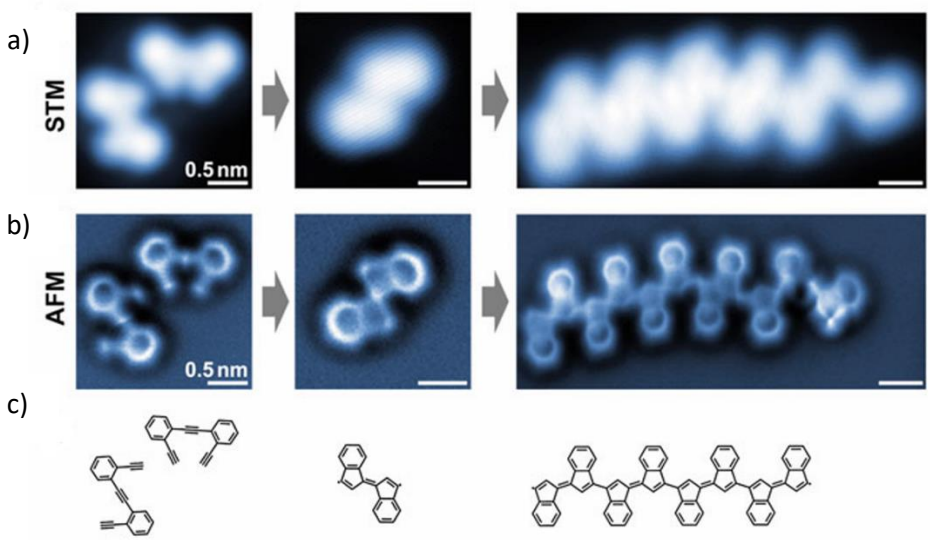

Figure I.8: a) STM and b) AFM images along with c) the derived chemical structure models show the thermally induced cyclization of 1,2-bis (2-ethynylphenyl)ethyne on Au(111) towards an (E)-1,1'-bi(indenylidene) diradical, which then reacts towards poly-(E)-1,1'-bi-(indenylidene) chains via radical step growth. [26]

For single-molecule studies of chemical transformations, scanning probe methods, especially scanning tunneling microscopy (STM) and atomic force microscopy (AFM) with functionalized tips offer better spatial resolution as shown in Figure I.8 for imaging the chemical structure of organic molecules, making this technique particularly suitable for investigations of on-surface chemistry.[26-33] However, the comparatively long acquisition time required to record images with chemical-structure resolution is one of the primary disadvantages of this approach. In principle, it is possible to control the reaction rate of a chemical transformation by variation of the reaction temperature, which opens up the possibility of investigating reactions in situ. They grew 1D chains of the oligoacetylene derivative oligo-(E)-1,1'-bi(indenylidene) on a surface through a thermally induced radical cyclization/step-growth polymerization process. Individual oligomer chains exhibit extended 1D electronic states and alternating bond lengths. This radical polymerization process on surfaces provides a new route toward fully conjugated low-bandgap derivatives of all-trans polyacetylene.

I.2.2 Precursor design

Naturally, the most crucial factor in regulating the reaction result is the thoughtful design of the precursor molecule. It is possible to modify the aromatic backbone without affecting the reactive groups. This allows for tight control over both the lattice size and the resultant network's symmetry. Precursor design is another way to modify the reaction pathway, for example, by adding side functionality (a substituent that does not contribute directly to the coupling reaction) providing steric hindrance, or modulating the whole reactivity. A great deal of research has been done on the impact of halogen type on Ullmann coupling reactions.[34-37] The strength of the carbon-halogen bond varies depending on the kind of halogen, which affects the dehalogenation temperature. However, the halogen type can also have indirect impacts on the extent, orientation, and structure of associated polymers. Next to the halogen type, fine control over the dimensions of subsequent nanostructures can be approached by altering both the number and exact positions of halogen atoms in molecules. The degree of halogenation in the molecules is a critical component that may be used to construct nanostructures with specific properties.

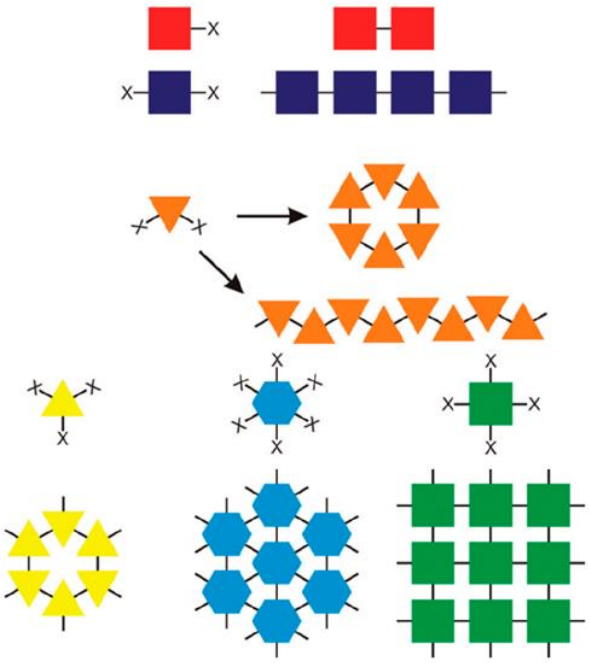

Figure I.9: This image illustrates the assembly of various molecular building blocks into supramolecular structures through covalent on-surface polymerization. Red and blue squares represent monomers forming linear polymers, orange triangles form cyclic structures and extended arrays; yellow triangles assemble into hexagonal rings; blue hexagons create a two-dimensional network; and green squares form a grid-like 2D network. The arrows indicate the progression from individual monomers to complex supramolecular structures, highlighting the versatility of covalent on-surface polymerization depending on the location of the active groups in the adsorbed monomers over the surface.[38]

This essential concept is shown in Figure I.10, different TPP-based monomer building blocks with one, two, and four Br substituents were synthesized to study the capacity to alter the architecture of the final molecular nanostructures (Fig. 10a-c), and all species were placed onto an Au(111) surface that was held at a low temperature and then thermally activated the Br dissociation. Using low evaporator temperatures, intact molecules were identified: the STM images following preparation demonstrate the predicted distinct structures (Fig. 10d-f). If the monomer building block only has one reactive side BrTPP, the only probable consequence is a dimer, as shown in Fig. 10 g j. Porphyrin building blocks with two reactive sides, such as trans-Br2TPP (Fig. 10b), allow for the production of long and linear chains, as seen in Fig. 10h, k. When all four porphyrin unit legs have Br substituents (Fig. 10c), the formation of a two-dimensional molecular network is possible (Fig. 10i, l). This demonstrates that careful molecular design, the arrangement of active end groups within the molecular framework of a single building block, and successful ex-situ organic synthesis of the initial building blocks provide high control over the final architecture of molecular structures.

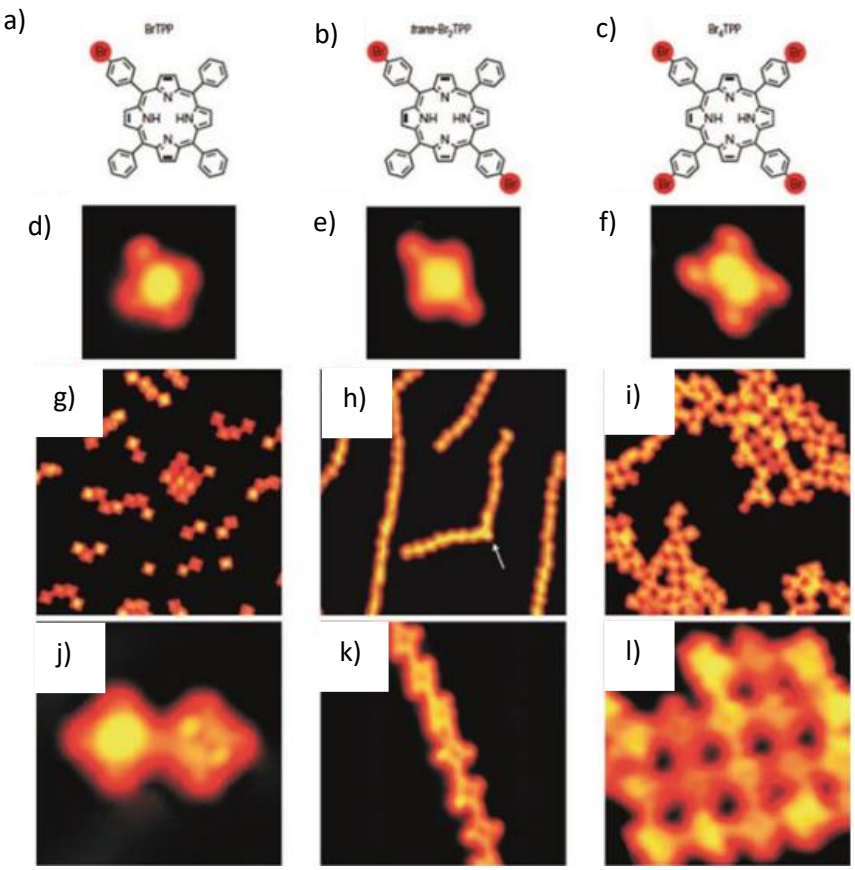

Figure I.10: Building nanoarchitectures using different monomer building blocks carrying one (left column, prepared by method I: intact molecules are deposited onto the surface, where they are subsequently activated by dissociation of the substituent atoms upon heating of the sample), two (middle column, prepared by method II: the molecules activation has already occurred in the evaporator, and the activated molecules are subsequently deposited on the surface, kept at room temperature), and four (right column, prepared by method I) Br substituents (a–c). STM images (3.5 × 3.5 nm^2) of the single intact molecules (d–f). Overview STM images (30 × 30 nm^2) of the nanostructures after activation and connection (g–i). Detailed STM images of the resulting nanoarchitectures (j 5 × 5 nm^2; k 10 × 10 nm^2; l 8.5 × 8.5 nm^2). [27]

I.2.1 Surface as active support for on-surface synthesis

The purpose of this section is to clarify the variety of substrate types that are utilized to initiate chemical reactions on the surface.

I.2.1.1 Metal surfaces

Metal surfaces are vital for on-surface synthesis because they can control and catalyze chemical processes at the interface between them and the adsorbates. Researchers can manipulate reaction routes and product selectivity by employing diverse metal surfaces. Different metal surfaces, often characterized by their low indices (hkl), are commonly employed in coupling reactions, sometimes even using the same molecule. This approach facilitates the examination of how altering the composition of surface constituents influences the reaction pathway. The 12 existing metal elements can be categorized into distinct groups: the Platinum group metals (Ru, Rh, Pd, Os, Ir, and Pt), the base metals (Fe, Co, Ni), and the coinage metals (Cu, Ag, Au). Each group showcases particular physical characteristics and the capacity of its constituent elements to interact with specific species. The enormous interest in highly stable and electronically conjugated networks calls for a coupling

chemistry that establishes new C–C bonds. To this end, the surface variant of classical Ullmann coupling as introduced by Grill et al. is highly appropriate.[27] The principal reaction scheme is relatively straightforward: halogenated precursor molecules are deposited onto a metal surface, and upon adsorption, the weakly bonded halogen substituents are split off with the aid of the catalytic properties of the metal surface and nature of halogen, dehalogenation results in so-called surface-stabilized radicals (SSR), the further progression of the coupling reaction strongly depends on the metal surface nature and molecule type. Typically the fcc(111) transition metal surfaces of Cu, Ag, or Au are the most used ones in literature, and to address the molecular building blocks are often functionalized with bromine and iodine. DFT calculations suggest that the total exothermic dehalogenation has an activation barrier in the range of 0.5–1.0 eV.[39] The comparatively high adsorption of the spit-off halogens is partially responsible for the energy gain. The activation barrier is almost 0.3 eV lower for iodine substituents than for bromine substituents on all surfaces examined, and it declines in the sequence Au > Ag > Cu, or with increasing reactivity of the metal surface as shown in Figure I.11. Taking into account the variations in the strength of the carbon-halogen bond, this tendency seems reasonable. However, the bond dissociation energy of C–I is almost 0.65 eV is lower than for C–Br in iodobenzene versus bromobenzene [40], indicating a distinct surface influence.

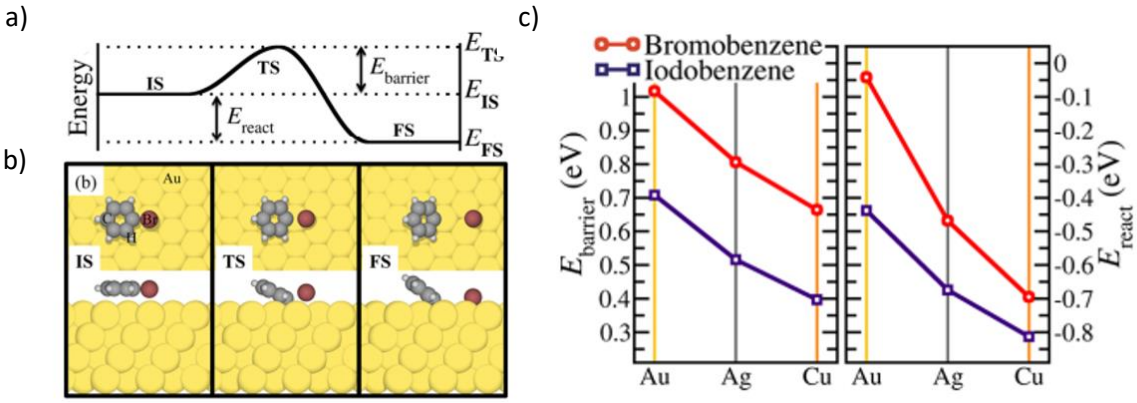

Figure I.11: (a) Definitions of the energy barrier ($E_{barrier}$) and reaction energy (E_{react}) for dehalogenation reactions. (b) The dissociation of bromobenzene on Au(111), depicts top and side views of the initial state (IS), transition state (TS), and final state (FS) of the reaction. (c) $E_{barrier}$ (left) and E_{react} (right) for the dissociation of bromobenzene and iodobenzene on the (111) facets of Au, Ag, and Cu. [39]

Precursors that have been iodinated are more reactive, and even on less reactive gold surfaces, deiodination happens efficiently at room temperature (RT). On the other hand, in the case of brominated chemicals, the metal surface's reactivity is crucial. While bromine may be removed from copper at ambient temperature, gold needs to be heated an additional 150–200°C.[41,42] At room temperature, the silver surface occupies an intriguing intermediate point where bromine is partially removed, but bromine must also be heated further to be completely removed. The experimental data that is currently available for the deiodination and debromination of several halogenated compounds following RT deposition on Au(111), Ag(111), and Cu(111) is summarized in Figure I.12. The stabilization of radicals produced during dehalogenation into so-called surface stabilized radicals (SSRs), in which the dangling carbon bonds attach to the underlying metal atoms on the surface, is another important function of the surface. This process makes the metal surface extremely important to the coupling reaction process. Intrinsic atoms break the bonding step on reactive Cu(111) and Ag(111) surfaces, causing SSRs to form intermediate organometallic complexes called protopolymers

based on carbon-metal-carbon bonds. To liberate the metal atoms and change the metastable organometallic linkages into irreversible covalent bonds, more heat treatment is needed. On the comparatively inert Au(111) surface, the widely held belief is that SSRs spread around and, upon impact, form covalent bonds. This implies that the creation of irregular networks with high defect density generally takes place and that the coupling process is kinetically regulated on the Au(111) surface. As a result, the characteristics of the metal surface affect the bottom-up development process. In conclusion, the reactivity of the surface and the mobility of precursor molecules are the two primary determinants. While an inert surface permits molecules to flow freely but would need more heat to initiate the dehalogenation process, a highly reactive surface lowers the dehalogenation barrier but is unable to offer adequate diffusion. Furthermore, more reactive surfaces might guide competing reaction routes and improve interactions with adsorbed precursors.

$d^{10}s^1$ metal	**Bromine Cleavage**	**Iodine Cleavage**
Cu(111) Organometallic	Full @ RT	Full @ RT
Ag(111) Organometallic	Partial @ RT Full @ 150°C	Full @ RT
Au(111) Rarely Organometallic	None @ RT Full @ 180°C	Full @ RT

Figure I.12: Dehalogenation of brominated versus iodinated precursors and occurrence of organometallic intermediates for different metal surfaces. [42]

The hexaiodo-substituted macrocycle CHP was shown to adsorb and self-assemble on the coinage metals Cu, Au, and Ag's well-defined (111) surfaces (figure I.13), according to research by Bieri and colleagues. STM analysis shows that the adsorption of CHP on both surfaces proceeds via a dissociative pathway with selective breaking of C-I bonds, leading to the generation of surface-stabilized CHP radicals and coadsorbed iodine atoms. Annealing the appropriate substrate to about 475 K (Cu), 525 K (Au), and 575 K (Ag) temperatures thermally activates the subsequent covalent intermolecular bond formation between CHP radicals toward covalently linked polyphenylene networks. On the three substrates, the polymer networks exhibit notably diverse morphologies: on Cu(111), they exhibit branching, fractal-like patterns, whereas on Ag(111), they exhibit extended, conventional 2D networks, while on Au(111) the homocoupling of CHP leads to a mixture of branched and denser polyphenylene clusters. The three different cases are shown in Figure I.13 as revealed by the STM images. The balance between the diffusion and coupling stages on Cu and Ag is noticeably different, according to the DFT study of the diffusion and coupling routes. After the first diffusion barrier is removed, the radicals on Cu spontaneously form covalent intermolecular connections. On the other hand, on Ag, diffusion prevails over intermolecular coupling, leading to regular 2D network creation and an overall increase in the mobility of the radicals on the surface. Furthermore, simulations clearly show that defects in the network clusters have to be predicted even under favorable growth circumstances, indicating the intrinsic structural imperfection of surface-supported two-dimensional polymers based on irreversible processes. The findings suggest that the substrate plays a crucial role in shaping the morphology of self-assembled covalently bound nanostructures, in addition to serving as a static support and actively participating in every stage of the reaction.

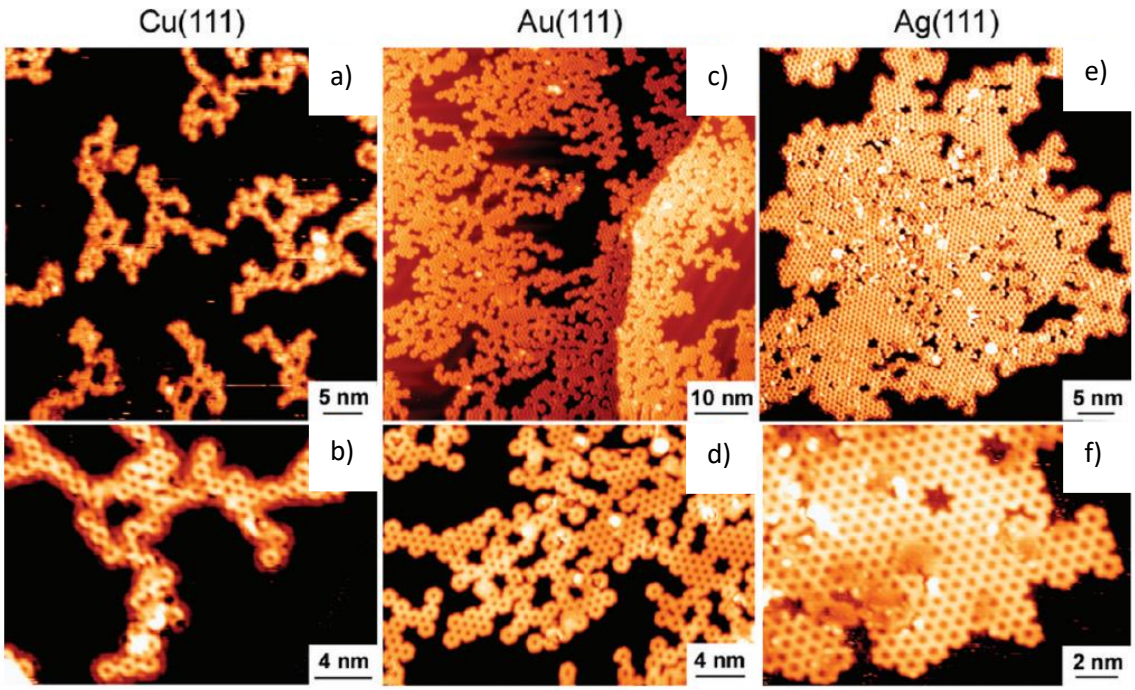

Figure I.13: Top panels: Overview STM images of polyphenylene networks on Cu(111), Au(111), and Ag(111). Bottom panels: High-resolution STM images of the polyphenylene networks shown above. Tunneling parameters are (-2 V, 20 pA) (a), (1.5 V, 300 pA) (b), (-1 V, 50 pA) (c), (-1 V, 50 pA) (d), (-0.8 V, 50 pA) (e), and (-1 V, 50 pA) (f). [43]

I.2.1.2 Semiconductor surfaces:

The extreme reactivity of semiconductor surfaces, which often restricts molecular transport and inhibits covalent coupling, has made them an uncommon choice for surface synthesis. In active places where reactions might occur, dangling bonds are often abundant on clean semiconductor surfaces created under UHV conditions. To comprehend molecule attachment processes and how they might be manipulated at the atomic level, research on the organic functionalization of semiconductor surfaces under vacuum is also active. The reactive sites of the semiconductor surface result in products remaining grafted to the surface, which can be problematic for bottom-up fabrication of organic nanostructures by on-surface coupling reactions. However, a saturation of surface dangling bonds could help to overcome such drawbacks by passivating the surface or by reconstructing the surface of the highly boron-doped silicon substrate, known as B-doped Si(111)-√3x√3R30°, leading to decoupling molecules from the substrate, thus to improve their mobility. Olszwski et al. reported that it is possible to induce aryl halide polymerization on hydrogen-passivated germanium surfaces. The molecular precursors, i.e., DIBA molecules, deposited onto a Ge(001): H surface at temperatures in the range 200–235°C formed short oligomers as shown in figure I.14.[44] The reaction yield was too low to make this strategy useful for building molecular-size electronics in the future. The passivating layer's thermal instability is the limiting factor. At temperatures higher than 250°C, the buffer layer undergoes substantial dehydrogenation. The absence of a buffer layer prevents the precursors from diffusing between molecules, which in turn prevents covalent interaction between molecules.

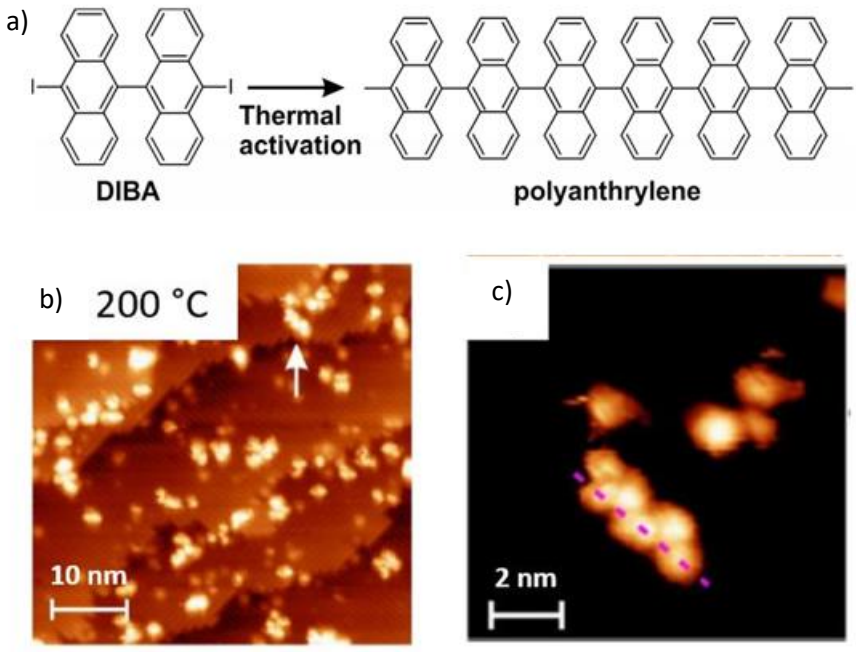

Figure I.14: a) Scheme for the polymerization of 10,10'diiodo9,9'bianthryl (DIBA) resulting in a polyanthrylene chain. b) STM image (-2V; 10 pA) of DIBA molecules deposited on Ge(001):H surfaces kept at 200 °C indicating the appearance of chain-like structures. c) Zoomed STM image indicating that the formed structure is a polyanthrylene trimer adsorbed on Ge(001):H surface. [44]

I.2.1.3 Bulk or thin insulator surfaces

On-surface synthesis processes on metallic substrates have been the subject of several research. However, on-surface synthesis on insulating substrates remains mainly unexplored. Comparatively speaking, insulating substrates are not easily accessible for experimentation, which presents a significant challenge for studying them. Conventional surface science techniques, such as scanning tunneling microscopy (STM), photoelectron emission spectroscopy (PES), and low-energy electron diffraction (LEED), are dependent on materials that conduct electricity, as a result, they are often not applicable to non-conductive surfaces.[45] For maintaining accessibility by standard surface science characterization methods such as STM, experiments have been carried out on a thin insulator film supported by a metallic substrate. In addition to this technical portion, the relatively weak and generally unknown interaction of the educt molecules with the supporting insulating substrate presents unique hurdles for on-surface synthesis on insulating substrates. Because the class of insulating materials is far more diverse than the class of metals, the interaction of organic molecules with electrically insulating surfaces is not as well-known as it is for metal surfaces.

For prototypical insulating surfaces studied so far, namely KBr(001), CaF2(111), and NaCl(001), the interaction with organic molecules is comparatively weak. This statement takes into account both the surface diffusion barrier and the binding energy of the molecules toward the surfaces. [46-51] On these surfaces, the weak contact inhibits molecule self-assembly and, in most circumstances, the performance of on-surface synthesis reactions since annealing would cause desorption rather than the start of the reaction. Investigating ways to improve the molecule-surface interaction is therefore a necessary first step. [52] In this regard, several approaches have been used, such as electron irradiation surface modification and giving the molecules certain anchor groups. [53,54] Another reason for favoring synthesis on inert (insulator) surfaces is the absence of a surface-mediated C-C coupling step consisting of the addition of surface-stabilized radicals SSRs (protopolymer) compared to metal surfaces.

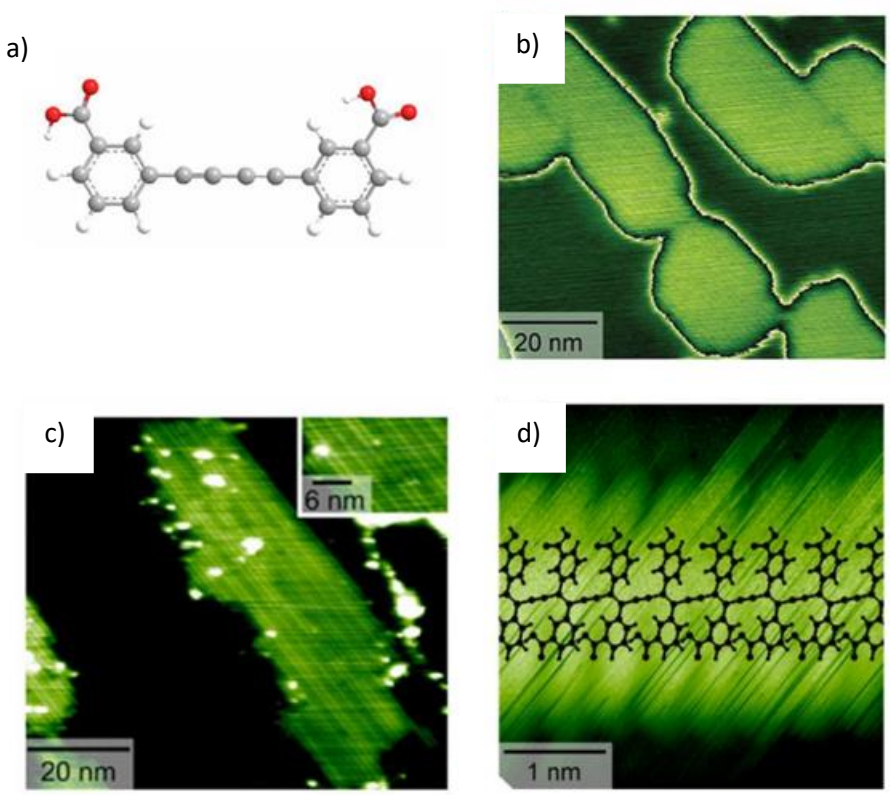

Figure I.15: On-surface reaction on a bulk insulating substrate. a) Representation of the 3,30-(1,3-butadiyne-1,4-diyl)-bisbenzoic acid molecule. b) AFM image of 3,30-(1,3-butadiyne-1,4-diyl)-bisbenzoic acid molecule deposited on calcite. c) AFM image of 3,30-(1,3-butadiyne-1,4-diyl) bisbenzoic acid molecule adlayer after overnight irradiation at 302nm. Lines correspond to polymerized chains (d) Zoom onto a chain-like molecular row with superimposed diacetylene polymer structure form DFT. [55]

Richter A. and his co-workers presented evidence for a diacetylene polymerization carried out on bulk insulator surface through adsorbate excitation, presented in Figure I.15. Using dynamic AFM under ultra-high vacuum conditions they showed that 3,3'-(1,3-butadiyne-1,4-diyl)bisbenzoic acid precursor molecules deposited on calcite form ordered islands with a (1x3) inner structure. Irradiation of the surface with a mercury lamp or annealing the substrate at 485 K results in a distinct change in the molecular structures. New row-like (figure I.15.d) structures formed on the surface that exactly match the expected polymer chains in appearance and repeat distance. This work highlights that the concept of diacetylene polymerization can be transferred to bulk insulator surfaces, this is vital for generating conductive polymer chains that connect functional molecular devices.

I.2.2 External stimuli

This section aims to elucidate the four distinct external triggers capable of initiating chemical reactions on surfaces.

I.2.2.1 Collision-induced reactions:

Chemistry is concerned with the manipulation of atomic bonds to harness chemical processes to generate desired compounds. To achieve this purpose, one must first understand how selection arises. Chemical reactions that occur as a result of molecule-surface collisions are both technologically and

fundamentally significant. Bond-selective reactions have been observed in a molecule-surface collision by stimulating certain vibrational modes of a molecule just before the surface impact. [56-59] This method works because the abrupt buildup of energy in a specific molecular degree of freedom causes a reaction to occur before the deposited energy spreads to other degrees of freedom not participating in the reaction, i.e., before thermalization. [60,61] Collision-driven reactions often occur when an accelerating molecule collides with another molecule or medium, dissipating enough kinetic energy to cross the activation barrier. These processes are crucial in numerous disciplines, including heterogeneous catalysis, epitaxial material creation, and biomolecular analysis.[62-64] Chemists have long been captivated by the interaction of gas molecules with solid crystal surfaces, a phenomenon known as heterogeneous reactions. Surface physicists have recently been interested in this subject matter, gaining expertise in ultra-high vacuum environments. Conducting collision-induced reactions at low pressures, where various characterization methods like STM and XPS may be employed, allows for a better understanding of the mechanisms that may initiate new reaction pathways.

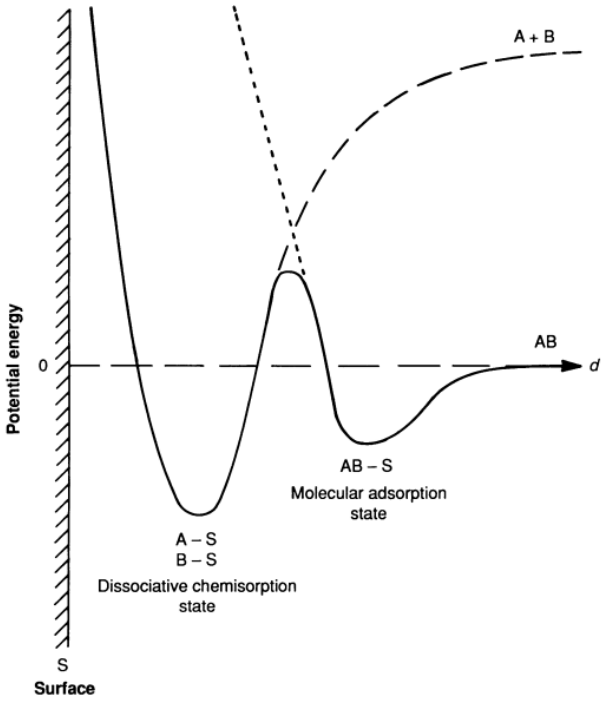

Figure I.16: Schematic diagram of the potential energy of interaction in one dimension between the center of mass of a molecule AB and a structureless surface as a function of the distance d between them. The outer well represents the molecular adsorption state and the deeper well represents the dissociative chemisorption state. [65]

In its most basic form, the adsorption of atoms or molecules on solid surfaces occurs while the molecular structure is preserved. This phenomenon, known as direct associative adsorption processes (Molecular adsorption in figure I.16), is common on metal surfaces containing tiny stable molecules like carbon monoxide and nitrogen oxide. To a first approximation, the interaction can be described by a one-dimensional potential in which the energy follows a Lennard-Jones-type behavior versus distance from the surface: an electrostatic attraction dominates far away from the surface until reaching an optimum (bonding) distance, beyond which a strong repulsive "wall" takes over, as shown in figure I.16.[66,67] One important implication of this potential energy dependency on distance is that there are no energy barriers to associative adsorption, the energy drops monotonically as the molecule approaches the surface until it reaches the equilibrium bonding position.

In many circumstances, there are several adsorption states possible on the surface, and each type of adsorbate may be characterized by its own potential curve. Those may cross paths, which implies that molecules may shift from one potential to another as they move toward the surface. One important category of adsorptions within this class is the crossing of physisorption and chemisorption potentials, in which case the incoming molecules may first adsorb weakly, possibly in an "intrinsic precursor" state, and then transition to the chemisorption potential and end up in a stronger bonded state. The transition from the precursor to the final chemisorption state necessitates the passage of an energy barrier, which may or may not be greater than the energy necessary for desorption. These dynamics are illustrated by the sticking coefficient's relatively complicated dependency on molecule energy, temperature, and angle of incidence. The sticking coefficient's reliance on the angle of incidence of the molecules is due to predicted normal energy scaling, sticking should increase with increasing angle of incidence.

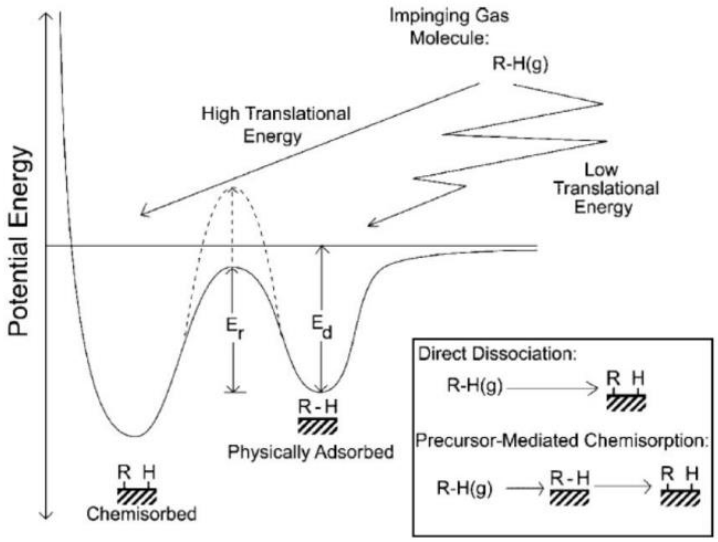

Figure I.17: One-dimensional diagram of the potential energy of precursor-mediated chemisorption of RH molecules. The dotted barrier above vacuum zero corresponds to an "activated" system, while the solid barrier below vacuum zero corresponds to a "light" system. E_d is the activation energy of the physisorbed state and E_r is the activation barrier of the chemisorbed state. [68]

Numerous adsorption experiments published in the literature have shown that dissociative chemisorption occurs mainly through two mechanisms: direct dissociation and precursor-mediated routes. Direct dissociative chemisorption happens when an impinging gas molecule has enough kinetic energy to overcome the reaction potential energy barrier and dissociates and chemisorbs directly to the surface. In this case, impulsion happens at quicker timeframes than thermalization, resulting in a selected, nonthermal reaction route, requiring high kinetic energy. Thus, through this pathway, one would anticipate the likelihood of dissociative chemisorption to be predominantly a function of the molecule's energy (translational and other modes), increasing as the molecule's energy increases. Meanwhile, in the case of precursor-mediated chemisorption, the impinging gas molecule must lose enough energy on impact to get stuck in a precursor state, which is often inside the surface's physical adsorption potential well. The energy generated by this binding is absorbed by the surface and/or distributed over all molecular degrees of freedom, causing trapped molecules to thermally adapt to the surface temperature. Intuitively, the chance of trapping should decrease as incoming energy

increases, because the more kinetic energy the impinging molecule possesses, the more energy must be wasted (or moved to other modes of the molecule) to physically adsorb to the surface. When a gas molecule becomes caught on the surface, it can either desorb from the surface back into the gas phase or chemisorb to the surface, usually breaking an internal bond. Precursor-mediated dissociation has been shown to play a dominant role in epitaxial silicon growth from disilane, a process employed to produce transistors and various microelectronic devices. [69]

The simple one-dimensional potential energy diagram shown in Figure I.17 illustrates the precursor-mediated chemisorption pathway. The term “facile” will be used henceforth to describe systems in which the potential barrier to chemisorption is below the vacuum zero; i.e. $(E_r - E_d) < 0$. Conversely, the term “activated” will be used to characterize systems in which the potential barrier to chemisorption lies above the vacuum zero line; $(E_r - E_d) > 0$. The barrier height varies with the incident molecule's energies (translation and vibration) and is affected by the molecule's orientation concerning the surface. Similarly, the height of the barrier may be affected by the surface's distinct crystal planes. Solid substrates, on the other hand, such as metal and narrow bandgap semiconductors, can fuel charge transfer between impinging molecules and the surface. As a result, altering molecule electronic states causes bond stretching and promotes dissociation.

One of the primary benefits of this mechanochemical reactivity is that it is performed at low pressure, often in ultra-high vacuum, allowing scanning probe microscopies to be utilized to detect compounds adsorbed by impact collisions. Krumbein et al. used an electrospray ion beam of accelerated Reichardt’s dye (RD) to induce collision on a Cu(100) surface at low hyperthermal translational energies (2-50 eV), [70] illustrated in Figure I.18, in which extensive compression of a molecule occur at timescales faster than thermalization leading to a selective, nonthermal reaction path. Upon molecules collide, they encounter selective bond compression for a very short period, resulting in the bending of certain bonds. The authors propose three outcomes from the collision of an RD ion with a Cu(100) surface: one nonreactive and two reactive outcomes indicated by STM imaging and modeling. These are the results of specialized collision dynamics, which may be obtained by focusing the ion beam at a normal incidence angle to the surface. The nonreactive pathway, “intact,” was found to yield an adsorbed intact RD with its two phenyl rings oriented vertically from the surface, as shown in Fig. 18.b (first column). The reactive pathways were discovered to be bond selective to CN bonds, breaking either of the two types of CN bonds in RD [see Fig. 18a]: the CN bond pointing at an angle "across" the N-O axis of the molecule, known as CN(AC), or the CN bond pointing "along" the N-O axis, known as CN(AL). A single CN(AC) was split in the "crack" route to provide a dissociated RD fragment (α fragment), as seen in Fig. 18(b). The CN(AL) bond was broken in the "split" route, yielding two products, as indicated in Fig. 18(b): a diphenylphenoxy (β fragment) and a triphenylpyridine (Δ fragment). The discovery of crack and split routes proves the presence of bond-selective pathways caused by molecule-surface contact at hyperthermal translational energy.

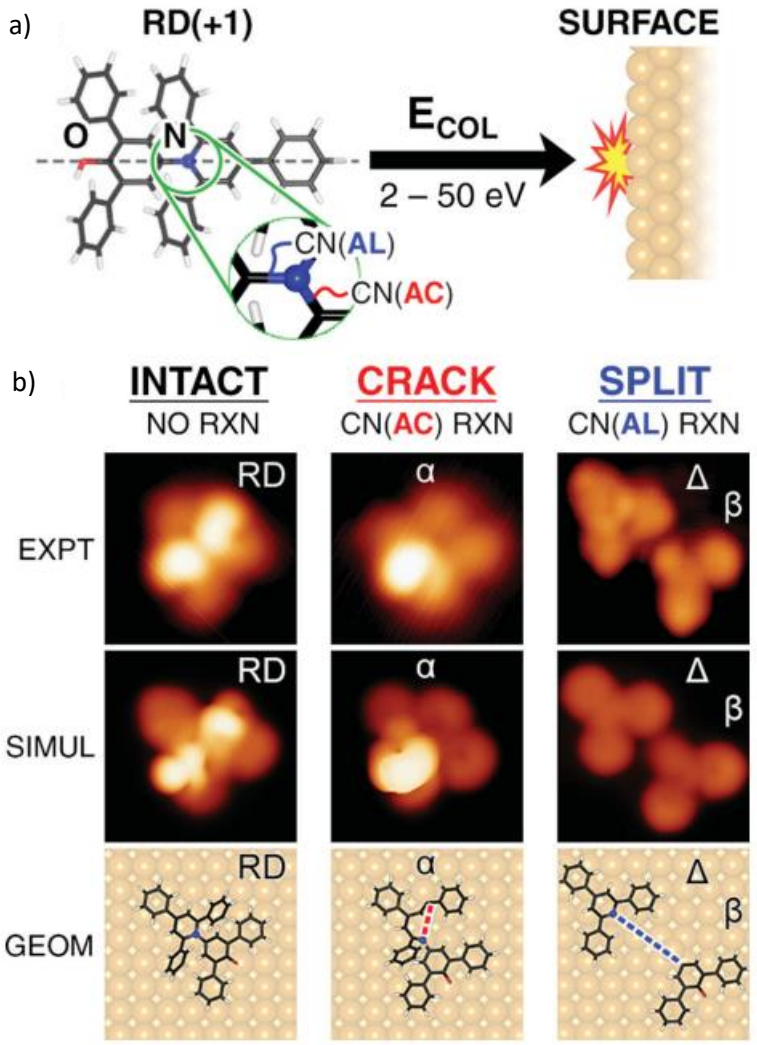

Figure I.18: Hyperthermal collision of RD on Cu(100) surface. (a) Schematics of the experiment, showing a beam of singly protonated RD aimed along the surface normal to the Cu surface at room temperature. Two types of C–N bonds are labeled as C–N(AC) and C–N(AL) based on their orientation against the N-O axis in RD (gray dashed line). (b) STM image (EXPT) and simulation (SIMUL) of the three collision outcomes imaged at 11 K. The intact pathway gives adsorbed RD. The crack pathway breaks a CN(AC) bond in the parent RD to give one α fragment, while the split pathway breaks the CN(AL) bond to give one β and one Δ fragment. Computed geometries (GEOM) show a broken CN(AC) bond (red dashed line) in the α fragment and a broken CN(AL) bond (blue dashed line) between β and Δ fragments. [70]

Krumbein et al. and his colleagues have reported here the first observation of a bond-selective reaction from a hyperthermal collision of a polyatomic ion with a metal surface, expanding a new promising experimental method that provides a new general tool to study and apply compressive mechanochemistry for any molecules that can be electrospray. On the other hand, very recently Jeongjin Kim reported the direct observations of CO_2 molecules' dissociative adsorption structures at the Rh(111) surface. Even at 300 K, the chemisorption of CO_2 molecules causes changes in local charge density at the interface, allowing the stimulated electronic interactions to have a sufficient impact on bond breakage for adsorbate O-CO*. Under 0.1 mbar of CO_2(g) molecules randomly collide with surface Rh atoms with kinetic energy (KE) at a given temperature in statistical velocity distribution

according to the Maxwell−Boltzmann function, direct imaging results show that dissociated O* and CO* occupy the hollow and atop sites of each on the atomically flat Rh surface, resulting in the spontaneous ordering formation of (2 x 2)-CO adsorption structures with a coverage of 0.25 monolayer (ML) at equilibrium. [71]

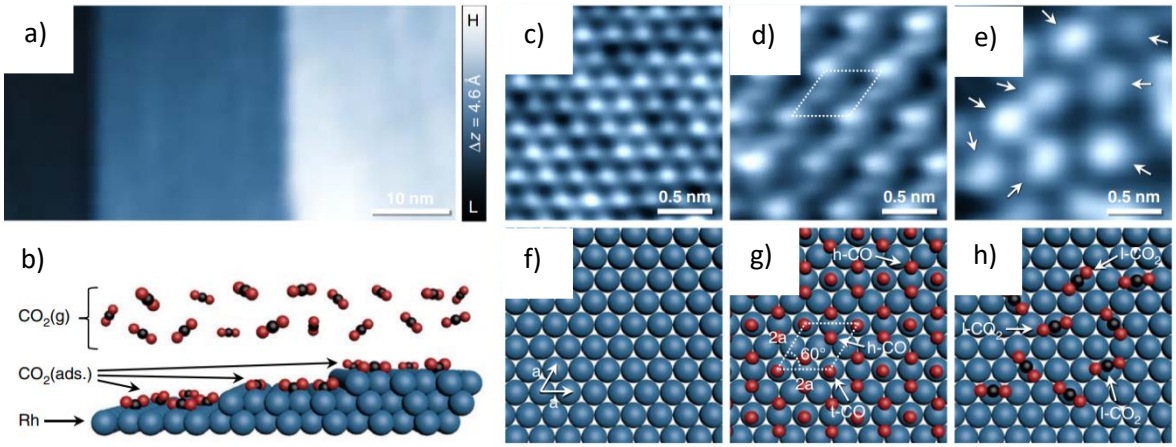

Figure I.19: a) Freshly prepared wide-range STM image in UHV after cleaning cycles (Vt = 1.25 V; It = 0.17 nA). b) Schematic illustration of the gaseous CO2/Rh(111) interface (side view). c−e) Representative atomic-resolution near ambient pressures scanning tunneling microscope (NAP-STM) images of clean in UHV (Vt = 0.23 V; It = 0.25 nA) (c), 0.75 ML of (2 × 2)-3CO chemisorption structure at 0.1 mbar CO (Vt = 1.03 V; It = 0.16 nA) (d) and CO2 physisorption structure at 0.1 mbar CO2 (Vt = 0.54 V; It = 0.16 nA) (e) on the Rh(111) surfaces. f−h) Corresponding atomistic ball model illustrations of the observed NAP-STM images. Dark blue, black, and red balls represent Rh, C, and O atoms, respectively. [71]

By raising the gas pressure to 0.1 mbar, an increased quantity of CO_2 may dissociate on the Rh(111) single-crystal surface and be monitored by near ambient pressures scanning tunneling microscope (NAP-STM). Figure I.19 shows both complete and dissociated species on the surface. These direct observations of CO_2 dissociation, an important step in the production of primary energy sources, show that active charge transfers between CO_2 molecules and metal surfaces at elevated pressures have a significant impact on intermediate product yields at the early stage of catalytic reactions. Furthermore, the proposed CO_2 dissociation pathway not only suggests a thermodynamic preference of Rh−carbonyl formation toward methane synthesis but also describes a distinct reaction direction against yields of intermediate format carrying on a route for methanol synthesis using Cu catalysts.

I.2.2.2 Light Irradiation:

Using light as a stimulus can be beneficial for eliciting responses on surfaces. This method has special benefits because of its capacity to elicit responses from surfaces. The use of light as a stimulus has obvious advantages:

- Selective excitation of desired chemical composition based on wavelength and polarization of light radiation.
- A non-invasive energy source that can excite molecular systems from a distance without using chemicals.
- Compared to thermal stimuli, photo-induced molecular responses on surfaces separate activation from temperature to selectively control specific chemical reactions and avoid some side reactions by modulating thermodynamic and kinetic aspects.

In the framework of on-surface reactions, light excitation for molecules adsorbed on a surface can occur in both UHV and air conditions via two distinct mechanisms known as adsorbate excitation (ADS) and hot electron attachment (HEA).[72] In the case of ADS, the adsorbed molecule absorbs an incoming photon with appropriate energy, causing intramolecular excitation of one electron from the HOMO towards the LUMO, as shown in Figure I.20a. As a result, the underlying surface can be a metal, semiconductor, or bulk insulator as long as its involvement is confined to a little alteration of the molecule's HOMO-LUMO gap caused by surface state and molecular orbital hybridization. This process occurs on metal, semi-conductor, or unoccupied states of the adsorbate, leading to the formation of a transient neutral state. This new excited state is involved as a precursor of the chemical transformation.

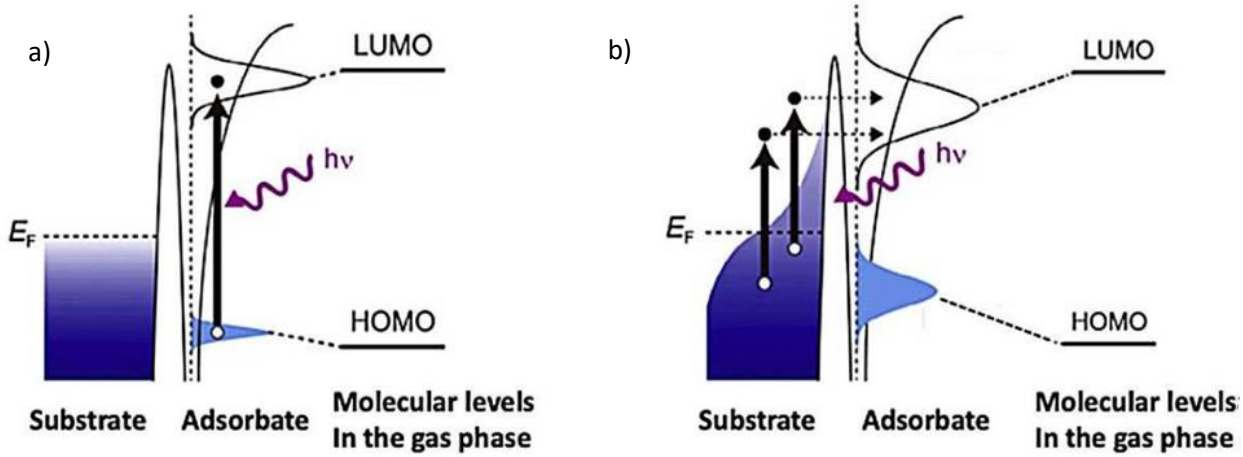

Figure I.20: Two mechanisms of photochemical reaction on a molecule adsorbed on a surface: a) Intermolecular excitation of one electron from the HOMO state to the LUMO state due to the light-absorption (ADS) and b) mechanism based on attachment of one photoexcited hot electron of the substrate to the LUMO state od adsorbates. White and black spots correspond to the holes and electrons, respectively. [72]

In the case of HEA which is a more dominant process compared to ADS because the cross section for optical adsorption is larger for the metal substrate than for the adsorbate monolayer, the surface captures light photons to produce one photo-excited hot electron, which connects to an unoccupied state of the adsorbed molecule (Figure I.20b), resulting in the development of a transitory anionic state. This technique requires primarily metal surfaces because of their plasmonic features, which allow the creation of high-temperature electrons upon light absorption. Despite the potential benefits, examples of light-induced reactions on surfaces are still uncommon, while some intriguing research has been published that portends a successful future for this topic.

Grossmann et al., for example, were able to synthesize ordered porous 2D polymers using two-step topo-chemical photopolymerization on an alkane-passivated graphite surface under ultra-high vacuum conditions.[73] First, he deposited fluorinated anthracene triptycene (Fantrip) molecules, which self-assembled into a highly structured monolayer structure with all anthracene fragments in optimal places for photopolymerization. The generated network is next exposed to violet light, which causes full covalent crosslinking by [4+4] photocycloaddition, yielding a two-dimensional polymer as illustrated in Figure I.21d-e. One asset of on-surface photo polymerization that is particularly relevant for fundamental and mechanistic studies is the analytic accessibility of the initial, intermediate, and final structures with fresh insights from sub-molecularly resolved imaging.

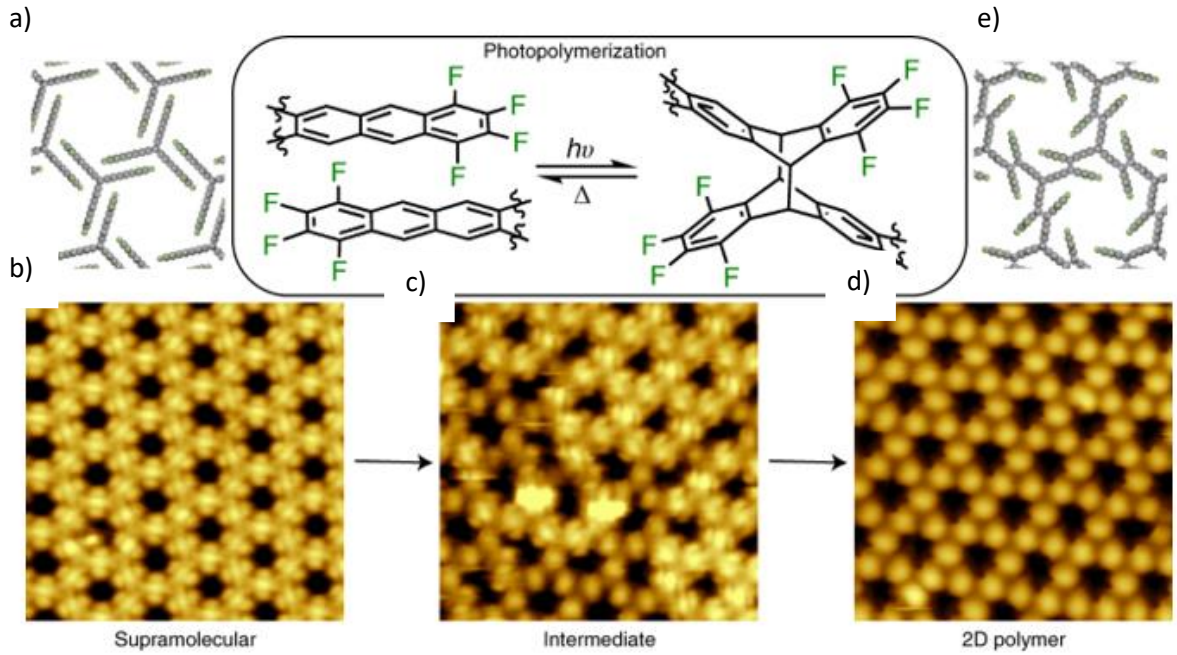

Figure I.21: a) Models (top views) of the self-assembled photopolymerizable fantrip monolayer with antiparallel stacking of all anthracene blades. b) STM images acquired after deposition of fantrip onto hexacosane-passivated graphite and mild heating at 80 °C. c) STM image of a partly photopolymerized fantrip network. d) STM image of the resulting likewise hexagonal 2D polymer formed upon UV irradiation of previously self-arranged network in the same geometrical configuration on passivated graphite. Polymer forms via a topochemical [4+4] photopolymerization reaction. e) Corresponding CPK model for obtained 2D polymer. [73]

I.2.2.3 Thermal annealing:

Dating back to 1901, Fritz Ullmann et al. discovered that the aromatic carbon-halogen bond can be cleaved to form diaryls with the help of the Cu powder catalyst.[74] Meanwhile, this reaction has become a standard example and is frequently utilized in synthetic chemistry due to its flexibility in combining substituted phenyls with complex biphenyl derivatives.[75,76] This process requires heating the entire sample, which makes it ideal for large-scale manufacturing but lacks spatial control over surface responses. Despite this constraint, the wide range of thermal energy available allows for fine control over the reaction paths of molecular precursors. Thermal stimuli's diversity makes them suitable for performing sequential on-surface activities, such as activating molecules with various reaction sites or facilitating two unique interaction types among molecules. Thermal control enables the exact and controlled production of polymeric nanostructures.

Roman Fasel pioneered a bottom-up method for synthesizing graphene nanoribbons (GNRs).[77] The procedure begins with a chemical precursor, 10,10'-dibromo-9,9'-bianthryl (DBBA), as shown in Figure I.22. This precursor is used to make atomically accurate armchair graphene nanoribbons (AGNRs) using a novel two-step approach utilizing Ullmann-type coupling and cyclodehydrogenation. The DBBA was deposited on the Au(111) surface, and the initial thermal annealing at 473 K raised the debromination of DBBA precursors, resulting in biradical intermediates that spread on the surface and formed non-planar linear polymers via C-C intermolecular interaction. Then, after annealing at 673 K, AGNRs are generated by intramolecular cyclodehydrogenation, resulting in the aromatization of the previously synthesized non-planar polymer. Figure I.22a depicts the full chemical process. This example

demonstrates thermal annealing's ability to influence the probability of certain reaction pathways, allowing for novel approaches to create useful products.

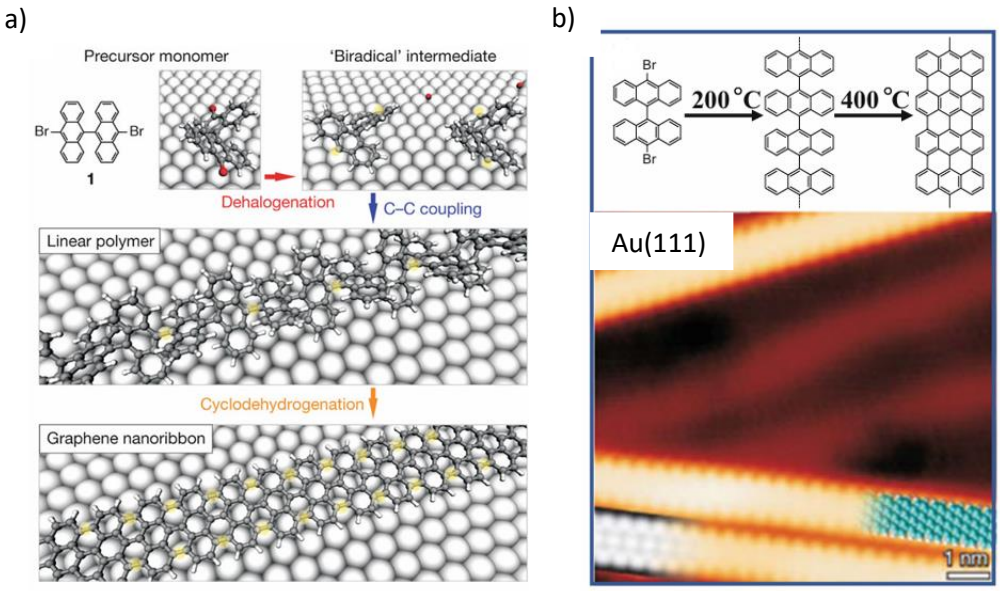

Figure I.22: a) Basic steps of surface-supported GNR synthesis. Top Dehalogenation of precursor monomers (here, 10,10'-dibromo-9,9'-bianthryl) after deposition on a noble metal substrate. Center Formation of linear polymers by covalent coupling of diffusing de-halogenated intermediates. Bottom Formation of fully aromatic GNRs (here, 7-AGNR) by cyclodehydrogenation. b) Bottom-up synthesis of graphene nanoribbons (GNRs), dehalogenation followed by cyclodehydrogenation to give fully aromatic GNRs over Au(111).[77]

I.2.2.4 Tip induced:

Sharp tips employed in scanning tunneling microscopy operate as electron emitters, making them a promising choice for provoking tip-induced reactions in addition to heat, collision, and light as external stimulants. Depending on the polarity of the applied bias voltage(dV), the tunneling current might travel from the tip to empty electron states above the sample's Fermi level (E_F) or vice versa. Aside from electrical structures, molecules include mechanical degrees of freedom such as translation, rotation, and vibration, which may be activated by tunneling electrons via an inelastic tunneling technique (I_{ET}). The energy of electron tunneling inside the STM junction may be regulated by modifying the applied bias. By modulating dV appropriately, electrons can tunnel inelastically by losing characteristic quanta (ΔE) owing to the activation of vibrational modes of an adsorbed molecule. Molecules are now in an adsorbate-induced resonant state. Bond breaking can occur if tunneling electrons have enough energy to exceed the vibrational dissociation barrier ($\Delta E \geq E_{diss}$, check Figure I.23).

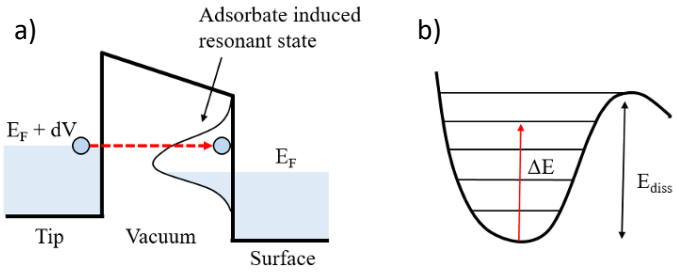

Figure I.23: Schematic representations of a) electron injection in inelastic-electron tunneling (I_{ET}) process and b) adsorbate-induced vibrational states. If energy dissipated by electrons is enough to overcome the barrier i.e. $\Delta E \geq E_{diss}$, adsorbed molecules can dissociate. Figures reproduced in conformity with the ones presented in the work of Hla et al. [78]

Rieder and coworkers were the first to exploit chemical reactivity created in an STM [79] tunneling junction to promote iodobenzene dimerization (Fig. 24a). The systematic step-by-step creation by moving, activating, and connecting individual monomers on a surface has received little attention since then, owing to the time-consuming nature of the serial processes needed in each connection step. In contrast to step growth, chain-growth polymerization of correctly structured monomers would only need control over the initiation step, with subsequent polymerization proceeding without further stimulation. On the other hand, Okawa and coworkers proved this notion for self-assembled monolayers of 10,12-nonacosadiynoic acid on graphite surfaces. Figure I.24b-c shows tip-induced chain polymerization on a molecular layer of 10,12-pentacosadiynoic acid. After forming the layer, they positioned the STM tip above the diacetylene molecule indicated by the arrow and applied a pulsed sample bias ($-4V_{in}$ amplitude, 5 µs width), as shown in Fig. I.24b. Figure I.24c depicts the pulse application product. It exhibits a brilliant line that originates at the place of stimulation. This is a single polydiacetylene chain generated using tip-induced chain polymerization. As a result, a single straight polydiacetylene chain may be produced with nm spatial accuracy at any desired location. It is worth noting that polymerization is interrupted when it reaches a domain border, a substrate step, or an artificial defect .[80,81] Therefore, when chain polymerization is initiated on larger, defect-free domains, the polydiacetylene chains can be micron-long.[82]

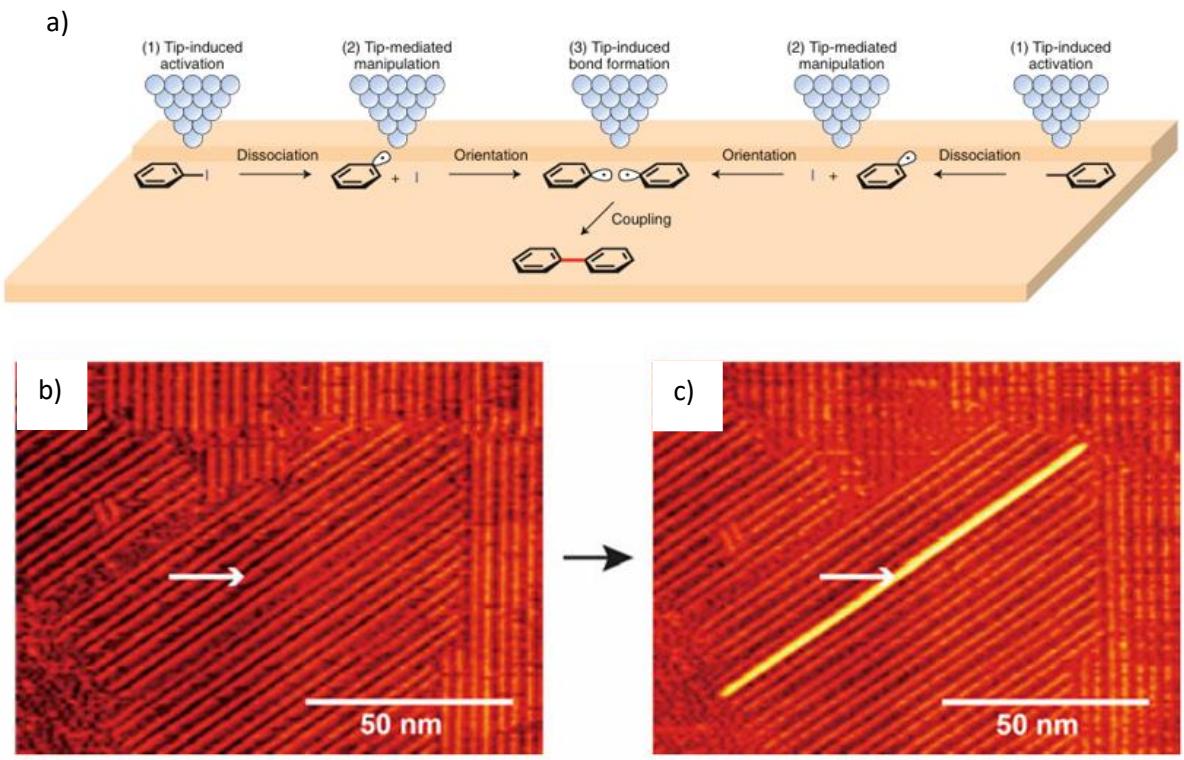

Figure I.24: a) Using the STM tip to induce the coupling of two iodobenzene moieties to generate biphenyl b) STM image of a molecular layer of 10,12-pentacosadiynoic acid on a HOPG substrate. C) STM image of the same area after applying a pulsed sample bias voltage (–4 V in amplitude, 5 µs in width) at the point indicated by the arrow. The fabricated single polydiacetylene chain is imaged as a brighter line. [80,81]

I.3 Extending on-surface synthesis from 2D to 3D

Constructing heterostructured molecular layers with atomic/molecular level precision and extending molecular engineering from two to three dimensions hold great importance for both fundamental science and application purposes in the fields of nanoelectronic devices, photonics, and quantum science. This shift in on-surface synthesis from two to three dimensions requires not only the lateral coupling parallel to the substrate but also the covalent bonding perpendicular to the substrate, e.g., interlayer coupling between molecular layers, which is yet to be realized. Lately, Pengcheng Ding and his colleagues have reported very recently the cycloaddition of C_{60} and 3,5-bis(carboxylic acid)-phenyl-3-maleimide (BCPM, $C_{12}H_7NO_6$) and their adducts on Au(111) surface. C_{60} and its derivatives have shown magnificent physical properties and potential, the unique 3D conjugated electronic structure and the geometric combination of pentagons and hexagons of C_{60} molecules make their reactions significantly distinct from those of graphene or planar polyaromatic molecules.[83] To electronically decouple C_{60} from the substrate and especially provide an appropriate steric configuration for the coupling between the lowest unoccupied molecular orbital (LUMO) of C_{60} and the highest occupied molecular orbital (HOMO) of BCPM.

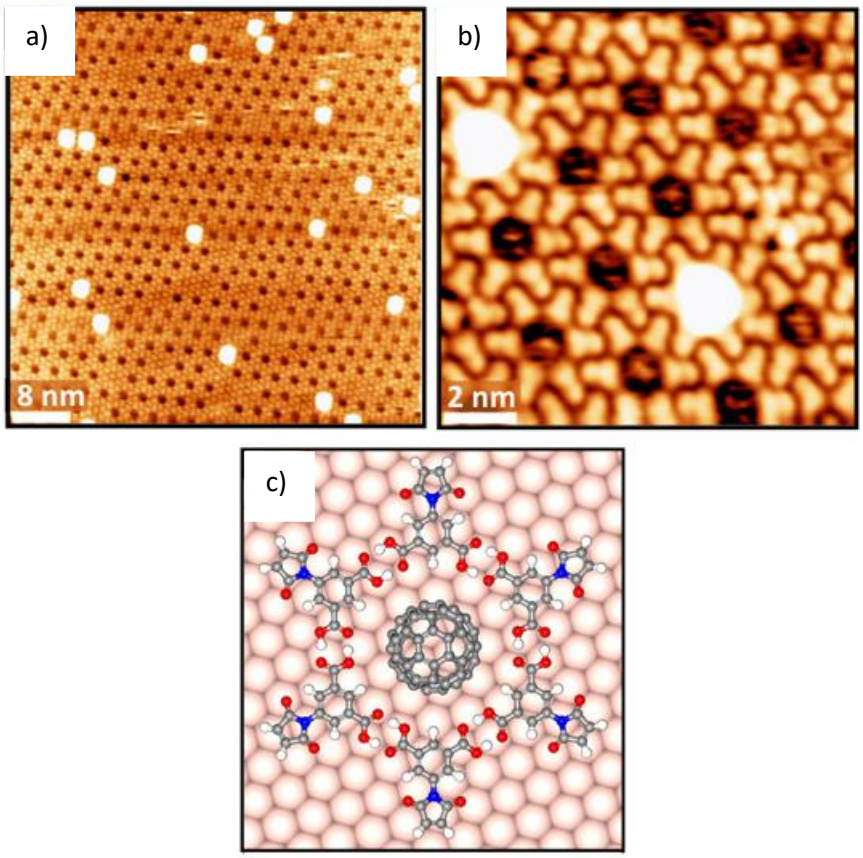

Figure I.25: Adsorption of C_{60} on BCPM-coated Au(111) subjected to a small C_{60} dosage. a) Large-scale (V_s = +1.25V, I_t = +0.28 nA) and (b) Close-view (V_s = −1250 mV, I_t = –0.42 nA) STM images of the surface, showing a host-guest structure with C_{60} located in the pores of the BCPM network. c) Top view structural model of a flower-like unit if six BCPM molecules hosting one C_{60}**.** [84]

Deposition of BCPM resulted in extended honeycomb network self-assembly over Au(111). C_{60} molecules were then deposited onto the BCPM layer-covered Au(111) at room temperature. At low dosages, C_{60} adsorbs preferentially in the circular pores of the BCPM network and is imaged as a bright circular protrusion (Fig. 25a, b). After all the pores of the BCPM network are occupied, further deposition of C_{60} at RT (without post-annealing) leads to a coating of the C_{60} layer on the BCPM layer. These C_{60} molecules followed the same symmetry and periodicity as the underlying BCPM network and formed a configuration with one C_{60} atop one BCPM (C_{60}-on-BCPM). The coverage increases with the C_{60} dosage until the BCPM network is fully covered. 3D covalent bonding has been realized by cycloaddition of C_{60} on Au(111). The carboxylic acid groups of BCPM enable the formation of a well-defined template for C_{60}, while the out-of-plane maleimide group enables strong adsorption of the molecules on the substrate.

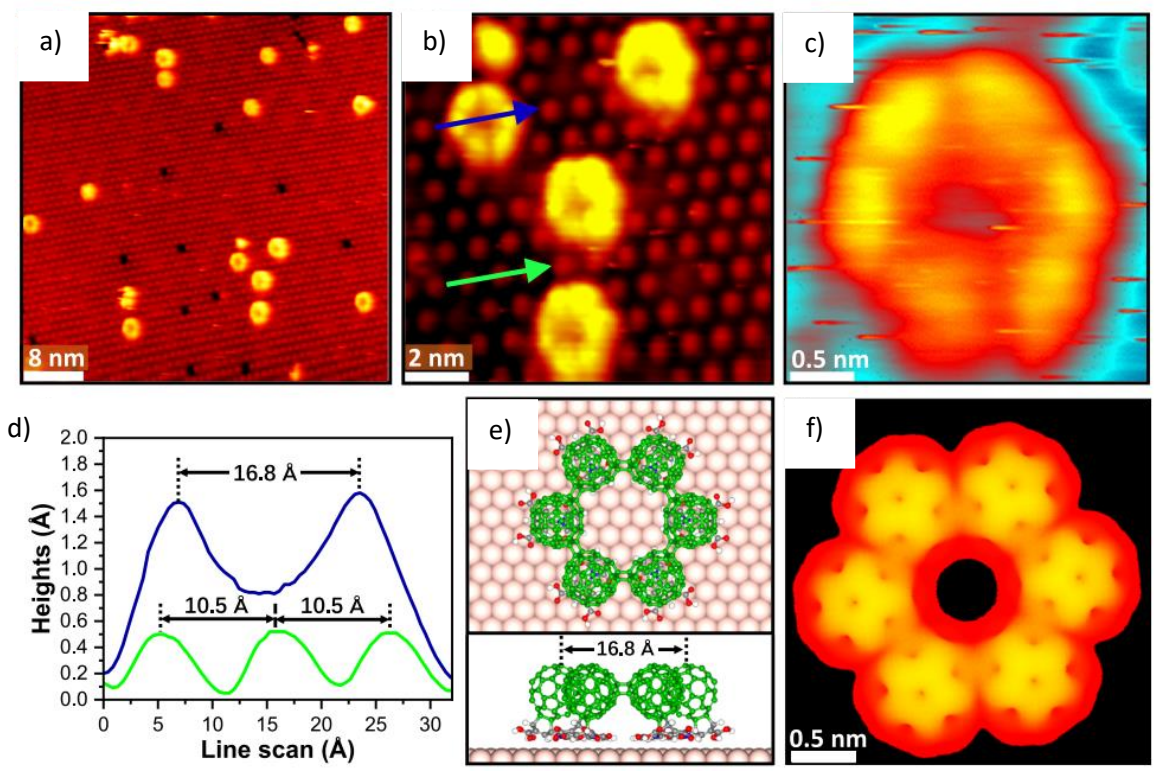

Figure I.26: Lateral [2 + 2] cycloaddition of C60-BCPM. a Large-scale (V_s = –1250 mV, I_t = –0.26 nA) and (b), close-view (V_s = −1250 mV, I_t = −0.29 nA) STM images showing the hexamer rings (HRs) after annealing C60-BCPM on Au(111) at 490 K for 30 min. c) High-resolution STM of an individual HR. d Linescans along the blue and green arrows in (b), showing the size of the HR compared with the periodicity of C60- BCPM in D1. e) Top and side views of the DFT-optimized structure of an HR on Au(111), where the six C_{60}-BCPM molecules are covalently bonded via [2 + 2] cycloaddition. f) Calculated STM image of an HR, showing consistent morphology as observed experimentally.[84]

After annealing the C_{60} layer on BCPM at 370 K for 30 min, two different types of territories are observed. One intact domain (D2) while the other domain (D1) contains molecules with greater height compared to before annealing which rationalized the thermo-activated coupling between C_{60} and BCPM. Confirmed by the frontier molecular orbital analysis, the orbital matching and the appropriate steric arrangement can enable [4 + 2] cycloaddition between [6,6] bond at the bottom of C_{60} and the C atoms in para-positions of BCPM phenyl ring, forming a covalently-bonded adduct, i.e., C_{60}-BCPM. Meanwhile, the cycloaddition confines the rotation of C_{60}, allowing the sub-molecular resolution. After forming C_{60}-BCPMs, the sample was further annealed at 490 K for 30 min. Upon elevated annealing, a next-step lateral [2 + 2] cycloaddition of C_{60}-BCPMs forms macrocycles, where the hexamer rings (HRs) are dominant. Each HR is composed of six protrusions, showing C_{6v} symmetry (Fig. 26b, c). Such macrocycles have been never observed from pristine C_{60} on Au(111) before. The vertical [4 + 2] cycloaddition between C_{60} and BCPM layers and this lateral [2 + 2] cycloaddition of C_{60}-BCPMs demonstrate the non-planar multiple covalent bonding capability of C_{60}. The multiple reactive sites of C_{60}, both the vertical covalent bonding via interlayer [4 + 2] cycloaddition between C_{60} and the phenyl ring of BCPM and the lateral covalent bonding between the C_{60} heads of C_{60}-BCPMs via [2 + 2] cycloaddition is constructed, representing a prototype of 3D synthesis on the surface. This study reveals a successful approach for bottom-up synthesis of covalently-bonded 3D organic frameworks on surfaces by cycloaddition of organic molecules with fullerenes--the steric multi-plug reactants, expanding on-surface synthesis from 2D to 3D.

I.4 Future prospects and motivation of the thesis

The success of combining organic chemistry with surface science two normally unrelated fields has been demonstrated by the growth of on-surface synthesis and polymerization in the last decade. Through the integration of essential competencies for designing and manufacturing appropriate molecular precursors and for carrying out and evaluating state-of-the-art spectroscopic and microscopic investigations. Gaining a comprehensive knowledge of the fundamental physical and chemical processes involved in on-surface polymerization will be crucial for future advancements in the discipline. To define reaction products and potential intermediates, this should incorporate both microscopic and spectroscopic tools—ideally with atomic resolution. Further refining these methods to track structural alterations in real-time during polymerization will yield important insights into the dynamics of the process. [85] By removing the molecular constructions from the surface and mapping their optical, mechanical, electrical, and other characteristics using STM, and AFM, respectively, more information may be obtained.[86,87]

The field has been mostly restricted to coinage metal substrates that are conveniently accessible conductive adequate for STM analysis. Newer methods are starting to appear, such as ncAFM with functionalized tips, which offer atomic resolution on non-conducting surfaces.[88] The thermal treatment, which is necessary for the production of covalent bonds, might present challenges depending on the surface reactivity and catalytical behavior, therefore the types of surfaces that can be combined with on-surface polymerization are still somewhat restricted. On the other side, photoinduced chemical reactions are a promising approach, remotely controlled, avoiding thermal treatment and at the same time providing exquisite selectivity via the choice of the photon source. Next to instrumentations and used methods for the synthesis of new structures, a deeper understanding of the electronic properties of the generated π-conjugated polymers hybridized with the underlying substrates is necessary for greater depth in interpreting the obtained spectroscopic signatures.

Extending into the third dimension is another promising direction to take in the future, as a triple meeting point where the natural sciences of chemistry, physics, and biology are encountered. Extending this topic from 2D to 3D entities requires a combination of scientific knowledge and engineering application to overcome limitations such as domain area, arranged alignment, thin-film transfer, and strategies for identifying vertical interactions. Although there is still a long way to go before assembled materials are put to use in real-world applications, ongoing efforts in this direction will eventually open up new research directions for understanding the architectures and characteristics of 3D supramolecular materials, which will be important for many organic and optoelectronic devices.

In this context, comes the work of this thesis in which we have studied many on-surface science for the fabrication of desired structures and promoting chemical reactions, following different approaches, using various substrate materials. The layout of this thesis is as follows:

- Chapter 2 represents the experimental techniques and equipment that are used for performing and monitoring experiments under UHV. As well, we give a brief presentation of used surfaces concerning their crystalline structures and the different used characterization techniques to conduct our experiments.
- Chapter 3 in the first part concentrates on the usage of highly reactive reconstructed Si(111)-7x7 surface, under UHV, to promote a facile dissociation of inert N_2 molecules upon soft collision at room temperature and low gas pressure. The second part will be

depicted to promote the exposure of atomic hydrogen over the N-adsorbed Si(111)-7x7 surface.

- Chapter 4 focuses on the expansion of monolayers to well-ordered multilayers to enhance the functionality and complexity of self-assemblies. In this study, we present the evolution of molecular conformation from 2D to 3D supramolecular networks adsorbed onto an HOPG surface.
- Chapter 5 chapter will delve into comparing the on-surface polymerization processes induced by thermal and photochemical methods on Au(111) using four distinct molecular building blocks.
- Chapter 6 is the last one in which we summarize the results of the whole thesis work and open the door for further perspective

References:

[1] Zwaneveld, N. A. A., Pawlak, R., Abel, M., Catalin, D., Gigmes, D., Bertin, D., & Porte, L. Organized Formation of 2D Extended Covalent Organic Frameworks at Surfaces. Journal of the American Chemical Society, 130(21), 6678–6679. (2008).

[2] Grill, L., Dyer, M., Lafferentz, L., Persson, M., Peters, M. V., & Hecht, S. Nano-architectures by covalent assembly of molecular building blocks. Nature Nanotechnology, 2(11), 687–691. (2007).

[3] Joachim, C., Gimzewski, J. K., & Aviram, A. Electronics using hybrid-molecular and mono-molecular devices. Nature, 408(6812), 541–548. (2000).

[4] Heath, J. R., & Ratner, M. A. Molecular Electronics. Physics Today, 56(5), 43–49. (2003).

[5] Wintterlin, J., & Bocquet, M.-L. Graphene on metal surfaces. Surface Science, 603(10-12), 1841–1852.(2009).

[6] K. Tahara, S. Furukawa, H. Uji, T. Uchino, T. Ichikawa, J. Zhang, W. Mamdouh, M. Sonoda, F.C. De Schryver, S. De Feyter and T. Tobe, "Two-Dimensional Porous Molecular Networks of Dehydrobenzo annulene Derivatives via Alkyl Chain Interdigitation ", J. Am. Chem. Soc., vol. 128, p. 16613, (2006).

[7] C. R. Martinez and B. L. Iverson, "Rethinking the term “pi-stacking”, Chem. Sci., vol. 3, p. 2191, (2012)

[8] T. Steiner, "The Hydrogen bond in the Solid State”, Angew. Chem. Int. Ed, vol. 41, p. 48, (2002).

[9] R. Wang, D. Hartnick and U. Englert, "Short is strong: experimental electron density in a very short N···I halogen bond ", Kristallogr. Cryst. Mater, vol. 233, p. 733, (2018)

[10] W. Wang, X. Shi, S. Wang, M. A. Van Hove and N. Lin, "Single-Molecule Resolution of an Organometallic Intermediate in a Surface-Supported Ullmann Coupling Reaction", J. Am. Chem. Soc., vol. 133, p. 13264, (2011).

[11] Barth, J. V., Costantini, G., & Kern, K. Engineering atomic and molecular nanostructures at surfaces. Nature, 437(7059), 671–679. (2005).

[12] De Greef, T. F. A., Smulders, M. M. J., Wolffs, M., Schenning, A. P. H. J., Sijbesma, R. P., & Meijer, E. W. Supramolecular Polymerization. Chemical Reviews, 109(11), 5687–5754. (2009).

[13] Cincotti, S., & Rabe, J. P. Self-assembled alkane monolayers on MoSe2 and MoS2. Applied Physics Letters, 62(26), 3531–3533.(1993).

[14] Groszek, A. J. Selective Adsorption at Graphite/Hydrocarbon Interfaces. Proceedings of the Royal Society A: Mathematical, Physical and Engineering Sciences, 314(1519), 473–498. (1970).

[15] Findenegg, G. H. Ordered layers of aliphatic alcohols and carboxylic acids at the pure liquid/graphite interface. Journal of the Chemical Society, Faraday Transactions 1: Physical Chemistry in Condensed Phases, 69(0), 1069. (1973).

[16] Wei, Y., Kannappan, K., Flynn, G. W., & Zimmt, M. B. Scanning Tunneling Microscopy of Prochiral Anthracene Derivatives on Graphite: Chain Length Effects on Monolayer Morphology. Journal of the American Chemical Society, 126(16), 5318–5322, (2004).

[17] Zeng X, Hu Y, Xie R, Khan SB, Lee SL. Monolayer and Bilayer Formation of Molecular 2D Networks Assembled at the Liquid/Solid Interfaces by Solution-Based Drop-Cast Method. Molecules. 26(24):7707. (2021).

[18] Li, R., Ma, P., Dong, S., Zhang, X., Chen, Y., Li, X., & Jiang, J. Synthesis, Characterization, and OFET Properties of Amphiphilic Heteroleptic Tris(phthalocyaninato) Europium(III) Complexes with Hydrophilic Poly(oxyethylene) Substituents. Inorganic Chemistry, 46(26), 11397–11404.(2007).

[19] A. G. Martynov,: Rare-earth based tetrapyrrolic sandwiches: chemistry, materials, and applications. Chem. Soc. Rev. 51, 9262, (2022).

[20] Champness, N. R. Building with molecules. Nature Nanotechnology, 2(11), 671–672. (2007).

[21] Martín-Gago, J.A. Polycyclic aromatics: On-surface molecular engineering. Nat. Chem. 3,11 (2011).

[22] Méndez, J., López, M. F., & Martín-Gago, J. A. On-surface synthesis of cyclic organic molecules. Chemical Society Reviews, 40(9), 4578.(2011).

[23] Grill, L., & Hecht, S. Covalent on-surface polymerization. Nature Chemistry, 12(2), 115–130. (2020).

[24] Carothers, W. H. Polymerization. Chemical Reviews, 8(3), 353–426.(1931).

[25] SZWARC, M. 'Living' Polymers. Nature 178, 1168–1169. (1956).

[26] Riss, A., Wickenburg, S., Gorman, P., Tan, L. Z., Tsai, H.-Z., de Oteyza, D. G., … Crommie, M. F. Local Electronic and Chemical Structure of Oligo-acetylene Derivatives Formed Through Radical Cyclizations at a Surface. Nano Letters, 14(5), 2251–2255. (2014).

[27] Grill, L., Dyer, M., Lafferentz, L., Persson, M., Peters, M. V., & Hecht, S. Nano-architectures by covalent assembly of molecular building blocks. Nature Nanotechnology, 2(11), 687–691. (2007).

[28] Hla, S.-W., Bartels, L., Meyer, G., & Rieder, K.-H. Inducing All Steps of a Chemical Reaction with the Scanning Tunneling Microscope Tip: Towards Single Molecule Engineering. Physical Review Letters, 85(13), 2777–2780. (2000).

[29] Lindner, R., & Kühnle, A. (2015). On-Surface Reactions. ChemPhysChem, 16(8), 1582–1592. (2015).

[30] Mali, K. S., Pearce, N., De Feyter, S., & Champness, N. R. Frontiers of supramolecular chemistry at solid surfaces. Chemical Society Reviews, 46(9), 2520–2542. (2017).

[31] Shen, Q., Gao, H.-Y., & Fuchs, H. Frontiers of on-surface synthesis: From principles to applications. Nano Today, 13, 77–96. (2017).

[32] Held, P. A., Fuchs, H., & Studer, A. Covalent-Bond Formation via On-Surface Chemistry. Chemistry - A European Journal, 23(25), 5874–5892. (2017).

[33] Klappenberger, F., Zhang, Y.-Q., Björk, J., Klyatskaya, S., Ruben, M., & Barth, J. V. On-Surface Synthesis of Carbon-Based Scaffolds and Nanomaterials Using Terminal Alkynes. Accounts of Chemical Research, 48(7), 2140–2150. (2015).

[34] Di Giovannantonio, M., Deniz, O., Urgel, J. I., Widmer, R., Dienel, T., Stolz, S., … Fasel, R. (2017). On-Surface Growth Dynamics of Graphene Nanoribbons: The Role of Halogen Functionalization. ACS Nano, 12(1), 74–81. (2018).

[35] Galeotti, G., Di Giovannantonio, M., Lipton-Duffin, J., Ebrahimi, M., Tebi, S., Verdini, A., Contini, G. The role of halogens in on-surface Ullmann polymerization. Faraday Discussions, 204, 453–469. (2017).

[36] Di Giovannantonio, M., El Garah, M., Lipton-Duffin, J., Meunier, V., Cardenas, L., Fagot Revurat, Y., Contini, G. Insight into Organometallic Intermediate and Its Evolution to Covalent Bonding in Surface-Confined Ullmann Polymerization. ACS Nano, 7(9), 8190–8198. (2013).

[37] Lischka, M., Michelitsch, G. S., Martsinovich, N., Eichhorn, J., Rastgoo-Lahrood, A., Strunskus, T., … Lackinger, M. Remote functionalization in surface-assisted dehalogenation by conformational mechanics: organometallic self-assembly of 3,3’,5,5’-tetrabromo-2,2’,4,4’,6,6’-hexafluorobiphenyl on Ag(111). Nanoscale, 10(25), 12035–12044. (2018).

[38] Lackinger, M. Surface-assisted Ullmann coupling. Chemical Communications, 53(56), 7872–7885. (2017).

[39] Björk, J., Hanke, F., & Stafström, S. Mechanisms of Halogen-Based Covalent Self-Assembly on Metal Surfaces. Journal of the American Chemical Society, 135(15), 5768–5775. (2013).

[40] McMillen, D. F., & Golden, D. M. (1982). Hydrocarbon Bond Dissociation Energies. Annual Review of Physical Chemistry, 33(1), 493–532. (1982).

[41] Blunt, M. O., Russell, J. C., Champness, N. R., & Beton, P. H. (2010). Templating molecular adsorption using a covalent organic framework. Chemical Communications, 46(38), 7157. (2010).

[42] Gourdon, A.: "On-Surface Synthesis: Proceedings of the International Workshop On Surface Synthesis". Springer International Publishing, (2016).

[43] Bieri, M., Nguyen, M.-T., Gröning, O., Cai, J., Treier, M., Aït-Mansour, K., Fasel, R. Two-Dimensional Polymer Formation on Surfaces: Insight into the Roles of Precursor Mobility and Reactivity. Journal of the American Chemical Society, 132(46), 16669–16676. (2010).

[44] lszowski, P.; Zapotoczny, B.; Prauzner-Bechcicki, J. S.; Vilas-Varela, M.; Pérez, D.; Guitián, E.; Peña, D.; Szymonski, M. Aryl Halide C-C Coupling on Ge(001):H Surfaces. J. Phys. Chem. C, 119 (49), 27478–27482. (2015).

[45] Giessibl, F. J. Advances in atomic force microscopy. Reviews of Modern Physics, 75(3), 949–983. (2003).

[46] Kunstmann, T., Schlarb, A., Fendrich, M., Wagner, T., Möller, R., & Hoffmann, R. Dynamic force microscopy study of 3,4,9,10-perylenetetracarboxylic dianhydride on KBr(001). Physical Review B, 71(12). (2005).

[47] Nony, L., Bennewitz, R., Pfeiffer, O., Gnecco, E., Baratoff, A., Meyer, E., Joachim, C. Cu-TBPP and PTCDA molecules on insulating surfaces studied by ultra-high-vacuum non-contact AFM. Nanotechnology, 15(2), S91–S96. (2004).

[48] Burke, S. A., Ji, W., Mativetsky, J. M., Topple, J. M., Fostner, S., Gao, H.-J., Grütter, P. Strain Induced Dewetting of a Molecular System: Bimodal Growth of PTCDA on NaCl. Physical Review Letters, 100(18). (2008).

[49] Schütte, J., Bechstein, R., Rohlfing, M., Reichling, M., & Kühnle, A. Cooperative mechanism for anchoring highly polar molecules at an ionic surface. Physical Review B, 80(20). (2009).

[50] Such, B., Trevethan, T., Glatzel, T., Kawai, S., Zimmerli, L., Meyer, E., … Echavarren, A. M. Functionalized Truxenes: Adsorption and Diffusion of Single Molecules on the KBr(001) Surface. ACS Nano, 4(6), 3429–3439. (2010).

[51] Pawlak, R., Nony, L., Bocquet, F., Oison, V., Sassi, M., Debierre, J.-M., Porte, L. Supramolecular Assemblies of 1,4-Benzene Diboronic Acid on KCl(001). The Journal of Physical Chemistry C, 114(20), 9290–9295. (2010).

[52] Rahe, P., Kittelmann, M., Neff, J. L., Nimmrich, M., Reichling, M., Maass, P., & Kühnle, A. Tuning Molecular Self-Assembly on Bulk Insulator Surfaces by Anchoring of the Organic Building Blocks. Advanced Materials, 25(29), 3948–3956. (2013).

[53] Mativetsky, J. M., Burke, S. A., Fostner, S., & Grutter, P. Nanoscale Pits as Templates for Building a Molecular Device. Small, 3(5), 818–821. (2007).

[54] Hinaut, A., Lekhal, K., Aivazian, G., Bataillé, S., Gourdon, A., Martrou, D., Gauthier, S. NC-AFM study of the adsorption of hexamethoxytriphenylene on KBr(001). J. Phys. Chem. C 115(27), 13338–13342 (2011)

[55] Richter, A., Haapasilta, V., Venturini, C., Bechstein, R., Gourdon, A., Foster, A. S., & Kühnle, A. (2017). Diacetylene polymerization on a bulk insulator surface. Physical Chemistry Chemical Physics, 19(23), 15172–15176. (2017).

[56] Killelea, D. R., Campbell, V. L., Shuman, N. S., & Utz, A. L. Isotope-Selective Chemical Vapor Deposition via Vibrational Activation. The Journal of Physical Chemistry C, 112(26), 9822–9827. (2008).

[57] Yoder, B. L., Bisson, R., & Beck, R. D. Steric Effects in the Chemisorption of Vibrationally Excited Methane on Ni(100). Science, 329(5991), 553–556. (2010).

[58] Chen, L., Ueta, H., Bisson, R., & Beck, R. D. (2012). Vibrationally bond-selected chemisorption of methane isotopologues on Pt(111) studied by reflection absorption infrared spectroscopy. Faraday Discussions, 157, 285. (2012).

[59] Shen, X. J., Lozano, A., Dong, W., Busnengo, H. F., & Yan, X. H. Towards Bond Selective Chemistry from First Principles: Methane on Metal Surfaces. Physical Review Letters, 112(4).(2014).

[60] Crim, F. F. Chemical dynamics of vibrationally excited molecules: Controlling reactions in gases and on surfaces. Proceedings of the National Academy of Sciences, 105(35), 12654–12661. (2008).

[61] Guo, H., & Jiang, B. The Sudden Vector Projection Model for Reactivity: Mode Specificity and Bond Selectivity Made Simple. Accounts of Chemical Research, 47(12), 3679–3685. (2014).

[62] Jiang, B., Yang, M., Xie, D., & Guo, H. Quantum dynamics of polyatomic dissociative chemisorption on transition metal surfaces: mode specificity and bond selectivity. Chemical Society Reviews, 45(13), 3621–3640. (2016).

[63] Jacobs, D. C. REACTIVECOLLISIONS OFHYPERTHERMALENERGYMOLECULARIONS WITHSOLIDSURFACES. Annual Review of Physical Chemistry, 53(1), 379–407. (2002).

[64] Harvey, S. R., Seffernick, J. T., Quintyn, R. S., Song, Y., Ju, Y., Yan, J., Wysocki, V. H. Relative interfacial cleavage energetics of protein complexes revealed by surface collisions. Proceedings of the National Academy of Sciences, 201817632. (2019).

[65] Ceyer, S. T. New Mechanisms for Chemistry at Surfaces. Science, 249(4965), 133–139. (1990).

[66] Lennard-Jones, J. E. Processes of adsorption and diffusion on solid surfaces. Transactions of the Faraday Society, 28, 333. (1932).

[67] A. Zangwill, Physics at Surfaces, Cambridge University Press, Cambridge, (1988).

[68] McClure, S. M., Reichman, M. I., Seets, D. C., Nolan, P. D., Sitz, G. O., & Mullins, C. B. Dynamics of precursors in activated dissociative chemisorption systems. The Chemical Physics of Solid Surfaces, 109–142. (2003).

[69] Ferguson, B. A., Reeves, C. T., Safarik, D. J., & Mullins, C. B. Silicon deposition from disilane on Si(100)-2×1: Microscopic model including adsorption. Journal of Applied Physics, 90(10), 4981–4989. (2001).

[70] Krumbein, L., Anggara, K., Stella, M., Michnowicz, T., Ochner, H., Abb, S., Rauschenbach, S. Fast Molecular Compression by a Hyperthermal Collision Gives Bond-Selective Mechanochemistry. Physical Review Letters, 126(5). (2021).

[71] Kim, J., Ha, H., Doh, W. H., Ueda, K., Mase, K., Kondoh, H., … Park, J. Y. How Rh surface breaks CO2 molecules under ambient pressure. Nature Communications, 11(1). (2020).

[72] a) X.-L. Zhou, X.-Y. Zhu, J.M. White, Surf. Sci. Rep. 1991, 13, 73—220; b) F.M. Zimmermann, W. Ho, Surf. Sci. Rep. 1995, 22, 127–247; c) R.T. Kidd, D. Lennon, S.R. Meech, J. Phys. Chem. B1999, 103, 7480–7488; d) C.D. Lindstrom, X.-Y. Zhu, Chem. Rev. 2006, 106, 4281–4300; e)E. Kazuma, J. Jung, H. Ueba, M. Trenary, Y. Kim, Prog. Surf. Sci. 93, 163–176, (2018).

[73] Grossmann, L., King, B. T., Reichlmaier, S., Hartmann, N., Rosen, J., Heckl, W. M., … Lackinger, M. On-surface photopolymerization of two-dimensional polymers ordered on the mesoscale. Nature Chemistry, 13(8), 730–736. (2021).

[74] Ullmann, F., & Bielecki, J. Ueber Synthesen in der Biphenylreihe. Berichte Der Deutschen Chemischen Gesellschaft, 34(2), 2174–2185. (1901).

[75] Ullmann, F., Meyer, G.M., Loewenthal, O., Gilli, O.: Justus Liebig's Annalen der Chemie 331,38–81 (1904).

[76] FANTA, P. E. The Ullmann Synthesis of Biaryls. Synthesis, 1974(01), 9–21. (1974).

[77] Cai, J., Ruffieux, P., Jaafar, R., Bieri, M., Braun, T., Blankenburg, S., Fasel, R. Atomically precise bottom-up fabrication of graphene nanoribbons. Nature, 466(7305), 470–473. (2010).

[78] Hla, S.-W., Bartels, L., Meyer, G., & Rieder, K.-H. Inducing All Steps of a Chemical Reaction with the Scanning Tunneling Microscope Tip: Towards Single Molecule Engineering. Physical Review Letters, 85(13), 2777–2780. (2000).

[79] Ho, W. Inducing and Viewing Bond Selected Chemistry with Tunneling Electrons. Accounts of Chemical Research, 31(9), 567–573. (1998).

[80] Okawa, Y., & Aono, M. Linear chain polymerization initiated by a scanning tunneling microscope tip at designated positions. The Journal of Chemical Physics, 115(5), 2317–2322. (2001).

[81] Okawa, Y., & Aono, M. Nanoscale control of chain polymerization. Nature, 409(6821), 683–684. (2001).

[82] Takajo, D., Okawa, Y., Hasegawa, T., & Aono, M. Chain Polymerization of Diacetylene Compound Multilayer Films on the Topmost Surface Initiated by a Scanning Tunneling Microscope Tip. Langmuir, 23(10), 5247–5250. (2007).

[83] Diederich, F. & Thilgen, C. Covalent fullerene chemistry. Science 271,317–324 (1996).

[84] Ding, P., Wang, S., Mattioli, C. et al. Extending on-surface synthesis from 2D to 3D by cycloaddition with C60. Nat Commun 14, 6075 (2023).

[85] Patera, L. L., Bianchini, F., Africh, C., Dri, C., Soldano, G., Mariscal, M. M., Comelli, G. Real-time imaging of adatom-promoted graphene growth on nickel. Science, 359(6381), 1243–1246. (2018).

[86] Chong, M. C., Sosa-Vargas, L., Bulou, H., Boeglin, A., Scheurer, F., Mathevet, F., & Schull, G. Ordinary and Hot Electroluminescence from Single-Molecule Devices: Controlling the Emission Color by Chemical Engineering. Nano Letters, 16(10), 6480–6484. (2016).

[87] Kawai, S., Koch, M., Gnecco, E., Sadeghi, A., Pawlak, R., Glatzel, T. Meyer, E. Quantifying the atomic-level mechanics of single long physisorbed molecular chains. Proceedings of the National Academy of Sciences, 111(11), 3968–3972. (2014).

[88] Pavlicek, N. & Gross, L. Generation, manipulation and characterization of molecules by atomic force microscopy. Nat. Rev. Chem. 1, 0005 (2017).

Chapter II: Experimental

Scanning Tunneling Microscopy (STM), a type of microscopy with a surface-sensitive, real space analysis approach, was invented in 1981 by Heinrich Rohrer and Gerd Binning at the IBM Zurich Research Laboratory in Switzerland [1,2,3]. Working in ultra-high vacuum (UHV) and at 1983 [4]. This finding revolutionized the atomic-scale monitoring of conductive and semi-conductive surfaces. Four years later, Gerd Binning invented another surface analysis technique called Atomic Force Microscopy (AFM) [5]. Indeed, because of their earlier capacity to resolve nanostructures in real space, these microscopies are now the foundation of nanotechnology accomplishments. Furthermore, these microscopies allow us to not only "see" atoms of substrates or the arrangement of molecules, but also to photograph and track on-surface synthesis processes for the production of ultrathin materials on the nanoscale. The general principle of STM will be explained in this section. The second section includes the presentation of the experimental environment, the preparation methods of different surfaces used in this thesis during the three years, as well as the tip fabrication and molecular deposition methods.

II.1 The Tunneling Effect:

The tunnel effect is used to power the STM. I will discuss quantum mechanics tunneling in this section of the second chapter. The electron behaves as a particle in quantum physics, but it also has a wavelike character. If we assume the electron to be a particle with mass m and velocity v, its total energy is given as the sum of potential energy V_0 and kinetic energy:

$$E = \frac{p_x^2}{m} + V_0 \qquad \text{(Eq 2.1)}$$

where the p_x is the momentum of the electron. If the energy of the electron is higher than potential energy V_0, the electron moves with a momentum

$$P_x = \sqrt{2m(E - V_0)} \qquad \text{(Eq 2.2)}$$

When the energy of the electron is lower than potential energy ($E < V_0$), the real solution of the equation does not exist. Therefore, the electron cannot pass through the potential barrier, which is already known as the classical forbidden region. The tunneling effect of the particle is the quantum mechanical phenomenon where the particle passes through the potential barrier, even if its energy is lower than the potential energy of the barrier. The tunneling effect is possible due to the wave-particle duality of the electron. If we consider that the electron is interacting with a 1D time-independent potential barrier in the z-direction, its wave function obeys the Schrodinger equation:

$$\left(-\frac{h^2}{(2\pi)^2 2m}\frac{d^2}{dx^2} + \mathrm{U(x)}\right)\varphi(x) = \mathrm{E}\,\varphi(x) \qquad \text{(Eq 2.3)}$$

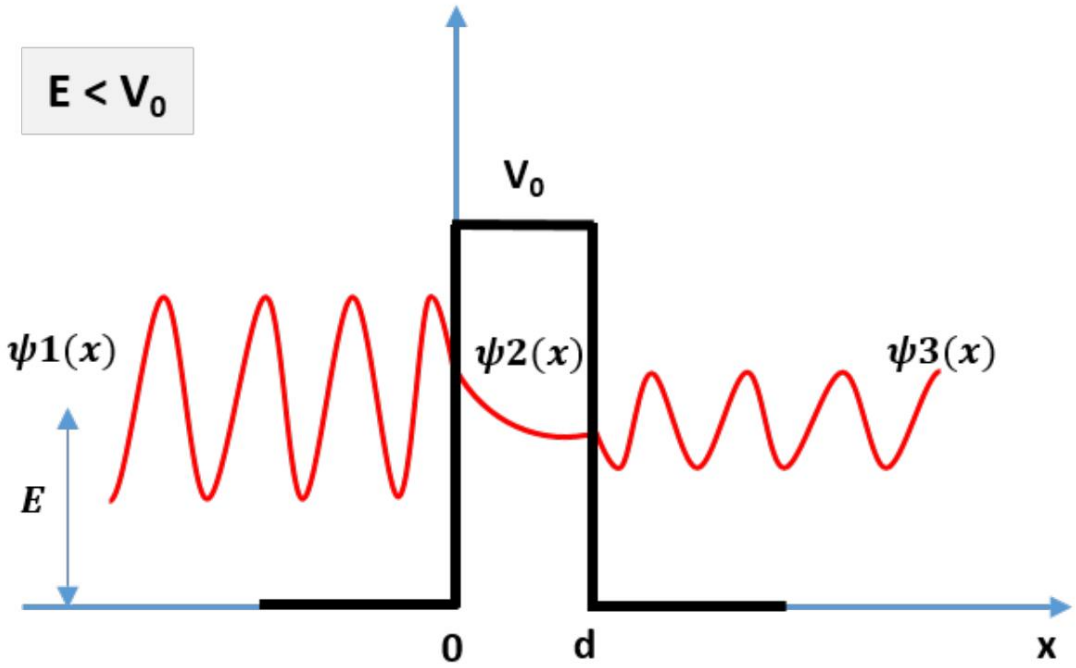

Figure II.1: Modeling of tunneling effect in the unidimensional case: an electron with energy E propagates from left to right, crossing through the rectangular barrier potential with the value of V0 and the width of d. ψ_1, ψ_2, and ψ_3 represent respectively the wave function of the electron in three regions: Region 1 at the left side of the barrier (x < 0), Region 2 in the middle of the barrier (0 < x < d), and Region 3 at the right side of the barrier: (x > d).

The potential is equal to 0 at the left and right side of the barrier (Region 1: x < 0 and Region 3: x > d), in the middle of the barrier (Region 2: 0 < x < d), the potential is a constant value V_0 independent of time. The solution of the wave function in each region is:

$$\psi(x) = \begin{cases} \psi_1(x) = A_1 e^{ikx} + B_1 e^{-ikx} & \text{if } (x < 0) \text{ (Region 1)} \\ \psi_2(x) = A_2 e^{\alpha x} + B_2 e^{-\alpha x} & \text{if } (0 < x < d) \text{ (Region 2)} \\ \psi_3(x) = A_3 e^{ikx} & if\ (x > d) \text{ (Region 3)} \end{cases} \qquad \text{(Eq 2.4)}$$

where

$$K^2 = \frac{(2\pi)^2 2mE}{h^2} \qquad \text{and} \qquad \alpha^2 = \frac{(2\pi)^2 2m(V_0 - E)}{h^2} \qquad \text{(Eq 2.5)}$$

Waves are classified into two types: propagation waves in regions 1 and 3 and evanescent waves in area 2. In Region 1, electrons propagate in the direction of the potential barrier (amplitude A_1); parts of electrons are reflected by the barrier and propagate in the opposite direction to the barrier (amplitude B_1); and parts of electrons transmit into the barrier as the evanescent wave (ψ_2 in Region 2) and then propagate into the other side of the barrier (amplitude A_3 in Region 3). The transmission factor expresses the likelihood of an electron passing through the potential barrier:

$$T = \frac{|A_3|^2}{|A_1|^2} \quad \text{(Eq. 2.6)}$$

|A1| and |A3| can be determined according to the continuous condition at x = 0, x = d. Therefore, the transmission factor could be obtained:

$$T = \frac{1}{1+\frac{(K^2+\alpha^2)}{4K^2\alpha^2}sinh^2(\alpha d)} \quad \text{(Eq 2.7)}$$

If αd >> 1 (low energy, wide barrier), $\sinh^2(\alpha d) \sim \frac{e^{(\alpha d)}}{2}$, in this case the transmission is equal to:

$$T \sim \frac{16K^2\alpha^2}{(K^2+\alpha^2)^2} e^{(-2\alpha d)} \quad \text{(Eq 2.8)}$$

where α denotes the decay constant, which normally has a value of roughly 10-15nm^{-1}. The tunneling effect is demonstrated by (Eq 2.8), which shows that a particle with energy E has a nonzero chance of passing through a potential barrier V_0 in the classical prohibited area (E< V_0). Furthermore, the transmission probability falls exponentially as the barrier width d increases. For example, if (V_0-E) = 4eV (the order of the metal's work function), = 10.2 nm^{-1}, an increase of 0.1 nm might result in a tenfold reduction in transmission probability.

In the potential barrier region (Region 2: 0 < x < d), the wave function is found to be:

$$\psi_2(x) = \psi_2(0)\, e^{(-\alpha x)} \quad \text{(Eq 2.9)}$$

The wave function in the potential barrier region decays exponentially with the distance. The probability of finding an electron at some distance x is defined by $|\psi_2(x)|^2$. At a distance x = d, $|\psi_2(d)|^2 = |\psi_2(0)|^2\, e^{(-2\alpha d)}$. This result is consistent with the calculated transmission value T.

II.2 The Basics of Scanning Tunneling Microscope

STM is one of the few methods that can provide genuine atomic resolution by permitting real-time examination of conductive and semi-conductive solid surfaces**.** The principle of the STM is based on the approach of a metal tip to the conductive or semiconductive surface, at a distance of a few angstroms to measure electric current by applying a bias voltage between the tip and the sample. The origin of the electric current is due to the electrons crossing by the tunnel effect, the potential barrier associated with separating the two electrodes formed by the tip and the surface when used in ultra-high vacuum. An STM tip is usually made of tungsten or a Pt-Ir alloy and is attached to a scanning unit a piezo tube scanner, as can be shown in Figure II.2

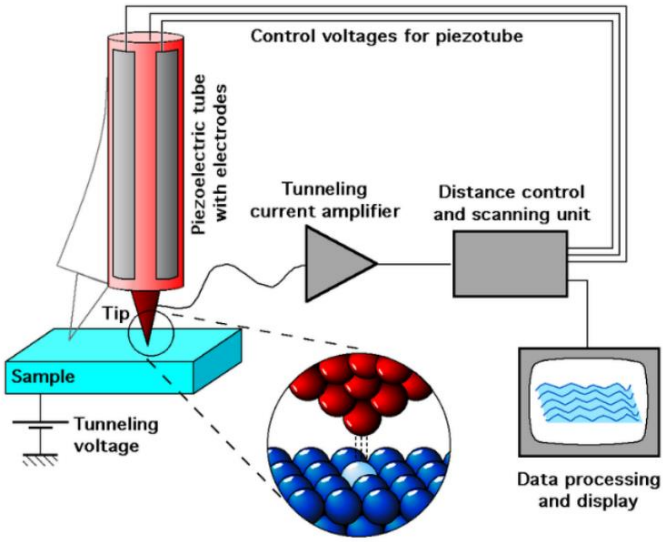

Figure II.2: Illustration of the working principle of STM. A bias voltage is applied between the sharp tip and the sample separated by a distance of a few angstroms. The tunneling current between the tip and sample is promoted and measured. The distance control unit adopts the position of the tip by using the piezoelectric material. Figure adapted from [6].

The piezoelectric scanning unit, the essential building block of the STM fabricated by ceramic material, the size of which can be changed by externally supplied voltages, enables the tip to be positioned relative to the sample (x, y, and z) with exceptionally high accuracy of roughly 1 pm. When the tip is close enough to the surface (0.1-1 nm), the I/V converter promotes a tunneling current through the air, insulator, or liquid depending on the operating circumstances, and converts it to a voltage. To detect these tunnel currents, the tip and sample are brought closer together such that the electron wave functions of the tip and sample begin to overlap at such small distances, producing an electric current. The tunneling probability density of the wavefunction, and hence the tunneling current I_t, depends exponentially on the tip-sample separation, as shown in Eq2.1:

$$I_t \propto V e^{-k.z\sqrt{u}} \qquad \text{(Eq2.10)}$$

- v: bias voltage applied between the tip and the sample
- k: constant
- z: tip-sample separation distance
- U: tunnel barrier height between the tip and the sample

The dependence on distance (z) in this approximation illustrates that STM may be used to recreate surface topography. As a result of the tunneling current's exponential reliance on tip-sample distance, with a perfect sharp tip in which the current flows predominantly via one atom at its apex, STM with high z sensibility delivers atomic resolution. This indicates that the entire recorded tunneling current is accounted for by the final atom of the highly sharp STM tip interacting with the nearest atom in the sample. To induce a tunneling current to flow from one side to the other, a bias voltage must be applied between the tip and the sample, since as long as the tip and the sample are at the same electrical potential, their Fermi levels will line up precisely or very near. As a result, no tunneling current can be observed since there are no vacant states on either side to tunnel into. Indeed, Pauli's exclusion Principle forbids two electrons from occupying the same quantum state. As a result, a bias voltage must be applied between the tip and the sample, thus raising the Fermi level on one side and making

empty energy levels available on the other side for tunneling into. In fact, placing a voltage between the tip and the sample defines the starting and ending states. As a result, it is critical to electrically bias the junction to allow current to flow in a specific direction. The STM tip is biased in our situation while the sample is grounded. Figure II.3 shows a schematic energy diagram of the tunneling process in an STM setup, where two cases can occur depending on the bias voltage:

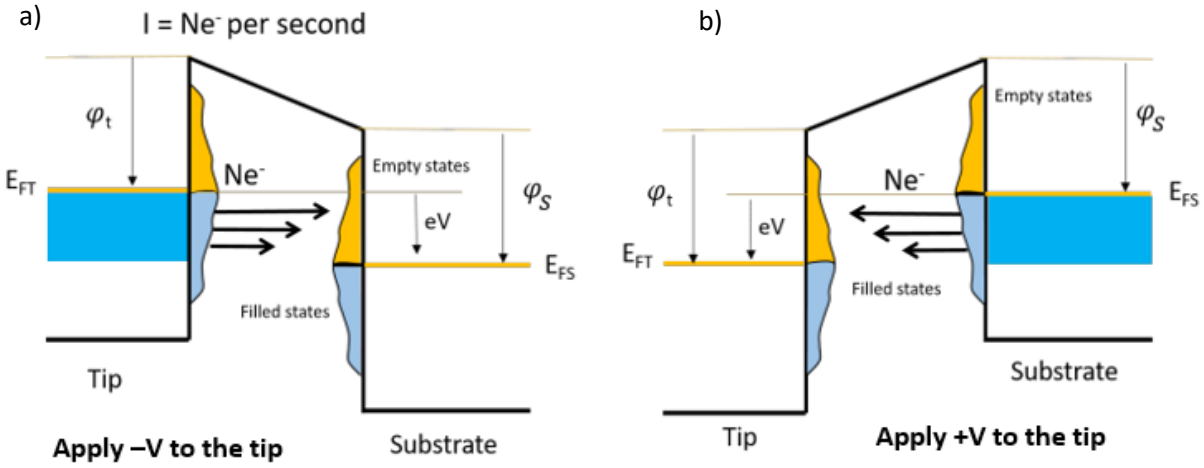

Figure II.3: The sample (metal)-vacuum-tip (metal) transfer junction scheme: (a) Positive bias voltage encourages electron transfer from the filled states of the tip to the empty states of the sample; (b) negative bias voltage encourages electron transfer from the filled states of the sample to the empty states of the tip. This image was copied from [7].

1- When the junction is positively biased ($V_{bias} > 0$), the Fermi level of the sample rises with respect to the tip (Figure II.3a), causing the tunneling current flow direction to reverse (I_t).
2- When the junction is negatively biased ($V_{bias} < 0$), the Fermi level of the sample lowers down by an amount eV_{bias} with respect to the Fermi level of the tip, enabling any electrons with energies between E_F and $E_F + eV_{bias}$ to tunnel from the tip to the sample (Figure II.3b).
3- When the STM junction is not biased ($V_{bias} = 0$), the Fermi levels of both the tip (E_{Ftip}) and the sample ($E_{Fsample}$) are aligned (E_F), and no net tunnel current flows through the barrier.

Bardeen devised a simpler model of a metal-vacuum-metal tunneling junction based on a time-dependent perturbation technique, which became the most widely used theoretical method for computing tunneling current [8]. This technique, however, results in an equation involving the wave functions of the tip and the sample, which is hard to determine. As a result, more simplification was required to assist in the computation of the tunneling current. J. Tersoff and D.R. Hamann [9], used a spherical-tip approximation to represent the STM probe and solved the problem using just an s-wave function:

$$I_t \propto V_{bias}\, \rho_{tip}\, \rho_{sample}\, (r_0, E_F) \quad \text{(Eq2.11)}$$

- V_{bias}: bias voltage applied between the tip and the sample
- ρ_{tip}: LDOS of the tip in the vicinity of the Fermi level

- ρ_{sample}: LDOS of the sample in the vicinity of the Fermi level
- r_0: center of curvature of tip

This equation (Eq2.11) demonstrates that the spatial resolution of STM is greatly dependent on the tip shape. Furthermore, the detected tunneling current is proportional to the sample's local density of states LDOS as measured at the Fermi level at the center of the tip curvature. In other words, STM pictures are the convolution of the tip's geometric and electronic structures with the surface's electronic structure and composition.

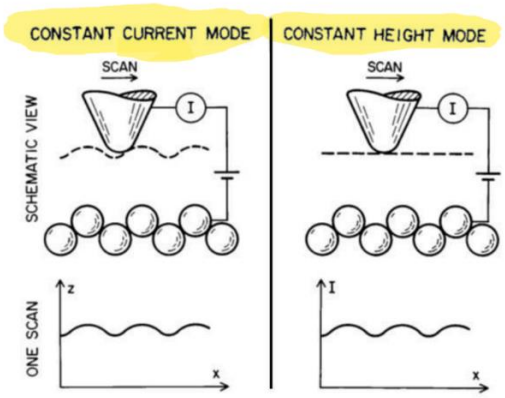

Figure II.4: Schematic illustration of the constant current and constant height modes of STM operation. Figure adapted from reference [10].

Experiments by STM are performed with two techniques: constant-height mode or a constant current mode which are illustrated in Figure II.4. [10] Constant current mode which is used in my thesis, mode requires a more elaborate setup where a feedback loop is used to keep the tunneling current equal to a user-defined setpoint by adjusting the tip height at each measurement point. For example, if the system detects a drop in tunneling current, it changes the voltage given to the piezoelectric scanner, reducing the distance between the tip and the sample. In this mode, the ensemble of data linked to the motion of the piezoelectric scanning tube in the z-direction to hold the current constant is utilized to reconstruct the surface's topography. The feedback loop enables continuous control of the tip location; uneven surface topography may be assessed with high accuracy without the risk of the tip colliding with the surface.

On the other hand, the constant height mode is often used for atomically flat surfaces. While tunneling current is detected, the tip must maintain a consistent tip-sample distance and scan the area of interest line after line. Because of the continuous tip-sample distance, the tip might collide with the surface due to pollution or differences in surface topology. This mode is much faster and offers better stability due to the absence of vertical movements, but requires pre-recognition of flatness and roughness of the surface to avoid breaking the tip.

STM is a powerful instrument that can offer local spectroscopic data at the size of an atom in addition to surface topography. Scanning tunneling spectroscopy (STS) is done in its most basic form by setting the tip-sample distance at a certain spot on the surface and adjusting the applied bias voltage (Vbias). As a result, an I-V curve may be recorded, from which relevant information on the surface's (or adsorbed molecule's) energy levels such as conduction band, valence band, HOMO and LUMO, band gap, and so on can be derived. However, it is vital to note that this needs mastery of the tip's

preparation and calibration on a reference sample in order to acquire knowledge of its densities of states before attempting to exploit an unknown sample [11].

II.3 Experimental setup:

Omicron Nanotechnology GmbH's Variable Temperature Ultra-High Vacuum Scanning Tunneling Microscope (VT-STM-XA) is utilized to capture all pictures for this thesis work in constant-current mode. The temperature of the sample put on the STM head may be adjusted from 100 K to 300K, allowing for temperature evolution studies during scanning. A cryogenic liquid nitrogen N_2 bath is used to chill the sample, which is thermally coupled to it by oxygen-free and highly conductive copper braiding. To effectively isolate external noise and vibrations, an eddy current magnetic dampening technology in conjunction with spring suspension is used. Figure II.5.b is a picture of the VT-STM-XA head showing the internal design where some key elements are highlighted.

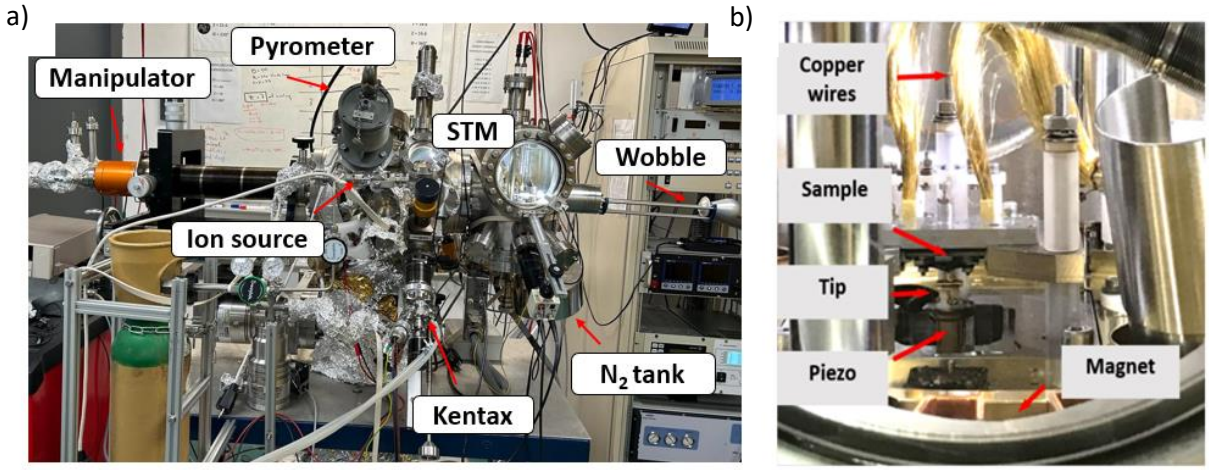

Figure II.5: a) Image of the VT-UHV-STM and the system's main components. b) STM's head from the side view.

The preparation chamber of ultra-high vacuum experimental equipment is dedicated to sample preparation and is linked directly to the STM chamber. To achieve an ultra-high vacuum below 2.10^{-10} mbar in the chamber, a combination of the main pump, turbomolecular pump, ion getter pump, and titanium sublimation is employed. The UHV conditions are reached after baking out all the setup for 24-48 hours at a temperature of roughly 125°C. The system uses three distinct types of pumps, all acquired from Agilent Inc., to achieve low-base pressure UHV chambers. The first, a rotary vane pump (Figure II.6 a), lowers the ambient pressure to 10^{-3} mbar. In addition, a rotary vane pump is linked to a turbomolecular pump (Figure II.6 b), allowing pressure to be reduced from 10^{-3} to 10^{-10} mbar. The fundamental problem with the turbomolecular pump is that it works at a high frequency, resulting in mechanical noise that might interfere with STM observations. The third pump is the ionic pump, Figure II.6 c), which maintains a pressure of around 10^{-10} mbar during STM experiments, without inducing mechanical noise. A high voltage field is introduced between two electrodes in this pump, resulting in electron emission. Titanium is used to make electrodes. A magnetic field is created, which supplies electrons with helical paths, the helical paths allow for effective collisions of electrons, atoms, and molecules in the inner chamber gas. The impact causes the gas molecules to become ionized and "glued" to the electrodes. Pressure is reduced as a result of this procedure. Because the metal surface has its own "lifetime" under ultra-high vacuum, it is believed that titanium electrodes would be squandered. In such a situation, the Titanium Sublimation Pump (TSP) plays a part in raising the ionic pump's speed by the evaporation of titanium atoms. As a result, collisions between gas molecules

inside the chamber and titanium atoms are encouraged and attached to titanium electrodes. In our experimental setting, the evaporation of titanium atoms is repeated every eight hours.

Figure II.6: System of the pumps for reaching ultrahigh-vacuum: a) rotary-vane pump, b) turbomolecular pump c) ionic pump. The images were adapted from [12].

The sample preparation chamber includes conventional sample preparation components such as an ion source (for metal substrates), direct-current heating (for silicon substrates), a three-axis manipulator (x, y, z, Θ)), and a molecular evaporator (Kentax). A magnetic manipulator allows the sample and tip to be transferred between two compartments. A rapid airlock system is used to introduce samples and tips from ex-situ. To eliminate the oxide layer and any other impurities, newly entering tungsten tips are annealed in the STM chamber using a tantalum sheet. Figure II.5.a depicts our setup and illustrates the essential pieces of equipment mentioned earlier.

II.4 Tip Preparation

The tip is most likely the most important component in achieving atomic resolution in STM. The tip should ideally be ultra-sharp, which implies it should have a single atom on its apex. The tip for the tests is composed of 0.20 mm diameter W (tungsten) wire. As a result, electrochemical etching is the method of choice for preparation [13]. After cutting a few millimeters of W (tungsten) wire, we apply current to it and attach it to a golden tip supporter. In addition, the tip of a tip supporter is put on a platinum electrode. As illustrated in Figure II.7 the tip's leading end is immersed vertically in a 5 mol/L NaOH solution, which serves as an electrolyte. We adjust the source to a 10 V potential difference and allow the closed electric circuit to create an electrochemical reaction.

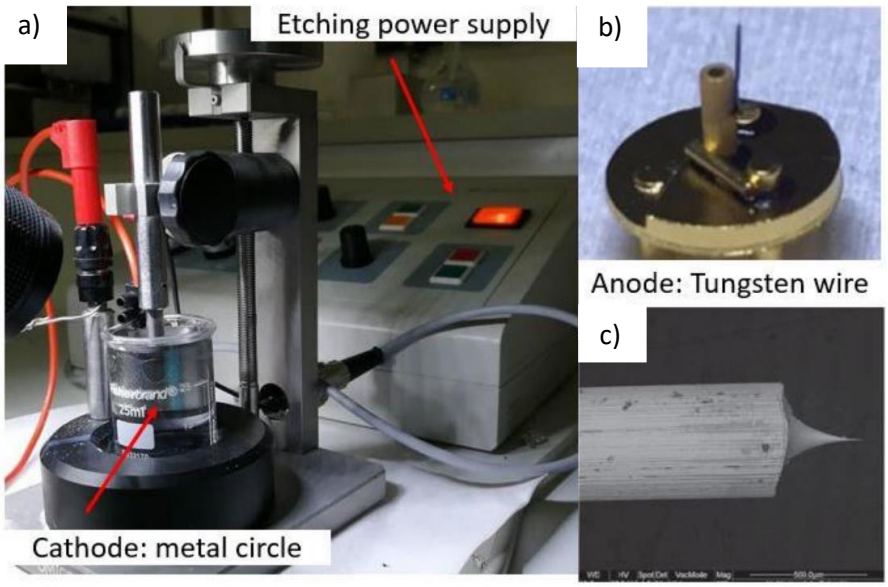

Figure II.7: a) Etching power supply with electro-chemical capabilities for etching the tip: cathode (metallic circle) within the glass containing NaOH solution. b) The etched tungsten wire serves as an anode. c) SEM picture of STM tip created by etching, derived from [14].

Electrochemical reaction attacks the immersed part of the wire and occurs in further steps:

$W(s) + 2OH^- + 2H_2O \longrightarrow WO_4^{2-} + 3H_2$ (Eq.2.4.1)

The corresponding half-reactions that occur on cathode and anode are:

Anode: $W(s) + 8OH^- \longrightarrow WO_4^{2-} + 4H20 + 6e^-$ (Eq.2.4.2)

Cathode: $6H_2O + 6e^- \longrightarrow 3H_2\,(g) + 6OH^-$ (Eq.2.4.3)

The tungsten wire becomes thinner as it continues to change into soluble WO_4^{2-} until the lowest portion of the wire breaks off. The described drop-off approach allows for a sharp tip form, which must be cleansed in warm water for 30 seconds before being introduced into UHV. Furthermore, the tip is placed into the UHV/preparation chamber via ex-situ load lock and annealed above 1050 K to eliminate the tungsten trioxide layer.

II.5 Used Substrates:

In this part, four distinct substrates utilized throughout this thesis will be discussed. A brief explanation of each crystallographic structure will be provided here.

II.5.1 Conductive substrate: Gold Au(111)

The gold crystallizes in a faced cubic structure (fcc) with a lattice constant of a = 4.08 Å, however, the atoms on the surface of the Au (111) substrate are rearranged in comparison to the atoms in the bulk owing to surface energy minimization. The contraction causes the rearrangement in the [1$\bar{1}$0] direction, where the distance between the final surface's layer's 23 atoms equals the distance between the bulk of the substrate's 22 atoms [15]. Because gold is a noble metal with an inert surface, we may prepare this reconstruction in ambient circumstances. The Au(111) surface is cleaned by a repetition of ion argon sputtering followed by annealing under ultra-high vacuum conditions. For each cycle, we use an ion beam energy of 1 kV for 20 minutes per cycle. Each bombarding cycle is followed by thermal annealing till 500°C for 30 minutes to ensure the crystallographic surface reconstruction by releasing defects and eliminating implemented Ar atoms.

To reduce surface energy, gold is the only fcc metal whose hexagonal structure of the (111) surface reconstructs in a (22x $\sqrt{3}$) overlayer structure known as herringbone reconstruction. As illustrated in Figure II.8a-b, the herringbone reconstruction is formed by a contraction of 23 atoms from the top layer over 22 atoms from the second layer. Surface atom contraction is consistent with a stacking-fault-domain model featuring periodic transitions between surface areas with fcc-type stacking and hexagonal-close-packed (hcp) top-layer atom stacking produced by surface elastic strain [16].

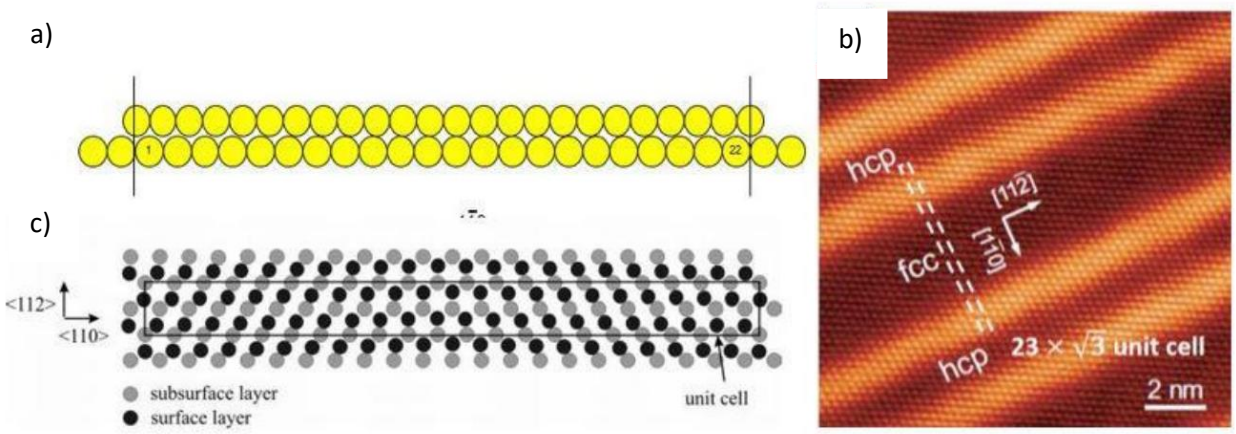

Figure II.8: a) Surface contraction produced by the registration of Au 23 atoms per unit cell on 22 Au atoms in the bulk. b) Top view schematic of the Au(111) reconstruction showing the integration of extra Au atoms (black spots-surface layer) and the resulting transition between fcc and hcp domains [17]. c) STM image of Au(111) surface.

Figure II.8b shows a high atomic resolution STM image of a clean reconstructed surface preparation of Au(111) where the picture clearly shows the herringbone reconstruction, with the atoms in the bridge sites appearing brighter. This surface condition is useful for testing and calibrating STM tips before doing spectroscopic measurements on unknown surfaces.

II.5.2 Semiconductors

II.5.2.1 Si(111)-7x7:

Among the numerous reconstructions of the Si(111) surface, the 7x7 reconstruction of the (111) face of silicon is the most stable phase at normal temperature. Takayanagi developed an atomic model, the dimer-atom-stacking fault (DAS), based on his transmission-electron diffraction investigation of this surface under UHV, which agreed with the initial STM photos of the 7x7 surface.[18] Figure II.9 depicts a 7x7 DAS model an accurate model of the Si(111)-7 X 7 surface is especially desirable because it is the most stable of all silicon crystal surfaces at room temperature and it is important involved in surface chemical reactions of that material, with 12 adatoms (atoms that saturate the first layer's dangling bonds) organized in two half-cells, 6 rest-atoms (atoms in the first layer not saturated by an adatom), and 1 corner-hole (gap). The adatoms are divided into two separate types with respect to their position in the unit cell. The first type of adatom is located in the corner of the unit cell, next to corner holes, and these are called corner adatoms. The second type is located in the center of the edges of the unit cell, and these are called center adatoms. The position of the restatoms, center adatoms, and corner adatoms in a unit cell. It can be seen that the corner adatoms are adjacent to one rest adatom, and the center adatoms are adjacent to two restatoms.

This intricate reconstruction has 102 atoms:

- 48 atoms above the 1x1 of Si(111)
- 42 atoms (including rest-atoms) in the upper layer.
- 12 adatoms

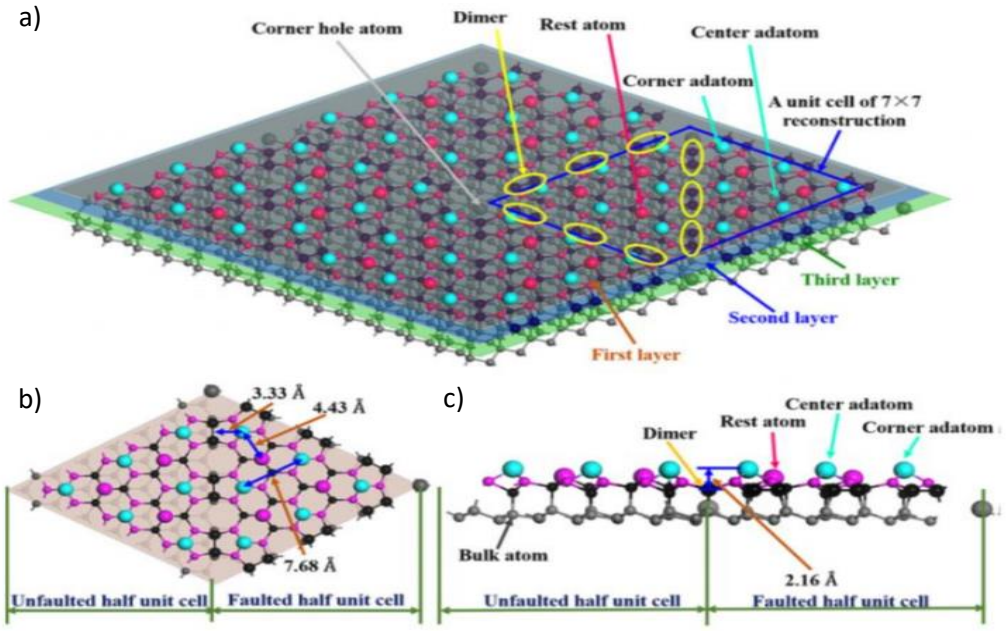

Figure II.9: The DAS model for the Si (111)-7x7 surface is depicted schematically. a) Top view schematics of the DAS model's 2X2 supercell. b,c) The matching top- and side-view structure of one unit cell, identified with lateral and vertical distance between the highlighted atoms, respectively. The figure is based on reference [19].

The DAS structure is constructed on a bulk terminated Si(111)-7x7 surface with one dangling bond per atom (the 'base layer'). Figure (II.10 a) depicts this stratum. The 'dimer layer' is the initial layer in this

structure. This layer is generated by atoms saturating the base layer's dangling bonds. Dimers occur between the two halves of the unit cell as well as along the unit cell's edge, linking the missing atoms, as shown in Figure (II.10 b). Atoms are missing on the corners of the 7x7 unit cell on this layer, which are referred to as "corner holes". These corner holes could be observed and employed in a typical topographical STM image to identify the unit cell. The distance between the corner holes is 2.69 nm. Each dimer atom has two dangling bonds, whereas the other atoms in this layer have three. To saturate these dangling bonds, the atoms on the following layer must create a stacking defect inside one-half of the unit cell. As seen in Figure (II.10 c), this layer is known as the 'rest atom' layer. This fault has two important consequences as far as the adatoms go. One is that they are on average physically higher by about 0.04 angstroms than the adatoms on the unfaulted half of the unit cell [20, 21]. The other is that there is charge transfer from the unfaulted to the faulted half of the unit cell, resulting in a difference in electronic structure. This difference in the electronic structure of two sides of the unit cell causes the STM contrast between the two halves in occupied states images (faulted half of the unit cell is imaged ~0.04Å above the unfaulted half of the unit cell at -2.0 V [20, 21, 22].

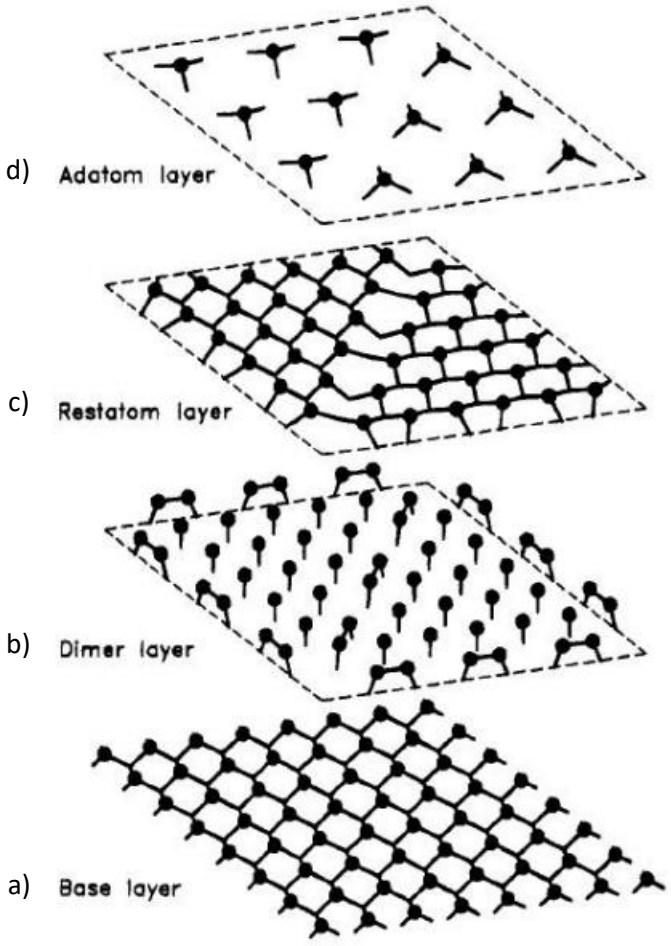

Figure II.10: Layer-by-layer construction of Si(111)-7x7 structure. a) (1x1) unreconstructed (bulked terminated) surface b) first layer, the dimer layer; c) second layer, the rest atom layer; d) top layer, the adatom layer (Diagram taken from Ref. [23])

On the rest atom layer, there are 21 dangling bonds perpendicular to the surface. The best way to saturate these dangling bonds in order to minimize the surface energy is by using 12 adatoms on top of this layer, the 'adatom layer', as shown in Figure (II.9 d). In this configuration, three dangling bonds

are left intact on the rest atom layer in each half of the unit cell. On the adatom layer, six adatom dangling bonds are present in each half of the unit cell. This 1x1 to 7x7 transformation is motivated by a drop in dangling bond density. As a consequence, the 7x7 surface decreases the number of dangling bonds from 49 to 19, which is more energetically advantageous (12 on adatoms, 6 on restatoms, and 1 on the corner hole). This reconstruction is also asymmetrical, resulting in inequivalent triangular half-cells. One half-silicon cell's layers are stacked in a regular sequence (unfaulted half-cell UF) and correspond to the left-hand triangle in Figure II.9b DAS model. The silicon layers in the opposite half-cell, on the other hand, are stacked in a faulty sequence (faulted half-cell FH) and correspond to the right-hand triangle in Figure II.9b DAS model.

Si(7x7) reconstruction may be produced in an ultra-high-vacuum (UHV) STM setup with a base pressure of $2x10^{-10}$mbar. The sample was then degassed to 800 °C using direct current heating to remove the native oxide layer and any other pollutants, while the pressure in the chamber was kept below $5x10^{-9}$ mbar. The sample was then flashed multiple times at 1200 °C until the temperature was maintained for 10 seconds without surpassing 10^{-10} mbar. Following the last flash, the temperature plummeted rapidly to roughly 950 °C, then progressively reduced at a rate of 10 °C/min until it reached 750 °C. We quickly decreased the current below 750 °C and allowed the sample to cool. Figure II.11a.b shows an STM image for the empty and filled states of the Si(111)-7x7 surface, respectively. Figure II.11a shows that STM images taken with a positive sample bias voltage often reveal 12 adatoms of similar height in each unit cell. Figure II.11.b depicts STM images obtained with a negative bias voltage, which show increased electronic contrast. The adatoms in the faulty half-cell are brighter than those in the unfaulted half. Furthermore, adatoms near a corner hole (known as a "corner adatom") are somewhat brighter than adatoms in the middle. In addition to the adatoms, the remaining atoms become apparent in the filled states when the negative polarity is scanned.

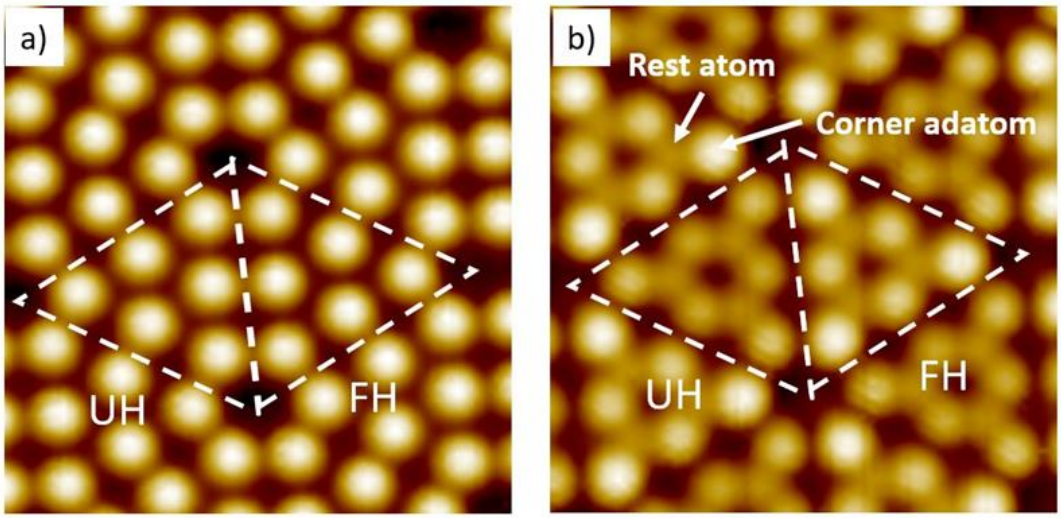

Figure II.11: STM images (6 nm x 6 nm) of the same zone of a Si(111)-7x7 surface: a) recorded at positive bias voltage (1.5 V, 150 pA) and b) recorded at negative bias voltage (-1.5 V, 150 pA). FH: faulted half-cell; UH: unfaulted half-cell.

II.5.2.2 Passivated Semiconductive substrate : Si(111)-B$\sqrt{3}$ x $\sqrt{3}$R30° :

Dangling bonds on the top atomic layer of the silicon surface result in extremely high reactivity. It has been demonstrated that doping with group III elements (B, Al, Ga, and In) with one fewer valence electrons than silicon may passivate the surface by saturating the dangling bonds [22]. The surface is

obtained in a controlled ultra-high vacuum environment, which includes meticulous degassing of the sample at as low a pressure as feasible till 800 °C to eliminate pollutants, flashing the sample until 1150 °C for numerous times, and annealing the sample at 850 °C for 50 minutes. During the annealing step, boron atoms diffused from the bulk to the surface layer, a phenomenon known as 'exodiffusion'. A maximum boron concentration in the 1/3 range of the monolayer may be reached by carefully controlling the annealing temperature and duration.

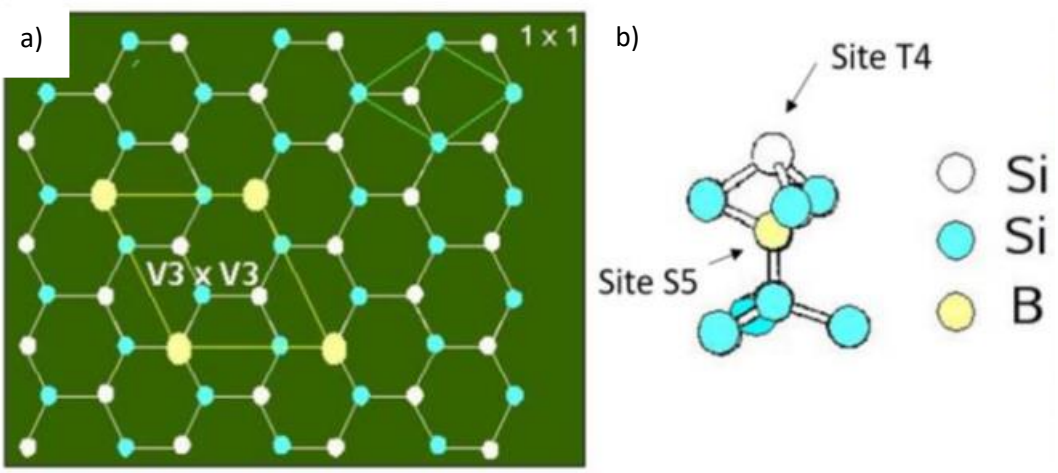

Figure II.12: a) Top view of a surface with silicon adatoms (blue and white circles) and boron atoms (yellow circles). The original Si(111) element lattice is represented by a blue rhombus marked 1x1 on the top right corner of the figure, with a lattice constant of 0.665 nm. b) Side view showing the atomic structure of the Si(111)-B$\sqrt{3}$ x $\sqrt{3}$R30° surface, with the Si adatoms sitting in top surface (T4) sites, while B atoms occupy the sub-surface sites (S5). The two models in a) and b) are adapted from [25].

The element lattice on the Si(111)-B$\sqrt{3}$ x $\sqrt{3}$R30° surface is rotated by 30 degrees relative to the basic Si(111) lattice. In comparison to the Si(111) lattice constant, the lattice constant is raised by a factor of $\sqrt{3}$. From an electronic point, the boron atom makes four bonds with silicon atoms in close proximity. One of its bonds is formed with a silicon adatom in position T4 through a charge transfer, which completes its valence shell and is responsible for the high stability of this reconstruction. While the Si(7x7) has 19 dangling bonds, the $\sqrt{3}$x$\sqrt{3}$ of SiB has none when the boron atom concentration is at its highest, lowering the surface energy.

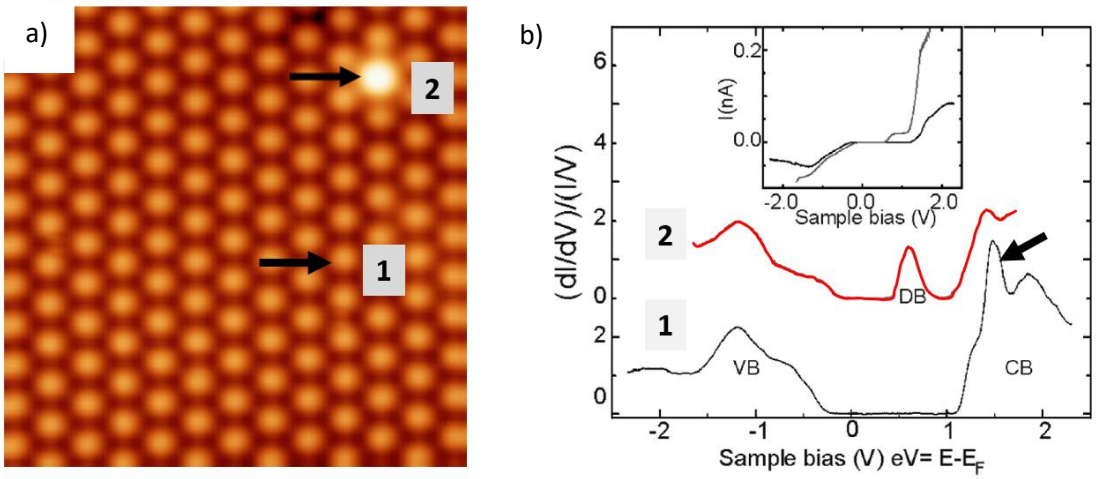

Figure II.13: a) High-resolution STM image of Si(111)-B$\sqrt{3}$ x $\sqrt{3}$R30° with maximal doping (about 0.33 monolayer), 8.7 x 8.7 nm^2, It = 50 pA, and Vs = 1.5 V. Bright atom (white arrow) corresponds to the absence of charge transfer toward the bulk due to the missing of an underlying boron atom. b) In differential-conductance spectroscopy dI/dV at 5 K, DB, CB, and VB denote the localized dangling-bond state, conduction, and valence bonds. The inset picture depicts the I(V) curve. Figures sourced from [26].

Due to the depopulation of virtually all dangling bonds, which makes it a passivated semi-conductive surface, the usage of Si(111)-B$\sqrt{3}$ x $\sqrt{3}$ is feasible. Figure II.13. a shows a high-resolution STM picture of the reconstructed Si(111)-B surface with the highest boron atom concentration in the subsurface (0.33 monolayer). The presence of boron atoms under the initial layer of Si creates a flawless hexagonal nanostructure formed of Si adatoms with a depopulated dangling bond state. The black arrow denotes an unusually brighter protrusion, showing a Si atom with a dangling bond filled by an e due to the lack of boron atoms beneath.

Berth and al [20, 21] used differential-conductance spectroscopy on bright and dark adatoms at 5 K. (Noted 1 and 2, see Figure II.13.b. The dI/dV spectrum (red curve 1) at point 1 shows that the reconstructed Si(111)-B surface has a 1.3 eV gap between the Valence Bonds (VB) and the Conduction Bonds (CB). Charge transport from Si to B is responsible for the existence of a prominent peak (black arrow) 0.4 eV above the bottom of CB. While the spectrum (black curve 2) on point 2 shows a noticeable peak in the band gap area with an energy of 0.6 eV, this corresponds to non-resonant Dangling Bonds (DB). The benefit of adopting a Si(111)-B$\sqrt{3}$ x $\sqrt{3}$ surface is that the local density of adsorbate states may be dissociated from the substrate due to the presence of the surface gap, which does not occur on commonly researched metallic surfaces.

II.5.3 Highly ordered pyrolytic graphite (HOPG):

HOPG (Highly Oriented Pyrolytic Graphite) surface was used as the substrate for the self-assembled molecular network studied by Atomic Force Microscopy in ambient conditions and STM under ultrahigh vacuum conditions. HOPG is a synthetic form of graphite that is created by the pyrolysis of organic precursors under high temperature and pressure conditions. The resulting material exhibits a high degree of crystallinity, with the carbon atoms arranged in a layered structure. The surface of HOPG is characterized by its basal planes, which consist of closely packed hexagonal arrays of carbon atoms. These basal planes are highly oriented, meaning that the majority of the carbon atoms lie within the

same plane. The layers stack on top of each other, with weak van der Waals forces holding them together, allowing for easy cleavage along the basal plane.

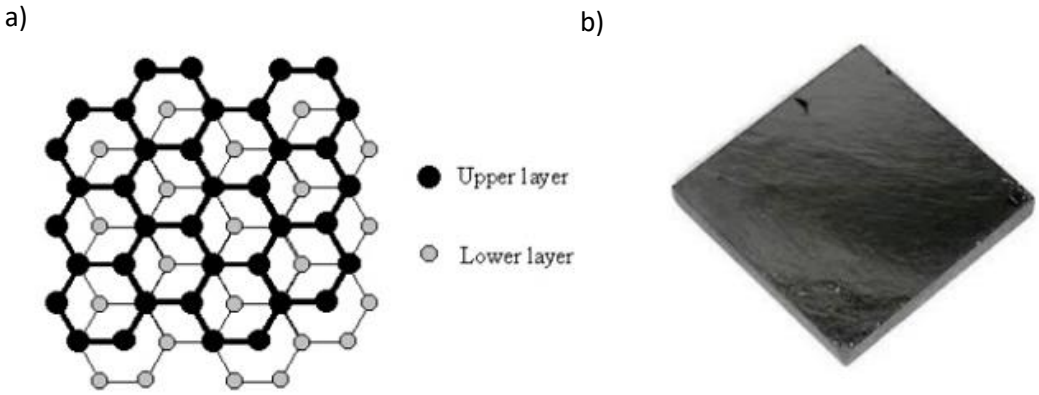

Figure II.14: a) The atomic structure of HOPG b) HOPG substrates are purchased from Bruker Company.

The crystal structure of HOPG is typically described using the notation of graphene, a single layer of graphite. Graphene consists of a two-dimensional lattice of carbon atoms arranged in a hexagonal pattern, forming a honeycomb structure. Each carbon atom is covalently bonded to three neighboring carbon atoms, resulting in a sp^2 hybridized structure. The carbon-carbon bond length in HOPG is approximately 0.142 nanometers [27,28]. The high crystallinity and surface orientation of HOPG make it a valuable material for various scientific techniques and applications. It is commonly used in scanning tunneling microscopy (STM) and atomic force microscopy (AFM) experiments, where the well-defined surface allows for high-resolution imaging of atomic and molecular structures. HOPG is also employed as a substrate for the growth of graphene and other two-dimensional materials due to its compatibility and controlled properties.

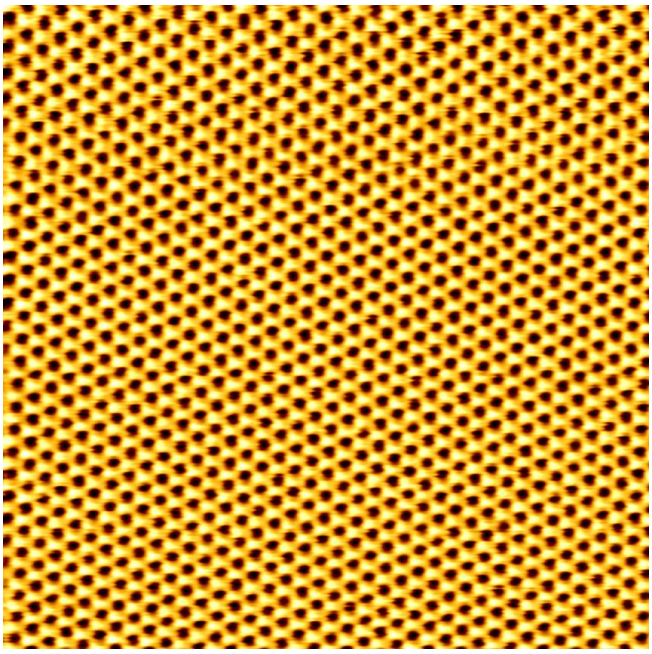

Figure II.15: High atomic resolution STM image of HOPG surface scanned at RT by STM under ultra-high vacuum conditions (V_s = 0.6 V, I_t = 800 pA, 9 x 9 nm^2)

II.6 Used Depositions Methods:

II.6.1 Evaporation system:

The molecular evaporator device has successfully deposited molecules on surfaces. The molecules are deposited in quartz crucibles in a powder-solid condition. The used evaporator contains three quartz crucibles, which allow for the storage of three distinct kinds of molecules. Each crucible is surrounded by a filament. A regulated current passed via filaments causes the powder to gradually heat up. The evaporation system also includes a thermocouple, which measures the temperature of molecules inside the crucibles. Furthermore, in every step of molecular evaporation, the cooling water system prevents nearby crucibles from overheating. At the temperature of sublimation, molecules transition from the solid-state phase to the gas-state phase. Sublimation occurs when molecules transition from the solid-state phase to the gas-state phase, resulting in deposition on a surface. The evaporation mechanism may deposit molecules on a surface in layers ranging from submonolayer to multiple layers. Furthermore, the thermocouple controls the deposit temperature, allowing for the homogenous deposition of molecules with excellent repeatability.

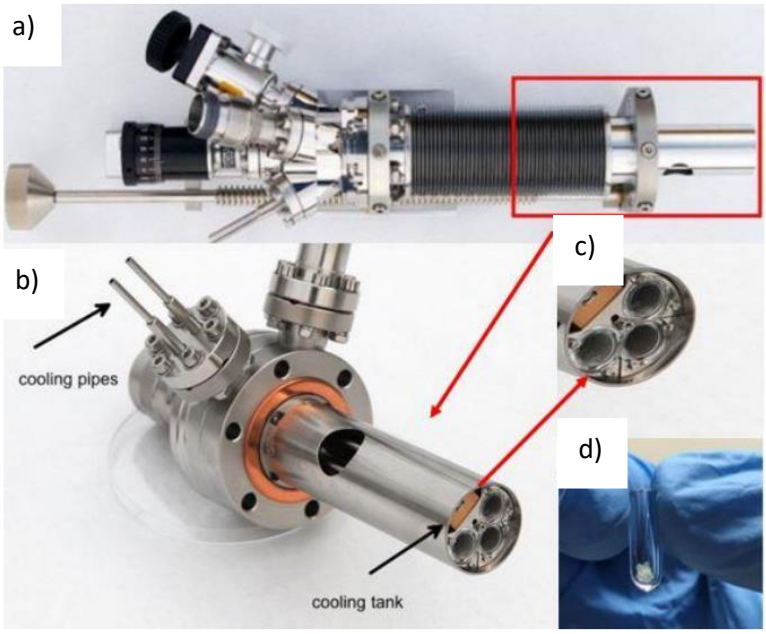

Figure II.16: Evaporation system for the sublimation of molecules: a) Kentax UHV molecular evaporator. b) Cooling pipes and cooling tank to prevent the adjacent crucibles from overheating during sublimation. c) Three places inside the Kentax for three crucibles. d) Quartz crucible with molecules in the solid state. Images adapted from. [29]

II.6.2 Spin coating:

Spin coating is the experimental technique that is used to produce thin films, ultrathin films, and nanostructures upon substrates. This approach was used to deposit organic molecules and build organic monolayers on surfaces investigated using Atomic Force Microscopy in ambient circumstances and STM in ultra-high vacuum conditions. The spin coating includes the deposition of a very low concentration of organic molecule solution on stationary substrates. The substrate is held on the spin coater vacuum chuck to securely hold substrates in place during high-speed rotation, ensuring uniform coating deposition and minimizing substrate movement. As the substrate rotates, centrifugal force is generated, causing the solution to spread throughout the substrate and a significant quantity of the solution to be ejected off the surface entirely.

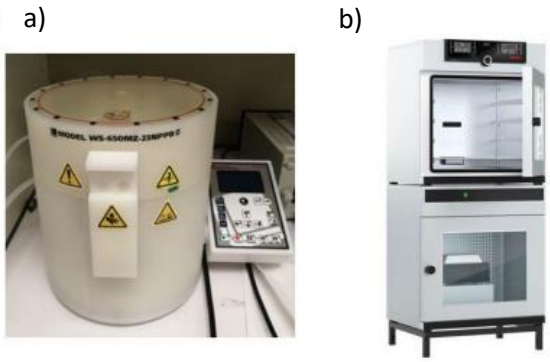

Figure II.17: a) Spin coater. b) VO Memmert Heater

Spin coating was used to prepare all molecular layers in the experiments in Chapter IV. Initially, the HOPG surface was cleaved with scotch tape until obtaining a completely clean and flattened layer. The solutions of organic molecules were deposited on the surface, and the spin coating was carried out for

20 seconds with a chosen value of rpm which is defined as a number of turns in a minute. For our experiments, we utilized a range of 850 to 1000 rpm to obtain one monolayer and less than one monolayer of molecules on the HOPG surface. After the spin coating technique, the sample was transferred to the VO Memmert Heater to evaporate the organic solvent in the temperature range between 80-100°C.

II.7 Used Characterization Techniques:

In this part, I will introduce the different types of characterization techniques used in our experiments to analyze the results starting from X-ray photoelectron spectroscopy, atomic force microscope, and AFM-based infrared spectroscopy.

II.7.1 X-ray photoelectron spectroscopy (XPS):

X-ray photoelectron spectroscopy (XPS) has become one of the most extensively utilized surface assessment techniques; it is based on Heinrich Hertz's discovery of the photoelectric effect in 1887 [30]. X-ray photoelectron spectroscopy is a surface-sensitive analytical method that involves bombarding a material's surface with X-rays and measuring the kinetic energy of the released electrons. The surface sensitivity and capacity to reveal chemical state information from the components in the sample are two significant properties of this approach that make it powerful as an analytical tool. Except for hydrogen and helium, all elements may be identified, and XPS has been used to analyze the surface of nearly every substance, from plastics to fabrics to dirt to semiconductors. All materials have surfaces, and it is those surfaces that interact with other materials. Factors such as surface wettability, adhesion, corrosion, charge transfer, and catalysis are all determined by surfaces and surface contamination, and, therefore, studying and understanding surfaces is important [31].

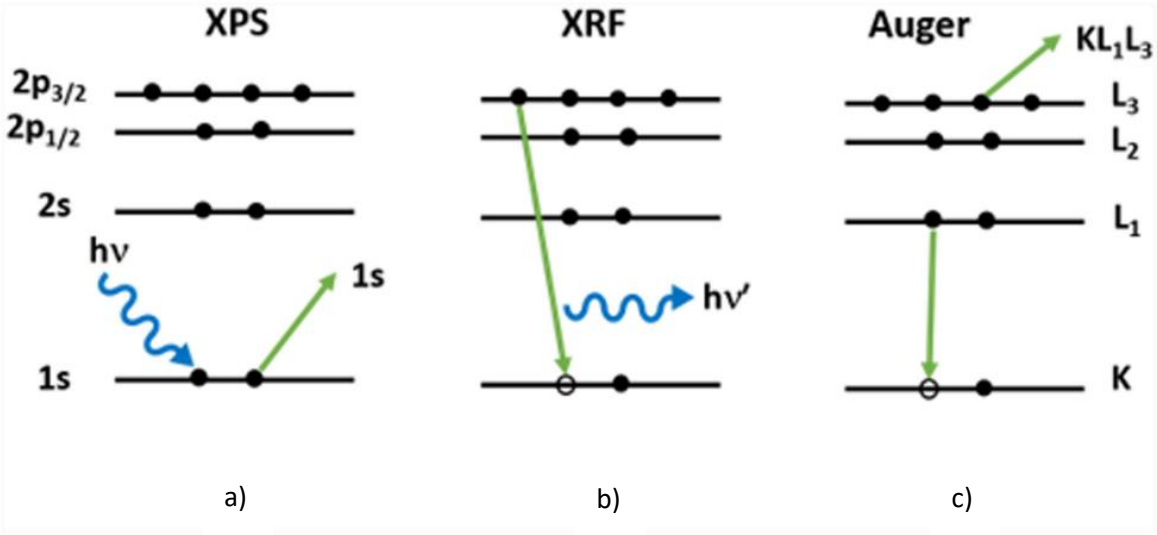

Figure II.18: Processes that result from x-ray bombardment of a surface include (a) emission of a photoelectron, (b) x-ray fluorescence, and (c) emission of an Auger electron [31].

In XPS, the sample is irradiated with soft X-rays (energies lower than ~6 keV), and the kinetic energy of the emitted electrons is analyzed Fig.2.19. The emitted photoelectron is the result of the complete transfer of the X-ray energy to a core-level electron. This is expressed mathematically in Eq. (6.1). It simply states that the energy of the x-ray (hvv) is equal to the binding energy (BE) of the electron (how

tightly it is bound to the atom/orbital to which it is attached), plus the kinetic energy (KE) of the electron that is emitted, plus the spectrometer work function (Φ_{spec}), a constant value.

$$Hv = BE + KE + \Phi_{spec} \quad \text{(Eq.6.1)}$$

To determine the binding energy of an electron, (Eq.6.1) can be rearranged to obtain (Eq.6.2), where the terms on the right are either known (hv and Φ_{spec}) or measured in the XPS experiment (KE)

$$BE = hv - KE - \Phi_{spec} \quad \text{(Eq.6.2)}$$

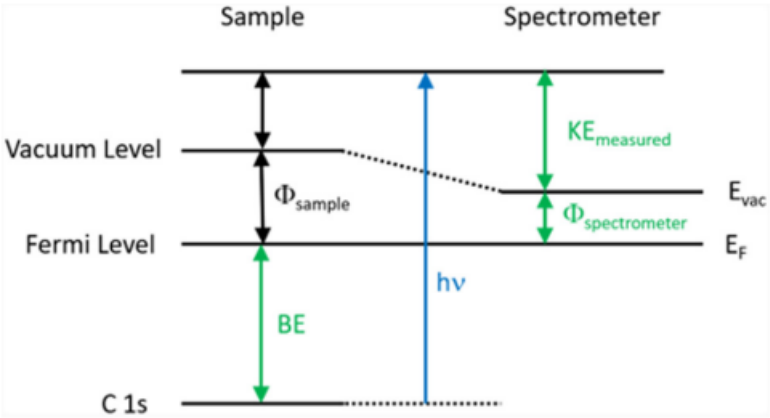

Figure II.19: The energy level diagram illustrates schematically the basic XPS equation, including the x-ray source energy (hu), the binding energy of the electron (BE), the measured kinetic energy of the electron ($KE_{measured}$), and the work function of the spectrometer ($\Phi_{spectrometer}$) [31].

This could be also illustrated diagrammatically in Figure II.19. Note that the photoelectron binding energy is measured concerning the sample Fermi level (not the vacuum level) which is the reason that Φ_{spec} is included [31].

XPS equipment is contained in ultra-high vacuum (UHV) chambers and comprises the following components: an X-ray source, a sample stage, extraction lenses, an analyzer, and a detector [32,33]. For two reasons, XPS instruments are housed in ultra-high vacuum (UHV) environments. First, the emitted electrons must not scatter off air molecules as they go to the analyzer, which necessitates vacuum levels of 10^{-5} -10^{-6} mbar. XPS systems have substantially lower base pressures, closer to 10^{-9} and 10^{-10} mbar. XPS is extremely sensitive to surface contamination since it is a surface-sensitive technology. As a result, XPS devices make use of the UHV environment to decrease surface contamination within the chamber. In Chapter III, we'll be collaborating with Haute-Alsace University, specifically with Professor Carmelo Pirri and Doctor Samar Hajjar, to incorporate XPS experiments.

II.7.2 Atomic Force Microscope:

The experimental advances enabled possibilities to resolve high-resolution images and in 1994 year the true atomic resolution on Si(111)–(7x7) was revealed by AFM [34]. The invention of AFM has overcome the limitation of STM and enabled imagining solid materials without the condition of surface conductivity, such as biological samples and polymers. The principle of AFM is based on measuring the forces between an AFM tip, which is mounted on a flexible cantilever, and the sample's surface under investigation, as the function of their mutual separation. Interaction between AFM tip and sample can

be easily explained by Lenard-Jones potential [36] which is used to represent the interaction between two non-charged atoms separated by distance r:

$$V_{LJ} = 4\varepsilon \left[\left(\frac{\sigma}{r} \right)^{12} - \left(\frac{\sigma}{r} \right)^{6} \right] = \frac{A}{r^{12}} - \frac{B}{r^{6}} \qquad \text{(Eq.2.6.1)}$$

where the ε is the depth of the potential well, and σ is the finite distance at which the interparticle potential is zero. The r^{-12} term corresponds to Pauli repulsion at short ranges, which occurs when the electron orbitals of two particles overlap. The r^{-6} term describes attraction forces (Van der Waals or dispersion force) at long ranges.

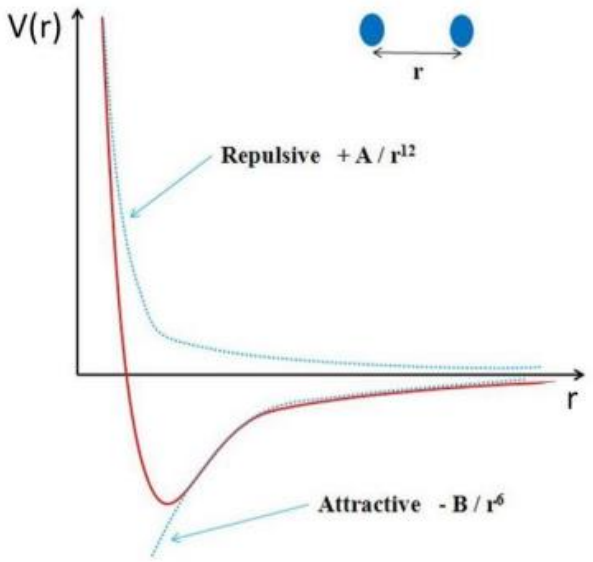

Figure II.20: The Lennard-Jones potential between two non-charged atoms. The image is adapted from [36].

The probe is the core element of AFM, consisting of an AFM tip and a force sensor, whose function is to precisely investigate the repulsive and attracting elements of potential. An AFM's force sensor is made of silicon or silicon nitride cantilever with optical detection. While the AFM tip tracks the material, changing attracting or repulsive forces change the deflection of torsion of the cantilever on which the AFM tip is climbing. A laser's output is focused on the backside of the cantilever and reflected in a quad-photodetector.

a) b)

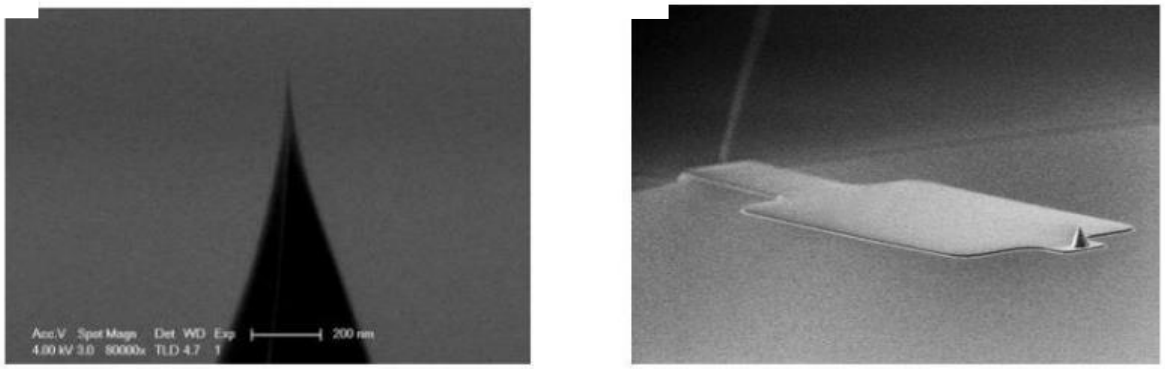

Figure II.21: The Bruker high-resolution AFM tip (SA-HPI-SS) made of silicon-nitride material: a) tip schematic and b) cantilever schematic representation. The images were adapted from [37].

When the cantilever interacts with the surface (bends or deflects due to attractive or repulsive forces), consequently the position of the laser beam on the detector changes. A quad-photodetector records the fluctuation of the laser's direction. A quad-photodetector is made up of four parts, each of which produces a voltage signal when the laser point is reflected. The voltage created by each segment is proportional to the quantity of laser light on that segment, and the total of the voltages generated by all four segments is known as a total signal. Vertical Deflection Signal is the difference between two top segments and two bottom segments, and Lateral Deflection Signal is the difference between two left signals and two right signals, which offers a measure of cantilever torsion. The three-dimensional image is thus captured in this manner.

The AFM technique is supported by a feedback loop, which is a mechanism that allows for consistent interaction between the tip and the surface of the sample, in the sense of maintaining the vertical deflection or amplitude constant, depending on the AFM mode utilized. The system's input is either Deflection Setpoint or Amplitude Setpoint. In its most basic form, an error is defined as the difference between the deflection setpoint and the actual defection that reflects the system's output. This error is contributed as gain (or signal) to control the Z drive of the scanner that will return cantilever motion (deflection or amplitude) constant as the tip traces the surface. The AFM mainly operates in three primary modes which are Contact Mode AFM, Non-contact mode AFM, Tapping Mode, and PeakForce mode. The PeakForce mode will be used in Chapter VI.

II.7.3 AFM-based infrared spectroscopy:

AFM-IR (atomic force microscopy-based infrared spectroscopy) is a hybrid technology that combines the spatial resolution of AFM with the chemical analysis capacity of infrared (IR) spectroscopy. It is commonly used for topographic imaging of various samples in materials and life science research, as well as a variety of industrial applications. Infrared spectroscopy measures infrared absorption spectra [i.e., the quantity of infrared light absorbed by a sample as a function of the frequency (or equivalently wavelength) of the IR light] to perform chemical characterization. The pattern of absorption peaks in the IR spectra acts as a fingerprint, allowing chemical species to be characterized and/or identified. This technique has also been extremely successful in providing imaging based on chemical contrast as well as the ability to chemically analyze microscopic regions of a sample [38,39,40,41].

Atomic force microscopy, on the other hand, can attain spatial resolution on the nanoscale regularly. The spatial resolution of AFM is exclusively limited by the radius of the apex of the AFM probe tip and

interaction depending on tip-sample interaction. AFM commercially available tips frequently reach a spatial resolution on length scales less than 20nm, sometimes down to the molecular and atomic scale. This is accomplished by utilizing the tip of an atomic force microscope to measure the local thermal expansion of a material caused by IR radiation absorption. As a result, the AFM tip serves as the IR detector. Because the AFM tip can detect thermal expansion with spatial resolution approaching the AFM tip radius, the AFM-IR technology can overcome the spatial resolution limitations of conventional IR microspectroscopy [42].

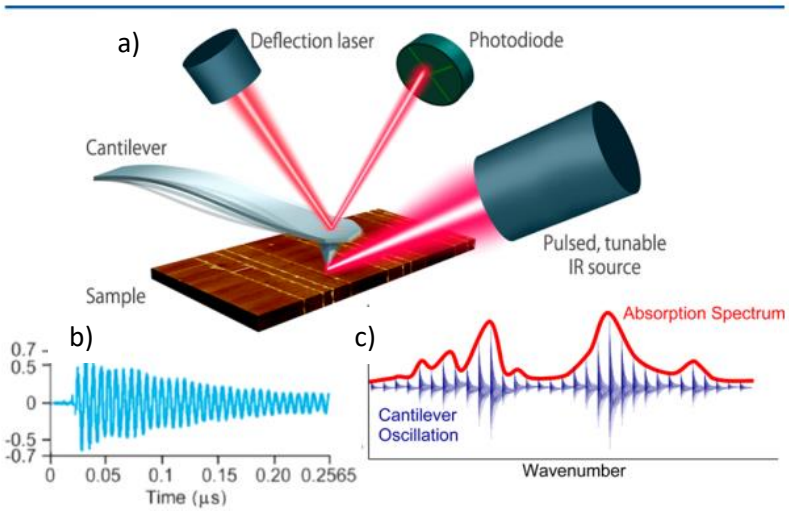

Figure II.22: a) Schematic diagram of AFM-IR. A pulsed tunable laser source is focused on a sample near the tip of an atomic force microscope. When the laser is tuned to an absorbing band of the sample, the absorbed light results in the photothermal expansion of absorbing regions of the sample. The AFM tip is used as a local detector of IR absorption. b) The sample's photothermal expansion induces a transient cantilever oscillation that is proportional to the IR absorption. c) Measuring the AFM cantilever oscillation amplitude as a function of wavelength (or wavenumber) results in a local absorption spectrum with nanoscale spatial resolution [42].

As shown in Figure II.22, AFM-IR is made up of a tunable infrared laser that is focused on a portion of a material near an atomic force microscope probe tip. The AFM tip may detect absorbed radiation if the tunable IR laser is tuned to a wavelength that matches an absorbing wavelength of the material. The most frequent method for detecting IR absorption is to take a direct measurement of the thermal expansion caused by optical absorption. The IR absorption generates a force impulse at the tip of the cantilever, causing the AFM cantilever probe to oscillate. As an alternative to monitoring the cantilever motion, the sample temperature rise owing to absorbed IR radiation can be measured. It is feasible to easily produce IR absorption spectra of nanoscale portions of a substance by measuring the AFM probe response to IR absorption as a function of wavelength. Furthermore, the laser may be tuned to a set wavelength, and the absorption measured as a function of position across the sample to produce chemical images that illustrate the distribution of chemical species throughout a sample [42].

AFM-IR detects light absorbed by the sample. The absorbed light causes a temperature increase, which may be monitored directly with a temperature measuring probe or, more typically, by a transient force created on the tip of an AFM in contact with the absorbing area of the sample surface. When light is absorbed by the sample, the consequent temperature increase produces practically immediate thermal expansion of the sample. This thermal expansion occurs until the light pulse ends, at which

point the sample temperature exponentially decays back toward the ambient temperature at a rate determined by the thermal characteristics of the sample. This thermal expansion acts as a force impulse on the cantilever, causing it to oscillate. The cantilever is forced into oscillation over many oscillatory modes (eigenmodes) due to the characteristic short duration of the force input. When used in contact mode AFM, the cantilever's eigenmodes correspond to contact resonances, the frequency of which can offer further information on the mechanical stiffness of the material.[43-50] In most circumstances, the cantilever's oscillation amplitude is directly proportional to the amount of light absorbed, which in turn is proportional to the absorption coefficient [51,52]. Although the AFM-IR signal strength does depend on other material properties of the sample (e.g., sample thermal expansion coefficient, heat capacity, density, and modulus), these properties remain constant at a specific point on the sample.

AFM-IR measurements are commonly accomplished by measuring the cantilever oscillation amplitude as a function of wavelength (for spectroscopy) or sample location (for chemical imaging). The peak-to-peak oscillation amplitude of the cantilever or the oscillation amplitude at any specific oscillation mode (eigenmode) of the cantilever is measured. Higher-order modes are used in some circumstances to increase the signal-to-noise ratio and/or the rejection of nonlocal background forces caused by the heating of the air surrounding the cantilever. Chapter IV will utilize AFM-IR experiments in cooperation with the University of Paris Saclay with Professor Alexandre Dazzi.

References:

[1] Binnig, G., Rohrer, H., Gerber, C., & Weibel, E. Surface Studies by Scanning Tunneling Microscopy. Physical Review Letters, 49(1), 57–61, (1982).

[2] Binnig, G., Rohrer, H. Scanning Tunneling Microscopy. IBM J. Res. Dev. 30 (4), 355–369, (1986).

[3] Binnig, G.; Rohrer, H. Scanning Tunneling Microscopy—from Birth to Adolescence (Nobel Lecture). Angew. Chemie Int. Ed. English, 26 (7), 606–614, (1987).

[4] Binnig, G.; Rohrer, H.; Gerber, C. 7x7 reconstruction on Si(111) Resolved in Real Space. Phys. Rev. Lett. 50 (2), 120-123, (1983).

[5] G. Binnig, C. F. Quate and Ch. Gerber, "Atomic Force Microscope", Phys. Rev. Lett., vol. 56, p. 930, (1986).

[6]"The Scanning Tunneling Microscope [IAP/TU Wien]". http://www.iap.tuwien.ac.at/www/surface/stm_gallery/stm_schematic (2020).

[7] G. Zhan, "Supramolecular networks and on surface polymerization studied by scanning tunneling microscopy", Theses, University Bourgogne Franche-Comté, (2017)

[8] Bardeen, J. Tunnelling from a Many-Particle Point of View. Physical Review Letters, 6(2), 57–59. (1961).

[9] Tersoff, J.; Hamann, D. R. Theory of the Scanning Tunneling Microscope. Phys. Rev. B, 31 (2), 805–813, (1985).

[10] Hansma, P. K.; Tersoff, J. Scanning Tunneling Microscopy. J. Appl. Phys, 61 (2), (1987).

[11] Chen, C. J., & Smith, W. F. Introduction to Scanning Tunneling Microscopy. American Journal of Physics, 62(6), 573–574. (1994).

[12] "Chemical Analysis, Life Sciences, and Diagnostics | Agilent" https://www.agilent.com. (2020).

[13] S. Kerfriden, A. Nahle, S. Campbell, F. Walsh and J. Smith, "The electrochemical etching of tungsten STM tips", Electrochim. Acta, vol. 43, p. 1939, (1998).

[14] Ibe, J. P., Bey, P. P., Brandow, S. L., Brizzolara, R. A., Burnham, N. A., DiLella, D. P., … Colton, R. J. On the electrochemical etching of tips for scanning tunneling microscopy. Journal of Vacuum Science & Technology A: Vacuum, Surfaces, and Films, 8(4), 3570–3575. (1990).

[15] Barth, J. V., Brune, H., Ertl, G., & Behm, R. J. Scanning tunneling microscopy observations on the reconstructed Au(111) surface: Atomic structure, long-range superstructure, rotational domains, and surface defects. Physical Review B, 42(15), 9307–9318. (1990).

[16] Hanke, F., & Björk, J. Structure and local reactivity of the Au(111) surface reconstruction. Physical Review B, 87(23). (2013).

[17] S. B. Darling, A. W. Rosenbaum, Y. C. Wang and S. J. Sibener, "Coexistence of the (23 × x 3) Au (111) Reconstruction and a Striped Phase Self-Assembled Monolayer", Langmuir, vol. 20, p.7462, (2002).

[18] Takayanagi, K., Tanishiro, Y., Takahashi, M., & Takahashi, S. Structural analysis of Si(111)-7×7 by UHV-transmission electron diffraction and microscopy. Journal of Vacuum Science & Technology A: Vacuum, Surfaces, and Films, 3(3), 1502–1506. (1985).

[19] Wang, J.; Jin, L.; Zhou, H.; Fu, H.; Song, C.; Meng, S.; Zhang, J. Direct Imaging of Surface States Hidden in the Third Layer of Si (111)-7×7 Surface by Pz-Wave Tip. Appl. Phys. Lett. 113 (3), 1-5, (2018).

[20] Brommer, K.D., B.E. Larson, M. Needels, and J.D. Joannopoulos, Modeling Large Surface Reconstructions on the Connection Machine. Japanese Journal of Applied Physics Part 1-Regular Papers Short Notes & Review Papers. 32(3B): p. 1360-1367, (1993).

[21] Brommer, K.D., M. Needels, B.E. Larson, and J.D. Joannopoulos, Abinitio Theory of the Si(111)-(7x7) Surface Reconstruction - a Challenge for Massively Parallel Computation. Physical Review Letters. 68(9): p. 1355-1358, (1992).

[22] Rogers, D.M., Scanning Tunneling Microscopy Study of Surfaces in Ultra High Vaccum, Ph.D. Thesis, Department of Physics, The University of British Columbia, (1994).

[23] Waltenburg, H.N. and J.T. Yates, Surface-Chemistry of Silicon. Chemical Reviews. 95(5): p. 1589-1673, (1995).

[24] Lander, J. J.; Morrison, J. Surface Reactions of Silicon with Aluminum and with Indium. Surf. Sci., 2, 553–565, (1964).

[25] Makoudi, Y. Etudes par microscopie STM de molécules organiques physisorbées sur semiconducteurs. Theses: University Bourgogne Franche-Comté, (2009).

[26] M. Berthe, R. Stiufiuc, B. Grandidier, D. Deresmes, C. Delerue, and D. Stiévenard, “Probing the Carrier Capture Rate of a Single Quantum Level,” Science, vol. 319, p. 436, (2008).

[27] Novoselov, K, Electric field effect in atomically thin carbon films. Science, 306(5696), 666-669, (2004).

[28] Eder, F., Stosch, R., Kahr, H., & Eng, L. M. Structure of Highly Oriented Pyrolytic Graphite (HOPG) surfaces studied by scanning tunneling microscopy. Surface Science, 500(1-3), 285-298, (2002).

[29] "Kentax UHV Equipment ". https://www.kentax.de/ (2020).

[30] Steinhardt, R. G., & Serfass, E. J. Surface Analysis with X-Ray Photoelectron Spectrometer. Analytical Chemistry, 25(5), 697–700. (1953).

[31] Stevie, F. A., & Donley, C. L. Introduction to x-ray photoelectron spectroscopy. Journal of Vacuum Science & Technology A, 38(6), 063204. (2020).

[32] J. F. Watts and J. Wolstenholme, An Introduction to Surface Analysis by XPS and AES (Wiley, Chichester, (2020).

[33] I. W. Drummond, “XPS: Instrumentation and performance,” in Surface Analysis by Auger and X-ray Photoelectron Spectroscopy, edited by D. Briggs and J. T. Grant (Surface Spectra, Chichester, 2003).

[34] Giessibl, F. J. Atomic Resolution of the Silicon (111)-(7x7) Surface by Atomic Force Microscopy. Science, 267(5194), 68–71. (1995).

[35] Barth, J. V., Brune, H., Ertl, G., & Behm, R. J. Scanning tunneling microscopy observations on the reconstructed Au(111) surface: Atomic structure, long-range superstructure, rotational domains, and surface defects. Physical Review B, 42(15), 9307–9318. (1990).

[36] Yu, N., & Polycarpou, A. A. Adhesive contact based on the Lennard–Jones potential: a correction to the value of the equilibrium distance as used in the potential. Journal of Colloid and Interface Science, 278(2), 428–435. (2004).

[37] "SAA-HPI-SS - Bruker AFM Probes ". https://www.brukerafmprobes.com/p-3965-saahpi-ss.aspx (2020).

[38] Dazzi. A., Prazeres, R.; Glotin, F.; Ortega, J. M. Local Infrared Microspectroscopy with Subwavelength Spatial Resolution with an Atomic Force Microscope Tip Used as a Photothermal Sensor. Opt. Lett., 30 (18), 2388−2390. (2005).

[39] Dazzi, A., Prazeres, R.; Glotin, F.; Ortega, J. Subwavelength Infrared Spectromicroscopy Using an Afm as a Local Absorption Sensor. Infrared Phys. Technol. 49 (1−2), 113−121. (2006).

[40] Dazzi, A., Kneipp, J., Lasch, P., Eds. Sub-100-Nanometer Infrared Spectroscopy and Imaging Based on a near-Field Photothermal Technique (PTIR). In Biomedical Vibrational Spectroscopy. Wiley: Hoboken, NJ, pp 291−312, (2008).

[41] Dazzi, A., Prater, C. B., Hu, Q., Chase, D. B., Rabolt, J. F., & Marcott, C. AFM–IR: Combining Atomic Force Microscopy and Infrared Spectroscopy for Nanoscale Chemical Characterization. Applied Spectroscopy, 66(12), 1365–1384. (2012).

[42] Dazzi, A., & Prater, C. B. AFM-IR: Technology and Applications in Nanoscale Infrared Spectroscopy and Chemical Imaging. Chemical Reviews, 117(7), 5146–5173. (2016).

[43] Rabe, U.; Arnold, W. Acoustic Microscopy by Atomic Force Microscopy. Appl. Phys. Lett. 64 (12), 1493−1493. (1994).

[44] Rabe, U., Janser, K., & Arnold, W. Vibrations of free and surface-coupled atomic force microscope cantilevers: Theory and experiment. Review of Scientific Instruments, 67(9), 3281–3293. (1996).

[45] Yamanaka, K., Nakano, S. Quantitative Elasticity Evaluation by Contact Resonance in an Atomic Force Microscope. Appl. Phys. A: Mater. Sci. Process. 66 (0), S313−S317, (1998).

[46] Yamanaka, K., Noguchi, A.; Tsuji, T.; Koike, T.; Goto, T. Quantitative Material Characterization by Ultrasonic Afm. Surf. Interface Anal. 27 (5−6), 600−606, (1999).

[47] Rabe, U., Amelio, S., Kester, E., Scherer, V., Hirsekorn, S., & Arnold, W. Quantitative determination of contact stiffness using atomic force acoustic microscopy. Ultrasonics, 38(1-8), 430–437. (2000).

[48] Yamanaka, K.; Maruyama, Y.; Tsuji, T.; Nakamoto, K. Resonance Frequency and Q Factor Mapping by Ultrasonic Atomic Force Microscopy. Appl. Phys. Lett. 78 (13), 1939−1941, (2001).

[49] Rabe, U., Kopycinska, M.; Hirsekorn, S.; Arnold, W. Evaluation of the Contact Resonance Frequencies in Atomic Force Microscopy as a Method for Surface Characterisation (Invited). Ultrasonics, 40 (1−8), 49−54, (2002).

[50] Rabe, U., Bhushan, B., Fuchs, H., Eds. Atomic Force Acoustic Microscopy. In Applied Scanning Probe Methods II. Springer: Berlin, pp 37−90, (2006).

[51] Dazzi A., Glotin, F., Carminati, R. Theory of Infrared Nanospectroscopy by Photothermal Induced Resonance. J. Appl. Phys. 107, 124519, (2010).

[52] Lahiri, B., Holland, G., & Centrone, A. Chemical Imaging Beyond the Diffraction Limit: Experimental Validation of the PTIR Technique. Small, 9(3), 439–445. (2012).

Chapter III: Facile collisional dissociation of N_2 on a Si(111)-7x7 surface at room temperature and the influence of atomic hydrogen over the N-adsorbed Si(111)-7x7 surface:

Nitrogen (N_2) is a common diatomic chemical that accounts for 78% of the Earth's atmosphere. As a result, it is highly advantageous to use this typically inert molecule in the synthesis of value-added products or to deploy it as a chemical energy reservoir.[1] Among the most often manufactured chemical compounds, consumption of ammonia NH_3 continues to rise year after year, with a current global yearly output of over 144 million tons. Ammonia has mostly been employed as a fertilizer in the agricultural sector during the last 100 years since it enhances the efficiency of food production and sustains a fast-rising population. It is also used as a refrigerant, detergent, insecticide, and in a variety of other chemical raw materials.[2] Most governments now aim to reduce global CO_2 emissions by replacing fossil fuels with green renewable energy sources such as solar, wind, and tidal energy.[3] To overcome the fluctuation effect in their creation, these sources must be caught and held inside batteries or in a chemical form. When compared to batteries, the employment of chemical forms for storage appears to be more cost-effective and favorable in terms of transportation convenience.[4] As a solution to this challenge, among all conceivable chemical compounds that might act as a hydrogen carrier, ammonia has proven to have a very high hydrogen density that can be sustained over time (3 hydrogen atoms for each nitrogen atom). The well-known Haber-Bosch method, which was established almost 100 years ago by F. Haber and C. Bosch, is used in the industrial activation and transformation of N_2 to ammonia. To convert N_2 and H_2 into NH_3, this process requires high pressure (300 atm) and high temperature (800 K) in the presence of an iron-based catalyzer. As a result, this reaction uses around 2% of the world's energy supply and contributes 1.44% of global CO_2 emissions. [5] Thus, the dissociation of N_2 from its triple N≡N bond, which is the strongest link in diatomic molecules, is the limiting step of this process. Even when metal-based complex catalyzers[6] are used to decrease the dissociation barrier, the process remains extremely energy-demanding. It is often referred to as the most important invention of the 20th century.[1]

Consequently, novel approaches to efficient ammonia synthesis at ambient pressure are being eagerly researched to reduce ammonia production costs and enable more compact manufacturing facilities. The reaction between hydrogen and adsorbed nitrogen on the surfaces has been investigated because of great interest in the synthesis of ammonia. The synthesis of ammonia (NH_3) from its elements (N_2 and H_2) is often considered one of the most important discoveries in the history of the science of catalysis. Typical examples of hydrogen and adsorbed nitrogen are the reactions on Cu(001) [7], Fe (001) [8], Ru(0001) [9], Pt(111) [10], and Rh(111) [11]. In these studies, the ammonia synthesis process on the surfaces can be divided into two. First is the dissociation of H_2 molecules, or generation of atomic hydrogens, and second is their reaction with the adsorbed N atoms. The latter is crucial to understanding the chemical reaction process through the synthesis of ammonia. Although the dissociation of H_2 molecules on the surfaces has been reported on various metal surfaces [12–17], there have been a few studies focusing on the reaction between atomic hydrogen and the N atoms [18]. Takehiro, et al. reported the reaction of atomic hydrogen on a Ni(110)-p(2 x 3)-N surface by high resolution electron energy loss spectroscopy (HREELS). The NH species and ammonia were produced by the reaction of the N atoms with atomic hydrogen at room temperature (RT).

On-surface synthesis on chemically reactive surfaces could be pursued by Scanning Tunneling Microscopy high-resolution images under UHV conditions to preserve cleanliness and emphasize accurate assessment of the reaction process to completely understand N_2 activation. In that context,

STM high-resolution images could track surface state modification with a combination of X-ray photoelectron spectra to identify molecular modifications at the surface level. The current state of the art recognizes numerous studies of the dissociation of N_2 is usually carried out at a high temperature and high pressure because N_2 molecules weakly interact with most surfaces below room temperature (RT), and remain physisorbed (i.e. non-dissociated). The development of new strategies to dissociate the N_2 molecule under mild conditions is of primary interest. Molecule-surface collisions represent an interesting alternative because these collisional processes induce electron-transfer reactions that promote the dissociation of reactants at low pressure and low temperature.[19] The conversion of kinetic energy into vibrational excitation following the collision of molecules with a surface was mainly investigated for hydrocarbon-based species[19a-b], even if a few examples of the dissociation of N_2 using a supersonic molecular beam to overcome the dissociation barrier via a hyperthermal collision were also investigated on metal surfaces.[19e-f] These vibrational excitations can lead to dissociative states of the incident molecules, resulting in dissociated fragments adsorption. In the case of electron transfer induced by molecular collision, a recent study showed that the C=O bond in CO_2 molecules can be cleaved by a nonuniform charge transfer from the substrate to the CO_2 molecule due to the conversion of the kinetic energy of incident CO_2 molecule into molecular deformation.[19i]

Moreover, surface selection is critical when seeking simple and direct dissociative adsorption of impinging gas particles, since inherently high surface reactivity necessitates less translational kinetic energy from the colliding gas sitting in the thermal range of energy distribution (Boltzmann-Maxwell). The Si(111)-7x7 surface might be a potentially highly reactive surface[20], especially because a catalytic feature was discovered in a recent work where NO toxic gas was changed via an on-surface heterogeneous process to N_2O gas that desorbs from the surface.[21] However, the dissociation of ammonia is widely investigated on Si(111)-7x7 surface, under UHV, in the function of surface temperature where the aim was to achieve the formation of silicon nitride after outgassing hydrogen atoms.[22-25]

Furthermore, hydrogen-treated silicon surfaces have been studied by various surface analysis techniques including electron-energy loss spectroscopy,[26] temperature programmed desorption, low-energy electron diffraction LEED [27,] and scanning tunneling microscopy STM. [28,29] Of these techniques STM is uniquely capable of resolving individual surface atoms. The chemisorption of hydrogen on various silicon surfaces has been investigated for many years from the beginning of semiconductor research and technology. Becker and Gobeli showed that the Si surface interacts only with atomic hydrogen and not with molecular hydrogen.[30] Ibach and Rowe applied ultraviolet photoemission spectroscopy (UPS) for the spectroscopic study of atomic hydrogen chemisorption on the Si(111)-7x7 surface.[31] Following the first self-consistent theoretical study by Appelbaum and Hamann on the Si (111)-H system, [32] Sakurai and Hagstrum successfully carried out a thorough INS (ion neutralization spectroscopy) and UPS investigation on the Si (111) 7 X 7-H system. [33] In good agreement with the theory, they showed that atomic hydrogen reacts with the surface Si atoms with a dangling bond to form a covalent Si-H bond on the surface and to stabilize the surface (monohydride phase). Subsequently, numerous investigations have been carried out both theoretically and experimentally to confirm the formation of the stable monohydride phase. [34,35]

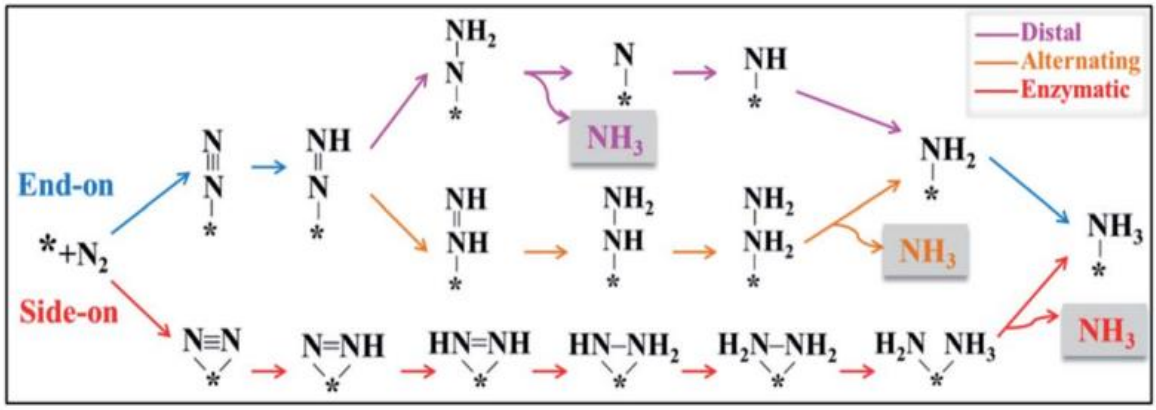

Figure III.1: A schematic depiction of three mechanisms for N_2 reduction to NH_3 on the SiC(111) surface. * denotes the SiC(111) surface.

The N_xH_x species and ammonia formed at room temperature (RT) by the interaction of the N-adsorbed Cu(001) surface with atomic hydrogen. At low atomic hydrogen exposure, it interacted with the N atoms and formed the NH species on the surface. The rate of reaction is related to the number of unreacted N atoms. The number of nitrogen species on the surface was reduced by increasing the exposure of atomic hydrogen from this state. This is linked to ammonia production and desorption from the surface. The NH species on the surface are converted to NH_3 by atomic hydrogen via the surface NH_2 species. [36] Mei Zheng evaluated the performance of the C- and Si-terminated SiC(111) surfaces for the conversion of the activated N_2 into NH_3. Exploring a subsequent N_2 reduction reaction was devoted by including three different mechanisms distal, alternating, and enzymatic as shown in Figure III.1 depending on the end-on and side-on fashions. The end-on adsorbed N_2 can be reduced to NH_3 through the distal or alternating pathway. From the distal pathway, the terminal N atom is firstly protonated to form NH_3 and then at the proximal N to release a second NH_3. While in the alternating pathway, the successive proton–electron pairs alternately bond with the two N atoms, and the two NH_3 molecules are formed and desorbed in the last two steps. For the side-on adsorption structure, the N_2 reduction reaction (NRR) process goes through the enzymatic mechanism, in which a hydrogenation reaction alternately occurs at the two N atoms, and the second NH_3 will be produced immediately after the first one is released. The atomic configurations at various stages of each elementary step on the C- and Si-terminated SiC(111) surfaces via the three different mechanisms over both fashions are all shown in Figure III.2.

In this chapter, the first part will be devoted to exploring the capability of the reactive Si(111)-7x7 surface to lower the kinetic barrier for direct dissociative impinging of the N_2 molecular gas, at low pressures and room temperature relying on the thermal distribution of translational kinetic energy of the reactant gas. The dissociation of N_2 was investigated by scanning tunneling microscopy (STM), X-ray photoelectron spectroscopy (XPS), and density functional theory (DFT) calculations. The initial section of this chapter is based on the contributions resulting from the work of two PhD students, together with my work and that of Dr. Elie GEAGEA. The second part will be concerned with the ability of the low-exposure of reactive atomic hydrogen to react with the N-adsorbed Si(111)-7x7 surface forming N-chemical-based species. Benefiting from the N_2 dissociation at low pressure and ambient temperature on a highly reactive Si(111)-7x7 surface, the next step was to expose the surface to atomic hydrogen leading to the formation of N-chemical-based species and ammonia. Scanning tunneling microscopy (STM) under ultra-high vacuum conditions was the only used powerful analytical tool monitoring the influence of atomic hydrogen over the N-adsorbed Si(111)-7x7 surface.

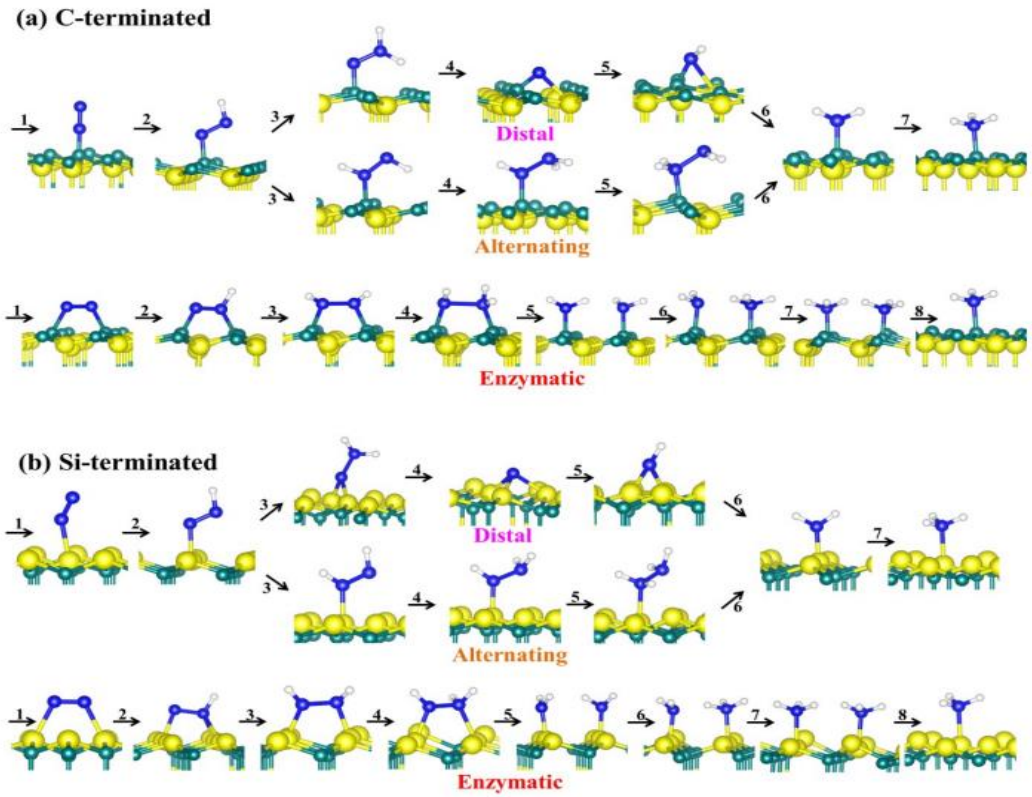

Figure III.2: Optimized structures of various intermediates along the reaction paths of the NRR proceeding on the (a) C- and (b) Si-terminated SiC (111) surfaces through distal, alternating, and enzymatic pathways.

III.1 Used materials and methods:

In this section, we present the preparation method of Si(111)-7x7 reconstructed surface under UHV in the first subsection. The following subsection introduces the employed N2 gas quality and surface exposition method.

III.1.1 Surface preparation:

A Si(111) substrate n-doped with phosphorus (0.001-0.002 Ω.cm) mounted on a molybdenum sample holder is used for the preparation of Si(111)-7x7 surface. Under UHV, the sample was degassed wisely until 800 °C by direct current heating, to eliminate the native oxide layer and any other contaminants that can be present on the surface, while the pressure is maintained below $8x10^{-10}$ mbar in the chamber. Then, the sample was flashed several times at 1200 °C until maintaining this temperature for 15 seconds without exceeding 10^{-10} mbar pressure range was feasible. After each flash cycle, we let the time for pressure normalize before we proceed to the next flash. Following the last flash, the temperature was dropped instantly to around 950 °C, then decreased gradually by adapting a rate of 10 °C/min until 750 °C. Below 750 °C, we cut the current rapidly and let the sample cool down for 30 minutes before putting it on the STM head to control the state of the surface as well as its cleanliness, as shown in the large-scale STM image of Figure III.3.

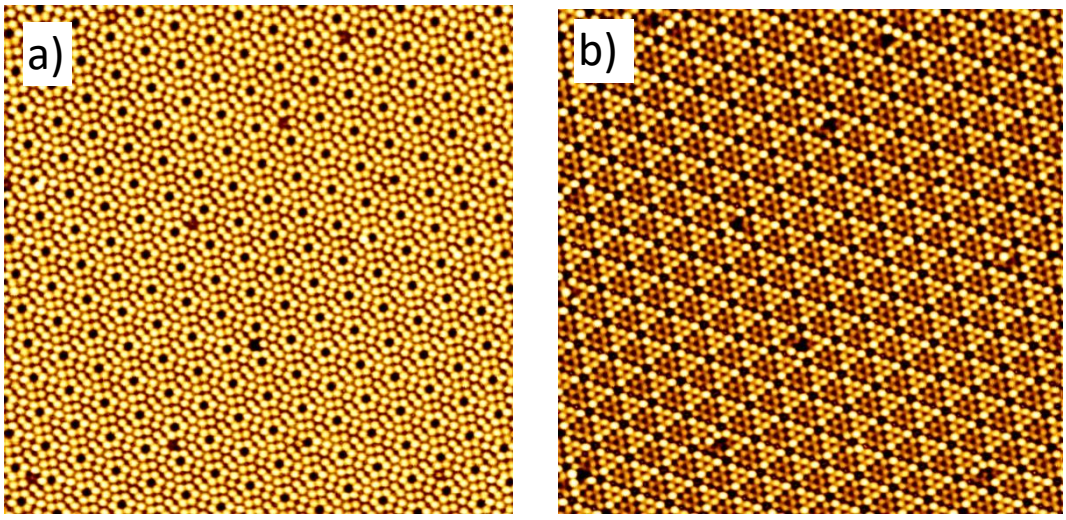

Figure III.3: High-resolution STM images of the reconstructed Si(111)-7x7 surface acquired at room temperature directly after preparation showing both empty and filled states of the surface by scanning both polarities. a) Empty states ES (40x40 nm^2, V_s = 1.5 V; I_t = 40 pA); b) Filled states FS (40x40 nm^2, V_s = -1.5 V; I_t = 40 pA).

III.1.2 N_2 and H_2 gas purity and injection method:

Scientific grade molecular N_2 and H_2gas of purity 99.9999%, purchased from Linde Gas, were used in this work. All details about the gas-contained impurities are presented in the datasheet of Figure III.4 and Figure III.5 In addition, the gas line that drives the gas from the compressed bottle to the chamber was pumped and baked until the achievement of UHV conditions similar to the one in the preparation chamber with a measured base pressure equal to $7.2x10^{-11}$ mbar after opening the leak valve responsible for N_2 injection. After scanning and approving the surface cleanness, the Si(111)-7x7 sample was placed on the manipulator and held at RT in front of the capillary of N_2 gas injecting. The distance between the sample surface and the extremity of the capillary is about 15 cm. Gas flow is controlled by using a high-precision leak valve and by following the pressure measured inside the preparation chamber using a filament gauge. This sample exposure to the gas is known as the “bulb method” where the flux of molecules is characterized by a thermal distribution of the kinetic energies following the law of Maxwell-Boltzmann distribution.

AZOTE SCIENTIFIQUE 6.0

Généralités — **Nom du gaz :** Azote Scientifique 6.0

Utilisations — Utilisé pour : surveillance de la qualité de l'air, chimie analytique, mélanges de gaz d'étalonnage, électronique et semi-conducteur, contrôle des émissions, surveillance de l'environnement, détection par Ionisation de Flamme (DIF), photométrie de flamme, Chromatographie en Phase Gazeuse (CPG), Chromatographie Liquide Haute Performance (HPLC), inertage, instruments de mesure de laboratoire, test des émissions, réglage du zéro pour les analyseurs.

Principales indications — N/A

Composition du produit — **Formule chimique :** N_2
Pureté, % volumique : ≥ 99,9999

Propriétés physico-chimiques — **Masse molaire** : 28,01 g/mol
Densité de gaz relative à l'air (1013 hPa/15°C) : 0.967

Point triple : Température : 63,2 K (-210,0 °C)
Pression : 125,3 mbar
Chaleur latente de fusion : 25,8 kJ/kg

Point d'ébullition : Température : 77,4 K (-195,8°C)
(1013 hPa) Chaleur latente de vaporisation : 198,7 kJ/kg
Masse volumique : 4,614 kg/m³ (phase gazeuse)

Point critique : Température : 126,2 K (-147,0°C)
Pression : 34,0 bar
Masse volumique : 314,0 kg/m³

Spécifications garanties — **Impuretés :**
$H_2O \leq 0,5$ ppm$_v$
$O_2 \leq 0,5$ ppm$_v$
$CO \leq 0,1$ ppm$_v$
$C_nH_m \leq 0,1$ ppm$_v$
$H_2 \leq 0,5$ ppm$_v$
$CO_2 \leq 0,1$ ppm$_v$

Figure III.4: Datasheet certifying the quality of the used N_2 gas and listing chemical and physical properties as well as all impurities quantities contained inside the gas.

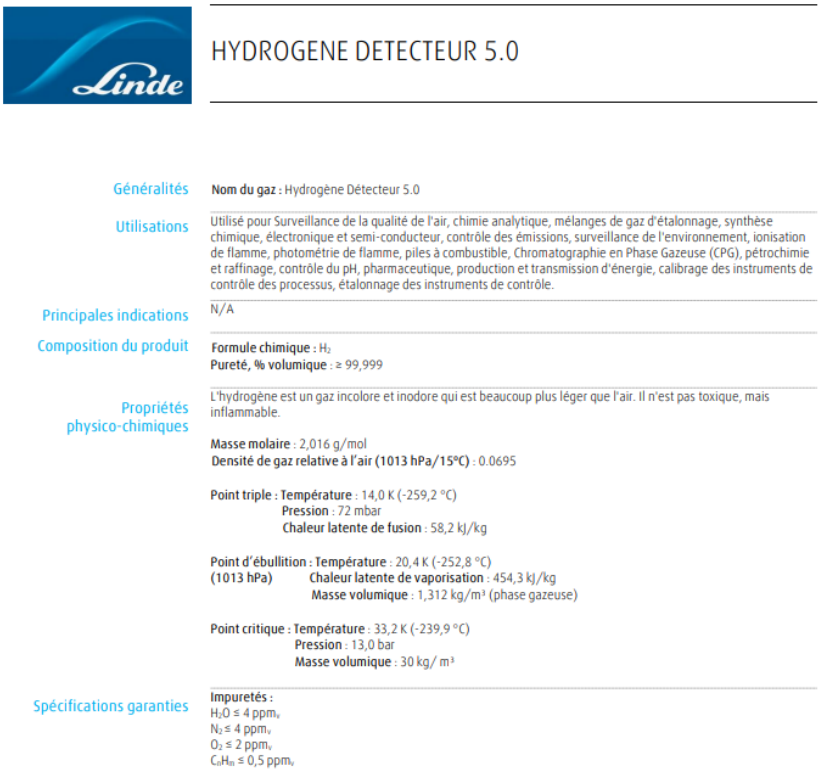

HYDROGENE DETECTEUR 5.0

Généralités — **Nom du gaz :** Hydrogène Détecteur 5.0

Utilisations — Utilisé pour Surveillance de la qualité de l'air, chimie analytique, mélanges de gaz d'étalonnage, synthèse chimique, électronique et semi-conducteur, contrôle des émissions, surveillance de l'environnement, ionisation de flamme, photométrie de flamme, piles à combustible, Chromatographie en Phase Gazeuse (CPG), pétrochimie et raffinage, contrôle du pH, pharmaceutique, production et transmission d'énergie, calibrage des instruments de contrôle des processus, étalonnage des instruments de contrôle.

Principales indications — N/A

Composition du produit — **Formule chimique :** H_2
Pureté, % volumique : ≥ 99,999

Propriétés physico-chimiques — L'hydrogène est un gaz incolore et inodore qui est beaucoup plus léger que l'air. Il n'est pas toxique, mais inflammable.

Masse molaire : 2,016 g/mol
Densité de gaz relative à l'air (1013 hPa/15°C) : 0.0695

Point triple : Température : 14,0 K (-259,2 °C)
Pression : 72 mbar
Chaleur latente de fusion : 58,2 kJ/kg

Point d'ébullition : Température : 20,4 K (-252,8 °C)
(1013 hPa) Chaleur latente de vaporisation : 454,3 kJ/kg
Masse volumique : 1,312 kg/m³ (phase gazeuse)

Point critique : Température : 33,2 K (-239,9 °C)
Pression : 13,0 bar
Masse volumique : 30 kg/ m³

Spécifications garanties — **Impuretés :**
$H_2O \leq 4$ ppm$_v$
$N_2 \leq 4$ ppm$_v$
$O_2 \leq 2$ ppm$_v$
$C_nH_m \leq 0,5$ ppm$_v$

Figure III.5: Datasheet certifying the quality of the used H_2 gas and listing chemical and physical properties as well as all impurities quantities contained inside the gas.

In the second section of our experiments, we did the deposition of atomic hydrogen over the N-adsorbed Si(111)-7x7 surface, so the H_2 molecular line gas was attached to Atomic Hydrogen source EFM H/ EFM Hs presented in Figure III.6. The EFM-H is an ideal instrument for surface passivation,

improvement of thin film growth, and other similar applications using atomic hydrogen. The EFM-H features a cracking efficiency close to 100%, a smooth, flat, and sharply defined spot profile, a low background pressure, and a surprisingly low power consumption demonstrating the outstanding performance of the EFM-H. The molecular hydrogen is let into the hydrogen source at the flange with a high-precision leak valve and enters the vacuum chamber through a heated tungsten capillary. This capillary is heated by means of electron bombardment up to 2600K. At this temperature, negligible molecules remain undissociated. The intensity of the beam thus depends mainly on the mass flow of hydrogen molecules. The angular distribution of the atomic hydrogen beam depends on the temperature of the tungsten capillary. A lower pressure inside the capillary gives a sharper angular distribution due to the fact that ballistic atoms can reach the sample from areas deep inside the capillary, whereas a higher pressure gives a virtual source point nearer to the exit of the capillary and broader distribution.

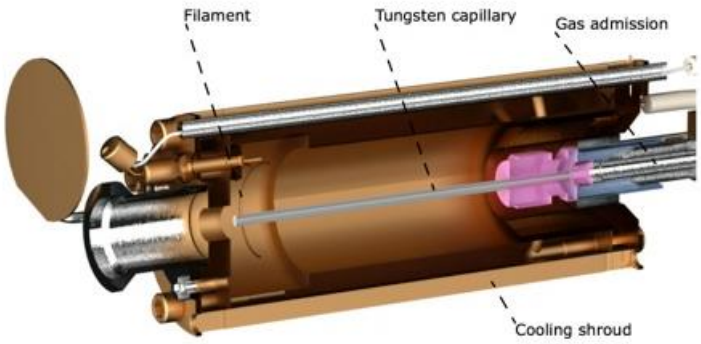

Figure III.6: Schematic cross-section of EFM-H with its different parts designed as a source to provide atomic hydrogen.

III.2 Experimental results STM:

The first portions of this section are dedicated to reporting the experimental work done in terms of N_2 gas deposition at various pressures and exposure times. After each step, the condition of the Si(111)-7x7 is evaluated by STM under UHV at RT (sample preparation, deposition). To eliminate any damage to the ionic pump during gas injection, the chamber was pumped using a turbomolecular pump, since we achieved N_2 gas pressures on the order of 10^{-5} mbar in our trials. To confirm that no contamination arises from this transition in the pumping system, a clean sample of Si(111)-7x7 was kept for four hours (longer than any exposure to N2) with no surface change detected. As a result, the kinetics of the reaction were determined using a quantitative statistical inquiry based on STM images.

Then, in another portion, we introduce the result of X-ray Photoelectron Spectroscopy (XPS) executed to identify the species persisting on the surface after deposition. Finally, the last portion presents a theoretical study based on DFT calculations to support and reinforce experimental results.

III.2.1 N_2 injection into the UHV chamber monitored by STM:

After constructing the Si(111)-7x7 sample and inspecting its surface cleanliness, a series of tests was performed that included exposing the sample to N_2 molecular gas at various pressures while keeping the deposition period constant at 30 minutes. Because we are operating under UHV conditions with a base pressure of 7.2×10^{-11} mbar, we begin our N_2 injection trails at 10^{-9} mbar and gradually increase the pressure by one magnitude each trial until we reach 10^{-5} mbar. STM pictures of the Si(111)-7x7 surface showed no changes at pressures less than 10^{-6} mbar. Interestingly, after 30 minutes of

exposure to N_2 gas at 10^{-5} mbar, a large alteration of the surface was generated, as shown by the STM picture in Figure III.7c.d.

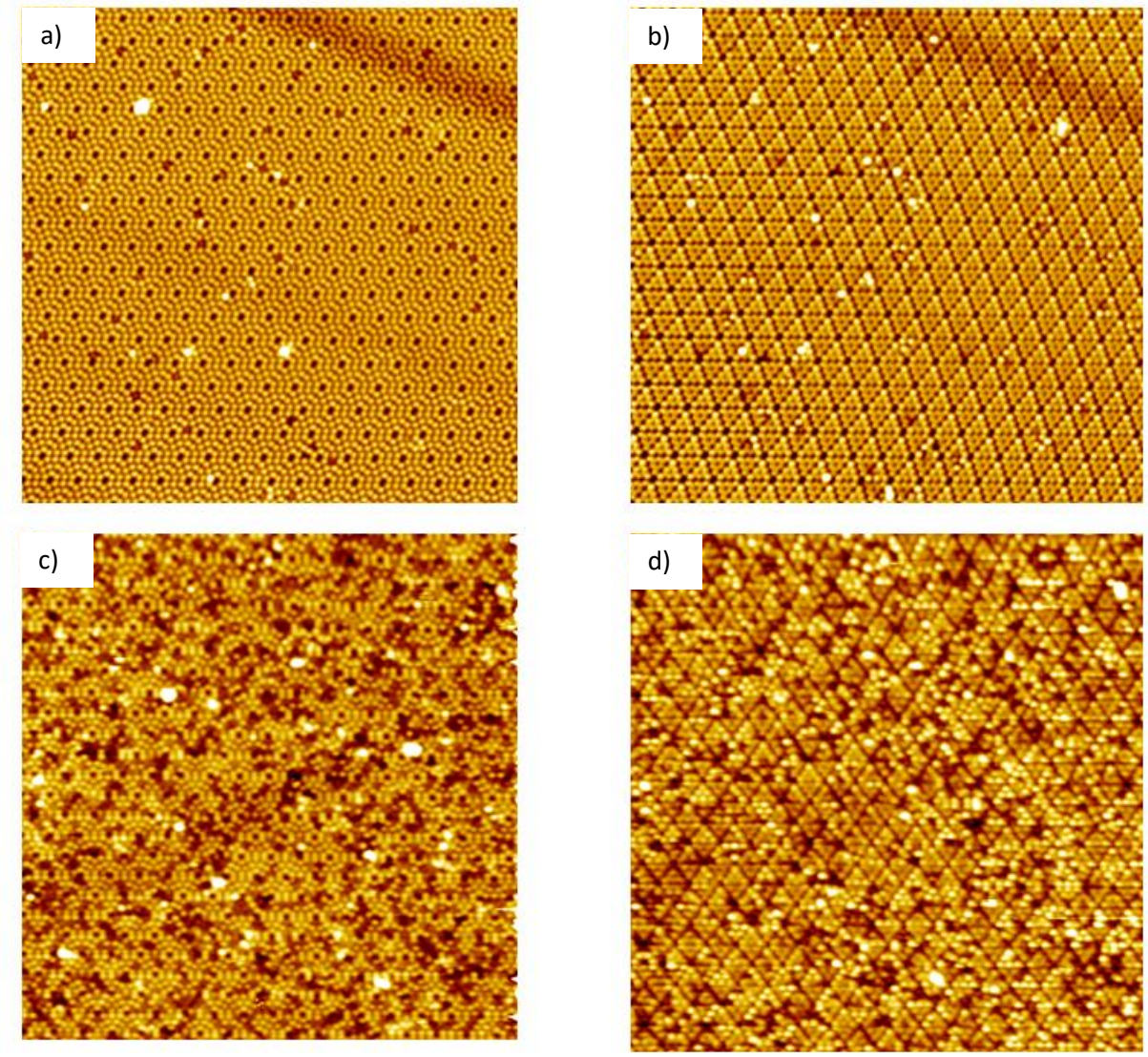

Figure III.7: STM images of the clean Si(111)-7x7 surface before and after exposition to N_2 gas during 30 min at 10^{-5} mbar. a,b) two STM images of the same zone (50 nm x 50 nm) of clean surface: a) Empty state ES (V_s = 2.0 V, I_t = 200 pA) and b) Filled state FS (V_s = -1.5 V, I_t = 200 pA). c,d) two STM images (50 nm x 50 nm) of Si(111)-7x7 surface after exposition: c) ES (V_s = 1.5 V, I_t = 200 pA) and d) FS (V_s = -1.5 V, I_t = 200 pA).

The two STM images of Figure III.7a, b shows the same zone of the clean Si(111)-7x7 surface before deposition where the first image (Figure III.7a) corresponds to the empty states ES and the second image (Figure III.7b) represents the filled states FS. Moreover, the STM images of (Figure III.7c, d) represent a zone of the Si(111)- 7x7 surface after exposition to N_2 gas at 10^{-5} mbar during 30 min, where we can see a clear alteration of the surface in comparison to its initial state. An inspection of the Si(111)-7x7 surface based on highly resolved STM images of a zoomed area (15 nm x 15 nm) captured at both bias voltage polarities allows a comparison of the appearance of surface adatoms (ES) and rest atoms (FS). We pick up a unit cell on the surface composed of one faulted half-cell FC highlighted by a yellow triangle and one un-faulted half-cell UFC highlighted by a black triangle. Unit cell issued from ES STM image (Figure III.8a) allows counting of surface adatoms, wherein the FC denotes the extinction of three adatoms and only one adatom in the UFC. Moreover, the corresponding unit cell on the FS image (Figure III.8b) allows investigation over rest atoms and

adatoms. We noticed the extinction of the same number of adatoms at the same positions in the two half-cells. Furthermore, one additional rest atom seems to be extinct due to the absence of bright protrusion in the UFC, as illustrated in the schemes of (Figure III.8c).

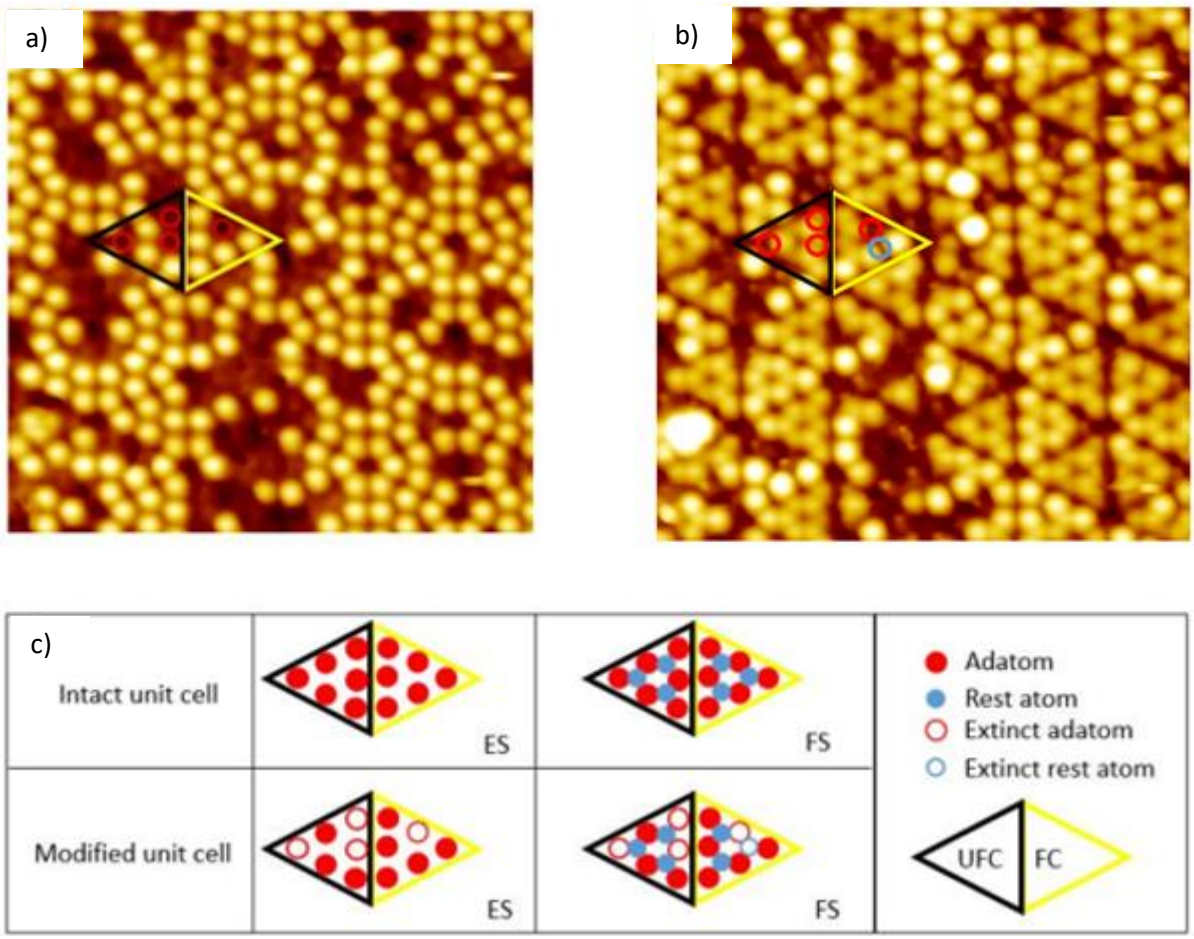

Figure III.8: a,b) Two zoomed STM images (15 nm x 15 nm) of Si(111)-7x7 surface after exposition to 10^{-5} mbar of N2 gas during 30 min: a) ES (V_s = 1.5 V, I_t = 200 pA) where a chosen unit cell reveals the extinction of 3 adatoms in the un-faulted cell UFC (black triangle) and one adatom in the faulted cell FC. b) FS (V_s = -1.5 V, I_t = 200 pA) where the same unit cell in which one rest atom inside the FC is extinct in addition to the adatoms determined based on the ES image. c) Schematic representation of the observed extinct atoms and adatoms observed in the chosen unit cell.

This observation indicates a probable surface alteration occurring on adatoms as well as rest atoms. Here, we might assume a multiplicity of alternatives in terms of affected cell configurations, for which statistical study is feasible but unreliable when it comes to comprehending what happens on the surface. As a result of this unexpected change in N2's capacity to affect the surface by raising pressure, we decided to conduct a more detailed examination of the pressure impact inside the transition period [10^{-6}; 10^{-5}] mbar. Furthermore, by varying deposition duration and pressure, the kinetics of the observed change may be studied.

After subjecting the surface to 30 minutes of exposure to N_2 gas at a total pressure of 10^{-5} mbar, it was annealed at 800K for the same duration. Subsequent scanning tunneling microscopy (STM) analysis conducted at room temperature showed no discernible variation in the surface characteristics, even upon scanning at both polarities. Furthermore, the percentage of extinct silicon atoms remained 35.8% the same as before annealing as depicted in Figure III.9.

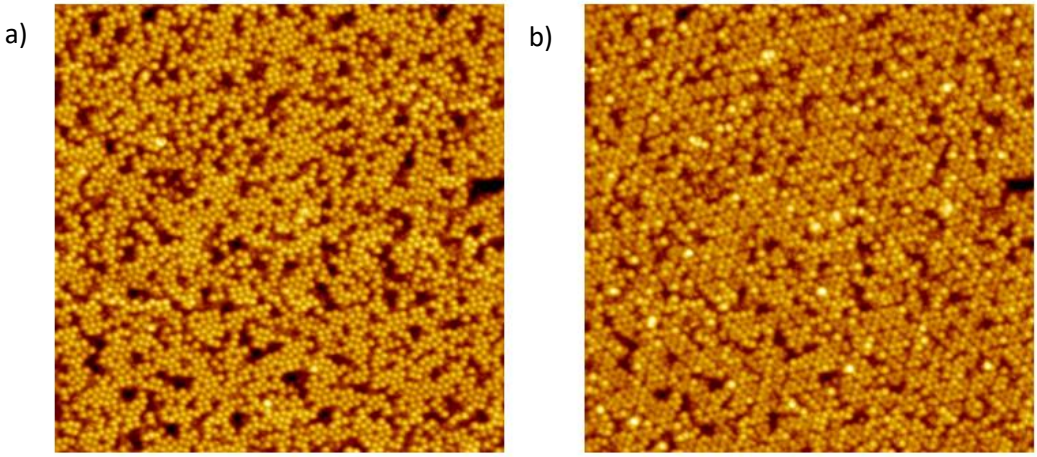

Figure III.9: STM images of the Si(111)-7x7 surface after an exposition to N_2 molecule at a pressure of $5 \cdot 10^{-5}$ mbar at 300 K during 30 minutes, followed by a thermal annealing of 800K for 30 min. a) 50x50 nm^2, I_t = 200 pA and V_s = + 1.5 V (empty states). b) a) 50x50 nm^2, I_t = 200 pA and V_s = - 1.5 V (filled states).

III.2.2 Statistical investigation of adatoms extinction:

The statistical study based on STM images, where the number of extinct atoms was counted using the particle detection module of SPIP software (Figure III.10), is limited to the surface adatoms, thus only ES images acquired at positive voltages are employed. This limitation was imposed by the fact that the study necessitates a large number of experiments, each of which must record several images for different zones on the surface, despite the fact that having a tip capable of extracting high resolution ensures the sensing of rest atoms is not always apparent, especially given that we work at RT. Every experiment we conducted for this purpose consisted of registering three images of distinct zones of the surface after preparation, followed by three images of different zones following exposure to N_2, with dimensions set to 50 nm x 50 nm. As a result, for each experiment, the proportion of defects before a deposition can be measured and then deduced from the percentage of extinct adatoms after deposition to ensure the highest accuracy and increase coherence between the two experiments.

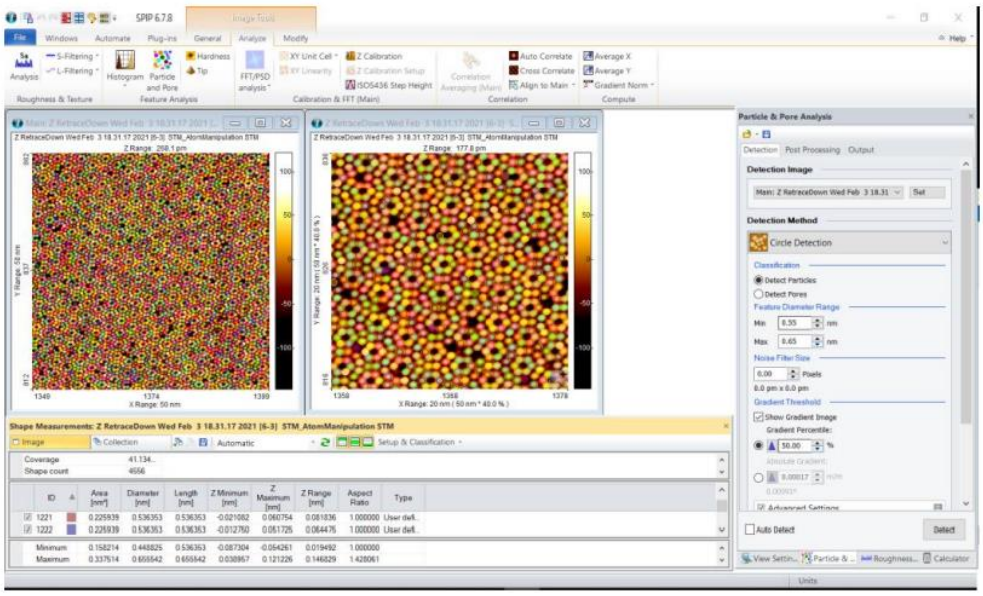

Figure III.10: SPIP 'particle and pore analysis' module showing the used parameters for detecting and counting surface adatoms.

III.2.2.1: Statistical investigation at fixed exposition time and variable pressures

In the first trial, N_2 gas is introduced at various pressures for a set duration of 30 minutes, resulting in a statistical assessment of the percentage of extinct Si adatoms at each pressure, as shown in the table in Figure III.11 The curve reflecting the evolution of extinct adatoms percentage as a function of pressure was produced using this data, as shown in Figure III.12. It should be noted that prior to each deposition, the sample was re-flashed and re-prepared to ensure consistent conditions for the subsequent deposition.

P (mbar)	10^{-6}	$3x10^{-6}$	$5x10^{-6}$	10^{-5}	$5x10^{-5}$
Extinct adatoms (%)	0	4.5	17	36	35.5

Figure III.11: Table of statistical values of the density of silicon adatoms upon the exposition of the Si(111)-7x7 surface to different pressures of N_2 gas during a fixed time equal to 30 minutes.

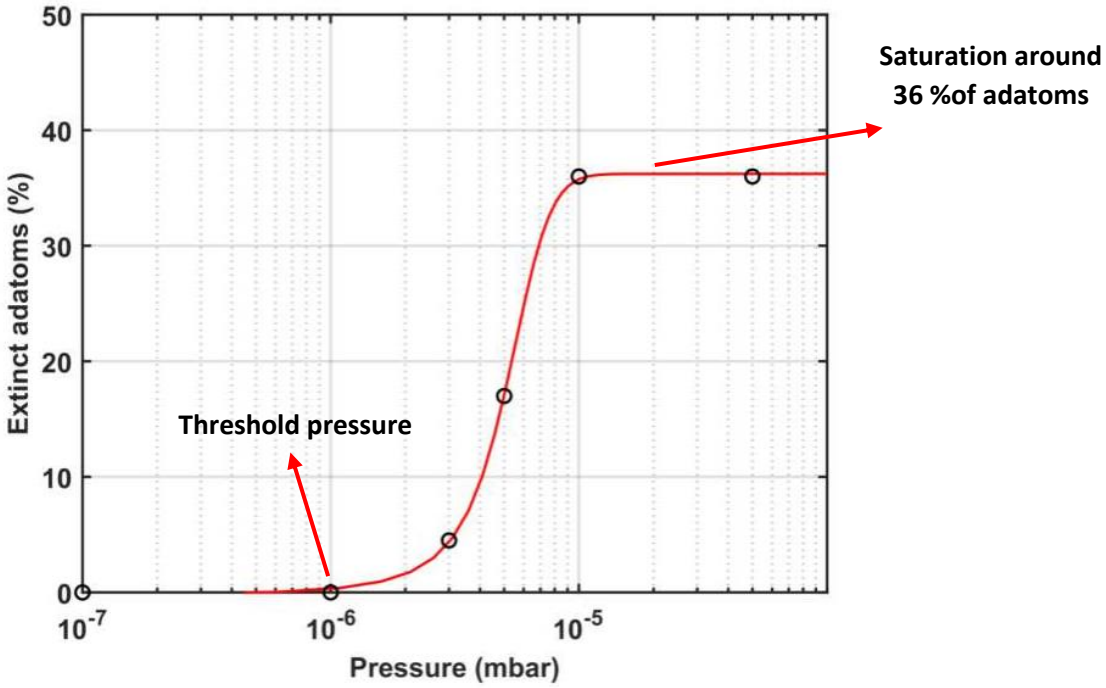

Figure III.12: Plot of the extinct adatoms for Si(111)-7x7 exposure to N_2 at various pressures for a fixed time of 30 min. The density of extinct Si adatoms increases starting from a threshold N_2 pressure of about 10^{-6} mbar and reaches a saturation value of 36 % of the total available surface adatoms. The experimental data (black circle) are fitted with the red line. Note: Each sample was re-prepared for each deposition, ensuring that each deposition is independent of the previous ones.

The graph analysis reveals two major points. The first is that at pressures below 10^{-6} mbar, no surface alteration was seen, indicating that it is a threshold pressure. The second point was approached at pressures greater than 10^{-5} mbar, with saturation at roughly 36% adatoms of the Si(111)-7x7 surface. The measured threshold remains relevant to the time of deposition (30 minutes) and might vary up and down according to the exposition time. In fact, the injected gas follows the Maxwell-Boltzmann distribution of kinetic energy, where only N_2 with enough energy to react are involved in the surface modification, so at higher pressure, should increase the absolute number (but not the fraction) of N_2 molecules that collide with the surface, including an increasing number with sufficient kinetic energy.

III.2.2.2 Statistical investigation at constant pressure and variable exposition time:

A statistical study was performed to investigate the kinetics of the reaction, which consisted of fixing the pressure of the injected N_2 gas and varying the period of exposition. It should be noted that prior

to each deposition, the sample was re-flashed and re-prepared to ensure consistent conditions for the subsequent deposition. The chemical reaction considered is defined by this equation:

$$N_{2\,(gas)} + 6\,Si_{\,(solid)} \rightarrow 2\,Si_3N$$

The Arrhenius equation, which determines the kinetics of a chemical process, is important here:

$$K = Ae^{-\frac{E_a}{RT}} \qquad \text{(Eq.III.1)}$$

- K: chemical reaction rate constant (s^{-1})
- A: pre-exponential factor or frequency factor (s^{-1})
- E_a: activation energy (kJ/mol)
- R: the gas constant (8.314 J/mol.K)
- T: absolute temperature (K)

From Eq.III.1, we can conclude that the chemical reaction rate constant depends only on the activation energy (E_a is considered constant as an approximation for the simplicity in the calculations, but actually it's dependent on the coverage of N atoms on the silicon surface) and the reaction's temperature. Therefore, these two parameters are constant in our experiment, thus the rate constant doesn't change. We consider two reactants involved in the reaction: silicon atoms of the Si(111)7x7 surface and the N_2 molecular gas. As a consequence, the rate equation for the reaction between the two species can be written in a simplified form, as follows:

$$V = K[N_2]^{\alpha}[Si]^{\beta} \qquad \text{(Eq. III.2)}$$

- V: rate of the reaction (s^{-1})
- $[N_2]$: density of N_2 molecules on surface
- α: order of reaction with respect to N_2
- [Si]: surface density of silicon adatoms
- α: order of reaction with respect to N_2

Since the pressure is maintained constant and only time change, this mean that the flux of N_2 is stable resulting in a constant density $[N_2]$, thus we can define an apparent rate constant K_{app}:

$$K_{app} = K[N_2]^{\alpha} \qquad \text{(Eq.III.3)}$$

So replacing K_{app} in the rate equation, we obtain the following form only dependent on the density of silicon atoms of Si(111)-7x7:

$$V = K_{app}[Si]^{\beta} \qquad \text{(Eq.III.4)}$$

In consequence, using statistical data from the experimental analysis, the determination of the reaction order is possible. Depending on the reaction order, the rate curve takes different forms following the equations presented below for each possible order (0,1,2):

$$V = K_{app}[Si]^{\beta} = -\frac{d[Si]}{dt} \qquad \text{(Eq.III.5)}$$

For a zero-order reaction (β = 0) with respect to the Si reactant, we obtain:

$$[Si]_0 - [Si]_t = K_{app}t \qquad \text{(Eq.III.6)}$$

- $[Si]_0$: density of silicon adatoms present at t = 0 min (equal to 1)
- $[Si]_t$: density of silicon adatoms present at time t

For a first-order reaction (β = 1) with respect to the Si reactant, we obtain:

$$\ln[Si]_0 - \ln[Si]_t = K_{app}t \text{ (Eq.III.7)}$$

For a second reaction (β = 2) in with respect to the Si reactant, we obtain:

$$\frac{1}{[Si]_t} - \frac{1}{[Si]_0} = K_{app}t \text{ (Eq.III.8)}$$

For this, we conducted a series of studies in which the pressure of N_2 molecular gas was held constant at $5x10^{-6}$ mbar and the density of silicon adatoms was calculated using STM pictures at different stages of the reaction. The obtained results are provided in the table of Figure III.13, where each density value was determined using statistics involving a large number of surface adatoms measured by SPIP software, as previously explained in order to minimize statistical error.

t (min)	10	20	40	60	90
Nb of adatoms	14354	9230	13496	13182	10472
$[Si]_t$ (%)	95.84	92.89	83.12	76.77	70.56

Figure III.13: Table presenting the statistical values of the silicon adatoms density at different exposition time 't' of the Si(111)-7x7 surface to $5x10^{-6}$ mbar of N_2 at room temperature and the corresponding number of adatoms evaluated to determine each value. Note: Each sample was re-prepared for each deposition, ensuring that each deposition is independent of the previous ones.

By considering, the three possible orders of reaction and their corresponding equation forms, using the experimental values of the density of silicon adatoms, three different curves were plotted, as presented in the graphs in Figure III.14. Since the equation at each order should satisfy the quantity $K_{app}t$, a fit of the experimental points with linear regression for each order should help to reveal the N_2 dissociation reaction order by comparing the associated regression factors R^2. We have found the greatest regression factor equal to 0.9924 in the case of order 2 reaction compared to 0.9006 and 0.9691 for order 1 and 0 reactions respectively. Consequently, the reaction is of second-order (β = 2) and the apparent rate constant K_{app} corresponds to the coefficient of the regression line which is equal to 0.0048 min^{-1}.

a)

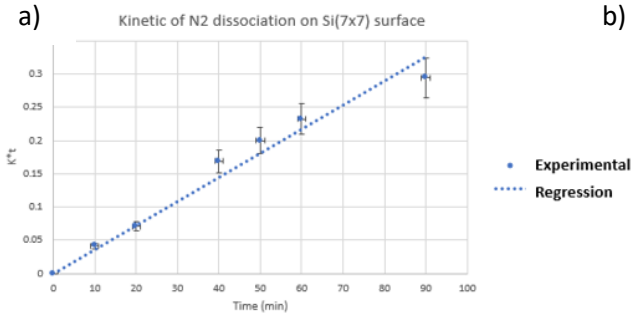

b)

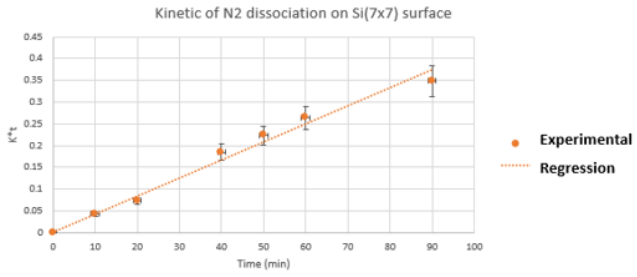

c)

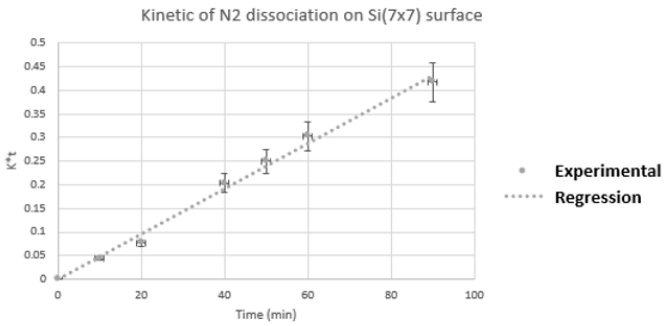

Figure III.14: Plots of the reaction rate at different exposition time 't' of the Si(111)-7x7 surface to $5x10^{-6}$ mbar of N_2 gas using different order equations: a) order 0, b) order 1, and c) order 2. In each case, the experimental values were fitted with linear regression, and the greater regression factor (0.9924) corresponds to a reactional order equal to 2.

III.3 X-ray photoelectron spectroscopy investigation:

X-ray photoelectron experiments were performed with a hemispherical analyzer Omicron EA 125 equipped with a dual anode X-ray source (Omicron, DAR 400) using Al Kα X-ray source (hv =1486.6 eV) radiation. The photoelectrons were collected at normal electron emission. The angle of acceptance of the photoelectron analyzer was set to ± 1. The spectra were recorded using a pass energy of 20 eV for high resolution and 50 eV for the wide scan. The peak was fitted to mixed Gaussian-Lorentzian components using XPS-CASA software,[37]after having subtracted a Shirley-type background. These experiments were done in collaboration with Dr. Samar Hajjar and Pr. Carmelo Pirri, from Université Haute-Alsace UHA.

Figure III.15.a depicts a wide-range XPS spectrum of the Si(111)-7x7 surface after preparation, with only Si(2s) and Si(2p) peaks visible, showing the surface's cleanliness. The N_2 gas was then injected at room temperature for 30 minutes at a pressure of $2x10^{-5}$ mbar. XPS spectrum following as illustrated in Figure III.15.b, gas exposition produces one new peak N(1s), marked by a red circle, showing the presence of nitrogen compound on the surface. The enlarged representation of the N(1s) peak, illustrated in the inset of Figure III.15.b, reveals an asymmetric broadened band corresponding to the nitrogen core level. This wide band suggests the presence of different nitrogen-based products on Si(111)-7x7 surface after N_2 gas exposition, at RT. The full width at half maximum (FWHM) of this large N(1s) is about 2.2 eV. Therefore, it can be fitted by three subcomponents A1, A2, and A3 positioned at binding energies equal to 400.09 ± 0.1 eV, 398.64 ± 0.1 eV, and 397.65 ± 0.1 eV, respectively, as presented in Figure III.16. Each component (A1, A2, and A3) was fitted with an FWHM value of 1.6 eV. We may identify the chemical components underlying each observable component forming the N(1s) core-level spectra using the previously disclosed XPS experimental database generated from the investigation of NH_3 dissociation of silicon surfaces.[38-40]

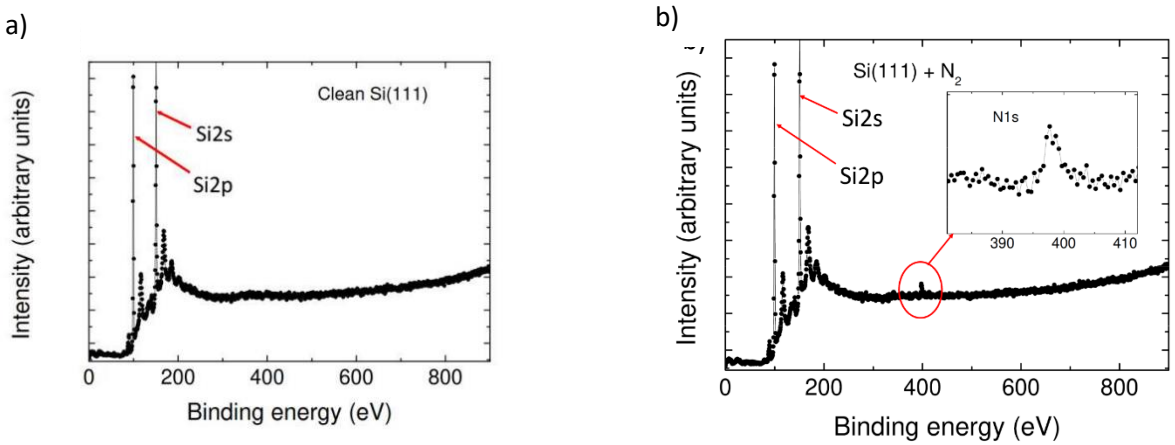

Figure III.15: Wide scan XPS spectrum of Si(111)-7x7 surface a) before and b) after exposition to N_2 gas during 30 minutes at RT under the pressure of $2x10^{-5}$ mbar.

According to the literature, the components A1, A2, and A3 might be ascribed to Si-NH_2, Si_2-NH, and Si_3-N, respectively. Nevertheless, no atomic hydrogen was used in the experiment, and the residual gas pressure in our UHV chamber includes just a bit of hydrogen in the molecular form H_2. As a result, we assume that there are no hydrogenated components on the surface, and only the A3 component may be assigned to Si_3-N. The remaining two components might be attributed to various N_2 molecule bonding states with the Si adatoms of the Si(111)-7x7 surface. In terms of coverage, the A3 component (Si_3-N) dominates the spectra, accounting for 64.89% of the total area, followed by the A2 component at 27.86% and the A1 component at the remaining occupation.

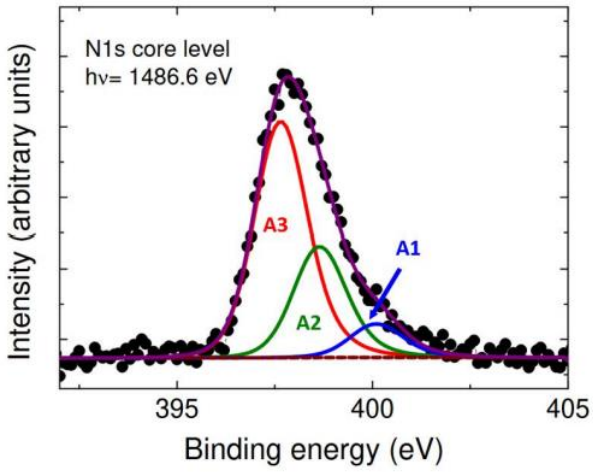

Figure III.16: N(1s) core-level spectra for an exposition of Si(111)-7x7 to N_2 gas during 30 minutes at RT under pressure of $2x10^{-5}$ mbar. The total signal is separated into three components each having a full width at half maximum (FWHM) equal to 1.6 eV: A1, A2, and A3.

Correspondingly, the N_2 exposed Si(111)-7x7 was thermally annealed for 30 minutes at 800 K. Upon annealing, the number of components was reduced to a single strong peak (FWHM = 1.5 eV) at 397.55 ± 0.1 eV, as shown in Figure III.17b XPS spectra, which corresponds to a completely dehydrogenated molecule, i.e., atomic N triply coordinated to silicon atoms Si_3- N.

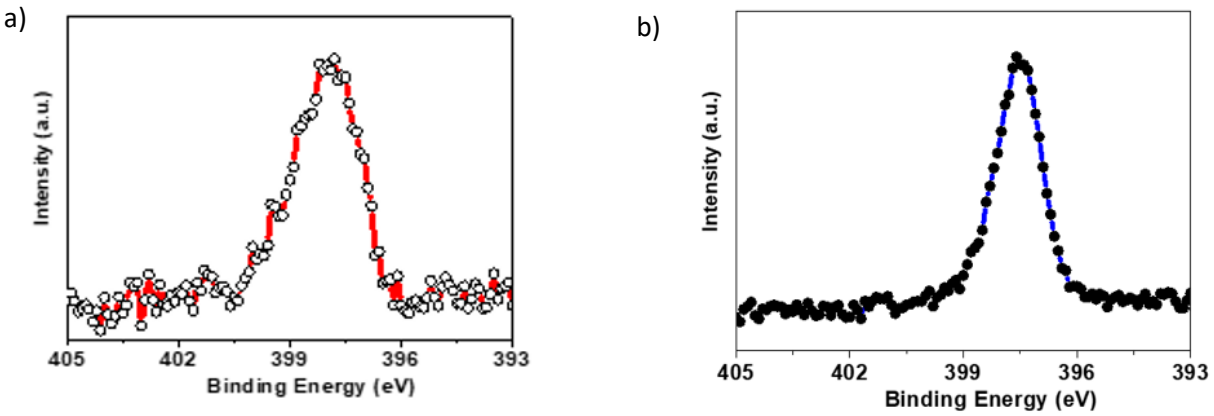

Figure III.17: a) Plot of nitrogen core levels before (red line) thermal annealing. b) N(1s) core level spectra obtained upon thermal annealing at 800 K for 30 minutes. Only one indecomposable peak (FWHM = 1.5 eV) remains with a binding energy of 397.55 ± 0.1 eV corresponding to atomic N triply bonded to the silicon surface. Circles represent the experimental data.

Furthermore, Figure III.17. depicts the plot of the nitrogen core level peaks N(1s) before (red plot) and after annealing (blue plot), with the area under the two peaks nearly identical (within a few percent), indicating that all existing N-based species (i.e. peaks A1 and A2 in Figure III.16) transform into Si_3-N. This is consistent with M. Björkqvist et al.[38] work on the dissociation of ammonia NH_3 on the Si(111)-7x7 surface, in which all intermediate N-based species transform to Si_3-N after thermal annealing at 800 K. It's worth noting that the equal area under both peaks indicates that no nitrogen compounds desorbed from the surface. Instead, all compounds transformed nitrogen atoms bonded to three silicon atoms, forming triple bonds, this experiment is in total agreement with the STM experiments performed before shown in part III.2 (Figure III.9).

III.4 Experimental data and injected N_2 datasheet:

The empirical evidence commencing with high-resolution scanning tunneling microscopy (STM) images has elucidated the presence of enigmatic dark regions following the introduction of nitrogen (N2) under pressures exceeding 10^{-6} millibars, while maintaining a consistent room temperature environment. Moreover, our analysis encompasses X-ray photoelectron spectroscopy (XPS) experiments conducted under these identical conditions, unveiling the emergence of a previously unobserved N(1s) peak. Checking the composition of the injected N_2 gas datasheet reveals a high purity in the gas contains nitrogen (99.9999%) with 1 ppm of impurities (reported as <0.5 ppm of H_2O, <0.5 ppm of O_2, <0.5 ppm of H_2, <0.1 ppm of CO, <0,1 ppm of CO_2, and <0.1 ppm of C_nH_m). The data sheet shows that there are no impurities containing nitrogen atoms (e.g. NH_3 or NO) in this type of N_2 gas which means that what we saw in STM and XPS can only originate from the dissociation of injected N_2 gas on Si(111)-7x7 surface at room temperature. To support our experimental results, we have evaluated the adsorption energy and the electronic structure of the N_2 molecule at different adsorption sites of a Si(111)-7x7 surface with DFT calculations.

III.5 Density functional theory DFT study of different adsorption models:

This theoretical study is done in collaboration with Professor Alain Rochefort from Polytechnique de Montreal. Density Functional Theory (DFT) calculations were carried out at T = 0 K with Siesta package [40] and the results were visualized with the Chimera software.[41] We used periodic boundary conditions with the well-known PBE functional in conjunction with the semi-classical van der Waals corrections developed by Grimme.[42] The computations were performed with norm-conserving Trouillier-Martins

pseudopotentials and double-ζ polarized atomic basis sets. The mesh cut-off used to form the real space grid in the DFT calculations was 500 Ry, and the structural relaxation and geometry optimization were carried out using the conjugate-gradient method until the forces and the variation of total energy were less than 0.01 eV/Å and 0.0001 eV, respectively. We considered a vacuum region of 35 Å to minimize the interactions between periodic images in the direction normal to the slab. The adsorbed N_2 molecule in the supercell was fully optimized as well as the first three upper layers (of the seven layers model), while the remaining four deeper layers of the Si(111)-7x7 surface slab model (298 Si atoms) were fixed at the optimized geometry of pristine Si(111)-7x7. The bottom layer of this Si model was saturated with hydrogen (49 H atoms) to avoid the effect of Si dangling bonds.

As a result, all experimental data, including STM images with atomic resolution and XPS spectra, show that adsorbed N_2 molecules dissolve on the Si(111)-7x7 surface at ambient temperature after 30 minutes of exposure to a pressure of N_2 more than 1.10^{-6} mbar. To support our experimental results, we used DFT simulations to determine the adsorption energy and electronic structure of N_2 molecules at various adsorption sites on a Si(111)-7x7 surface. Over a Si adatom and rest-atom, we investigated both "end-on" and "side-on" adsorption sites (Figure III.18). In contrast to the SiC(111) surface, our DFT results show that N_2 is weakly bonded to the Si(111)-7x7 surface (E_{ads} 0.3 to 0.6 eV, Figure III.19) with relatively long Si-N equilibrium distances (d_{Si-N} 0.19 to 0.23 nm, Figure III.19)m, reminiscent of a physisorbed state.

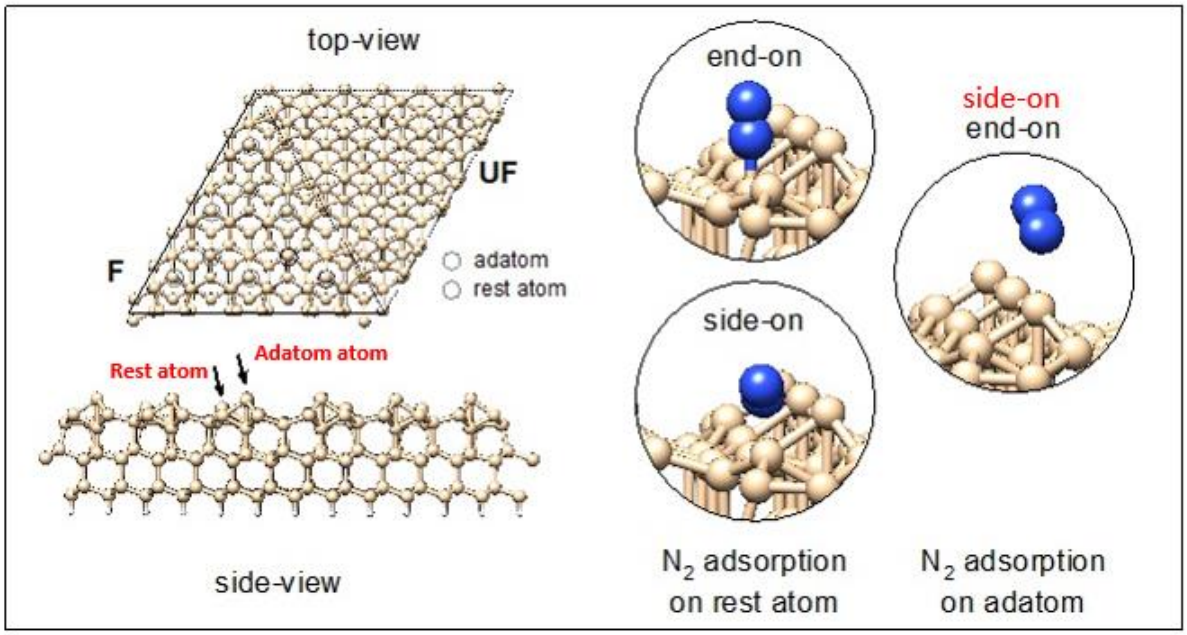

Figure III.18: Identification of the most reactive adsorption sites on the Si(111)-7x7 surface. The black circles are the adsorption site considered. The optimized end-on and side-on adsorption geometries on the Si rest atom are shown in the middle, and the optimized geometry obtained for both end-on and side-on adsorption on the Si adatom is reported on the right image. White: A hydrogen atom, yellow is: Silicon atom and blue is: Nitrogen atom.

Adsorption site	E_{ads} (eV)	Si-N_2 (nm)	N-N (nm)	Bader charge on N_2
End-on rest atom	0.49	0.192	0.113	-0.32
Side-on rest atom	0.60	0.229	0.114	-0.20
End-on and side-on adatom	0.33	0.270	0.112	-0.03

Figure III.19: DFT calculations for different adsorption sites for N_2 on Si(111)-7x7 revealing weak adsorption energies and long equilibrium distances.

Following optimization, an identical geometric configuration was obtained for both the end-on and side-on adsorption sites on a Si adatom. In this equilibrium state (as depicted in Figure III.19), a tilted N_2 molecule is positioned between a Si rest atom and a Si adatom. For the Si(111)-7x7 surface, the relevant equilibrium distance between N_2 and Si atoms is recorded as d(Si-N) = 0.27 nm (as outlined in Figure III.19), and the associated adsorption energy is 0.33 eV. Interestingly, the orientation of N_2 remains consistent for both the end-on and side-on adsorption sites when N_2 is adsorbed across the Si rest atom, despite the equilibrium Si-N distances being distinct at 0.19 nm and 0.23 nm, respectively. Notably, the adsorption energies for the end-on and side-on sites are found to be 0.49 eV and 0.60 eV, respectively. These findings, derived from Density Functional Theory (DFT) calculations, validate that Si rest-atoms exhibit greater reactivity compared to adatoms in this context. Additionally, a charge distribution analysis employing the Bader approach indicates a tangible transfer of charge from Si(111)-7x7 to N_2, with the magnitude of this charge transfer increasing as the Si-N distance decreases, as shown in Figure III.19.

Figure III.20 depicts the projected density of states (PDOS) of N_2 adsorbed on the Si adatom (green line) and the Si rest-atom (blue line) in end-on (blue line) and side-on (red line) geometries. For reference, the PDOS of a gas phase N_2 molecule (black dashed line) is also presented. The PDOS clearly indicates that the energy of the lowest π^*-antibonding level of gas phase N_2 centered at ~3 eV above the Fermi level is drastically influenced by the adsorption site. For all adsorption sites considered, this low-lying $N_2(\pi^*)$ state becomes strongly shifted toward the Fermi level, and even becomes partially occupied (see inset in Figure III.20). The two cases where N_2 is adsorbed in a side-on fashion (over rest-atom or an adatom) exhibit the larger overlap between the π^* state of N_2 and the surface Si atoms.

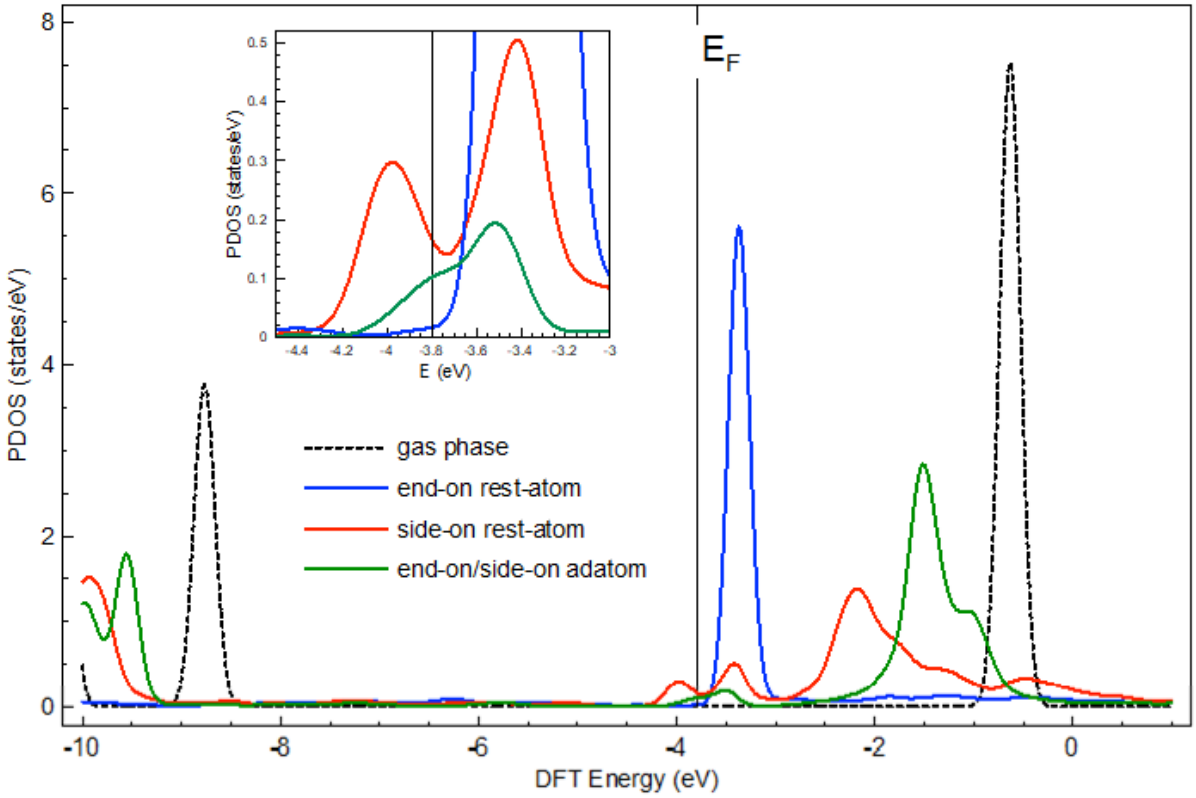

Figure III.20: Projected DOS of an N_2 molecule in the gas phase (black dashed line), and at equilibrium over a Si adatom (green line), and over a rest atom into an end-on (blue line) and side-on (green line) geometry with respect to the calculated Fermi level (E_F). A zoom of the different $N_2(\pi^*)$-Si overlaps around E_F is shown in the inset. White: Hydrogen atoms, light brown: Silicon atoms, and blue: Nitrogen atoms.

III.6 Result analysis:

In this study, N_2 molecular gas was injected into a UHV chamber with a base pressure of 7.2×10^{-11} mbar, and a Si(111)-7x7 surface was put on a manipulator and kept at room temperature. After 30 minutes of exposure and pressures below 10^{-6} mbar, no surface alteration was seen, as confirmed by STM. Interestingly, when the flow of injected N_2 gas was increased (pressure), a significant alteration of the Si(111)-7x7 surface was detected in both FC and UFC, as evidenced by the extinction of certain surface adatoms and rest atoms. In order to explore the nature of species existing on the surface after deposition, XPS characterization was done. The resulting XPS spectrum reveals a large N(1s) band that can be dissected into three components. The main component (A3) has a binding energy of 397.65±0.1 eV and represents 64.89 % of the coexisting species on the surface is attributed to Si_3N species. The two other components, A1 and A2, at 398.64±0.1 eV and 400.09±0.1 eV, respectively, correspond to intermediate species, partially dissociated N_2 molecules, grafted onto Si(111)-7x7 surface. Following thermal annealing of the sample at approximately 800 K for 30 minutes, the number of components was reduced to a single peak with a binding energy of 397.55 ± 0.1 eV which corresponds to N triply coordinated to silicon atoms. Aside from the surface area under the nitrogen N1s core level large band remains unchanged compared to the area under the single peak obtained after annealing. Therefore, this result clearly indicates that the nitrogen species, adsorbed on Si(111)-7x7 after exposition at room temperature, are not desorbed after annealing at 800 K, yet transformed into atomic N triply coordinated with silicon adatoms, e. g. Si_3-N, in which each N_2 molecule is fully dissociated into two nitrogen atoms bonded to the surface. Until now it is evident that we have intermediates species bonded to silicon atoms on the Si(111)-7x7 surface that can only originate from the dissociation of

injected N_2 molecular gas, a phenomenon that becomes observable upon the exposition of Si(111)-7x7 surface to the gas at a pressure greater than 10^{-6} mbar during 30 min.

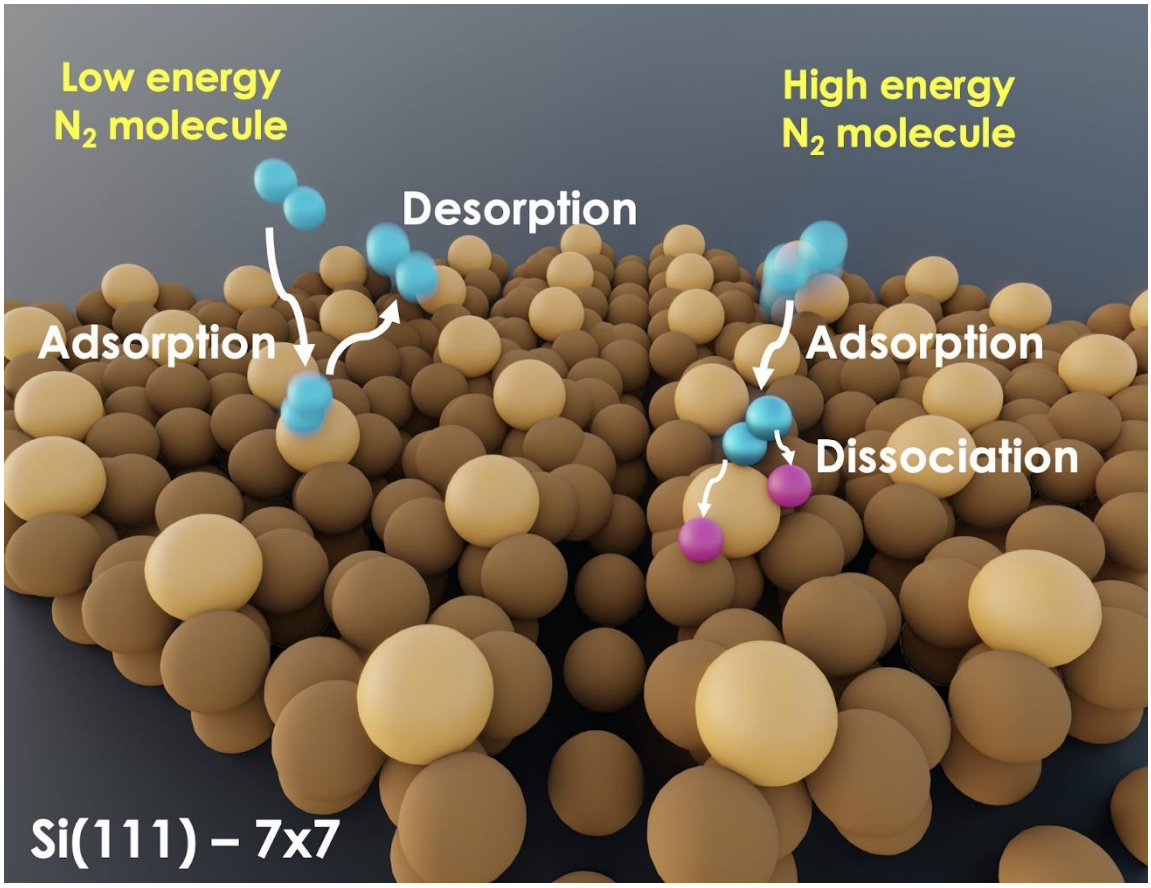

Figure III.21: Illustration depicting the scenario where N_2 molecules, whether have high or low energy, are either broken down and bonded to the Si(111)-7x7 surface or released back into the environment.

Therefore, for more understanding of the mechanism governing the breakage of such a strong bond, DFT calculation was employed to investigate the adsorption of N_2 molecules on different sites of the Si(111)-7x7 surface in two different fashions side-on and end-on. In the study, possible adsorption sites all reveal weak bonding energy with long equilibrium distances revealing a physisorbed state. From the done calculations, we noticed that the rest atoms are more reactive than adatoms. Moreover, the PDOS of the π*-antibonding level moves below the Fermi level to become partially occupied, and the electron transfer from the Si(111)-7x7 surface to the lowest π*-antibonding states of N_2(Figure III.20), such electron transfer into N_2-π* state favors a subsequent spontaneous N≡N partial bond cleavage at the interface. The charge transfer into N_2-π* state is higher for molecules with a side-on fashion because the overlap between N_2-π* and Si states is larger than the case of end-on orientation (see inset, Figure III.20). In contrast to hyperthermal collisions where choc induced compression and bend of specific bonds leads to the dissociation of the impinging molecules, in our case, collision impulse facilitate charge transfer from the surface to the molecule resulting in an electronic excitation dissociation.

Since N_2 follows the Boltzmann-Maxwell distribution, molecules at constant temperature will have a wide variety of kinetic energies, allowing a specified partition of the injected gas to overcome the activation barrier. As a result, an increase in pressure should increase the absolute number (but not

the fraction) of N_2 molecules that collide with the surface, including an increasing number with enough kinetic energy to bring N_2 closer to the Si(111)-7x7 surface, and thus improving the partial occupation of the π* states of N_2 and facilitating the breaking of the N atoms triple bond. This hypothesis is supported by experimental data, which show that more surface atoms are extinct under higher pressures and for the same period of time. Fewer molecules may respond when the partial pressure of N_2 gas is lowered, 30 minutes of deposition at pressures below 10^{-6} mbar was insufficient to detect any change in the Si(111)-7x7 surface. In consequence, statistical analysis of extinct silicon adatoms at fixed pressure and variable time of deposition revealed that dissociation of nitrogen N_2 on Si(111)- 7x7 surface possesses a partial second order in terms of kinetics law. The Langmuir-Hinshelwood mechanism is the major adopted mechanism for ammonia synthesis, where the kinetics is governed by the on-surface dissociation of N_2 molecules.[44] Therefore, if we adopt the same mechanism, the rate-determining step is the dissociation of N_2 on Si(111)-7x7 and any following reaction involving the dissociated nitrogen atoms will obey the kinetics law of a partial order of 2.

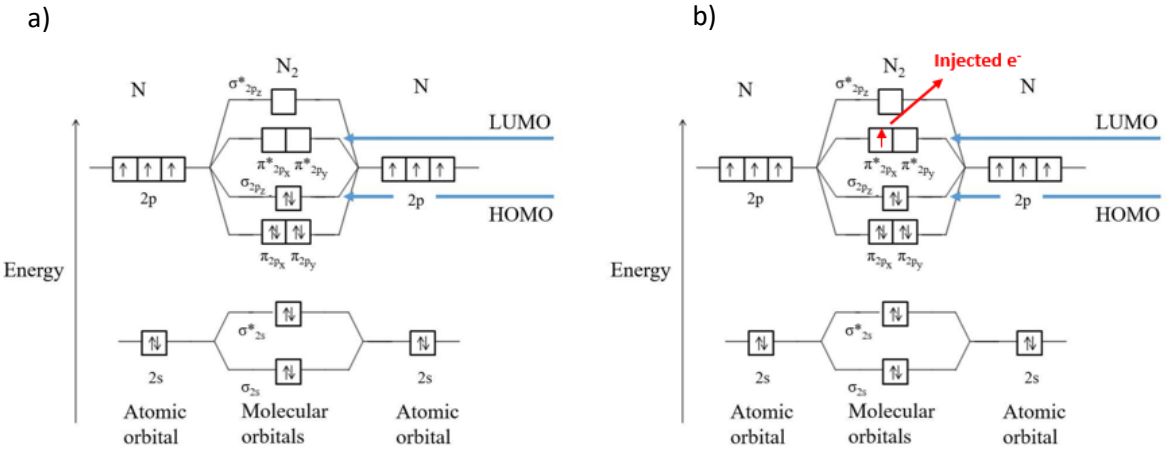

Figure III.22: Molecular orbitals of N_2 molecule indicating that the LUMO is essentially formed of antibonding orbitals at the lower energy levels. a) before dissociation, b) after dissociation electron is injected into the antibonding orbitals.

III.7: STM observation of the chemical reaction of atomic hydrogen on the N-adsorbed Si(111)-7x7 surface:

In this section, we propose to investigate the ability of the low-exposure reactive atomic hydrogen to react with the N-adsorbed Si(111)-7x7 surface forming N-chemical-based species. Benefiting from the N_2 dissociation at low pressure and ambient temperature on a highly reactive Si(111)-7x7 surface, the next step was to expose the surface to atomic hydrogen leading to the formation of NH species and ammonia. Scanning tunnel microscopy (STM) under ultra-high vacuum conditions was investigated as a powerful tool for detecting the influence of atomic hydrogen over the N-adsorbed Si(111)-7x7 surface.

III.7.1 Experimental results STM:

The first portion of this section is devoted to detailing the experimental procedures related to the deposition of atomic hydrogen gas at constant pressures with varying exposure durations. After each stage of the process (sample preparation and deposition), the condition of the Si(111)-7x7 surface is assessed using scanning tunneling microscopy (STM) in an ultra-high vacuum environment at room temperature. To test the cleanliness of the EFM H, rigorous degassing and removal of any potential

contaminants were carried out. Subsequently, a Si(111)-7x7 sample was positioned in front of the EFM H without hydrogen for 15 minutes and subjected to scanning, revealing no alterations to the surface.

Then, the second portion focuses on the exposure of atomic Hydrogen over the N-adsorbed Si(7x7) surface. To eliminate any damage to the ionic pump during N_2 gas injection, the chamber was pumped using a turbomolecular pump, since we achieved N_2 gas pressures on the order of 10^{-5} mbar in our trials. To confirm that no contamination arises from this transition in the pumping system, a clean sample of Si(111)-7x7 was kept for four hours (longer than any exposure to N_2) with no surface change detected.

III.8 Atomic hydrogen exposure to Si(111)-7x7 surface monitored by STM:

After constructing the Si(111)-7x7 sample and inspecting its surface cleanliness, a series of tests was carried out, which included exposing the sample to a fixed pressure of atomic Hydrogen gas and different deposition durations. We proceeded under UHV conditions with a base pressure of $9.2x10^{-11}$ mbar, and because both Si(111)-7x7 is a very reactive surface loaded with dangling bonds and H atomic is also extremely reactive, the deposition time was short, starting with total pressure inside the setup for H atomic deposition at $5x10^{-10}$ mbar. Starting with the first deposition of H atomic for the 40s at RT a clear modification on the surface was obtained, as revealed in the STM image of Figure III.23.a showing the empty states of Si(111)-7x7 after deposition. As we extend the exposure time of atomic hydrogen to 100 seconds, 160 seconds, and 250 seconds (accumulated deposition duration), there is a noticeable increase in the presence of darker spots on the surface. These dark spots correspond to the disappearance of silicon adatoms, indicating a clear transformation of the Si(111)-7x7 surface due to the exposure to atomic hydrogen as clearly illustrated in Figure III.23b, c, and d.

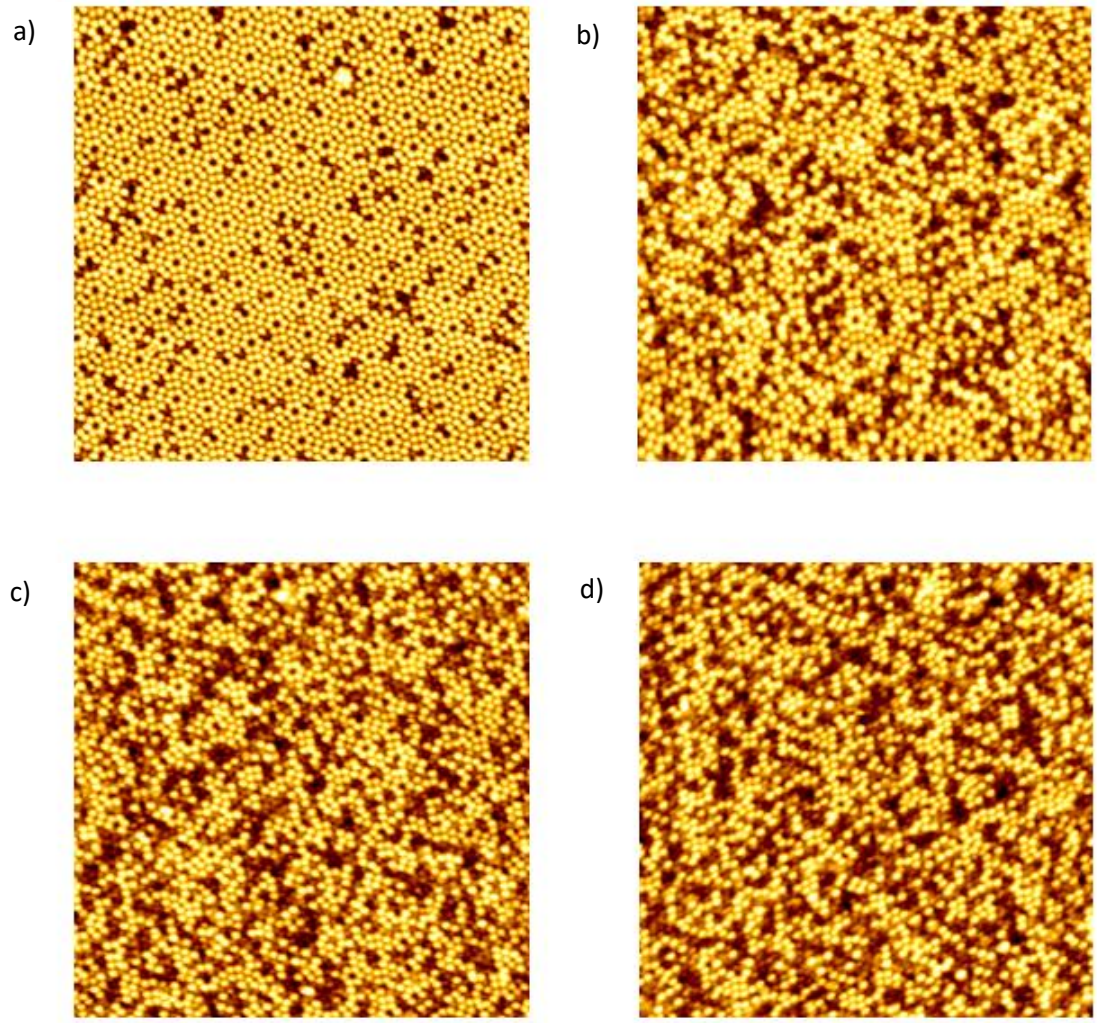

Figure III.23: STM images of the clean Si(111)-7x7 surface after exposition to atomic hydrogen gas at RT during for different depositions duration with fixed pressure at $5x10^{-10}$mbar. a) Empty states of Si(111)-7x7 after exposition to 40s of atomic hydrogen (40x40nm, V_s = 1.5 V, I_t = 90 pA), b) Empty states of Si(111)-7x7 after exposition to 100s of atomic hydrogen (40x40nm, V_s = 1.5 V, I_t = 90 pA), c) Empty states of Si(111)-7x7 after exposition to 160s of atomic hydrogen (40x40nm, V_s = 1.5 V, I_t = 90 pA), d) Empty states of Si(111)-7x7 after exposition to 250s of atomic hydrogen (40x40nm, V_s = 1.5 V, I_t = 90 pA).

A graphical illustration based on STM images, where the number of extinct atoms was calculated using the particle detection module of SPIP software (shown in Figure III.10), is limited to the surface adatoms, thus only ES images acquired at positive voltages are employed. This limitation was imposed by the fact that the study necessitates a large number of experiments, each of which must record several images for different zones on the surface, despite the fact that having a tip capable of extracting high resolution ensures the sensing of rest atoms is not always apparent, especially given that we work at RT. Every experiment we conducted for this purpose consisted of registering three images of distinct surface zones after preparation, followed by three images of different zones after exposure to atomic hydrogen, with dimensions set to 40 nm x 40 nm. As a result, for each experiment, the proportion of defects before a deposition can be measured and then deduced from the percentage of extinct adatoms after deposition to ensure the highest accuracy and increase coherence between the two experiments.

Duration (s)	40	100	160	250
Extinct adatoms (%)	7.8	33.7	48.6	58.7

Figure III.24: Table of statistical values of the density of silicon adatoms upon the exposition of the Si(111)-7x7 surface to different durations of atomic hydrogen gas during a fixed pressure equal to $5x10^{-10}$ mbar.

Thus the graph in Figure III.25 clearly shows that as we increase the exposure duration of atomic hydrogen on Si(111)-7x7 surface the number of extinct silicon adatoms increases with no limitations till destroying the surface construction completely.

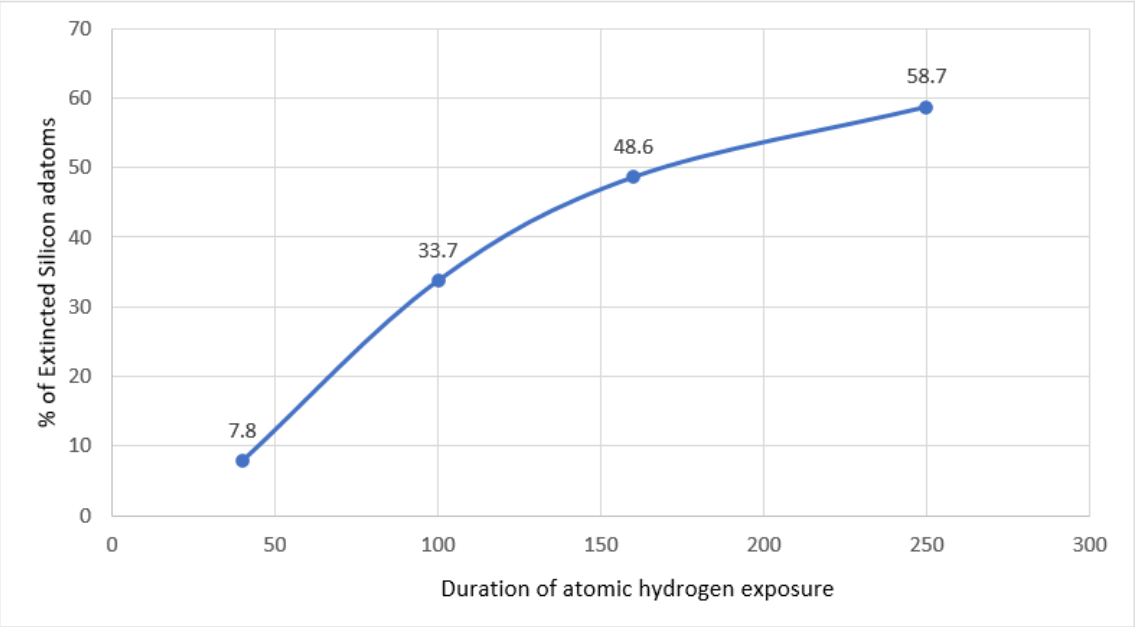

FigureIII.25: A graph depicting the number of adatoms that have vanished from the Si(111)-7x7 surface when exposed to various durations of atomic hydrogen gas, while maintaining a constant pressure of $5x10^{-10}$ mbar. Note: Each sample was re-prepared for each deposition, ensuring that each deposition is independent of the previous ones.

Annealing the Si(111)-7x7 after H atomic exposure at 800 K (in our setup) resulted in the desorption of an extensive density of atomic hydrogen chemisorbed on the surface, as shown in Figure III.26, but we can clearly see the remnants of some amount of atomic hydrogen chemisorbed to the surface, highlighted by the red flashes in the Figure.III.26 Furthermore, annealing the surface at 850K resulted in full H atomic desorption from the surface, regeneration of the Si(111)-7x7 DAS without disrupting the silicon substrate, no corrosive interaction with atomic hydrogen, and formation of the well-known monohydride phase. As a result, at ambient temperature, atomic hydrogen adsorbs on the well-ordered clean defect-free 7 X 7 surface to produce the stable monohydride phase.

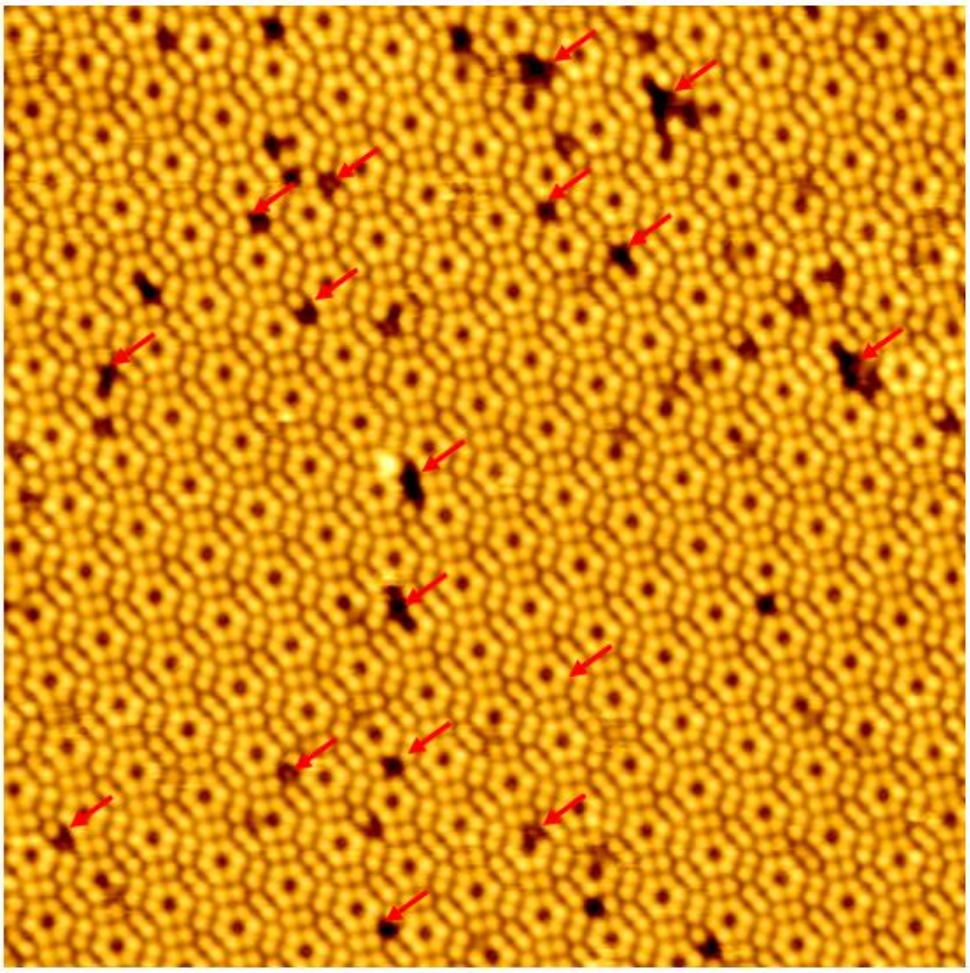

Figure III.26: High-resolution STM image of Si(111)-7x7 after the thermal annealing of the surface at 800K for 15 minutes showing the desorption of H atomic completely from the surface. Red flashes correspond to the remaining H atomic on the surface after thermal annealing at 800K (40x40nm, V_s = 1.5 V, I_t = 90 pA).

The work done over H atomic deposition over Si(111)-7x7 and thermal desorption experiments are in total agreement with previously observed experiments by Toshio Sakurai, Y. [33]

III.9 Atomic hydrogen influence over the N-adsorbed Si(111)-7x7 monitored by STM:

So after we have successfully demonstrated that N_2 dissociation can be achieved at low pressure and ambient temperature on a highly reactive Si(111)-7x7 surface. Our results suggest that the low energy collision of N_2 with the surface can promote an electron transfer from Si(111)-7x7 to the π^*-states of N_2 to finally stretching the N≡N bond leading to the cleavage of the N_2 triple bond and bonds to the surface via facile collisional dissociation. According to the Maxwell-Boltzmann distribution, only a fraction of N_2 molecules incident on the surface will have the necessary kinetical energy to overcome the dissociation barrier at room temperature. At room temperature, several adsorbed intermediates coexist, yet after thermal annealing at 800K uniquely Si_3N species, XPS experiments detect the full dissociation of N_2. The next step of our experiment was to expose the N-adsorbed Si(111)-7x7 surface to H atomic in order to promote the synthesis of nitrogen-based species in an energy-efficient manner, as the dissociation occurs under relatively mild conditions.

After preparing the Si(111)-7x7 sample and checking surface cleanliness by scanning several zones, exposing the surface to N_2 gas with a total pressure inside the setup $5x10^{-6}$ mbar for 30 mins at RT

placing the surface at the manipulator just facing the capillary of the injected N_2 gas obeying Maxwell Boltzmann distribution of the kinetic energies. Monitoring the surface after the exposition of N_2 gas on the STM head at RT, shows us the clear alteration of N_2 gas on the surface with the appearance of dark spots with a percentage of 28.8% corresponding to the dissociation of N_2 into several intermediates on the surface (explained by XPS), as revealed by the STM image of Figure.III.27. b.

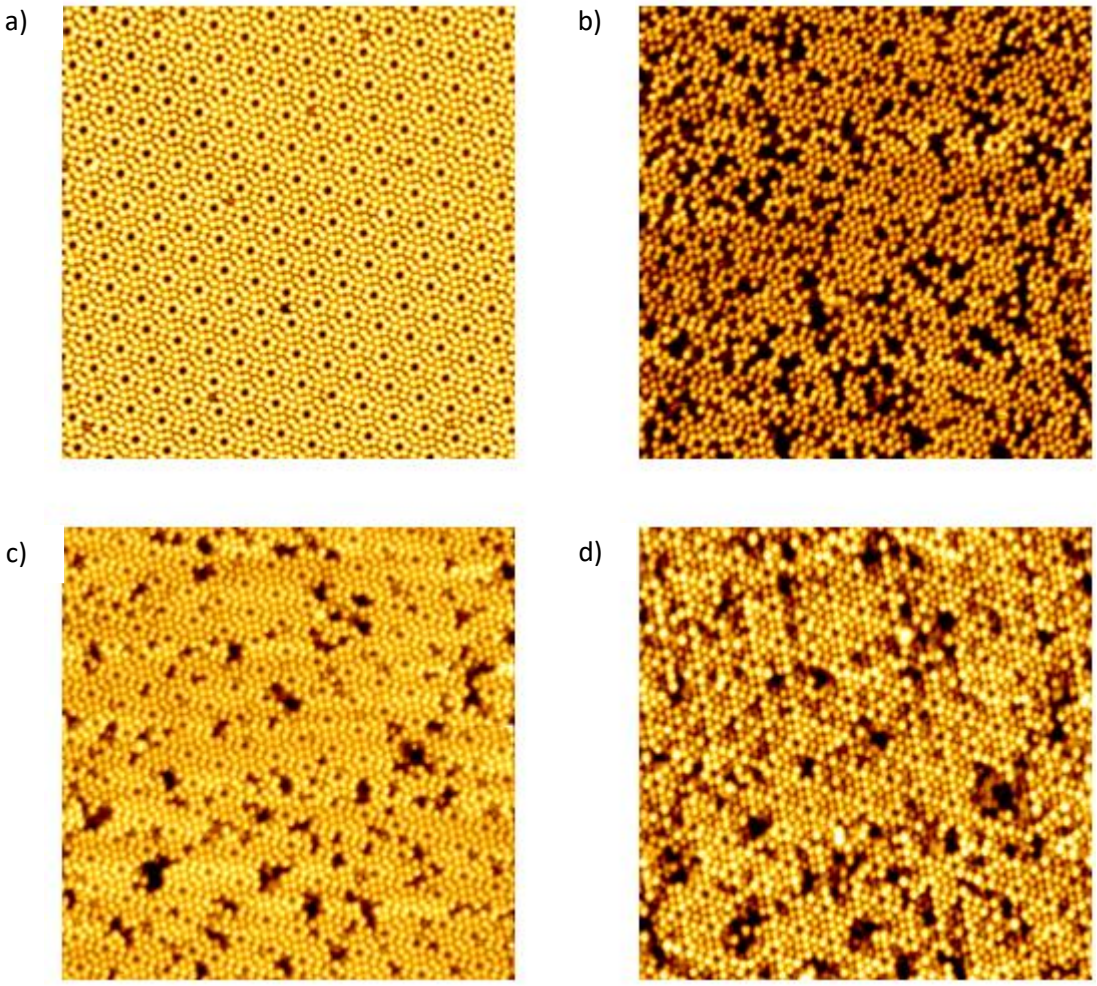

Figure III.27 a) STM images of the clean Si(111)-7x7 surface before any deposition (40x40nm, V_s = 1.8 V, I_t = 80 pA), b) Empty states of Si(111)-7x7 after N_2 deposition (40x40nm, V_s = 1.8 V, I_t = 50 pA), c) Empty states of the surface after the exposure of N-adsorbed Si(111)-7x7 to atomic hydrogen (40x40nm, V_s = 1 V, I_t = 40 pA), d) Filled states of the surface after the exposure of N-adsorbed Si(111)-7x7 to atomic hydrogen (40x40nm, V_s = -0.8V, I_t = 40 pA).

Based on the findings from XPS experiments, it has been observed that subjecting the Si(111)-7x7 surface with adsorbed nitrogen to annealing at 800 Kelvin results in the conversion of all nitrogen intermediates on the surface into Si_3N. Additionally, it is important to highlight that 800 Kelvin represents the temperature at which a significant portion of hydrogen atoms desorbs from the silicon surface. Combining the two scenarios of transformation of all N-intermediates and desorption of H atomic at this temperature, the optimal idea was to shoot the N-adsorbed Si(111)-7x7 surface with H atomic while annealing the surface at 800K. Surprisingly after the first attempt, shooting N-adsorbed Si(111)-7x7 surface while annealing at 800K placing it just facing the EFM H with a distance of almost 10 cm for 5mins with a total pressure for H atomic inside the setup $5x10^{-10}$ mbar, huge modification in the surface structure as revealed by the STM images in Figure III.27.c.d inspecting both polarities displaying the empty and filled states of the surface scanning both polarities. The exposure of H atomic while annealing the surface at 800K led to a decrease in the number of defects from 28.8% to between

10.2-12% (less than half), reconstructing the 7x7 surface in many zones of the surface. It's important to note that subjecting the Si(111)-7x7 surface with adsorbed nitrogen to annealing at 800 K for a duration of 5 minutes, which coincides with the period of atomic hydrogen deposition, does not induce any alterations in the surface structure. The percentage of dark spots observed on the surface, as verified by STM, remains exactly the same before and after this treatment.

With the assistance of thermal annealing at 800K, the remarkable activity of the H atomic over the N-adsorbed Si(111)-7x7 contributed to a sharp decrease of dark spots to less than half of the initial percentage. Annealing the surface at 800K transforms all N-intermediates into N triply bonded to three silicon atoms, and at the same time, it enhances N-intermediates mobility at the surface and prevents many H atoms from sticking to the surface and chemisorbing it. The significant decrease in the dark spot percentage and the subsequent restoration of most of the surface to its Si(7x7)-DAS configuration can be attributed to the removal of nitrogen atoms from the surface through the action of atomic hydrogen. It can be suggested that with the exposure of atomic hydrogen, N atoms adsorbed on the surface react with an atomic hydrogen to form NH, NH_2 species leading to NH_3 or N_2H_2.

The appearance of the surface recovery and lowering of the number of dark spots is attributed to the formation of N-species and its desorption from the surface. The remaining deep holes as observed by STM images in Figure III.27 c.d on the surface after H-atomic deposition with thermal annealing indicate that Si adatoms are still not visible at the applied bias voltage. This can be attributed to several reasons such as the possibility that Si atoms can be etched from the surface with the N atoms during annealing and shooting with H atomic, the possibility of a small percentage of N atoms remaining on the surface, and also the probability of some H atomic chemisorb to the surface because we already know that annealing the surface at 800K doesn't desorb H atomic totally from the surface.

III.10 Discussion and result analysis:

In this study, N_2 molecular gas was injected into a UHV chamber with a base pressure of $6.7x10^{-11}$ mbar, and a Si(111)-7x7 surface was placed on a manipulator and kept at room temperature. After 30 minutes of exposure and pressures below 10^{-6} mbar, no surface alteration was seen, as confirmed by STM. Surprisingly, when the flow of injected N_2 gas was increased (pressure), a noticeable alteration of the Si(111)-7x7 surface was detected in both FC and UFC, as evidenced by the extinction of certain surface adatoms and rest atoms. XPS characterization was performed to investigate the type of species found on the surface following deposition. The corresponding XPS spectra show a broad N1s band that can be dissected down into three components. After 30 minutes of thermal annealing at 800 K, the number of components was reduced to a single peak corresponding to N triply coordinated to silicon atoms.[23,24] Furthermore, the surface area under the vast band of nitrogen N1s stays unaltered when compared to the area under the single peak produced after annealing. As a result, the nitrogen species adsorbed on Si(111)-7x7 after room temperature exposure are not desorbed after 800 K annealing, but rather transformed into atomic N triply coordinated with silicon atoms, e.g. Si_3-N, in which each N_2 molecule is fully dissociated into two nitrogen atoms bonded to the surface. Until now, it has been demonstrated that intermediate species bonded to silicon atoms on the Si(111)-7x7 surface can only result from the dissociation of injected N_2 molecular gas, a phenomenon that becomes visible after 30 minutes of exposing the Si(111)-7x7 surface to the gas at a pressure higher than 10^{-6} mbar.

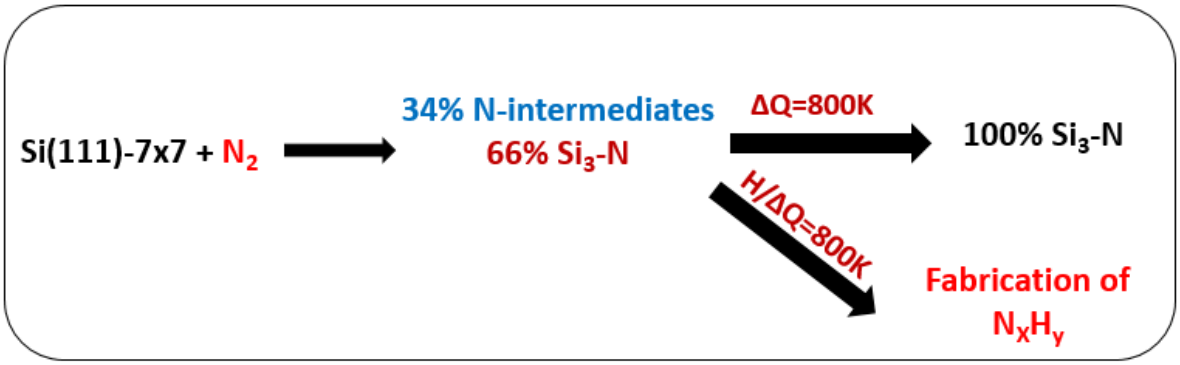

Figure III.28: Schematic illustration showing the pathway toward N_xH_x fabrication over Si(111)-7x7.

H atomic low exposure deposition over the N-adsorbed Si(111)-7x7 with the assistance of thermal annealing led to magnificent modification on the surface structure, synthesizing nitrogen-based chemicals in an energy-efficient manner. The appearance of the surface recovery and lowering of the number of dark spots is attributed to the formation of N-species and its desorption from the surface. The remaining number of dark spots on the surface can be attributed to a variety of factors, but the main one is that 800K does not completely desorb H atoms from the surface in our experimental setup, 850K is the temperature of H atomic total desorption from the Si(111)-7x7 surface recovering the surface full reconstruction, so some H atoms may still be present on the surface.

Therefore, discrimination requires the use of more elemental analysis techniques that can operate in UHV. Spectroscopic methods such as FTIR, Raman, XPS, and thermal desorption spectroscopy can give valuable information that can facilitate the identification of the species observed by local probe probes under UHV. However, for the moment these techniques are not developed to work in these conditions, hoping that they will be in the future. Furthermore, the reactive surface of Si(111)-7x7 is emphasized as a potential candidate for the efficient and easy dissociation of inert molecules at ambient temperature and low pressure, as well as the high possibility of synthesizing nitrogen-based chemicals in an energy-efficient manner under mild conditions. Our future research will concentrate on this topic, with the explicit goal of investigating the feasibility of dissociating CO_2 gas in the same way that we accomplished N_2.

III.11 Conclusion:

In this chapter, we have successfully demonstrated that N_2 dissociation can be achieved at low pressure and ambient temperature on a highly reactive Si(111)-7x7 surface. Our results suggest that the low energy collision of N_2 with the surface can promote an electron transfer from Si(111)-7x7 to the π^*-states of N_2 to finally stretching the N≡N bond leading to the cleavage of the N_2 triple bond and bonds to the surface via facile collisional dissociation. According to the Maxwell-Boltzmann distribution, only a fraction of N_2 molecules incident on the surface will have the necessary kinetical energy to overcome the dissociation barrier at room temperature. At room temperature, several adsorbed intermediates coexist, yet after thermal annealing at 800K uniquely Si_3N species are detected by XPS experiments indicating the full dissociation of N_2.

The profound impact of atomic hydrogen with the assistance of controlled thermal annealing over the N-adsorbed Si(111)-7x7 is a promising avenue for energy-efficient synthesis of nitrogen-based chemicals in an energy-efficient manner. Shedding light on the surface's remarkable capability to produce ammonia. The potential applications of this approach extend to various industries, offering a sustainable and cost-effective means of chemical production. This development represents a promising contribution to green and efficient chemistry.

References:

[1] Tolman, W. B. : Activation of Small Molecules: Organometallic and Bioinorganic Perspectives, Wiley-VCH Verlag GmbH & Co. KGaA, Weinheim, (2006).

[2] Smil, V.: Population Growth and Nitrogen: An Exploration of a Critical Existential Link. Popul. Dev. Rev., 17 (4), 569–601, (1991).

[3] United Nations, Kyoto Protocol, available at http: //unfccc.int/resource/docs/convkp/kpeng.pdf.

[4] Kobayashi, H., Hayakawa, A., Somarathne, K. D. K. A., & Okafor, E. C. Science and technology of ammonia combustion. Proceedings of the Combustion Institute., (2019).

[5] Kyriakou, V., Garagounis, I., Vourros, A., Vasileiou, E., & Stoukides, M. An Electrochemical Haber-Bosch Process. Joule 4,1-17, (2019).

[6] Kitano, M.; Kanbara, S.; Inoue, Y.; Kuganathan, N.; Sushko, P. V.; Yokoyama, T.; Hara, M.; Hosono, H. Electride Support Boosts Nitrogen Dissociation over Ruthenium Catalyst and Shifts the Bottleneck in Ammonia Synthesis. Nat. Commun. 6 (1), 1–9, (2015).

[7] Hattori, T., Yamada, M., & Komori, F. STM observation of the chemical reaction of atomic hydrogen on the N-adsorbed Cu(001) surface. Surface Science, 655, 1–6, (2017).

[8] Ertl, G., Huber, M., Lee, S. B., Paál, Z., & Weiss, M. Interactions of nitrogen and hydrogen on iron surfaces. Applications of Surface Science, 8(4), 373–386, (1981).

[9] Shi, H., Jacobi, K., & Ertl, G. Interaction of hydrogen with nitrogen atoms chemisorbed on a Ru(0001) surface. The Journal of Chemical Physics, 102(3), 1432–1439, (1995).

[10] Liang, Z., Yang, H. J., Oh, J., Jung, J., Kim, Y., & Trenary, M. Atomic-Scale Dynamics of Surface-Catalyzed Hydrogenation/Dehydrogenation: NH on Pt(111). ACS Nano, 9(8), 8303–8311, (2015).

[11] R.M. van Hardeveld, R.A. van Santen, J.W. Niemantsverdriet. Kinetics and Mechanism of NH_3 Formation by the Hydrogenation of Atomic Nitrogen on Rh(111)J. Phys. Chem. B 101,998, (1997).

[12] Christmann, K. Interaction of hydrogen with solid surfaces. Surface Science Reports, 9(1-3), 1–163, (1988).

[13] Gross, A. Hydrogen on metal surfaces: Forever young. Surface Science, 606(7-8), 690–691, (2012).

[14] Chornet, E. Chemisorption of hydrogen on iron. Journal of Catalysis, 27(2), 246–265, (1972).

[15] Groot, I. M. N., Ueta, H., van der Niet, M. J. T. C., Kleyn, A. W., & Juurlink, L. B. F. Supersonic molecular beam studies of dissociative adsorption of H2 on Ru(0001). The Journal of Chemical Physics, 127(24), 244701, (2007).

[16] Luntz, A. C., Brown, J. K., & Williams, M. D. Molecular beam studies of H2 and D2 dissociative chemisorption on Pt(111). The Journal of Chemical Physics, 93(7), 5240–5246, (1990).

[17] Yates, J. T., Thiel, P. A., & Weinberg, W. H. The chemisorption of hydrogen on Rh(111). Surface Science, 84(2), 427–439, (1979).

[18] Takehiro, N., Mukai, K., & Tanaka, K. Reaction of N on a Ni(110) surface with H atoms. The Journal of Chemical Physics, 103(4), 1650–1654, (1995).

[19] Ceyer, S. T. New Mechanisms for Chemisrty at Surfaces. Science **1990**, 249, 133-139; b) Krumbein, L.; Anggara, K.; Stella, M.; Michnowicz, T.; Ochner, H.; Abb, S.; Rinke, G.; Portz, A.; Durr, M.; Schlickum, U.; Baldwin, A.; Floris, A.; Kern K.; Rauschenbach, S. Fast Molecular Compression by a Hyperthermal Collision Gives Bond-Selective Mechanochemistry. Phys. Rev. Lett. **2021**, 126, 056001; c) B. Jiang, M. Yang and D. Xie, H. Guo, Chem. Soc. Rev., 2016, 45, 3621; d) Asscher M.; Zeiri, Y. Surface Processes induced by Collisions. J. Phys. Chem. B **2003**, 107, 6903-6919; d) Nosir, M. A.; Martin-Gindre, L.; Bocan G. A.; Diez Muino, R. Dissociative Adsorption Dynamics of Nitrogen on a Fe(111) Surface. Phys. Chem. Chem. Phys. **2017**, 19, 24626-24635; e) Rettner, C. T.; Stein H.; Schweizer, E. K. Effect of Collision Energy and Incidence Angle on the Precursor-Mediated Dissociative Chemisorption of N_2 on W(100). J. Chem. Phys. **1988**, 89, 3337-3341; f) Egeberg, R. C.; Larsen J. H.; Chorkendorff, I. Molecular Beam Study of N_2 Dissociation on Ru(0001). Phys. Chem. Chem. Phys. **2001**, 3, 2007-2011; g) McClure, S. M.; Reichman, M. I.; Seets, D. C.; Nolan, P. D.; Sitz G. O.; Mullins, C. B. in Surface Dynamics, Vol. 11 (Eds.: D. P. Woodruff), Elsevier, Amsterdam, **2003**, pp. 109-143; h) Chan, J. R.; Lambie, S. G.; Trodahl, H. J.; Lefebvre, D.; Le Ster, M.; Shaib, A.; Ullstad, F.; Brown, S. A.; Ruck, B. J.; Garden A. L.; Natali, F. Facile Dissociation of Molecular Nitrogen using Lanthanide Surfaces: Towards Ambient Temperature Ammonia Synthesis. Phys. Rev. Materials **2020**, 4, 115003; i) Kim, J.; Ha, H.; Doh, W. H.; Ueda, K.; Mase, K.; Kondoh, H.; Mun, B. S.; Kim H. Y. Park, J. Y. How Rh Surface Breaks CO_2 Molecules under Ambient Pressure. Nature Communications , 11, 5649. (2020).

[20] Joannopoulos, J. D.; Arias, T. A.; Brommer, K.; Capaz, R. B.; Cho, K. Chapter 2 . Semiconductor Surface Studies. (Research Laboratory of Electronics (RLE) at the Massachusetts Institute of Technology (MIT), (1994).

[21] Ying, Z. C.; Ho, W. Thermo- and Photo-Induced Reactions of NO on Si(111)-7x7. I. Adsorption and Chemical Reactions. J. Chem. Phys. 91 (4), 2689–2705, (1989).

[22] Cho, I. K.; Kim, Y. K.; Yeom, H. W. Temperature-Dependent Adsorption and Dissociation Behaviors Of NH3 on Si(111)7×7: A High-Resolution Core-Level Photoemission Study. Physical Review. B.73 (11), 1-6, (2006).

[23] Björkqvist, M.; Göthelid, M.; Grehk, T. M.; Karlsson, U. O. NH3 on Si(111)-7x7: Dissociation and surface reactions. Physical Review. B.57, 2327–2333, (1998).

[24] Bischoff, J. L.; Lutz, F.; Bolmont, D.; Kubler, L. Use of Multilayer Techniques for XPS Identification of Various Nitrogen Environments in the Si/NH3 System. Surf. Sci. 251 252 (C), 170–174, (1991).

[25] Kim, J. W.; Yeom, H. W. Surface and Interface Structures of Epitaxial Silicon Nitride on Si(111). Phys. Rev. B - Condens. Matter Mater. Phys. 67 (3), 1–5, (2003).

[26] Kobayashi, H., Edamoto, K., Onchi, M., & Nishijima, M. Reactions of atomic hydrogen with the Si(111) (7×7) surface by high resolution electron energy loss spectroscopy. The Journal of Chemical Physics, 78(12), 7429–7436, (1983).

[27] Schulze, G., & Henzler, M. Adsorption of atomic hydrogen on clean cleaved silicon (111). Surface Science, 124(2-3), 336–350, (1983).

[28] Mortensen, K., Chen, D. M., Bedrossian, P. J., Golovchenko, J. A., & Besenbacher, F. Two reaction channels directly observed for atomic hydrogen on the Si(111)-7×7 surface. Physical Review B, 43(2), 1816–1819, (1991).

[29] Boland, J. J. Role of bond-strain in the chemistry of hydrogen on the Si(100) surface. Surface Science, 261(1-3), 17–28, (1992).

[30] Becker, G. E., & Gobeli, G. W. Surface Studies by Spectral Analysis of Internally Reflected Infrared Radiation: Hydrogen on Silicon. The Journal of Chemical Physics, 38(12), 2942–2945, (1963).

[31] H. Ibach and J. E. Rowe. Interaction of atomic hydrogen with the Si(100)2x1 surface. Surf. Sci. 43, 481 (1974).

[32] Hamann, D. Theoretical studies of the electronic structure of semiconductor surfaces. Surface Science, 68, 167–177, (1977).

[33] Sakurai, T., Pandey, K. C., & Hagstrum, H. D. Chemisorption of atomic hydrogen on the silicon (110) 5 x 1 surface (UPS and LEED). Physics Letters A, 56(3), 204–206, (1976).

[34] Pandey, K. C. Realistic tight-binding model for chemisorption: H on Si and Ge (111). Physical Review B, 14(4), 1557–1570, (1976).

[35] Hattori, T., Yamada, M., & Komori, F. STM observation of the chemical reaction of atomic hydrogen on the N-adsorbed Cu(001) surface. Surface Science, 655, 1–6, (2017).

[36] Zheng, M., Li, Y., Ding, K., Zhang, Y., Chen, W., & Lin, W. Nitrogen fixation on metal-free SiC(111) polar surfaces. Journal of Materials Chemistry A, 8(15), 7412–7421, (2020).

[37] CasaXPS version 2.3.18 Ltd., Teignmouth, UK. www.casaxps.com

[38] Björkqvist, M.; Göthelid, M.; Grehk, T. M.; Karlsson, U. O. NH3 on Si(111)-7x7: Dissociation and surface reactions. Phys. Rev. B. 57, 2327–2333, (1998).

[39] Bischoff, J. L.; Lutz, F.; Bolmont, D.; Kubler, L. Use of Multilayer Techniques for XPS Identification of Various Nitrogen Environments in the Si/NH3 System. Surf. Sci. 251 252 (C), 170–174, (1991).

[40] Kim, J. W.; Yeom, H. W. Surface and Interface Structures of Epitaxial Silicon Nitride on Si(111). Phys. Rev. B - Condens. Matter Mater. Phys. 67 (3), 1–5, (2003).

[41] J. M. Soler, E. Artacho, J. D. Gale, A. García, J. Junquera, P. Ordejón, D. Sánchez-Portal, J. Phys. Condens. Matter, 14, 2745-2779, (2002).

[42] E. F. Pettersen, T. D. Goddard, C. C. Huang, G. S. Couch, D. M. Greenblatt, E. C. Meng, T. E. Ferrin, *J.* Comput. Chem. 25, 1605-1612,(2004).

[43] S. Grimme, J. Comput. Chem. *27*, 1787-1799, (2006)

[44] Zeinalipour-Yazdi, C. D.; Hargreaves, J. S. J.; Laassiri, S.; Catlow, C. R. A. A Comparative Analysis of the Mechanisms of Ammonia Synthesis on Various Catalysts Using Density Functional Theory. R. Soc. Open Sci. 8 (11), 210952, (2021).

Chapter IV: Toward Conformational Identification of Molecules in 2D and 3D Self-Assemblies

On-surface self-assembly as a spontaneous association of nanoscale units from a disorder-to-order process has emerged as the bottom-up construction of nanostructures based on molecular building blocks adsorbed on a surface with planned functions in nanoscience and nanotechnology. This approach has seen successful development over the three past decades. [1-4] Organic molecules are potentially the most thoroughly researched nanoscale objects as building blocks for two-dimensional (2D) self-assembled structures. The discovery that organic molecules may interact with each other in specific ways to condense into well-ordered structures held together by non-covalent interactions gave rise to a completely new area of chemistry known as supramolecular chemistry[5]. Given the fact that electron delocalization can occur when molecules are π-stacked [6,7]. Thus, the amplitude of the bandgap may be maintained in a controllable manner. Typically, the self-assembly process mainly relies on noncovalent interactions such as hydrogen bonding,[8–9] halogen bonding,[10–12] van der Waals interaction,[13-15] π–π interaction, [16–18] electrostatic interaction[19-21] and metal-ligand coordination[22-24]. Understanding the topography and the multiple molecular interactions allows the controlled formation of hierarchical assemblies and thus their unique functionalities, especially for molecular electronics, surface functionalization, crystal engineering, and catalysis.

However, one of the significant remaining challenges in this research field is the transition from two-dimensional (2D) to three-dimensional (3D) nanostructures[25,26]. Such a shift holds the potential to enable numerous organic-based devices in electronics, optoelectronics, or spintronics. Despite notable progress, the mastery of 3D self-organization remains incomplete, this might be due to a considerably more sophisticated process behind these structural formations, as well as the difficulty of regulating the method and effectively reproducing the subsequent consequences. Achieving this critical goal requires two primary challenges: i) controlling molecule-molecule interaction out-of-the-plane of the underlying surface and ii) developing accurate analytical tools capable of non-invasively probing through the thickness of materials at the nanoscale. The investigation of molecule-molecule interactions beyond the surface plane is being explored through the use of 3D molecular blocks[27-29] or controlled growth of multilayers composed of planar molecules[30-32].

Yet, these 3D structures often retain surface-like characteristics, extending only to a limited depth, generally bi- or a three-layer thickness. The restriction in 3D extension primarily stems from an incomplete understanding of growth mechanisms transitioning from 2D to 3D, particularly under ambient conditions. Regarding analytical tool development, several prominent surface characterization techniques such as Scanning Tunneling Microscopy (STM) or Atomic Force Microscopy (AFM), offer new insights into on-surface self-assembly. Both are nondestructive analytical instruments. 3D supramolecular structures may arise in solution, on a solid surface, or at an interface, AFM is frequently used to investigate these morphologies. Unlike STM, AFM provides for a larger-scale vision for molecular aggregates, but it does not achieve high resolution in general until combined with an ultrahigh vacuum (UHV) and tip modification [33,34]. STM, on the other hand, is the favored instrument for exploring these organizations at the atomic or submolecular level due to its high-space resolution capability [35-37]. It can be done in both UHV and ambient environments. Aside from the more detailed information on a molecular structure that can be obtained, STM has an integrated function, scanning tunneling spectroscopy (STS)[38,39]. This can give a critical range for the research of semiconductor organic materials. On the other hand, these methods possess limited chemical sensitivity and are largely constrained to investigation within the surface plane. These experimental constraints hinder their development and broad adoption across various communities, thereby reducing the overall impact of on-surface 3D self-assembly. Polarization modulation-infrared reflection-adsorption

spectroscopy (PMIRRAS) stands out as a valuable tool for characterizing thin films or monolayers adsorbed onto metal surfaces due to its high surface sensitivity[40].

Nonetheless, while PM-IRRAS provides insight into the conformational organization of molecules in a monolayer, it lacks the high spatial resolution of scanning probe microscopies. In response, infrared (IR) and Raman nanospectroscopy, coupled with AFM, have undergone significant enhancement in the past decade[41,42]. Tip-Enhanced Raman Spectroscopy (TERS)[43] combines AFM and visible light for nanoscale Raman spectroscopy, but it relies on the tip properties and is challenging to implement. AFM-IR, in contrast, aims to combine AFM's high spatial resolution with IR spectroscopy's chemical identification capabilities[44-46]. Additionally, AFM-IR can probe layers in depth, making it a promising tool for studying 3D self-assemblies on surfaces. However, it's worth noting that in the literature, there are only reports of AFM-IR studies conducted on few-layered samples, specifically those with a thickness of a few nanometers[47-49]. Investigating monolayers remains a significant challenge but is possible here due to the specifications of our AFM setup. Nevertheless, AFM-IR's lateral resolution currently hinders the determination of supramolecular assembly patterns if their periodicity is smaller than 25 nm[47].

To address this, we have developed an effective approach combining STM under ultra-high vacuum, AFM, and AFM-IR under ambient conditions. This approach enables the exploration of supramolecular self-assembly resulting from the deposition of precisely designed molecules on a Highly Ordered Pyrolytic Graphite (HOPG) surface. We aim to definitively address the question: "How can we determine the conformation of molecules within a 2D monolayer or a 3D multilayered supramolecular network adsorbed onto a surface?" This approach not only identifies the adsorption model of molecules on the HOPG surface and the entire 2D supramolecular organization within the surface plane but also delves into the 3D organization of multilayered supramolecular assemblies by deeply investigation the IR fingerprint of the molecules. This method holds general applicability and has the potential to significantly enhance our understanding of molecular conformation during self-assembly on surfaces.

In this chapter, we report the use of a non-planar guest molecule called EsterOC18 onto Highly Oriented Pyrolytic Graphite (HOPG) surfaces. The deposition of Ester-OC18 is achieved through two distinct methods, namely spin coating and dip coating methods in ambient conditions. Following this deposition, we initiate a demanding characterization procedure in which we apply advanced techniques to uncover the structural complexities of the molecular assembly.
Our research involves Variable Temperature Scanning Tunneling Microscopy (VT-STM) in an ultra-high vacuum environment, the use of VT-STM allows us to examine the organization of the assembly at the atomic resolution level. Simultaneously, Atomic Force Microscopy (AFM) is used to analyze the surface topography and structure of the molecular layers under typical laboratory settings. The study we are conducting aims to criticize how molecular assemblies change from two-dimensional (2D) monolayers to three-dimensional (3D) bilayers and multilayers. To dive deeper into the molecular composition and structural intricacies of the deposited layers, we employ the Atomic Force Microscopy-Based Infrared Spectroscopy technique in order to gain more insights into the chemical groups and their spatial arrangement within the deposited molecular assembly.

IV.1 Material and Methods of Depositions:

In this section, we will present the molecular guest that has been selected for our study, along with detailed information regarding its size, shape, and functional groups. In the subsequent section, we will shed light on the deposition methods employed for our experiments and the surface to which these methods were applied.

IV.1.1 Molecule EsterOC18:

Herein we present the molecule EsterOC18 investigated all along this chapter. The structural model of Figure IV.1 shows the optimized geometry of the molecule isolated as well as its specific dimensions. Our molecular design incorporates two crucial components:(i) a carbonyl functional group serving as an IR tag and (ii) C18 alkyl chains to facilitate the formation of 2D or 3D extended supramolecular network on a HOPG surface guided by the subtle balance of molecule-surface and molecule-molecule interactions. We synthesized an ester derivative (octadecyl 4'-octadecyloxy-4-biphenylcarboxyloate, EsterC18, Figure IV.1a), based on a biphenyl core surrounded by two n-octadecyl chains, one linked to the aromatic core through an ester function. The side chain length of the EsterOC18 molecule measures 5.12 nm (Figure IV.1).

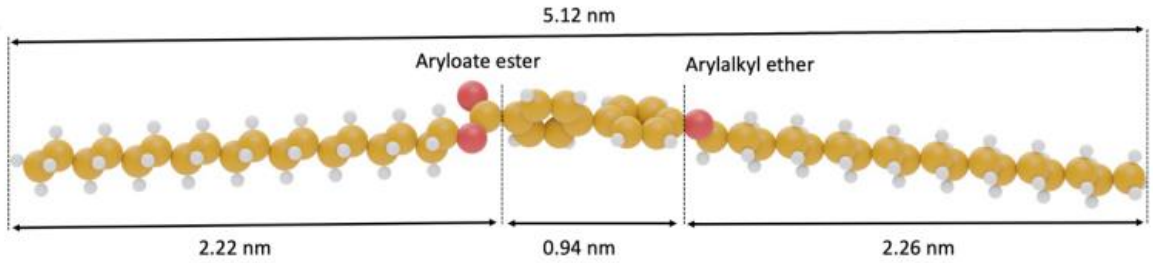

Figure IV.1: Structural model of octadecyl 4'-octadecyloxy-4-biphenylcarboxyloate (EsterC18) Oxygen atoms: red, Carbon atoms: yellow, Hydrogen Atoms: grey.

Regarding the synthesis of the molecule, all reagents were purchased from TCI and used as received. The deuterated NMR solvents were purchased from Euriso-top. The NMR spectra were recorded using a Bruker AC-300 MHz spectrometer. FT-IR spectrum was recorded using Spectrum Two FT-IR spectrometer from PerkinElmer (ATR, transmission, and absorption).

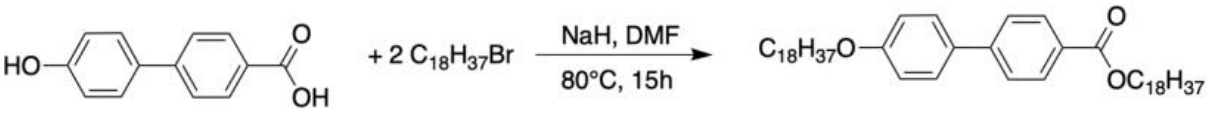

4'-hydroxy-4-biphenylcarboxylic acid (1g, 42mmol) was dissolved in dimethylformamide (10mL) at room temperature. Then NaH (112mg, 42mmol) was added. Then 1- bromooctadecane was added (6.22g, 168mmol, in 40mL of dimethylformamide solution) was added for 30 minutes. The mixture is heated at 80° for 15h. The grey solid is filtered and washed three times with 50 mL of water. The pure octadecyl 4'-octadecyloxy-4- biphenylcarboxyloate is obtained as a white solid (Yield: 65%). 1 H RMN (300 MHz, CDCl3) δ = 8.07 (d, J=8.2, 4H), 7.61 (d, J=8.2, 4H), 7.55 (d, J=8.2, 4H), 6.98 (d, J=8.2, 4H), 4.32 (t, J=6,4, 2H), 4.00 (t, J=6,4, 2H), 1.79 (h, J=6.4, 4H), 1.26 (m, 60H), 0.88 (t, J=6.4, 6H). 13C RMN (75 MHz, CDCl3) δ = 166.69, 159.42, 145.19, 132.22, 130.06, 128.31, 126.41, 114.93, 68.16, 65.11, 31.94, 29.71, 29.67, 29.61, 29.56, 29.41, 29.38, 29.32, 29.27, 28.77, 26.08, 26.06, 22.70

IV.1.2 Used Surface:

The selection of Highly Oriented Pyrolytic Graphite (HOPG) as a model for an air-stable crystalline conductive surface for creating extended 2D supramolecular networks has already been demonstrated [50]. The used HOPG surface (Figure IV.1.a) purchased from Bruker Company was as the substrate for the self-assembled molecular network studied by Atomic Force Microscopy in ambient conditions and STM under ultrahigh vacuum conditions. The surface exhibits a high degree of crystallinity, which consists of closely packed hexagonal arrays of carbon atoms. The layers stack on top of each other, with weak van der Waals forces holding them together, allowing for easy cleavage along the basal plane. Figure IV.2b shows the high atomic resolution of a clean HOPG surface before any deposition of molecules after cleavage of the first layers.

a) b)

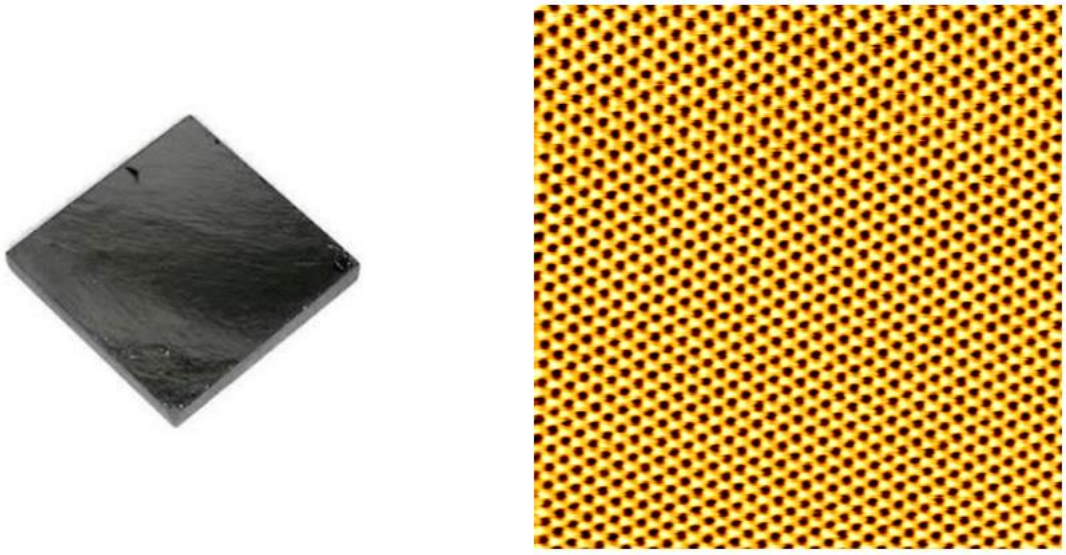

Figure IV.2: a) HOPG substrates are purchased from Bruker Company (12x12 mm^2, 2mm thick). b) High atomic resolution STM image of HOPG surface scanned at RT by VT-STM under ultra-high vacuum conditions (V_s = 0.6 V, I_t = 800 pA, 9 x 9 nm^2)

IV.1.3 Used Deposition Methods:

The utilized deposition methods were to obtain the perfect samples of monolayers, bilayers, and multilayers by immersion and spin coating under ambient conditions after preparing proper solutions for the deposition considering the molar mass of the molecule to have the best-concentrated solutions. Spin coating is a widely used technique in the deposition of organic molecules on substrates. Meanwhile, micropipettes (Figure IV.3a) play a crucial role in having precise small volumes of organic molecule solutions on the substrate. It's designed to enable researchers to deposit organic molecule solutions in microliter or even in nanoliter volumes.

a) b)

Figure IV.3: a) Micropipette used in the spin coating method for the deposition of the organic solutions on substrates b) Image taken to show the immersing of the sample in the solution in the dip coating method.

On the other hand, the second used method for organic molecules deposition is the immersion process. This technique of deposition involves immersing the substrate in a solution containing the organic molecules, the composition of the solution is well formulated with a solvent chosen to be suitable for both organic molecules and the substrate surface. During the immersion of the substrate, the solution adheres to the surface of the substrate. The substrate is then slowly withdrawn from the bottom of the solvent and begins to evaporate from the surface leading to the formation of a self-assembled network on the surface. Many factors such as solution concentration, withdrawal speed, and the rate of solvent evaporation play a significant role in the deposition uniformity.

IV.2 AFM and STM experimental results:

In this section, we commence by outlining the development of two-dimensional(2D) supramolecular networks of EsterOC18 over the HOPG surface. Following this, we go on to the creation of three-dimensional (3D) structures, including bilayers and multilayers, all of which are systematically described using Atomic Force Microscopy (AFM) methods under typical ambient circumstances. The following section of this study will dive into a deeper evaluation of the 2D network, utilizing Scanning Tunneling Microscopy (STM) under ultra-high vacuum, an approach that allows us to achieve atomic-level resolution.

IV.2.1 Networks Characterization with AFM at Ambient Conditions:

The basic purpose of this subsection was devoted to the development of a two-dimensional self-assembled network of EsterOC18 and following that the formation of three-dimensional networks, specifically bilayers and multilayers. These structural arrangements were symmetrically investigated and characterized utilizing atomic force microscopy under ambient conditions. This experimental technique enabled a thorough analysis of the surface morphologies and molecular structures, revealing information on the complex interplay of molecular interactions driving EsterOC18 assembly on the substrate. Therefore, we prepared a set of solutions of EsterOC18 molecules in dichloromethane at a molar concentration range between 10^{-3} mol L^{-1} until 10^{-7} mol L^{-1}. We started our experiments using the dip coating method, immersing the HOPG substrate in 5mL solutions of four different concentrations which are the following 10^{-6} mol. L^{-1}, 5 x 10^{-6} mol. L^{-1}, 7 x 10^{-6} mol. L^{-1}, and 10^{-5} mol L^{-1} for a fixed duration of 30 minutes, followed by the sample withdrawal from the solution. After dip coating, each sample was thoroughly dried at 80° C for 30 minutes in the VO Memmert Heater to

evaporate dichloromethane from the substrate. The initial phase of our experiments, involving four distinct dip-coating processes, yielded remarkable outcomes. These processes led to the formation of extended and compact domains, each exhibiting varying degrees of network coverage. The experimental imaging was performed at ambient conditions and monitored by AFM with Peak Force Mode by Bruker Icon using a super sharp probe (SSB) tip.

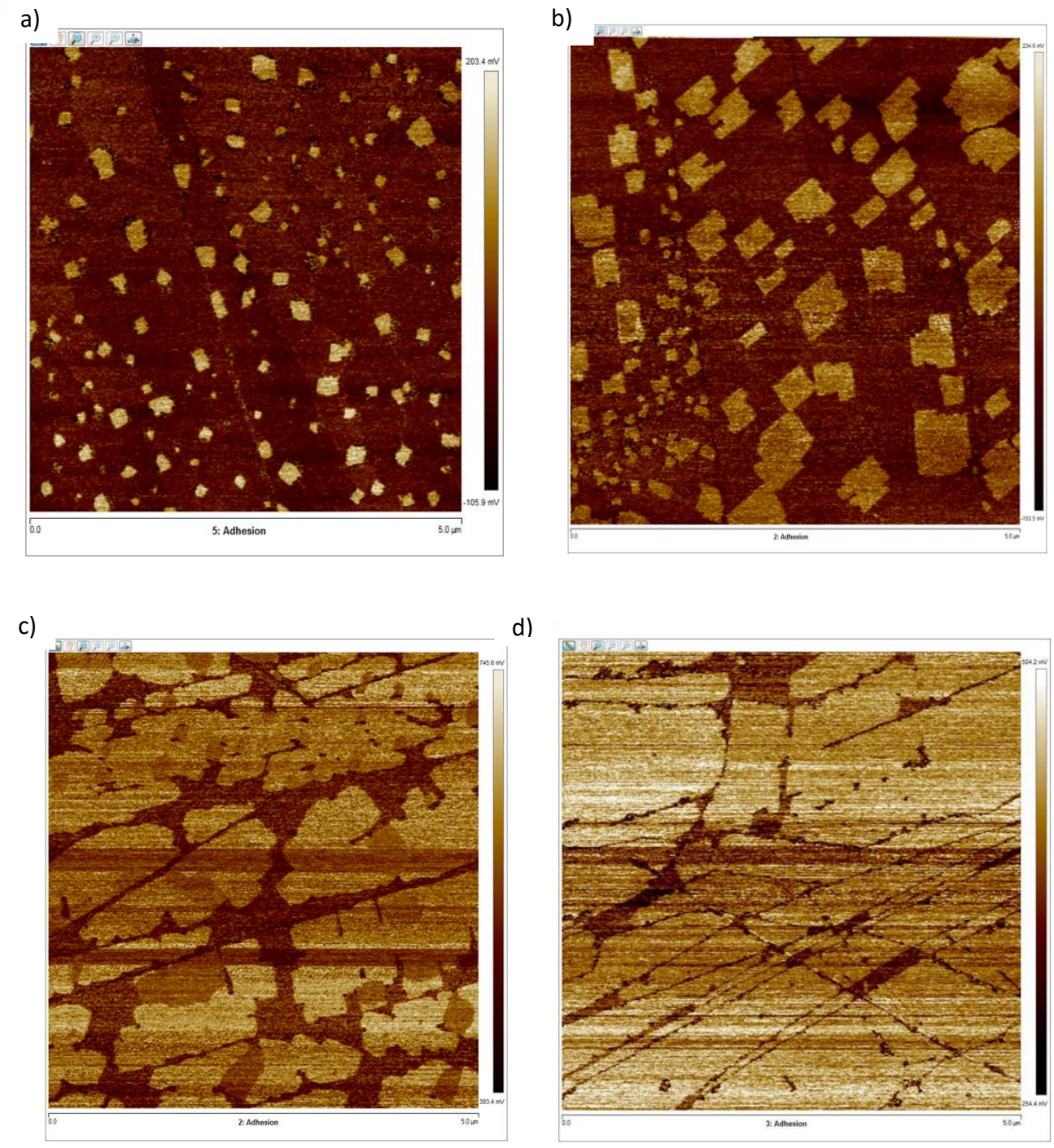

Figure IV.4: AFM adhesion large-scale images (5×5 µm²) for distinct depositions of Ester-OC18 with a fixed deposition duration of 30 minutes a) 10^{-6} mol. L^{-1}, b) 5 x 10^{-6} mol. L^{-1}, c) 7 x 10^{-6} mol. L^{-1}, and d) 10^{-5} mol L^{-1}.

Deposition Concentrations (mol L^{-1})	10^{-6}	5 x 10^{-6}	7 x 10^{-6}	10^{-5}
Percentage %	10	24	70	90

Figure IV.5: Table presenting the statistical values of the network coverage over the surface with different used concentrations with fixed deposition duration for 30 minutes.

The distinctions in network coverage were attributed to the different concentrations of the solutions employed in the dip coating procedures. Figure IV.4 represents the adhesion AFM images of the four EsterOC18 dip-coating depositions, we can clearly recognize two prominent features that are evident, highlighting the contrasting nature of the surface and network. Narrowing toward these zones and conducting high-resolution small-scale scan images, we were able to distinguish between the surface and the network, noticing that the yellow regions correspond to the EsterOC18 network located on the surface. The HOPG surface appears notably smoother, characterized by a relatively uniform adhesion force profile, indicative of a consistent topographic plane. In contrast, the network exhibits a distinctive pattern of raised features and depressions, a mesh-like structure. Referring to Figure IV.4, it becomes evident that the network's coverage percentages across the surface do not follow a linear trend. After conducting multiple approaches on each sample (a minimum of three approaches per sample), we computed the network coverage percentages. These percentages exhibited a variation in response concerning different used solutions concentrations, with an approximate 45% disparity between the deposition at 5 x 10^{-6} mol L^{-1} and 7 x 10^{-6} mol L^{-1}, favoring the latter concentration all represented in Figure IV.5. Using this data, the curve representing the network coverage in the function of the depositions concentrations was plotted, as shown in Figure IV.6

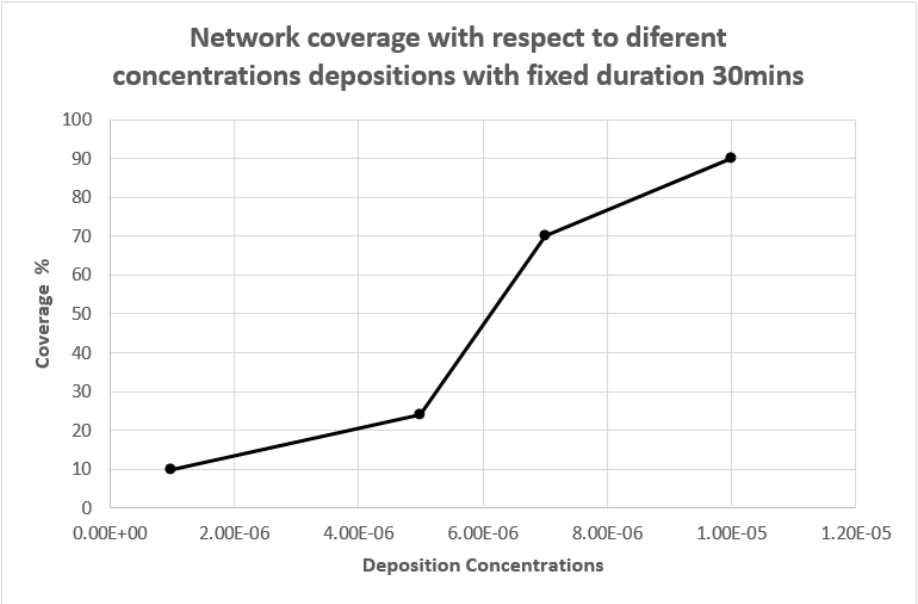

Figure IV.6: Graph representing the network coverage percentage on HOPG with respect to the distinct concentrations of the solutions at fixed deposition duration for 30 minutes.

After the dip coating process, we conducted experiments using the spin coating deposition technique to create single layers (monolayers), double layers (bilayers), and multiple layers of EsterOC18 on a Highly Oriented Pyrolytic Graphite (HOPG) surface. Deposition of 20 µl of EsterOC18 solution with a

concentration of $5 \cdot 10^{-5}$ mol·L^{-1} was deposited onto the HOPG surface and the spin coating was carried out for 20 seconds with an angular velocity of 300 rpm. After spin coating, the sample was thoroughly dried at 80° C for 30 minutes in a vacuum oven Memmert Heater in order to evaporate dichloromethane from the substrate. A large-scale topography AFM (5×5 μm^2) of less than a monolayer of EsterOC18 molecules on a HOPG surface as shown in Figure IV.7.a. The thickness of the two-dimensional domains was evaluated by analyzing the AFM topography of a HOPG surface coated with a sub-monolayer of Ester-OC18 molecules, resulting in a thickness of 0.8 ± 0.05 nm, as depicted in graph IV.7 b.

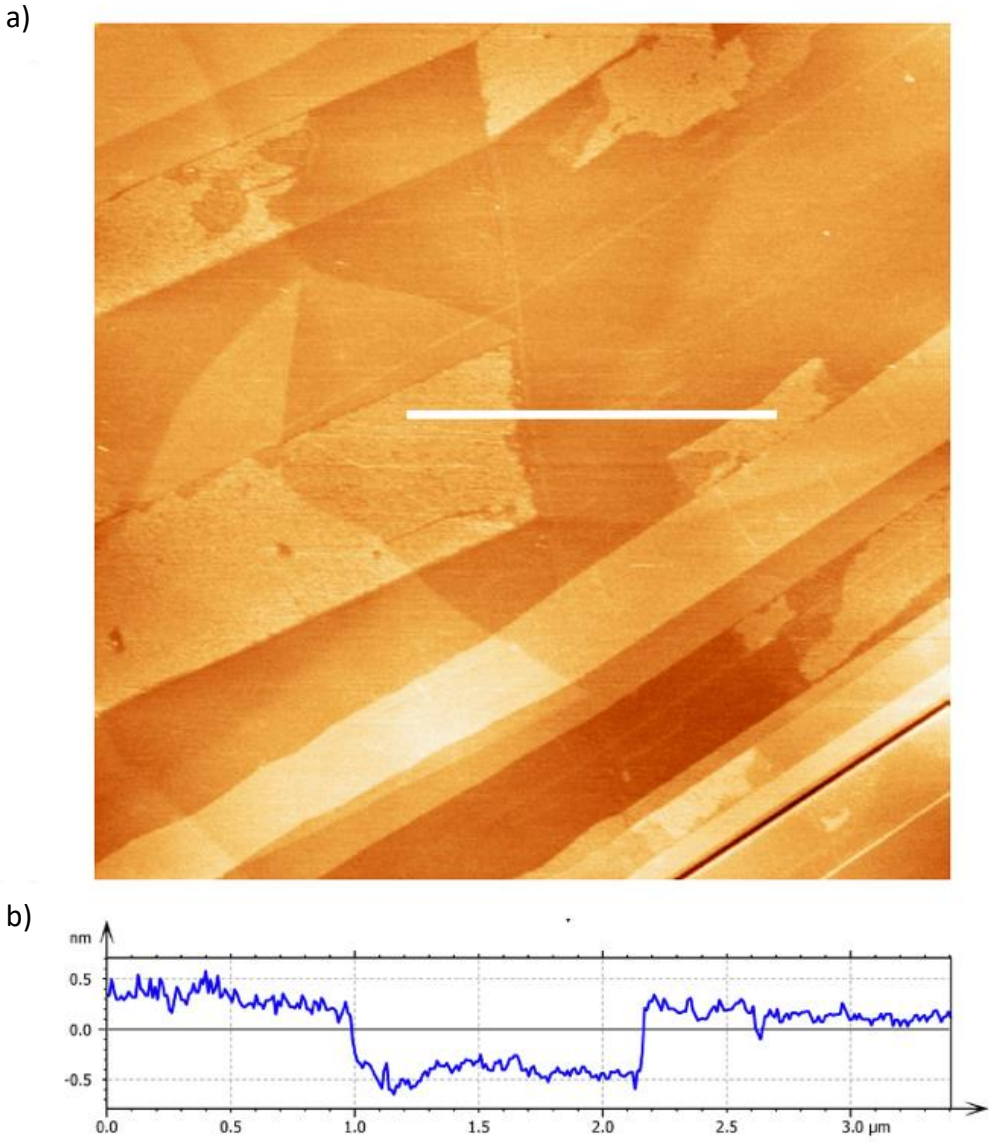

Figure IV.7: a) Topography AFM (5×5 μm^2) of a monolayer of EsterOC18 molecules on a HOPG surface. b) Z-profile taken along the white line of a) highlighting the monolayer's thickness of 0.8 ± 0.05 nm.

Upon closer examination, we conducted a detailed investigation into the supramolecular self-assembly of EsterOC18 molecules, employing high-resolution Atomic Force Microscopy (AFM) to capture a topographical image covering an area of 65x65 nm^2, as depicted in Figure IV.8a. These two-dimensional domains exhibited organized patterns, consisting of well-arranged bright stripes that were separated by darker stripes. Mainly, these stripes exhibited a consistent periodicity, with the distance between

the bright lines measuring at a constant value of 5.60 ± 0.1 nm. This detailed zoomed inspection suggests that the EsterOC18 molecules possess a striking ability to self-assemble into a highly ordered and structured configuration on the substrate's surface. The periodicity of these domains is a key finding, indicating a regularity in the arrangement of the molecule's structure. Figure IV.8.b shows the z-profile of the marked set of stripes by the white line in Figure IV.8.a.

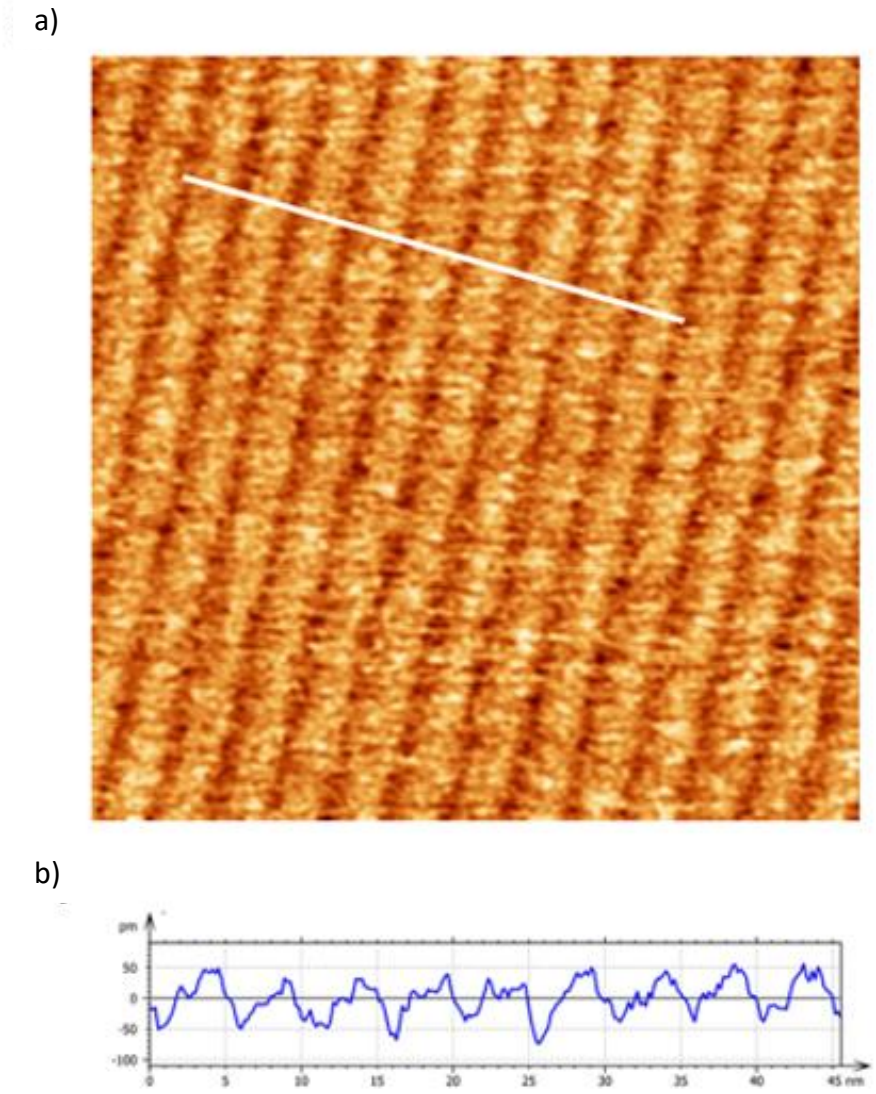

Figure IV.8: a) Topography AFM (65×65 nm^2) of a monolayer of Ester-OC18 molecules on a HOPG surface. b) Z-profile taken along the white line.

Shifting from two-dimensional supramolecular self-assemblies (monolayer) to three-dimensional (bilayer and multilayer), we needed to use higher concentrations of Ester-OC18. For this purpose, a sample was prepared with the deposition of 20 µl of Ester-OC18 solution with a concentration of 10^{-3} mol L^{-1} onto the HOPG surface, and the spin coating was carried out for 20 seconds with an angular velocity of 300 rpm. After spin coating, the sample was thoroughly dried at 80° C for 30 minutes in a vacuum oven Memmert Heater in order to evaporate dichloromethane from the substrate. Figure IV.8a shows a topography AFM image (2×2 μm^2) recorded after the deposition of a concentrated solution of Ester-OC18 molecules by spin coating on a HOPG surface. This process led to the formation of substantial, densely packed islands, as depicted in Figure IV.9.a. The thickness of these islands varies

from 0.7 to 6 nm (Figure IV.9.b). Upon deeper examination of the topography AFM images, it becomes evident that the 3D compact islands are still constituted by alternating bright and dark lines, with the previously observed periodicity of 5.60 ± 0.1 nm, irrespective of their thickness, as shown in Figure IV.9.d. This extensive examination highlights the persistence of a structured and orderly arrangement of Ester-OC18 molecules even in three-dimensional assemblies, and the consistent periodicity reveals a remarkable level of regularity in molecular organization.

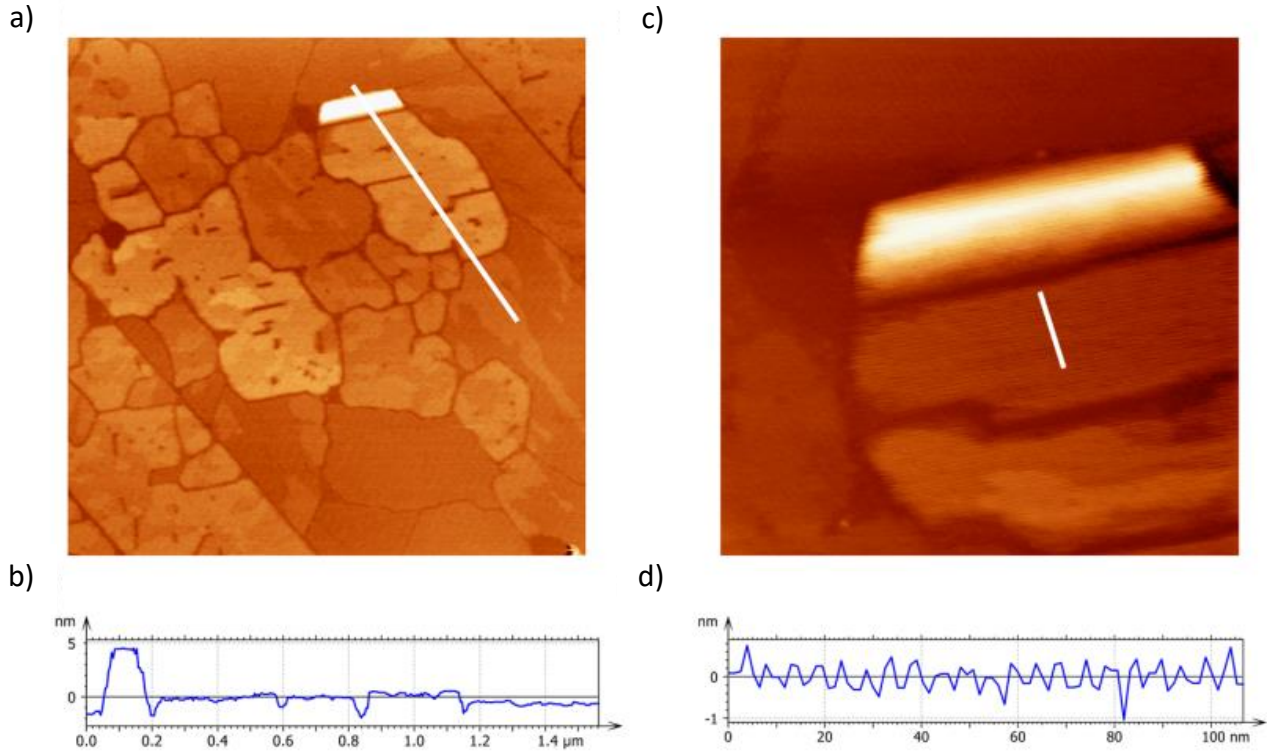

Figure IV.9: a) Large-scale (2×2 µm^2) topography AFM of multilayers of Ester-OC18 molecules deposited on a HOPG surface. b) Z-profile has taken along the white line showing the formation of islands with different apparent heights. c) Zoom (600×600 nm^2) over multilayered islands d) Z-profile taken along the white line of c).

IV.2.2 Networks Characterization with STM Under Ultra-high Vacuum:

Following the initial process of characterizing the deposition of EsterOC18 onto a substrate made of Highly Oriented Pyrolytic Graphite (HOPG) using Atomic Force Microscopy (AFM) in atmospheric conditions, the subsequent phase involved the characterization of the molecular network utilizing a Scanning Tunneling Microscope (VT-STM) under ultra-high vacuum conditions. This experimental approach was accustomed to yield resolutions at an atomic scale, providing a detailed view of the molecular network's structure and composition. Using the same substrate characterized in AFM for a monolayer, a deposition of 20 µl of EsterOC18 solution with a concentration of $5 \cdot 10^{-5}$ mol·L^{-1} was deposited onto the HOPG surface and the spin coating was carried out for 20 seconds with an angular velocity of 300 rpm. After spin coating, the sample was thoroughly dried at 80° C for 30 minutes in a vacuum oven Memmert Heater in order to evaporate dichloromethane from the substrate. Subsequently, the resulting substrate was introduced to UHV. After treating the tungsten tip over the Silicon Boron surface for both polarities releasing all the contaminants that can present on the tip apex effectively, we proceeded to scan the HOPG surface with EsterOC18 deposition on the STM head. Scanning the positive polarity over the monolayer, focusing on the network the only obtained resolution is a well-defined compact periodic network constituted by bright lines separated by darker stripes as shown in Figure IV.10.a. The extracted periodicity between the bright lines is 5.60 nm as

calculated by Z-profile along the white line highlighted in Figure IV.10.a. It is notable to mention that measured periodicities possess a statistical error of ± 0.1 nm which is calculated as a difference among measured periodicities on the recorded STM images.

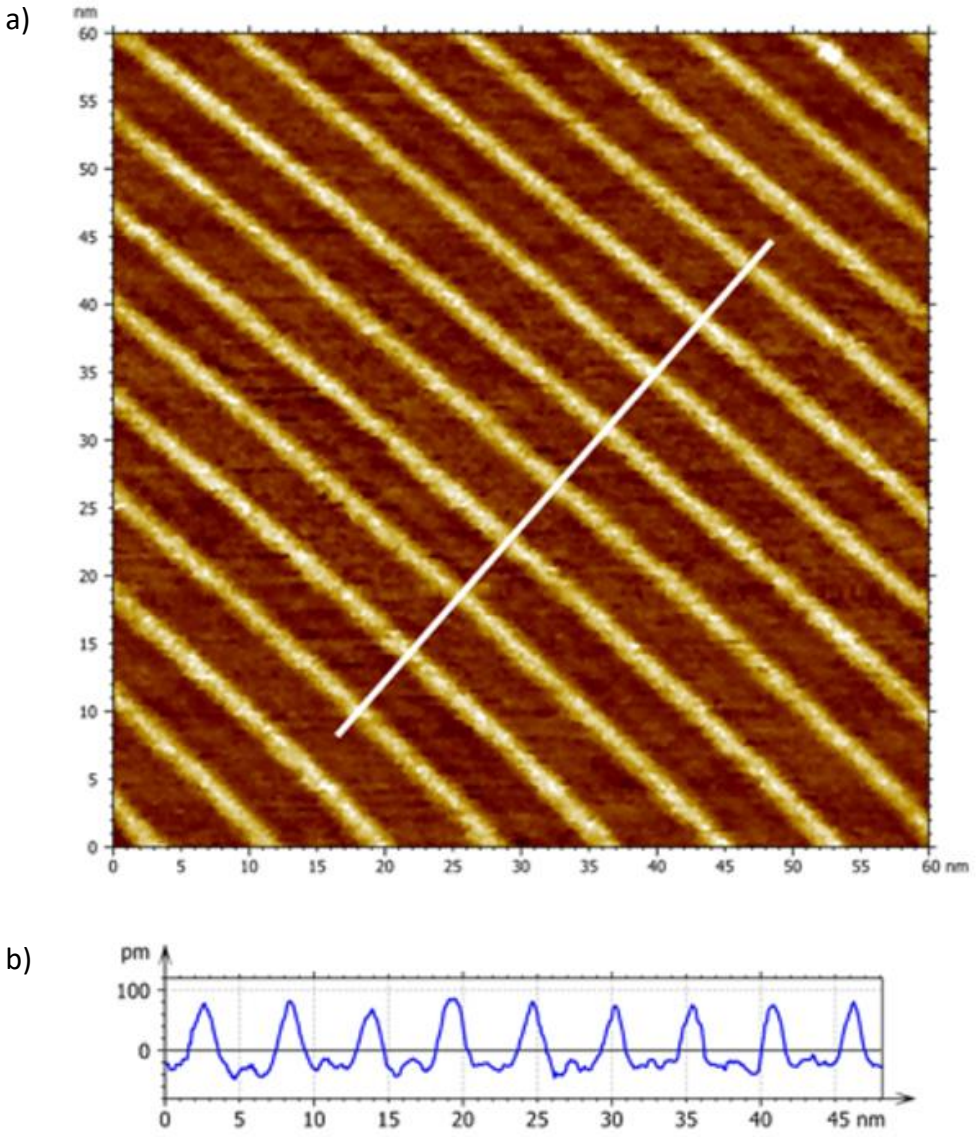

Figure IV.10: a) STM image (60×60 nm^2, V_s = 1.3 V, I_t = 20 pA, T = RT) of a monolayer of EsterOC18 molecules on a HOPG surface. b) Z-profile taken along the white line of a) highlighting the periodicity of 5.60 nm between two lines.

For the same sample but shifting the scanning to the negative polarity, Figure IV.11.b depicts a high-resolution STM image, acquired at room temperature (RT) under ultra-high vacuum (UHV) of the EsterOC18/HOPG interface. Within the STM image, a well-defined compact periodic network constituted by bright lines separated by darker strips is observed. The periodicity between the bright lines is 5.60 ± 0.1 nm. Notably, leveraging the high resolution of STM, we discern that the darker stripes consist of two parallel nanorods, each measuring 2.1± 0.2 nm in length (white double arrows, Figure IV.11.b). These nanorods align within the same row and exhibit a 120° rotation from one dark stripe to the next. Following this, it was taken out of the UHV setup and analyzed again using AFM under ambient conditions. In both STM and AFM images, 2D domains exhibit well-structured bright stripes interspersed with darker stripes, maintaining a consistent distance of 5.60 ± 0.1 nm. Afterward, the sample was removed from the UHV setup and re-examined using AFM in ambient conditions. We

observed the same network with unchanged periodicity, confirming that the networks remain unaffected by the imaging conditions, whether under UHV or ambient conditions.

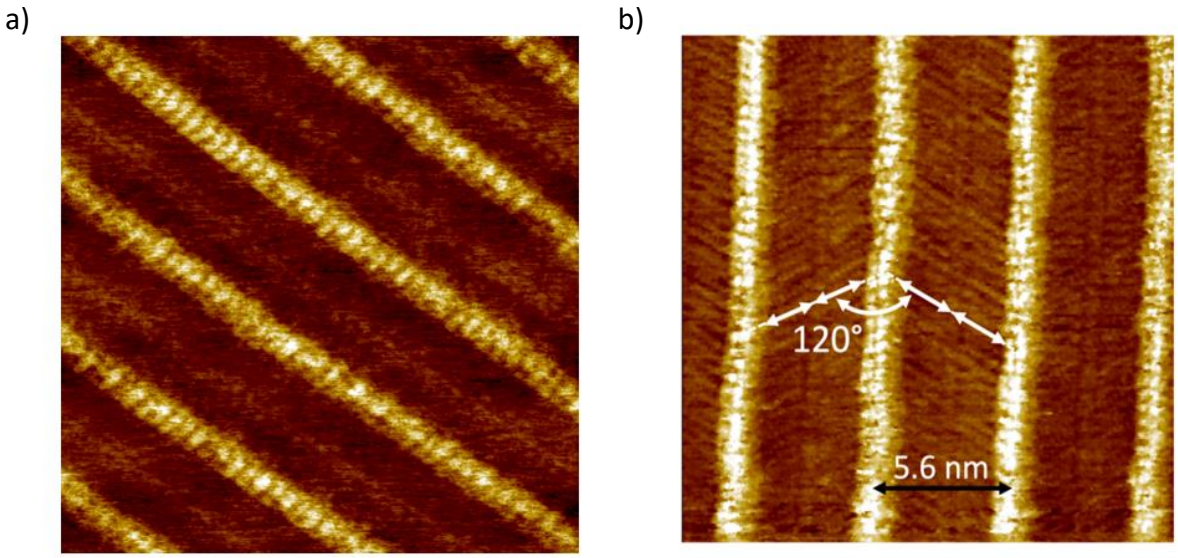

Figure IV.11: a) STM image (20×20 nm^2, V_s = -1 V, I_t = 20 pA, T = RT) of a monolayer of EsterOC18 molecules deposited on a HOPG surface. b) STM image (20×20 nm^2, V_s = -1.3 V, I_t = 20 pA, T = RT) of a monolayer of EsterOC18 molecules deposited on a HOPG surface.

Based on the AFM and STM imaging for the network the initial model that can be attributed to the network monolayer over the HOPG surface is presented in Figure IV.12. The robustness and stability of EsterOC18 networks on the HOPG surface at air conditions and under ultra-high vacuum is mostly attributed to the suitable balance between the large molecule-surface interaction and molecule-molecule interactions (Hydrogen bonds, π-π interactions, etc.). The structure of the Ester-OC18 molecule possesses a π-conjugated "core" constituted of two conjugated phenyl rings, although these two rings are not horizontally adsorbed upon the surface as they possess an "out-of-plane" structure compared to the chains. Therefore, we assume that observed bright stripes on topography AFM and STM images correspond to the "core" of EsterOC18 molecules, while the dark contrast AFM signal on topography images is correlated to the chains, meanwhile, STM high molecular resolution assures that the dark stripes are the chains of the molecules due to the appearance of nanorods align within the same row and exhibit a 120° rotation from one dark stripe to the next, exhibiting the surface structure. This rotational alignment of nanorods signifies a distinctive surface structure, strongly suggesting that the dark stripes indeed represent molecular chains. Indeed, an overview of the reported work of Korolkov et al. describes observed bright AFM contrast in the formation of nanolines attributed to the "core" of π-conjugated segments while darker AFM contrasts are described as alkyl chains, both belonging to the polythiophene polymers.[51]

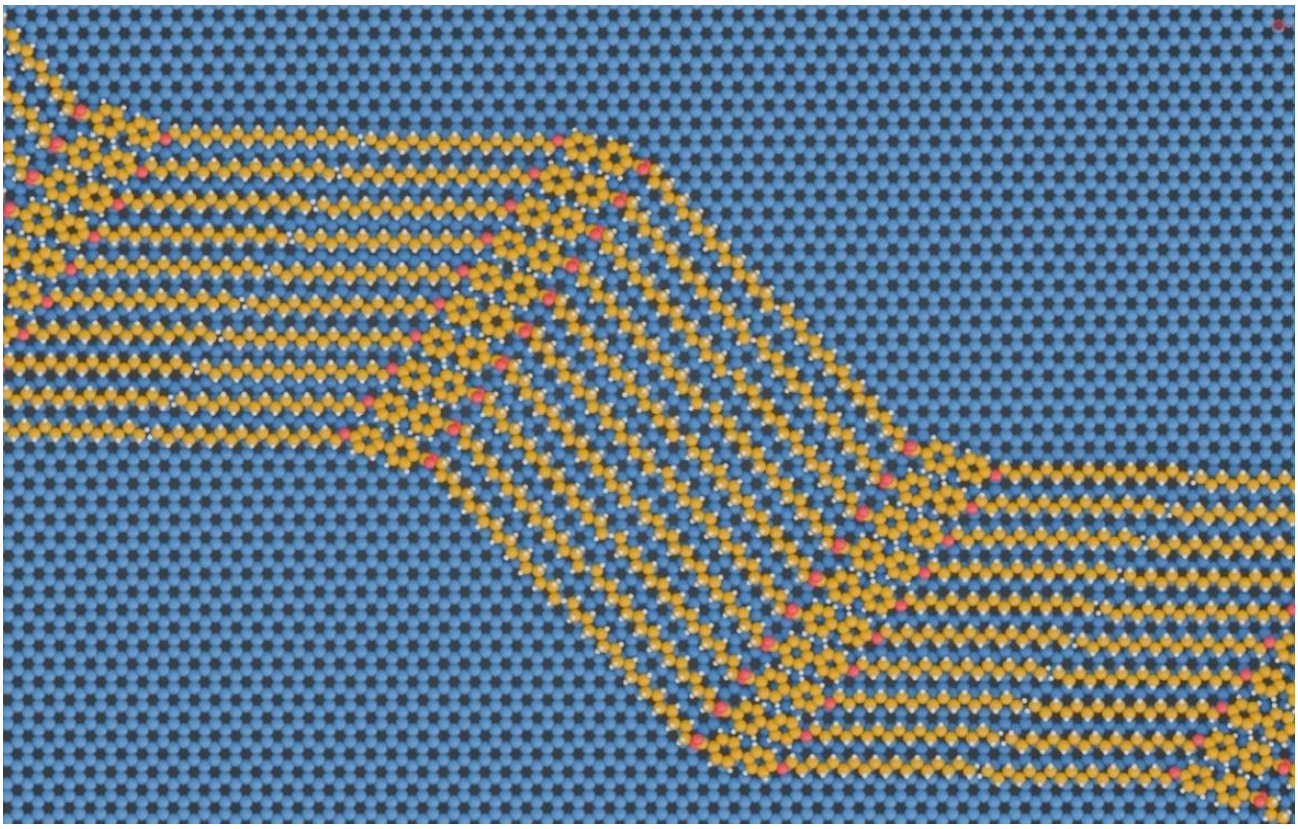

Figure IV.12: A designed initial model of Ester-OC18 over HOPG substrate based on AFM and STM images.

IV.3 AFM-IR Characterization Technique:

This part was done in collaboration with Professor Alexandre Dazzi from Paris-Saclay University, who did all AFM-IR experiments. Therefore, we focus our interest on the information that we can extract from these experiments as support to analyze and understand more the previously observed experimental results. The main objective of our research is to examine the transformation of the molecular arrangement from a two-dimensional configuration to a three-dimensional supramolecular network when these molecules adhere to the surface of HOPG under normal environmental conditions. Our hypothesis revolves around the notion that the molecular structure varies across different layers on account of alterations in the dihedral angle between the carbonyl (C=O) group and the adjacent phenyl ring.

The AFM-IR system was an Icon-IR from Bruker using a multi-chip Quantum Cascade Laser (QCL, Daylight Solutions) covering the mid-IR range from 900 cm^{-1} up to 1900 cm^{-1}. In this study, AFM-IR was used in tapping AFM-IR mode with a gold-coated silicon AFM tip (Nanoandmore PPP-NCHAu-MB-10). The Drive frequency was around 1680 kHz and the IR detection was around 272 kHz. To compensate for the topography or mechanical change, PLL (Phase Loop Lock) has been activated for IR channel detection. The IR mapping acquisitions were made using a 0.3 Hz scan rate with a laser power of around 1-3% with a pulse width of 100 ns. All spectra are recorded after IR maps to select relevant regions of interest considering the chemical distribution. Due to the laser illumination configuration and the gold coating of tips, the polarization of the IR light is mainly perpendicular to the surface of the sample.

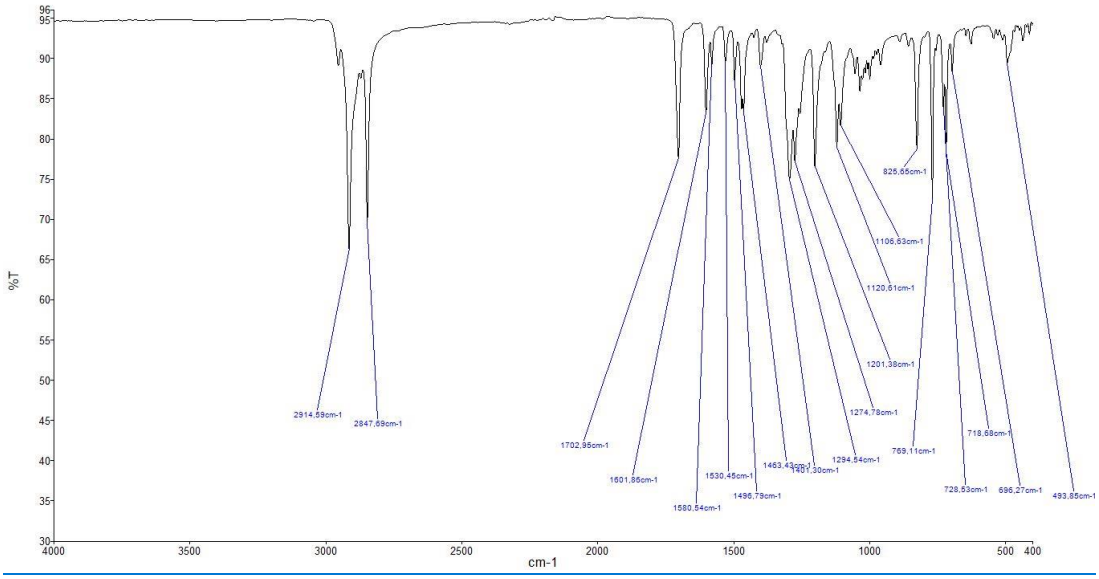

Figure IV.13: FT-IR spectrum of powdered EsterOC18 molecules in their pristine solid state (bulk).

We have conducted a thorough analysis of the Fourier Transform Infrared (FT-IR) spectrum of powdered EsterOC18 molecules in their pristine solid state (bulk) as presented in Figure IV.13. Our focus has been on accurately identifying and examining the significant wavelengths associated with these molecules. The spectroscopic analysis plays a pivotal role in facilitating a thorough investigation of the molecular properties, thereby providing valuable insights into the structure and chemical features of EsterOC18 in its solid-state form. In addition, when compared to data obtained from Atomic Force Microscopy Infrared (AFM-IR) in the following parts of the chapter, this FT-IR analysis acts as a complementary and essential element, enhancing our understanding of the molecular behavior of EsterOC18 and enabling a comprehensive exploration of its distinctive characteristics.

The IR fingerprint of the compact islands, in relation to their thickness, was subsequently investigated through AFM-IR experiments. AFM-IR absorption spectra were recorded on another HOPG substrate, a sample with the deposition of 20 µl of Ester-OC18 solution with a concentration of 10^{-3} mol L^{-1} onto the HOPG surface, and the spin coating was carried out for 20 seconds with an angular velocity of 300 rpm. After spin coating, the sample was thoroughly dried at 80° C for 30 minutes in a vacuum oven Memmert Heater in order to evaporate, dichloromethane from the substrate dichloromethane from the substrate. The existence of 3D compact islands with varying thicknesses (ranging from monolayer to 4 layers) on the substrate was confirmed by obtaining AFM topography images (Figure IV.14.a). Consequently, AFM-IR absorption spectra were captured from compact islands with differing thicknesses. Figure IV.14.b represents AFM-IR absorption spectra recorded for multilayers (red line) and a monolayer (blue line) on the red or blue cross respectively in Figure IV.14.a, while the black dashed line represents the FT-IR spectrum of a pure powder of EsterOC18. Meanwhile, Figure IV.14.c stands for a zoomed range of Figure IV.14.b between 1550cm^{-1} till 1800cm^{-1} belonging to the C=O and C=C bonds stretching region.

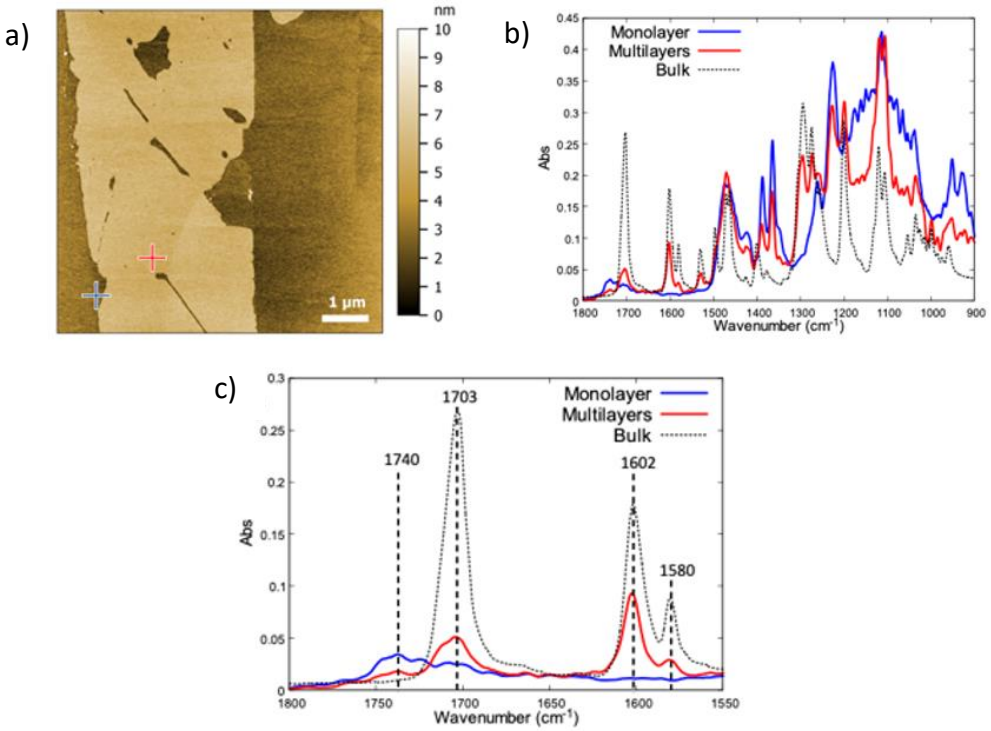

Figure IV.14: a) Large-scale (7×7 µm²) topography AFM of multilayers (thickness of 3 nm) and a monolayer of EsterOC18 on a HOPG surface. b) AFM-IR absorption spectra recorded for multilayers (red line) and a monolayer (blue line) on the red or blue cross of a), respectively. The FT-IR spectrum of a pure powder of EsterOC18 is represented by the black dashed line c) Zoom of b) in the C=O and C=C bonds stretching region (1550-1800 cm^{-1}).

The chemical mapping of the area depicted in Figure IV.14.a was conducted using a quantum cascade laser (QCL) tuned to the fixed wavenumbers 1600 cm^{-1} (Figure IV.15.a), 1700 cm^{-1} (Figure IV.15.b), and 1730 cm^{-1} (Figure IV.15.c). In all instances, the signal intensity is evenly distributed across the surface of the islands with the same thickness, as highlighted by adsorption spectra collected at various points within the multilayered network area (Figure IV.15.a). Specifically, within the chemical mapping at 1600 cm^{-1} corresponding to the C=C bond stretching, the signal is virtually absent (in blue, Figure IV.15.a) in the region attributed to the monolayer. Conversely, a strong signal is detected in the area corresponding to the multilayered network (illustrated in red, Figure IV.15.a). Similarly, for the chemical mapping at the 1700 cm^{-1} band, the highest signal intensity is situated over the multilayer as shown in Figure IV.15.b. Meanwhile the chemical mapping for the band centered at 1730 cm^{-1}, the maximum signal intensity is observed in the monolayer zone as observed in Figure IV.15.c.

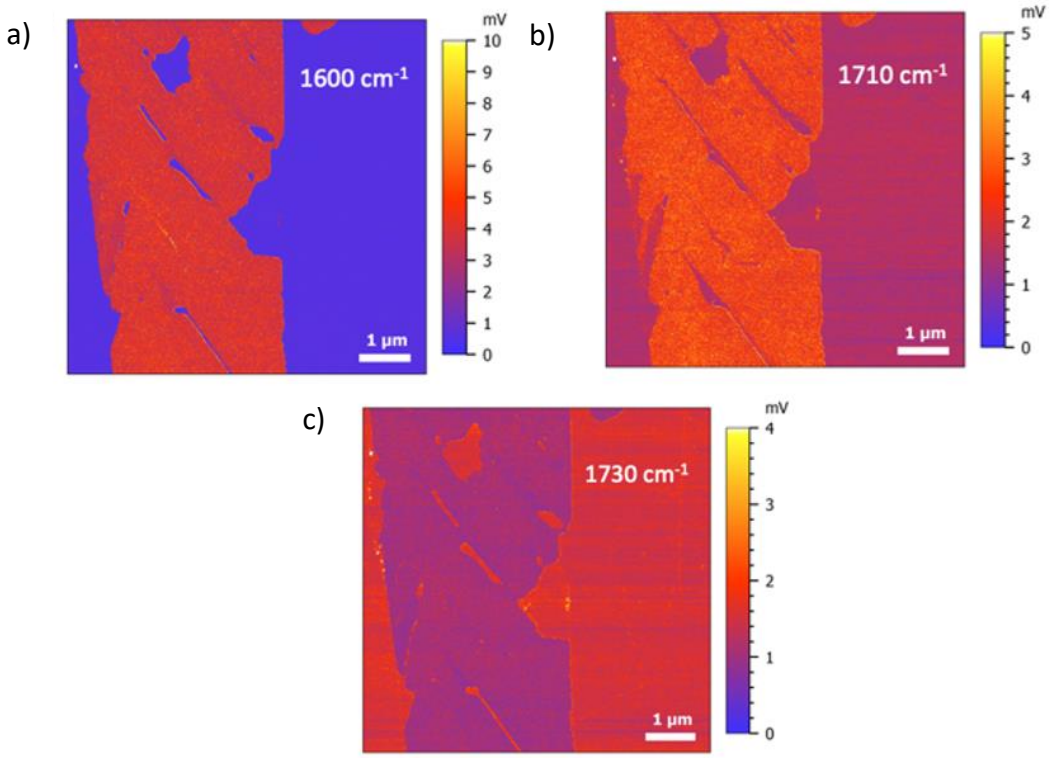

Figure IV.15: AFM-IR mapping corresponding to the topography shown in Figure 3.13a recorded at a)1600 cm^{-1}, b) 1710 cm^{-1} c)1730 cm^{-1}. At 1710 cm^{-1} and at 1600 cm^{-1}, the intensity of the AFM-IR signal is stronger on the multilayers compared to the monolayer, while the case is different at 1730 cm^{-1} the intensity is stronger at the monolayer than the multilayer.

In Figure IV.16.a, a topographic scan using Atomic Force Microscopy (AFM) displays a large-scale surface area measuring 7×7 µm², The surface features both multilayers, with a thickness of 3 nm, and a monolayer of EsterOC18 molecules on HOPG substrate. Three distinct points have been highlighted in red within this figure, representing the chosen locations for recording AFM-IR spectra. Figure IV.16.b showcases the AFM-IR absorption spectra obtained from these three selected points situated within the region covered by the EsterOC18 multilayers.

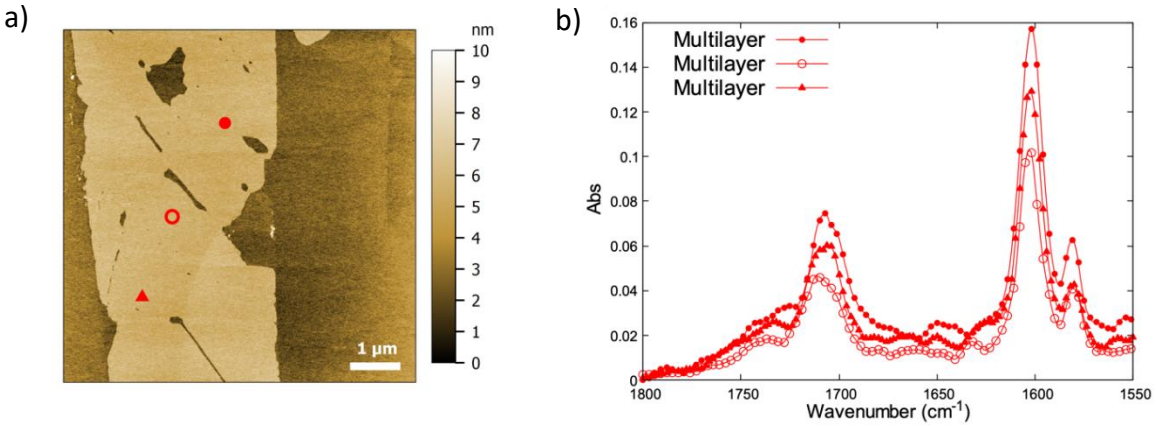

Figure IV.16: A large-scale (7×7 µm²) topography AFM of multilayers (thickness of 3 nm) and a monolayer of EsterOC18 on a HOPG surface. The three points selected for the recording of AFM-IR spectra are highlighted in three red forms. b) AFM-IR absorption spectra recorded on the three different points (highlighted in a) of the area covered by multilayers of EsterOC18 molecules.

IV.4 Results Analysis:

Close examination of STM and AFM images reveals the consistent periodicity exhibited by the supramolecular networks formed after depositing EsterOC18 molecules onto a graphite surface, regardless of whether they take the form of 3D islands or 2D monolayers. Leveraging the high-resolution capabilities of STM images, we were able to observe the spatial arrangement of aliphatic chains surrounding the EsterOC18 molecules, resulting in the development of an adsorption model describing the 2D monolayers. In the monolayer scenario, the experimental periodicity (5.60 ± 0.1 nm) closely matches the length of EsterOC18 molecules (5.12 nm), suggesting the absence of lateral n-octadecyl chain interdigitation, as demonstrated in the STM images (depicted in Figure IV.11.b). Furthermore, since the nanorods are rotated at 120° between adjacent dark stripes (as shown in Figure IV.11.b), we infer that EsterOC18 molecules align along the direction of the HOPG surface, forming a densely packed 2D lamellae of parallel-aligned, straight n-octadecyl chains, aligning with the Groszek model [52]. Importantly, the identical periodicity observed in both 2D and 3D layers enabled us to extend the proposed 2D organizational model to elucidate the arrangement of 3D islands. Furthermore, AFM-IR signatures provide additional insightful details compared to STM and AFM images. Notably, the infrared signature of monolayers displays distinct differences when compared to that of multilayers or bulk solids. This divergence in the IR signatures furnishes essential insights for understanding the unique attributes and characteristics of supramolecular structures in different dimensions. AFM-IR exhibits high sensitivity to the incident polarization of IR light[53,54]. In the used experimental setup, the incident light has an angle of about 30° from the surface and is polarized in the plane of incidence. Considering the gold coating of the tip and this configuration of illumination, they have already demonstrated that the electric field below the tip is dominated by its perpendicular component. [53] Consequently, for functional groups situated in the plane of the underlying HOPG surface, the dipole's cross-section of these functional groups and the incident electric field is nearly zero, causing their IR fingerprint to cancel out. Utilizing this phenomenon, it becomes feasible to determine the relative configuration of functional groups comprising EsterOC18 molecules within supramolecular self-assemblies on an HOPG surface.

In the AFM-IR spectrum of a monolayer, the absence of C=C stretching peaks at 1602 cm^{-1} and 1580 cm^{-1}, present in the bulk, provides substantial evidence that the aromatic rings align parallel to the HOPG surface plane. This observation indicates that the aromatic rings within the monolayer adopt an in-plane orientation concerning the substrate. Notably, within our research framework, we observed a significant phenomenon related to C=O stretching in the EsterOC18 monolayer. The C=O stretching band appears at 1740 cm^{-1}, showcasing a hypsochromic shift of 37 cm^{-1} from the C=O stretching band in the FT-IR spectrum of the pure solid (bulk). This shift holds particular interest, as it signifies the absence of electronic conjugation between the C=O group and the surrounding phenyl ring. These collective findings provide compelling evidence that the C=O bond within the EsterOC18 monolayer is oriented out of the HOPG surface plane and distinct from the neighboring phenyl ring. With these features in mind, the adsorption model corresponding to the monolayer of EsterOC18 molecules adsorbed on a HOPG surface is illustrated in Figures IV.17a-b. This model effectively accounts for all experimental data, with the phenyl rings aligned parallel to the HOPG surface due to molecule-surface interactions, while the C=O groups reside out of the surface plane (depicted in Figure IV.17b).

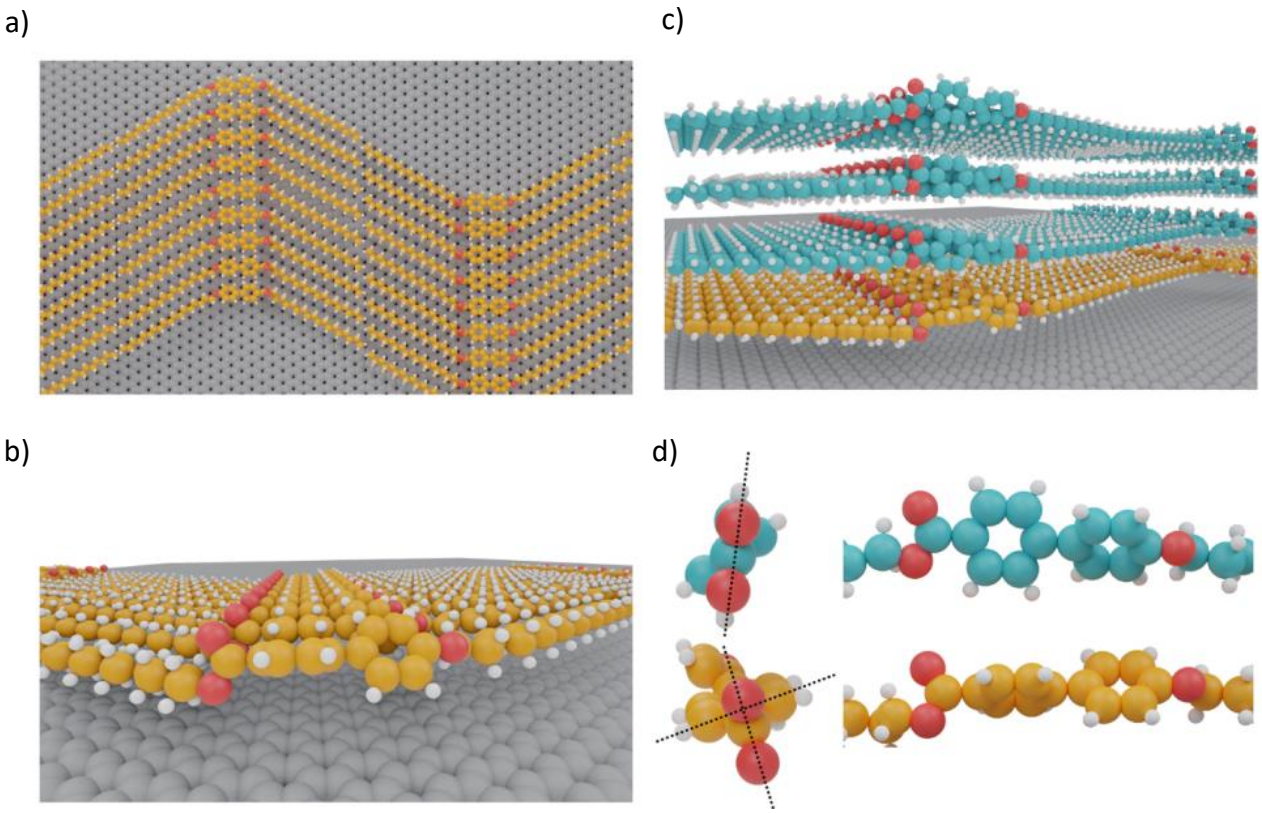

Figure IV.17: a) Top view of the proposed molecular model for a monolayer of EsterOC18. b) Side view of a). The phenyl ring linked to the ester function is out-of-the-plane of the ester function and in-the-plane of the HOPG surface. c) Side view of the proposed molecular model of a 4-layered EsterOC18 supramolecular network. The carbon atoms of the first adlayer are painted in yellow, while the carbon atoms of the other layer are painted in blue. d) Two side-views of EsterOC18 molecules involved in the first layer (carbon atoms painted in yellow) and in other layers (carbon atoms painted in blue) of a multilayered supramolecular network. The noctadecyl chains have been omitted for clarity. In the layer close to the HOPG surface, the phenyl ring is out of the-plane of the neighboring ester function and in the plane of the HOPG surface. In the other layers, the phenyl ring is now in-plane of the neighboring ester function and out-of-plane of the HOPG surface. The conformational difference of EsterOC18 molecules is highlighted by dashed black lines.

In the case of multilayers, the band associated with C=C bond stretching is now observed at 1602 cm^{-1}, similar to the bulk (depicted in Figure IV.14.a). However, two bands related to C=O bond stretching are detected. One is situated at 1702 cm^{-1}, identical to the bulk spectrum, while the second, with a weaker intensity, appears at 1740 cm^{-1}, resembling the AFM-IR spectrum of the monolayer. Consequently, it can be inferred that two orientations or conformations of EsterOC18 molecules comprise the multilayered networks (depicted in Figure IV.17.c). The first layer, closest to the surface (highlighted in yellow in Figure IV.17.c), assumes the same conformation as the one constituting the monolayer, attributed to the molecule-surface interaction (Figure IV.17.c). The corresponding C=O bond stretching occurs at 1740 cm^{-1}. In contrast, the conformation of EsterOC18 molecules in the upper layers of a multilayer system (illustrated in blue in Figure IV.17.c) differs significantly. The phenyl rings rotate to enhance their conjugation with the C=O group, resulting in the shift of the C=O bond stretching to 1702 cm^{-1}, akin to the bulk (depicted in Figure IV.17.d). As the phenyl rings are now out of the HOPG surface plane, the C=C stretching bonds become observable in the AFM-IR spectrum.

In the monolayer, the band linked to C=O bond stretching is notably broad (ranging from 1700 to 1750 cm^{-1}), and within the region covered by the EsterOC18 multilayer, the signal intensity of C=C stretching bonds and C=O bonds fluctuates by a factor of two between minimum and maximum intensity (Figure IV.14). This observation leads to the assumption that the angle between the phenyl rings of EsterOC18 molecules and the HOPG surface, as well as the dihedral angle between the C=O group and the adjacent phenyl ring, is not fixed but varies from 0 to 90°. These variations arise from the modulation of the molecule-surface interaction based on the distance between the molecules and the HOPG surface. This

finding underscores the sensitivity of AFM-IR in identifying these subtle differences in molecular conformation within mono- or multilayered supramolecular networks adsorbed on a surface.

IV.5 Conclusion:

In conclusion, we have the ability to create extensive and well-organized networks adsorbed on the HOPG surface that can be formed via a simple solution deposition protocol, exhibiting remarkable stability both at ambient conditions and under ultra-high vacuum. We may affect the topology of the network created on the surface by modifying the concentration of the deposited solutions, ranging from a single monolayer to several multilayers, as proven by AFM and STM analyses. On the other hand, this study has showcased the high sensitivity and non-invasiveness of AFM-IR as a potent technique for exploring molecular conformation within supramolecular networks. By leveraging IR fingerprints obtained through AFM-IR experiments, we have highlighted the variation of the dihedral angle between the C=O group and the adjacent phenyl ring, within 2D to 3D supramolecular networks adsorbed onto a HOPG surface under ambient conditions. Notably, in the context of a 3D supramolecular network formed by stacked molecular layers, the conformation of molecules varies from one layer to another. The layer proximate to the substrate mirrors the conformation of the corresponding 2D monolayer, while the others closely resemble the bulk conformation. This study has successfully demonstrated that the amalgamation of STM, AFM, and AFM-IR not only elucidates the orientation and arrangement of surface-adsorbed molecules but also discerns the molecular conformation across different layers of 3D multilayered supramolecular networks. This combined analytical approach could be universally applied to unravel the intricacies of on-surface supramolecular self-assemblies.

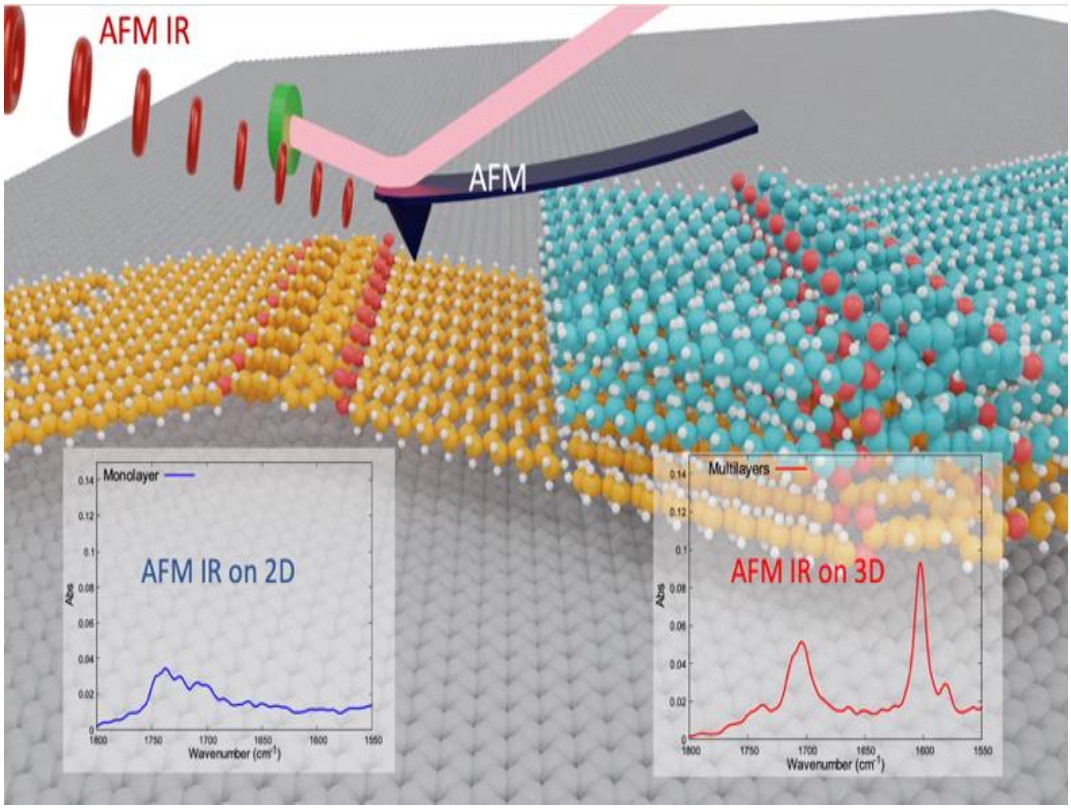

Figure IV.18: Schematic illustration of the shifting from 2D to 3D self-assemblies, showing the high sensitivity of AFM IR in identifying these subtle differences in molecular conformation within mono- or multilayered supramolecular networks adsorbed on a surface**.**

References:

[1] Elemans, J. A. A. W., Lei, S. & De Feyter, S. Molecular and supramolecular networks on surfaces: from two-dimensional crystal engineering to reactivity. Angew. Chem. Int. Ed 58, 7298–7333 (2009).

[2] Makoudi, Y., Jeannoutot, J., Palmino, F., Chérioux, F., Copie, G., Krzeminski, C., Cleri, F., & Grandidier, B. Supramolecular self-assembly on the B-Si(111)-3´3)R30° surface: from single molecules to mul component networks. Surf. Sci. Rep. 72, 316-349 (2017).

[3] Bartels, L. Tailoring molecular layers at metal surfaces. Nat. Chem. 2,87–95 (2010).

[4] Barth, J. V., Constantini, G. & Kern, K. Engineering atomic and molecular nanostructures at surfaces. Nature 437, 671–679 (2005).

[5] J. Lehn, Supramolecular Chemistry: Concepts and Perspectives, VCH-Wiley, Weinheim (1995).

[6] Yokoyama, T., Yokoyama, S., Kamikado, T., Okuno, Y., & Mashiko, S. Selective assembly on a surface of supramolecular aggregates with controlled size and shape. Nature, 413(6856), 619–621, (2001).

[7] Nishio, M. The CH/π hydrogen bond in chemistry. Conformation, supramolecules, optical resolution and interactions involving carbohydrates. Physical Chemistry Chemical Physics, 13(31), 13873, (2011).

[8] Boese, A. D. Density Functional Theory and Hydrogen Bonds: Are We There Yet? ChemPhysChem, 16(5), 978–985, (2015).

[9] Dong, M., Hu, T., Wang, Y., Pang, P., Wang, Y., Miao, X., Deng, W. Halogen-Bonded Building Block for 2D Self-Assembly: Triggered by Hydrogen-Bonding Motifs Relative to the Terminal Functions of the Side Chains. Applied Surface Science, 145983, (2020).

[10] Wu, J., Li, J., Miao, X., Ying, L., Dong, M., & Deng, W. Br···π Halogen Bond Assisted Self-Assembly of Asymmetric Molecule Regulated by Concentration. Chemical Communications, (2020).

[11] Y.Kikkawa, M.Nagasaki, E. Koyama, S. Ito, S.Tsuzuki, “Halogen bond-directed self-assembly in bicomponent blends at the solid/liquid interface: effect of the alkyl chain substitution position,” Chem. Chem. Phys., vol. 24, pp. 17088-17098, (2022).

[12] X. Zeng, Toward Two-Dimensional Tessellation through Halogen Bonding between Molecules and On-Surface-Synthesized Covalent Multimers. Phys. Chem. C, 126, 5777, (2022).

[13] Zambelli, T., Goudeau, S., Lagoute, J., Gourdon, A., Bouju, X., & Gauthier, S. Molecular Self-Assembly of Jointed Molecules on a Metallic Substrate: From Single Molecule to Monolayer. ChemPhysChem, 7(9), 1917–1920. (2006).

[14] Guillermet, O., Niemi, E., Nagarajan, S., Bouju, X., Martrou, D., Gourdon, A., & Gauthier, S. Self-Assembly of Fivefold-Symmetric Molecules on a Threefold-Symmetric Surface. Angewandte Chemie International Edition, 48(11), 1970–1973. (2009).

[15] Fang, Y., Ghijsens, E., Ivasenko, O., Cao, H., Noguchi, A., Mali, K. S., De Feyter, S. Dynamic control over supramolecular handedness by selecting chiral induction pathways at the solution–solid interface. Nature Chemistry, 8(7), 711–717. (2016).

[16] Parschau, M., Fasel, R., Ernst, K.-H., Gröning, O., Brandenberger, L., Schillinger, R., … Siegel, J. S. Buckybowls on Metal Surfaces: Symmetry Mismatch and Enantiomorphism of Corannulene on Cu(110). Angewandte Chemie International Edition, 46(43), 8258–8261. (2007).

[17] Zhang, Z., Huang, H., Yang, X., & Zang, L. Tailoring Electronic Properties of Graphene by π–π Stacking with Aromatic Molecules. The Journal of Physical Chemistry Letters, 2(22), 2897–2905. (2011).

[18] Karmel, H. J., Garramone, J. J., Emery, J. D., Kewalramani, S., Bedzyk, M. J., & Hersam, M. C. Self-assembled organic monolayers on epitaxial graphene with enhanced structural and thermal stability. Chem. Commun., 50(64), 8852–8855. (2014).

[19] F. Jackel, U. G. Perera, V. Iancu, K. F. Braun, N. Koch, J. P. Rabe, S. W. Hla, Interfacial Charge Transfer Enhancement via Formation of Binary Molecular Assemblies on Electronically Corrugated Boron Nitride, Phys. Rev. Lett., 100, 126102, (2008).

[20] Z. Mu, Q. Shao, J. Ye, Z. Zeng, Y. Zhao, H. H. Hng, F. Y. Boey, J. Wu, X. Chen, Interfacial supramolecular assemblies with advanced functions, Langmuir, 27, 1314, (2011).

[21] Niederhausen, J., Kersell, H. R., Christodoulou, C., Heimel, G., Wonneberger, H., Müllen, K., Koch, N. Monolayer Phases of a Dipolar Perylene Derivative on Au(111) and Surface Potential Build-Up in Multilayers. Langmuir, 32(15), 3587–3600. (2016).

[22] S. L. Tait, Y. Wang, Metal-Organic Coordination Interactions in Fe-Terephthalic Acid Networks on Cu(100). Chem. Soc. 130, 2108,(2008).

[23] Henningsen, N., Rurali, R., Limbach, C., Drost, R., Pascual, J. I., & Franke, K. J. Site-Dependent Coordination Bonding in Self-Assembled Metal−Organic Networks. The Journal of Physical Chemistry Letters, 2(2), 55–61. (2010).

[24] Weber, P. B., Hellwig, R., Paintner, T., Lattelais, M., Paszkiewicz, M., Casado Aguilar, P., Klappenberger, F. *Surface-Guided Formation of an Organocobalt Complex. Angewandte Chemie International Edition, 55(19), 5754–5759.* (2016).

[25] Koepf, M., Chérioux, F., Wytko, J. A., & Weiss, J. 1D and 3D surface-assisted self-organization. Coord. Chem. Rev. 256, 2872-2892 (2012).

[26] Xie, R., Hu, Y. & Lee, S.-L. A paradigm shift from 2D to 3D: surface supramolecular assemblies and their electronic properties explored by scanning tunneling microscopy and spectroscopy. Small 19, 2300413 (2023).

[27] Bléger, D., Mathevet, F., Kreher, D., A as, A.-J., Bocheux, A., La l, S., Douillard, L., Fiorini Debuisschert, C., & Charra, F. Janus-like 3D tectons, Self-assembled 2D arrays of functional units at a defined distance from the substrate. Angew. Chem. Int. Ed. 50, 6562-6566 (2011).

[28] Kitagawa, T., Matsubara, H., Komatsu, K., Hirai, K., Okazaki, T. & Hase, T. Ideal redox behavior of the high-density self-assembled monolayer of a molecular tripod on an Au(111) surface with a terminal ferrocene group. Langmuir 29, 4275-4282 (2013).

[29] Blunt, M. O., Russell, J. C., del Carmen Gimenez-Lopez, M., Taleb, N., Lin, X., Schröder, M., Champness, N. R., & Beton, P. H. Guest-induced growth of a surface-based supramolecular bilayer. Nature Chem. 3, 74-78 (2011).

[30] Ivasenko, O., MacLoed, J. M., Chernichenko, K. Y., Balenkova, E. S., Shpanchenko, R. V., Nenajdenko, V. G., Rosei, F. & Perepichka, D. F. Supramolecular assembly of heterocirculenes in 2D and 3D. Chem. Commun. 1192-1194 (2009).

[31] Wang, Z.; Qian, K., Oner, M. A., Deimel, P. S., Wang, Y., Zhang, S., Zhang, X., Gupta, V., Gao, H.-J., Duncan, D. A., Barth, J. V., Lin, X., Allegre , F., Du, S., & Palma, C.-A. Layer-by-layer epitaxy of porphyrin-ligand Fe(II)-Fe(III) nanoarchitectures for advanced metal-organic framework growth. ACS Appl. Nano Mater 3, 11752-11759 (2020).

[32] Fang, Y., Lindner, B. D., Destoop, I., Tsuji, T., Zhang, Z., Khaliullin, Perepichka, D. F., Tahara, K., De Feyter, S., & Tobe, Y. Stereospecific epitaxial growth of bilayered porous molecular networks. J. Am. Chem. Soc. 142, 8662-8671 (2020).

[33] Fang, S., & Hu, Y. H. Open the door to the atomic world by single-molecule atomic force microscopy. Matter, 4(4), 1189–1223. (2021).

[34] Kim, M., Chelikowsky, J. R. CO tip functionalization in subatomic resolution atomic force microscopy. Applied Physics Letters, 107(16), 163109. (2015).

[35] Eigler, D. M., Schweizer, E. K. Positioning single atoms with a scanning tunnelling microscope. Nature, 344(6266), 524–526. (1990).

[36] Assig, M., Etzkorn, M., Enders, A., Stiepany, W., Ast, C. R., & Kern, K. A 10 mK scanning tunneling microscope operating in ultra high vacuum and high magnetic fields. Review of Scientific Instruments, 84(3), 033903. (2013).

[37] Zhang, R., Zhang, Y., Dong, Z. C., Jiang, S., Zhang, C., Chen, L. G., … Hou, J. G. Chemical mapping of a single molecule by plasmon-enhanced Raman scattering. Nature, 498(7452), 82–86. (2013).

[38] Repp, J., Meyer, G., Stojković, S. M., Gourdon, A., & Joachim, C. Molecules on Insulating Films: Scanning-Tunneling Microscopy Imaging of Individual Molecular Orbitals. Physical Review Letters, 94(2). (2005).

[39] J. Guo, Rui Wang, Xue-Guang Ren, Zhi-Yuan Zhang, Dan-Hui Li, and Zhi-Gang Wang. Zero-point fluctuation of hydrogen bond in water dimer from *ab initio* molecular dynamics, Science, 352, 321,(2016).

[40] Ramin, M. A., Le Bourdon, G., Daugey, N., Benneteau, B., Vellu ni, & L., Buffeteau, T. PM IRRAS investigation on of self-assembled monolayers grafted onto SiO_2/Au substrates. Langmuir, 27, 6076-6084 (2011).

[41] Kurouski, D., Dazzi, A., Zenobi, R. & Centrone, A. Infrared and Raman chemical imaging and spectroscopy at the nanoscale. Chem. Soc. Rev. 49, 3315–3347 (2020).

[42] Centrone, A. Infrared imaging and spectroscopy beyond the diffraction limit. Ann. Rev. An. Rev. 8, 101–126 (2015).

[43] Yin, H. Zheng, L.-Q., Fang, W., Lai, Y.-H., Porenta, N., Goubert, G., Zhang, H., Su, H.-S., Ren, B., Richardson, J. O., Li, J.-F. & Zenobi, R. Nanometre-scale spectroscopic visualiza on of cataly c sites during a hydrogena on reac on on a Pd/Au bimetallic catalyst. Nature Cat. 3, 834-842 (2020).

[44] Dazzi, A. & Prater, C. B. AFM-IR: technology and applications in nanoscale infrared spectroscopy and chemical imaging. Chem. Rev. 117, 5146–5173 (2017).

[45] Mathurin, J., Deniset-Besseau, A., Bazin, D., Dartois, E., Wagner, M. & Dazzi, A. Photothermal AFM-IR spectroscopy and imaging: Status, challenges and trends. J. Appl. Phys. 131, 010901 (2022)

[46] Grossmann, L., King, B. T., Reichlmaier, S.; Hartmann, N., Rosen, J., Heckl, W. M., Björk, J. & Lackinger, M. On-surface photopolymerization on of two-dimensional polymers ordered on the mesoscale. Nature Chem. 13, 730-736 (2021).

[47] Lu, F., Jin, M. & Belkin, M. A. Tip-enhanced infrared nanospectroscopy via molecular expansion force detection. Nat. Photon. 8, 307–312 (2014).

[48] Ruggeri, F. S., Mannini, B., Schmid, R., Vendruscolo, M. & Knowles, T. P. J. Single molecule secondary structure determination of proteins through infrared absorption nanospectroscopy. Nat. Comm. 11, 2945 (2020).

[49] Chae, J., An, S., Ramer, G., Stavila, V., Holland, G., Yoon, Y., Centrone, A. Nanophotonic Atomic Force Microscope Transducers Enable Chemical Composition and Thermal Conductivity Measurements at the Nanoscale. Nano Letters, 17(9), 5587–5594. (2017).

[50] Tahara, K., Furukawa, S., Uji-I, H., Uchino, T., Ichikawa, T., Zhang, J., Mamdouh, W., Sonoda, M., De Schryver, F., De Feyter, S. & Tobe, Y. Two-dimensional porous molecular networks of dehydrobenzo[12]annulene derivatives via alkyl chain interdigitation on. J. Am. Chem. Soc. 128, 16613-16625 (2006).

[51] Korolkov, V. V., Summerfield, A., Murphy, A., Amabilino, D. B., Watanabe, K., Taniguchi, T., & Beton, P. H. Ultra-high resolution imaging of thin films and single strands of polythiophene using atomic force microscopy. Nature Communications, 10(1), 1537, (2019).

[52] Groszek, A. J. Selective adsorption on at graphite/hydrocarbon interfaces. Proc. R. Soc. London Ser. A 314, 473-498 (1970).

[53] Waeytens, J., Mathurin, J., Deniset-Besseau, A., Arluison, V., Bousset, L., Rezaei, H., Raussens, V., & Dazzi, A. Probing amyloid fibril secondary structures by infrared nanospectroscopy: Experimental and theoretical considerations. Analyst 146, 132-145 (2021).

[54] Gong, L., Chase, D. B., Noda, I., Liu, J., Mar n, D. C., Ni, C., & Rabolt, J. F. Discovery of β-Form Crystal Structure in Electrospun Poly[(R)-3-hydroxybutyrate-co-(R)-3-hydroxyhexanoate] (PHBHx) Nanofibers: From Fiber Mats to Single Fibers. Macromol. 48, 6197-6205 (2015).

Chapter V: Light vs thermal-induced on-surface Polymerization on Au(111)

One of ultimate objective of molecular electronics is to build devices out of a few functional molecules that can perform fundamental operations like rectification, amplification, or information storage that are coupled by atomic-scale wires on substrates. [1,2] Conjugated polymers are potential prospects for atomic-scale wires that link molecular building pieces. Conventional organic synthesis may produce polymers of almost any length and structure, however polymerizations on planar crystalline surfaces have two distinguishing characteristics. On the one hand, the surface limits monomers, intermediate oligomers, and polymers in two dimensions, creating an anisotropic environment with spatially defined sites for reactivity (catalysis) and preorganization (templation). On the other hand, the atomically defined surface allows for real-time investigation of elementary chemical processes using scanning probe microscopies. Indeed, the use of atomically flat surfaces as underlying substrates and molecular building blocks with potential reactive sites that enhance region-selective activation upon external stimuli (thermal annealing, light, tip-induced, etc.) has become a popular research tool for improving the integration and applicability of formed covalently bonded nanostructures as nanocomponents in functional devices.

Thermal heating is the preferred approach to initiate the reaction often via cleavage of halogen substituents from the molecular building blocks, although it leads to high defect densities and relatively small domain sizes. The Ullmann reaction begins with an initial surface-assisted homolytic dissociation of the C-X bond, which is followed by a further coupling reaction. Cu, Ag, and Au surfaces have been the most extensively researched substrates for two-dimensional Ullmann-like coupling processes. On Cu and Ag the de-halogenation is already active at room temperature (RT) [3,4] or can be activated by mild annealing,[5] whereas on Au it is necessary to anneal at more than 120 C to break the C–Br bond.[6] On Cu and Ag, to complete the covalent coupling by removing the bridging metal atoms, a thermal treatment at a relatively high temperature is required. This treatment in certain cases leads to molecular desorption or the partial decomposition of the precursor, especially in the case of thermolabile substances.[7] By contrast, this step on Au is already activated at RT. The metal–organic intermediate is almost not observed after the de-halogenation the final covalently linked structure is directly obtained. [8]

Recently, photochemical activation of certain functional groups has shown to be an alternate technique for stabilizing self-organized structures while maintaining long-range order.[9] Light has various advantages over other ways. Fine-tuning of photon energy, polarization, and flux is possible and can be done consistently in a variety of situations. [10] The lack of high temperatures allows for better control over precursor diffusion across the surface and avoids possible temperature-related issues such as desorption and chemical degradation of molecular precursors. Only a few investigations have been conducted on photoinduced surface chemical reactions in comparison to those occurring in gas and solution phases.[11] While two-dimensional (2D) confinement of molecular species on the surface reduces complexity, it introduces additional problems due to molecule-substrate and molecule-molecule interactions.[12] As a result, understanding these fundamental characteristics is critical for controlling light-induced activities on surfaces.

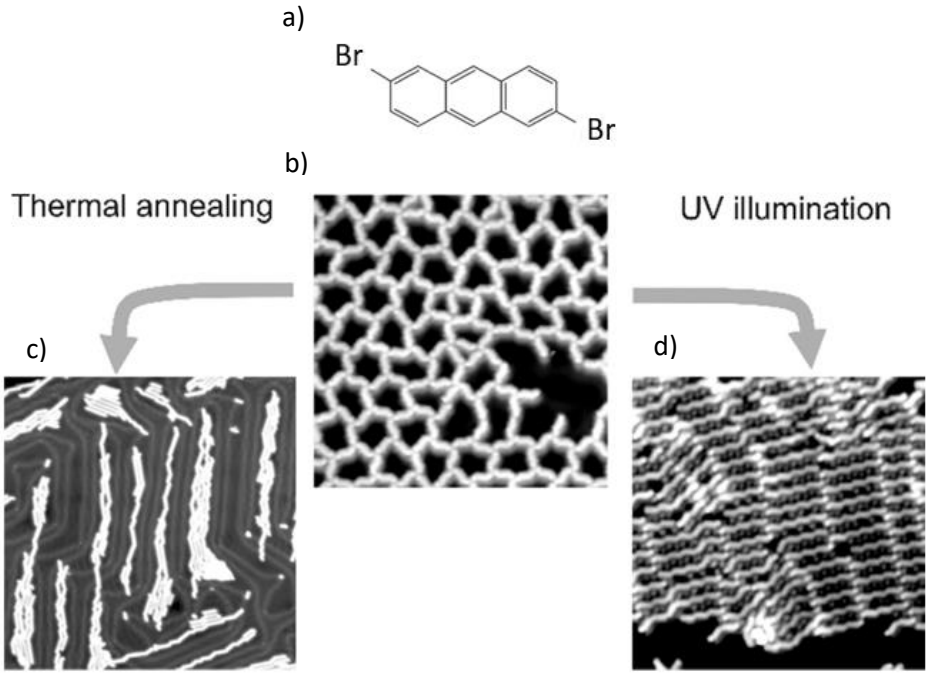

Figure V.1: a) Chemical structure of DBA molecule. b) Scanning tunneling microscopy image of a porous network with a functionalized STM tip (50 mV, 4 pA). Representative STM images of the thermally grown polymers (c) and the polymers obtained by UV illumination (d). Thermal annealing provides longer polymers due to improved diffusion. [13]

Light-induced reactions on surfaces are relatively uncommon, but some intriguing research has been published that points to a promising future for this discipline. In this manner of thermal and light-induced chemical reactions Nacci et al. reported a direct comparison of on-surface polymerization of dibromo-anthracene molecules (Figure V.1.a), induced either thermally or by light, and studied the differences between the two approaches.[13] Dibromo anthracene (DBA) molecules were deposited on an Au(111) surface that was kept at room temperature. The sample was then exposed to UV radiation under UHV conditions for an hour, resulting in the creation of covalently bound linear polymers. This finding indicates that photoinduced debromination of DBA molecules was effective, followed by a chemical occurrence involving C-C coupling between the generated biradicals. The investigators carried out the same process using thermal annealing and discovered that the polymeric chains generated by the photoinduced technique are shorter, indicating diffusion-limited polymer development, as illustrated in Figure V.1.

Chemical bonds within adsorbed molecules have been dissociated using either the STM tip, heat, or light.[14,15] A comprehensive comparative analysis of the thermal and photochemical processes, from initial intact molecules to the formation of polymers, has not yet been conducted deeply. It is crucial to investigate whether these processes follow similar pathways or diverge, resulting in comparable or distinct intermediate molecular arrangements and covalent structures. Therefore, it is essential to discern the mechanisms at play in both thermal and light-induced approaches, how they interact, and the significance of each in on-surface synthesis. This chapter will delve into comparing the on-surface polymerization processes induced by thermal and photochemical methods on Au(111) using four distinct molecular building blocks.

V.1 Material and methods

In this part, we provide the selected molecular building blocks, their size, and the chemical structure employed for functionalization. In the second part, we describe the equipment and the technique for preparing the Au(111) surface.

V.1.1 Molecules:

Herein we present the four molecules investigated all along this chapter. CPK models of Figure V.2 show the optimized geometry of each molecule isolated as well as their specific dimensions. The first two molecules presented in Figure V.2a.b derive from the family of naphthalene diimides (NDIs). The first molecule (Figure V.2.a) is N,N'-Bis(4-bromophenyl)naphthalenediimide (NDB) while the second N,N'-Bis(4-iodophenyl) naphthalenediimide (NDI) presented in Figure V.2.b. NDB is a symmetric organic compound composed of a naphthalene core bridged by two imide groups, with each imide group being substituted by a 4-bromophenyl moiety. The bromine atoms attached to the phenyl rings confer reactivity and potential for further functionalization, while the conjugated system of the naphthalene core contributes to its electronic properties. The same applies to NDI but instead of bromine, we used iodine. The naphthalenediimide molecules exhibit remarkable optoelectronic and optical properties.[16] Although these molecules have been deposited onto surfaces to create supramolecular self-assemblies,[17] their behavior in on-surface synthesis remains unexplored, despite their appealing properties.

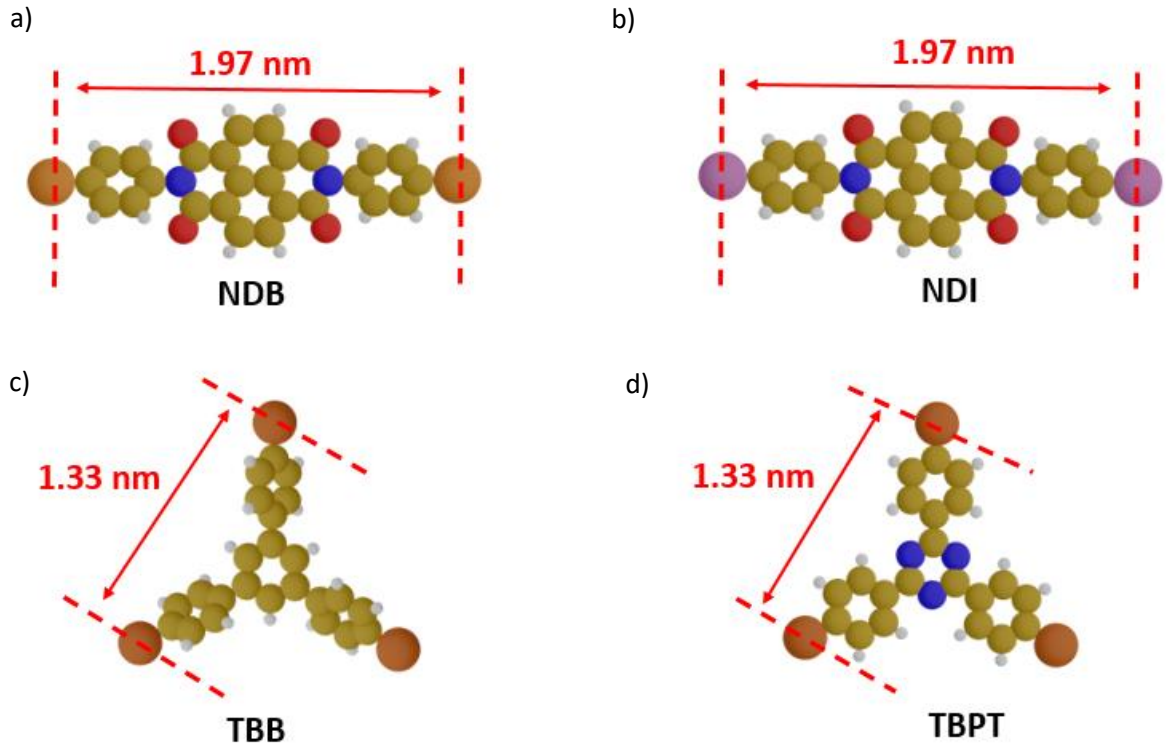

Figure V.2: CPK models of the four used molecules (Yellow: Carbon, White: Hydrogen and Blue: Nitrogen, Red: Oxygen, Orange: Bromine, Purple: Iodine) of a) N,N'-Bis(4-bromophenyl)naphthalenediimide (NDB), b) N,N'-Bis(4-iodophenyl) naphthalenediimide (NDI), c) 1,3,5-tri(4'-bromophenyl)benzene (TBB), d) 2,4,6-Tris(4-bromophenyl)- 1,3,5-triazine(TBPT).

In the second section of this chapter, we will use two other molecules. The first molecule 1,3,5-tri(4'-bromophenyl)benzene (TBB) presented in Figure V.2.c. (TBB) is a trisubstituted benzene derivative featuring three 4'-bromophenyl groups symmetrically attached to the benzene ring at positions 1, 3,

and 5. The last molecule 2,4,6-Tris(4-bromophenyl)-1,3,5-triazine (TBPT Figure V.2.d) is composed of a central 1,3,5-triazine ring substituted with three 4-bromophenyl groups at positions 2, 4, and 6. Among all the proposed precursors for creating 2D covalent networks, the molecule 1,3,5-tris(4'-bromophenyl)benzene (TBB, Fig. V.2.c) stands out as the most extensively examined molecule under ultra-high vacuum conditions using scanning tunneling microscopy (UHV-STM).[18,19] The sublimation temperatures of the four molecules in our experimental setup are 488 K for NDB, 495 K for NDI, 430 K for TBB, and 420K for TBPT.

The graphs in Figure V.3 depict the absorption spectra of the used molecules, demonstrating how these molecules absorb light at specific wavelengths. The x-axis represents the wavelength of light in nanometers, while the y-axis indicates the absorbance. Notable features of the graph include distinct peaks at various wavelengths, which signify the wavelengths at which each molecule absorbs light most strongly. These peaks are indicative of electronic transitions within the molecules. Figure V.3.a demonstrates that both NDI and NDB exhibit significant light absorption at 245 nm and within the 350-380 nm range. In contrast, Figure V.3.b shows that TBB and TBPT absorb light at different wavelengths, with TBB absorbing at 260 nm and TBPT at 290 nm. These adsorption spectra attribute to the possible $\pi \rightarrow \pi^*$ transitions between the states of the molecule.[20] These differences in absorption spectra highlight the distinct behaviors of TBB and TBPT in response to light, which can be attributed to variations in their molecular structures. This variation suggests that the electronic configurations and molecular interactions within TBB and TBPT lead to their unique absorption characteristics at specific wavelengths. In the subsequent illumination experiments, the light used will correspond to the spectra displayed in Figure V.3.

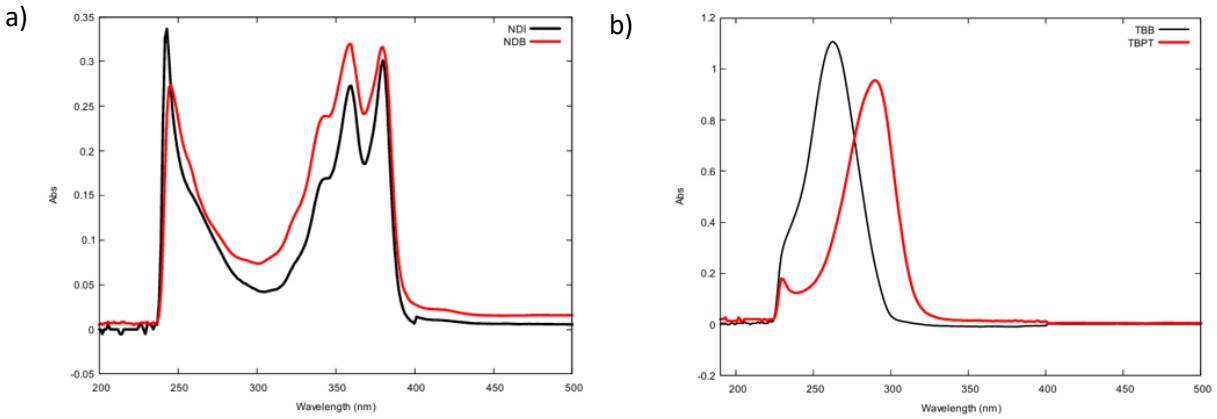

Figure V.3: The absorption spectra of the used molecules, demonstrating how these molecules absorb light at specific wavelengths. a) NDB and NDI adsorption spectra b) TBB and TBPT adsorption spectra.

V.1.2 Surface preparation

The process as a whole was carried out in a chamber under UHV with a base pressure of less than 8.8×10^{-11} mbar. Inside the same chamber, a variable temperature Scanning Tunnelling Microscope (VT-STM) is utilized to investigate samples. The molecules are loaded into quartz crucibles and put into a molecular evaporator (Kentax). Since molecules are created and delivered from air conditions, each one is heated until it reaches its sublimation temperature under UHV to eliminate any contaminants. To determine the sublimation temperature, a series of deposition trials are performed while increasing the degassing temperature. The gold surface was prepared by repeating ion argon sputtering followed by annealing. We employ 1 kV of ion beam energy for 20 minutes every cycle. Each bombarding cycle is followed by thermal annealing to guarantee that crystallographic surfaces are reconstructed by

releasing defects and removing Ar atoms. The annealing temperature for gold is 773 K. Surface cleanliness is monitored by STM scanning, we continue sputtering cycles until we acquire a high-resolution large-scale picture of clean, defect-free terraces, as shown in Figure V.4.

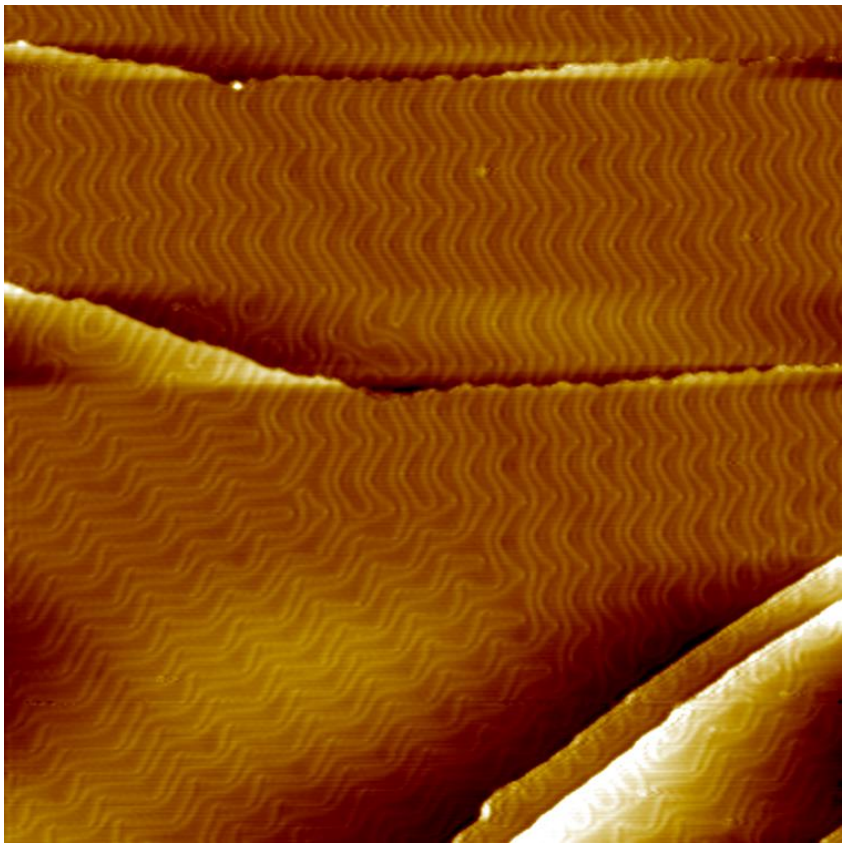

Figure V.4: Large-scale STM images showing clean gold surface (200 nm x200 nm, V=-1.4v, It=80pA, RT).

V.2: STM experimental results

The first part of this section will focus on examining the formation of 2D supramolecular networks of N,N'-Bis(4-bromophenyl)naphthalenediimide (NDB) and N,N'-Bis(4-iodophenyl)naphthalenediimide (NDI) on an Au(111) surface. Subsequent subsections will explore the impact of thermal annealing and light exposure on each network as stimuli for reactions. The second part will address the same investigation but with different molecules: 1,3,5-tri(4'-bromophenyl)benzene (TBB) and 2,4,6-Tris(4-bromophenyl)-1.3.5-triazine (TBPT). This section will follow the same structure as the preceding one, analyzing the formation and behavior of their 2D supramolecular networks on the Au(111) surface under the influence of thermal annealing and light exposure. STM will be the exclusive analytical tool utilized for characterizing our experiments.

V.2.1 Supramolecular networks of NDB and NDI on Au(111) and thermal annealing impact on both networks:

At room temperature, when NDB and NDI were deposited on Au(111), their behavior differed based on the halogen atoms they contained. NDB deposition on Au(111) at room temperature led to the formation of a highly organized 2D supramolecular close-packed network, as depicted in Figure V.5. The network is characterized by a periodic grid-like pattern of bright spots as presented in the STM image, where each bright dot represents one NDB monomer.

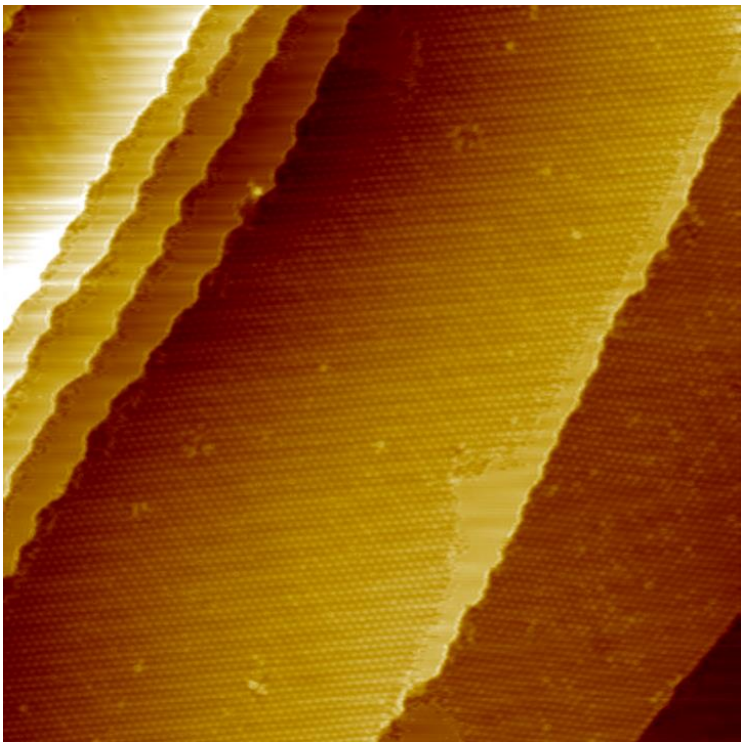

Figure V.5: Large scale STM image recorded at room temperature of the 2D formed supramolecular network of NDB/Au(111). (V_s = 0.8V, I_t = 20 pA, RT, 120 nm x 120nm).

Every line itself is constructed by an accumulation of disjoint bright dots, which are spaced by 1.38 ± 0.1 nm indicating the periodicity of the NDB network and the distance separating consecutive lines is 1.34 ± 0.05 nm, highlighted by the black arrows in Figure V.6.a. Based on the represented STM images analysis and geometric measurements, by associating the NDB molecule to the disjoint bright dots we build the corresponding supramolecular model for NDB/Au(111). The unit cell of the supramolecular network formed by self-assembly of NDB molecular building blocks on Au(111) surface has a parallelogram shape constituted of the repetitive presence of disjoint bright dots features arranged into parallel lines as presented in Figure V.6.a. The vectors of the unit cell, U_{NDB} and V_{NDB} with their corresponding length value of U_{NDB} = 1.38 ± 0.1 nm and V_{NDB} = 1.34 ± 0.05 nm, are enclosing the angle θ_{NDB} = 61° as presented in Figure V.6.b. The unit cell of the NDB supramolecular network is constituted of one NDB molecule within a surface area of 1.63 nm^2 corresponding to a molecular density of 0.613 mol/nm^2 for the NDB/Au(111) supramolecular network. Based on the identification of the unit cell we shall constitute a representative supramolecular model of the NDB network. Figure V.6.b represents the supramolecular model of NDB on Au(111) surface elucidating the distance between Br-Br of adjacent NDB molecules is about 0.45 nm, falling in the range of halogen-halogen interactions type I (θ_1=θ_2=145°, indicated in Figure V.6.b),[21] and the distance between two parallel phenyl rings of adjacent NDB molecules about 0.57 nm falling in the range of parallel face-to-face π-π interactions.[22] Therefore the driving forces behind the supramolecular self-assembly of NDB on an Au(111) surface include the intermolecular interactions, specifically parallel face-to-face π-π interactions (between phenyl rings), halogen-halogen (Br-Br) interaction, and interactions between the molecules and the surface presented in Figure V.6.c. The latter occurs due to the bending of the molecule's lateral side towards the surface, facilitated by the interaction between oxygen and the Au(111) surface.[23]

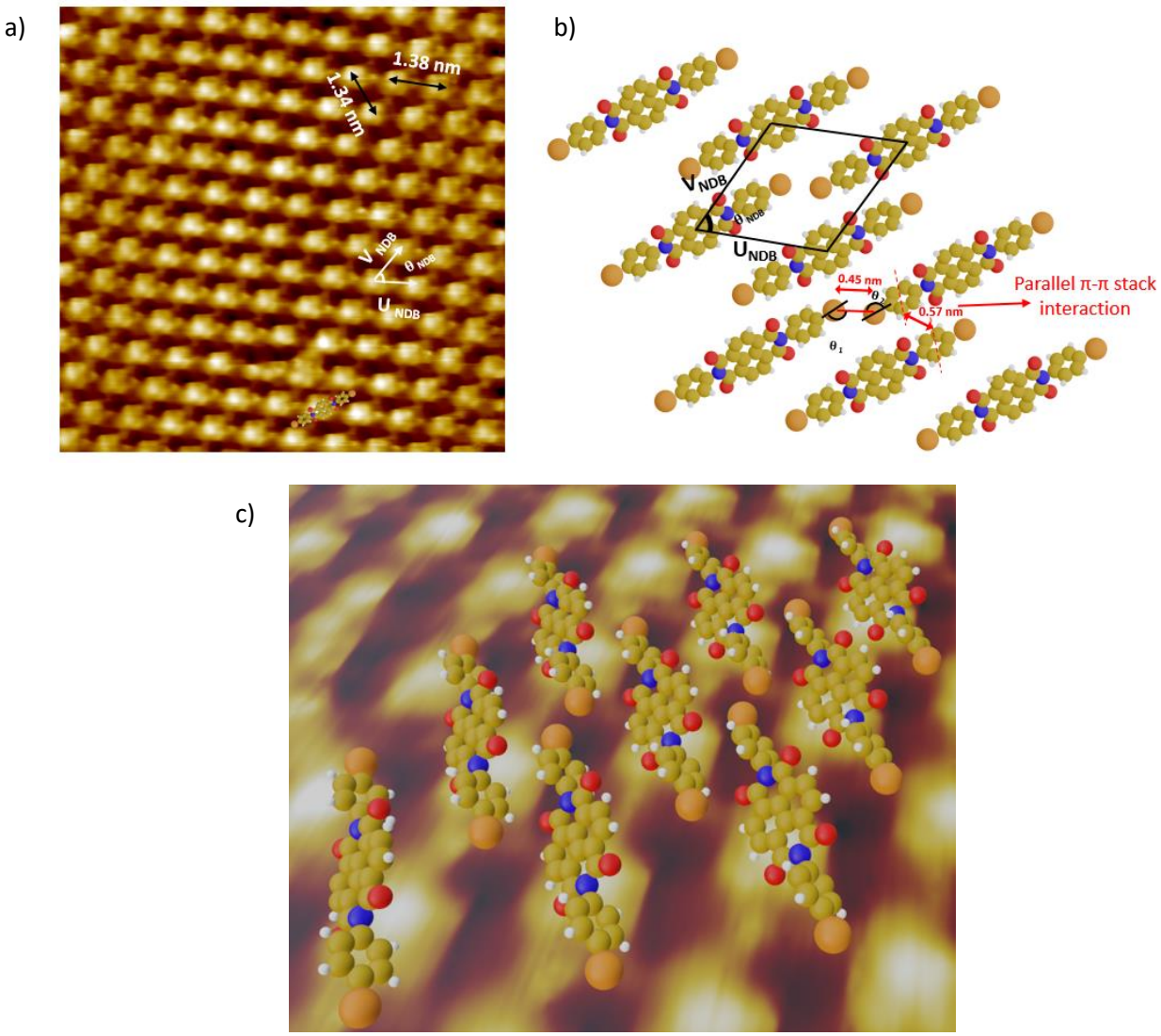

Figure V.6: a) Zoomed STM images over the NDB network (V_s = 1 V, I_t = 20 pA, RT, 15 nm x 15nm), showing the corresponding unit cell vectors (U_{NDB} = 1.38 ± 0.1 nm, V_{NDB} = 1.34 ± 0.05 nm, θ_{NDB} = 61°), the repetitive unit pattern constituting the network of disjoint bright dots. b) The proposed model for the 2D supramolecular network formed by the deposition of the NDB molecule on Au(111) at room temperature features key interactions. c) Upper view showing a lateral side of the NDB molecule bending toward the surface due to oxygen and Au(111) interaction.

Depositing NDI onto Au(111) at room temperature resulted in the formation of two distinct 2D supramolecular networks across the surface. This deposition process was monitored using LT-STM at 10 K. In both observed phases, NDI molecules formed compact structures. Notably, there was no evidence of partial de-iodination after the molecules were deposited onto Au(111) at room temperature, indicating that all monomers remained intact throughout the process. This preservation of monomers contributes to the stability and integrity of the resulting supramolecular networks. For the NDI molecules on the Au(111) surface, the first detected network is characterized by a highly dense packing arrangement of NDI molecules. Each line in this network consists of disjoint bright dots, spaced 0.925 ± 0.01 nm apart, indicating the periodicity of the NDB network and the distance separating consecutive lines is 1.43 ± 0.02 nm, as highlighted by the black arrows in Figure V.7.a. Based on STM image analysis and geometric measurements, the NDI molecule corresponds to the disjoint bright dots, allowing us to construct the supramolecular model for NDI/Au(111). The unit cell of this network, formed by the self-assembly of NDI molecules on the Au(111) surface, has a parallelogram shape. The vectors of the unit cell, U_{NDI}, and V_{NDI}, have lengths of 0.925 ± 0.01 nm and 1.43 ± 0.02 nm, respectively,

and enclose an angle of θ_{NDI}= 65°, as shown in Figure V.7.a. This unit cell contains one NDI molecule and covers a surface area of 1.28 nm², corresponding to a molecular density of 0.78 mol/nm² for the NDI/Au(111) supramolecular network. Using the identification of the unit cell, we can construct a representative supramolecular model of the NDI network, as shown in Figure V.7.b. This figure illustrates the supramolecular model of NDI on the Au(111) surface, highlighting the distances of 0.48 ± 0.02 nm between the phenyl rings of adjacent NDI molecules. From these measured distances, we can conclude the presence of parallel displaced π-π interaction between the phenyl rings of different molecules. Additionally, the distance between iodine atoms of different NDI molecules is approximately 0.3 nm falling in the range of repulsive halogen-halogen (θ_1=θ_2=90°, indicated in Figure V.7.b). Consequently, the self-assembly of NDI on the Au(111) surface is driven by molecule-molecule interactions, particularly the strong parallel displaced π-π interactions between the phenyl rings, which outweigh the repulsive forces between the iodine atoms. Additionally, interactions between the molecules and the surface play a significant role, facilitated by the bending of the molecule's lateral sides toward the surface and the enhanced interaction between oxygen atoms and the Au(111) surface as presented in Figure V.7.c. [23]

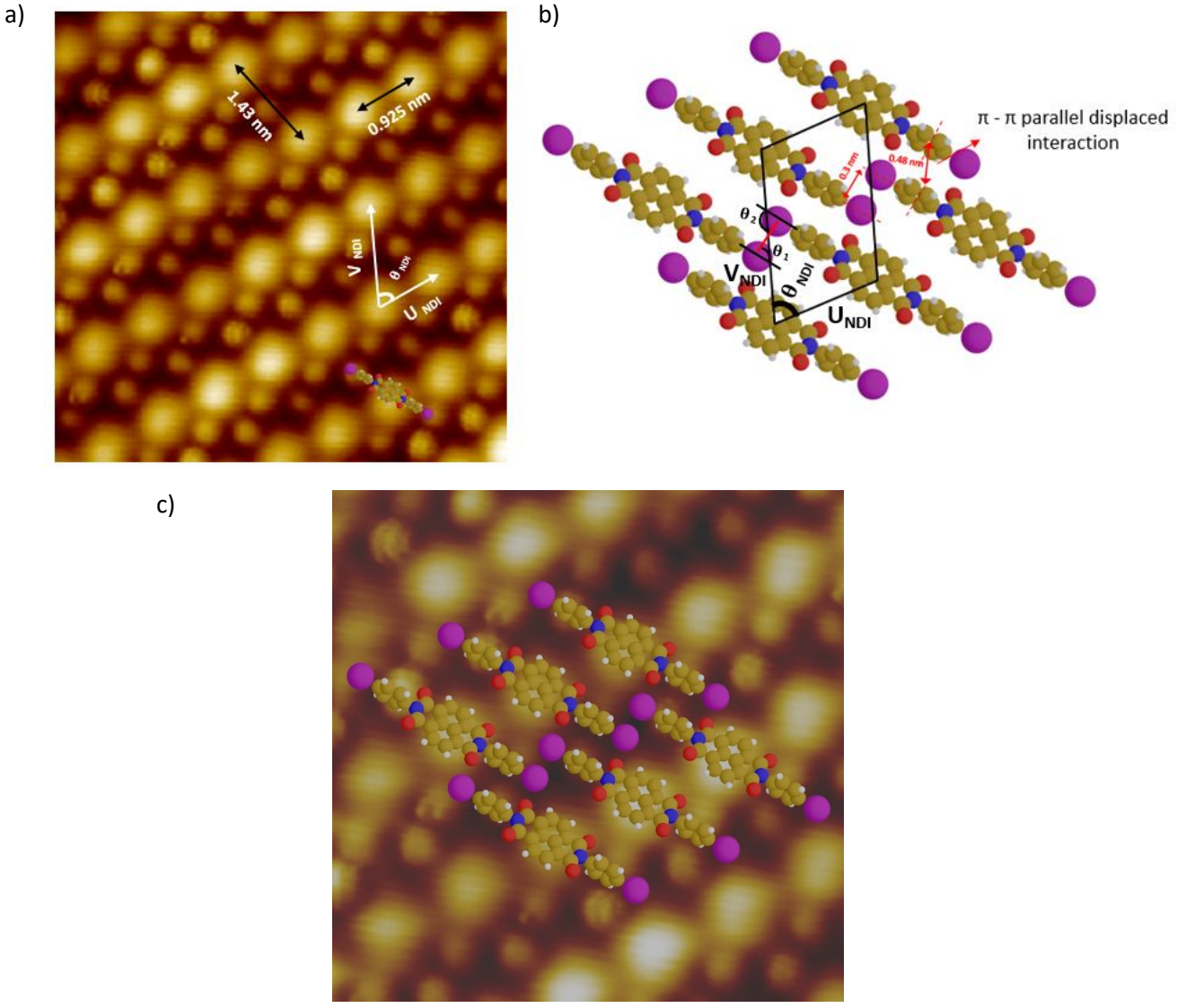

Figure V.7: a) Zoomed STM image recorded at 10 k of the 2D-formed supramolecular network of NDI/Au(111), (V_s = -0.3 V, I_t = 3 pA, 7 nm x 7 nm), showing the corresponding unit cell vectors (U_{NDI} = 0.92 ± 0.01 nm, V_{NDI} =1.43 ± 0.02 nm, θ_{NDI} = 65°),

the repetitive unit pattern. b) The proposed model for the 2D supramolecular network of the NDI molecule. c) Upper view showing a lateral side of the NDI molecule bending toward the surface due to oxygen and Au(111) interaction.

The second detected supramolecular self-assembly upon deposition of NDI on Au(111) is presented in Figure V.8. The network is build up by highly dense packing arrangement of NDI molecules on Au(111), the supramolecular self-assembly reveals the appearance the pattern of columns separated by a darker stripes. The molecules orientation in the network exhibits two possible directions opposite to each other's as revealed on the bottom of figure V.8.a by the four superimposed molecules. This assembly lacks any repetitive unit cell due to the shift in the molecule's alignment between different columns according to this STM image. Figure V.8.b illustrates the supramolecular model of NDI on the Au(111) surface, highlighting the distances between the iodine and oxygen atoms ranging between 0.3-0.4 nm falling in the range of halogen bond interaction, this interaction is described due to the σ-hole region in iodine bending toward the electron rich area of oxygen (lone pair of electrons).[25] Consequently, the driving forces behind the supramolecular self-assembly of NDI on an Au(111) surface include interactions between molecules, specifically I-O interactions, and interactions between the molecules and the surface. The latter occurs due to the bending of the molecule's lateral side towards the surface, facilitated by the interaction between oxygen and the Au(111) surface as presented in figure V.8.c.[23]

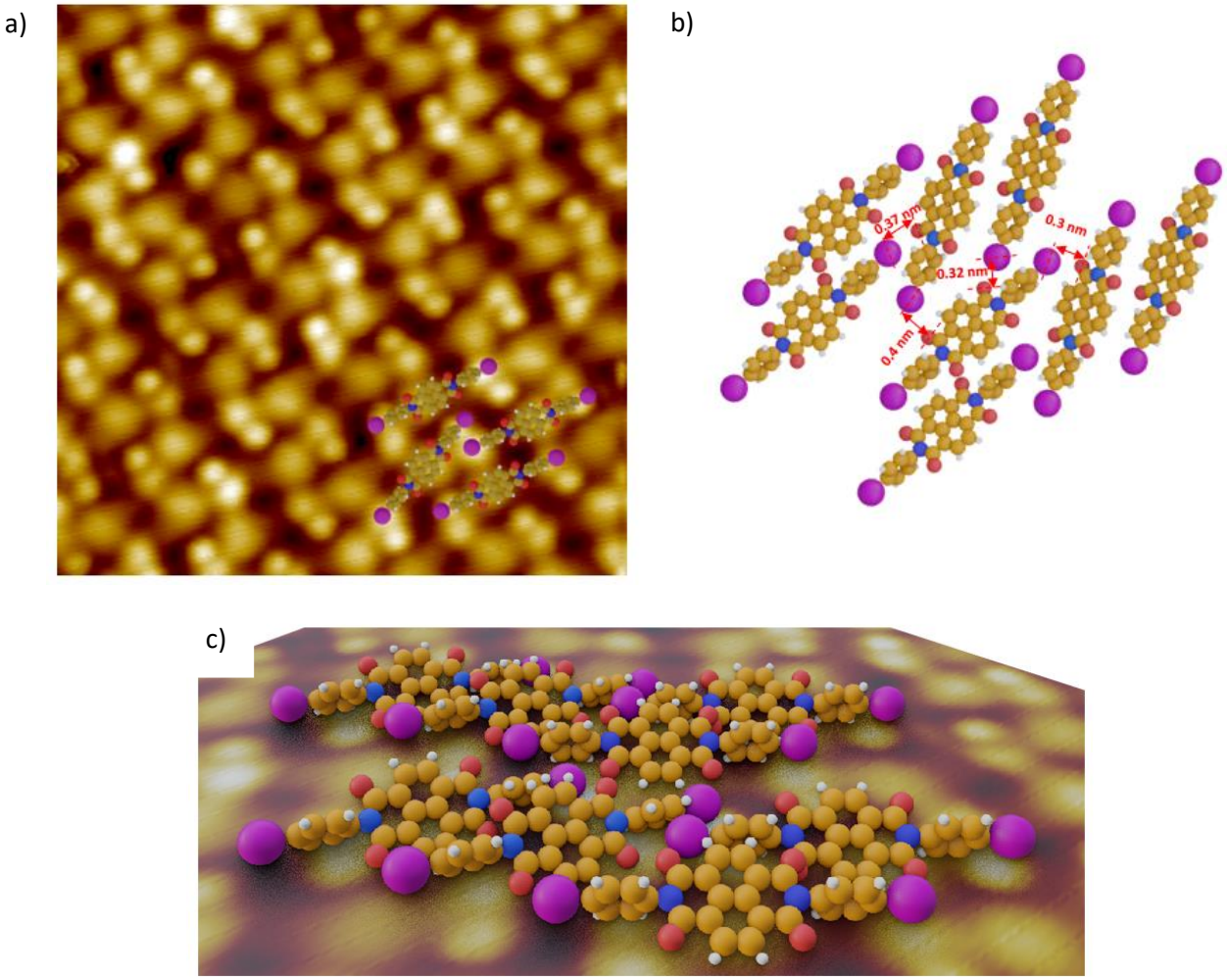

Figure V.8: a) Zoomed STM image recorded at 10 k of the second 2D-formed supramolecular network of NDI/Au(111), (V_s = -0.425 V, I_t = 9 pA, 8.47 nm x 8.47 nm). b) The proposed model for the 2D supramolecular network of the NDI molecule. c) Side view showing a lateral side of the molecule bending toward the surface due to oxygen and Au(111) interaction.

The extended 2D supramolecular networks of NDB and NDI molecules on Au(111) underwent a series of thermal annealing treatments, each lasting a fixed duration of 30 minutes. The structural changes induced by these thermal processes were monitored using Scanning Tunneling Microscopy (STM). This approach enabled precise observation of the network's evolution and stability under thermal stress, providing insights into the dynamics and resilience of the intermolecular interactions (halogen-halogen and π-π stacking) within the supramolecular assembly. Annealing the 2D supramolecular network of NDB on Au(111) beyond 220°C caused a complete structural transformation of the self-assembled network, as illustrated in the STM image of Figure V.9. During this thermal annealing process, the C-Br bonds broke, facilitating aryl-aryl coupling reactions between the molecules. This led to the formation of 2D self-assembly of oligomerized NDB molecules. Concurrently, the freed bromine atoms aggregated on the surface, clustering in distinct regions. From the STM image depicted in Figure V.9 we can see clearly the formation of a close packed oligomers arranged in 2D networks of covalently bonded molecules over the surface. This arrangement is enhanced by the π-π interactions between the cores of the molecules that possess an aromatic nature. These π-π interactions between the cores of the molecules are highlighted by white ellipses in Figure V.9, display a distance measuring approximately 0.68 ± 0.01 nm between the cores. This transformation underscores the significant impact of thermal annealing on the structural and chemical properties of the supramolecular network, paving the way for the formation of more complex polymeric structures.

a) b)

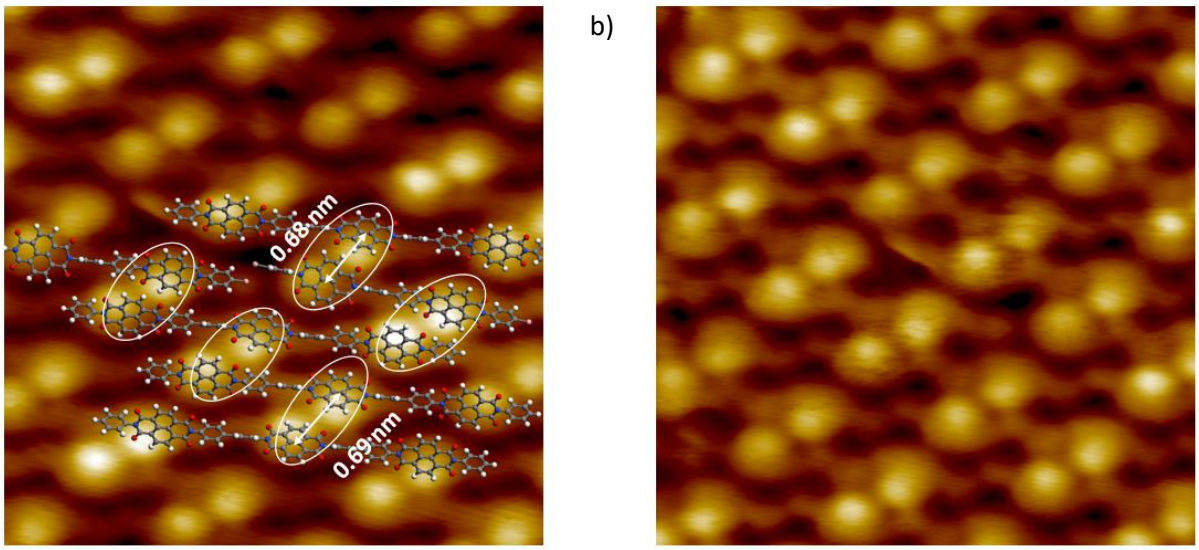

Figure V.9: STM images after annealing the NDB molecules over Au(111) surface at 220C for 30 mins. a) (V_s = 0.2 V, I_t = 20 pA, RT, 8 nm x 8nm) b) (V_s = -0.2 V, I_t = 20 pA, RT, 8 nm x 8nm).

Simultaneously, the extended 2D supramolecular network of NDI molecules on Au(111) was subjected to a series of thermal annealing treatments, each with a fixed duration of 30 minutes. These processes were monitored at 10 K using low-temperature Scanning Tunneling Microscopy (LT-STM). When subjected to annealing at approximately 200°C, these structures underwent partial de-iodination, involving catalytic cleavage of the C–I bond. This process converted all monomers present on the surface into dimers. Notably, no intact monomers were observed after this annealing, indicating a complete transformation. Furthermore, iodine atoms were found to agglomerate on the surface, concentrating in specific regions. Figure V.10.b presents a zoomed-in STM image of a fully dimerized NDI network after annealing, with the resulting dimers measuring approximately 3.4 nm in length (Figure V.10.a). The formation of these dimers is attributed to the cleavage of C-I bonds on two sides of obliquely-facing molecules, followed by aryl-aryl coupling reactions between the neighboring molecules. We can see clearly from the STM image that the dimers are arranged in a closed packed

linear row defect-free advanced by the face-to-face π-π interactions between the iodophenyl rings at the edges of the molecules between rows (highlighted by the black ellipses in Figure V.10.a), and by the face-to-face π-π interactions between the coupled phenyl rings of neighboring dimers in the same row (highlighted by the white ellipses in Figure V.10.a). Figure V.10.b provides a detailed view of the formed dimers, showing parallel dark stripes that suggest aryl-aryl coupling. These stripes are measured at 0.95 nm, which is very close to the theoretical value of 0.98 nm. Additionally, the bright dots, representing the core of each molecule, have a measured size of 0.67 nm.

a) b)

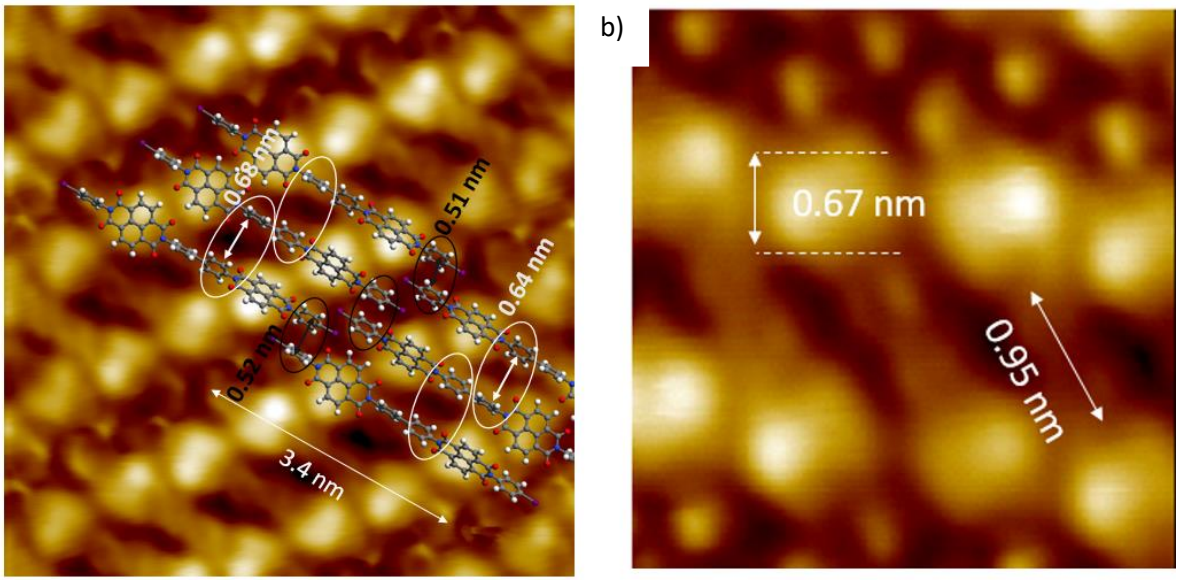

Figure V.10: STM images after annealing the NDI molecule over Au(111) at 200°C we can recognize that all monomers transformed into dimers. a) (V_s = -0.4 V, I_t = 2 pA, 10 K, 7 nm x 7 nm). b) (V_s = -0.4 V, I_t = 2 pA, 10 K, 3 nm x 3 nm).

V.2.2 Light Illumination Impact on NDB and NDI:

In this section, we employed two varieties of lighting devices: a UV lamp emitting light in a range between 115-400 nm, and a UV LED emitting light at 365 nm. We used these two types of light according to the spectra displayed in Figure V.3. The samples were exposed to these light sources within a UHV chamber through UV viewports, ensuring nearly perfect transmission. The samples were positioned approximately 10 cm from the light sources, and their temperature remained constant throughout the illumination period.

Exposing the NDB supramolecular network on Au(111) to a UV lamp (115-400 nm) for 15 hours at room temperature did not induce notable changes. Figure V.11 illustrates the sample post-illumination, revealing only disrupted areas within the network exhibiting disordered and random characteristics devoid of any discernible periodicity or order. We can see clearly that the molecules surrounding these irregular structures remained intact with consistent periodicity akin to pre-illumination. On the other hand, illuminating the same network with a UV LED lamp emitting light at a wavelength of 365 nm didn't result in modification the network remained on the surface intact for illuminations till 18hrs.

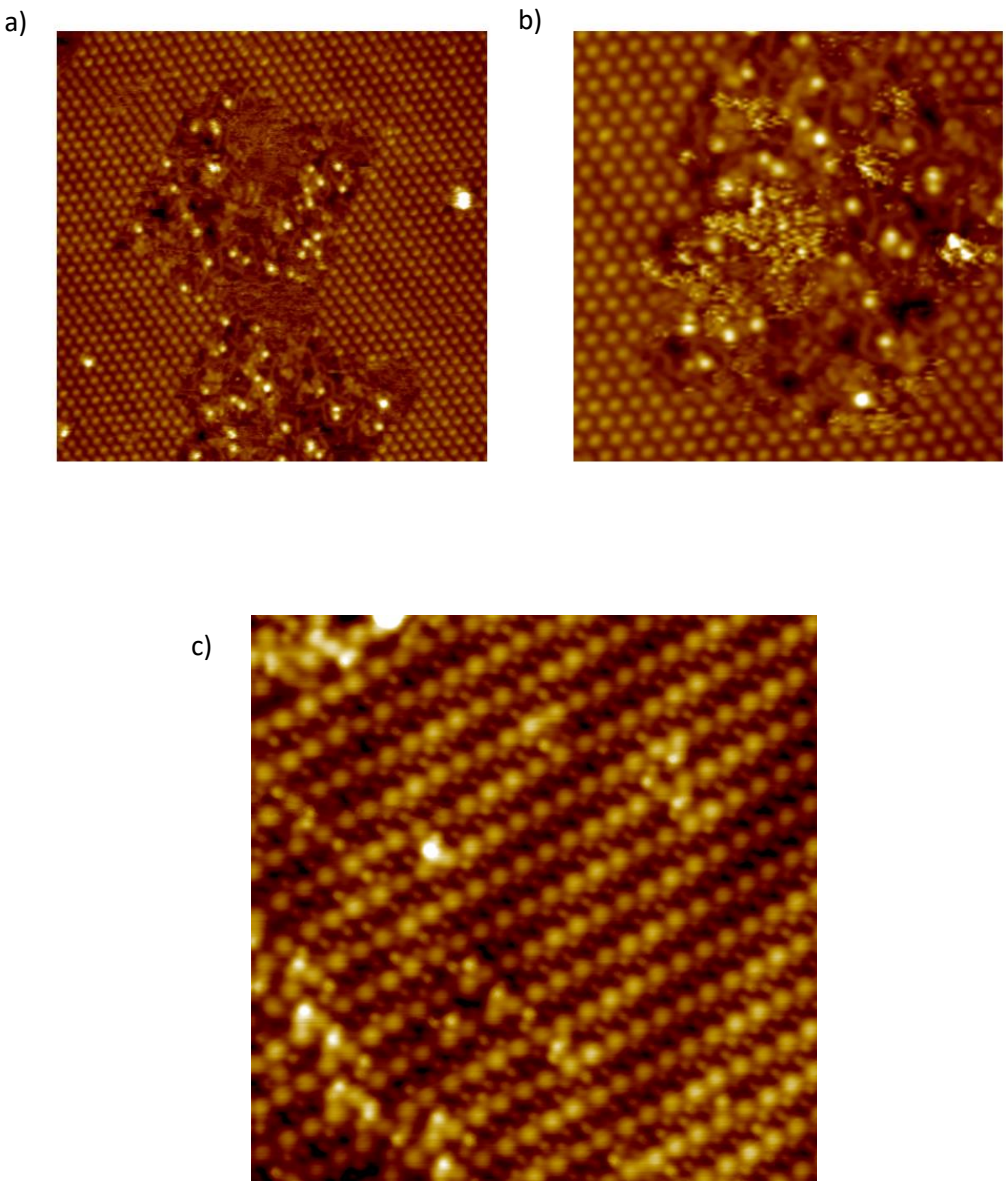

Figure V.11: a-b) STM images after exposing the NDB supramolecular network to a UV lamp for 18 hours at room temperature, showing disrupted areas within the network. a) (V_s = 1.2 V, I_t = 20 pA, RT, 50 nm x 50 nm). b) (V_s = 1.2 V, I_t = 20 pA, RT, 30 nm x 30 nm). c) STM images taken after exposing the NDI supramolecular network to a UV lamp for 15 hours at room temperature with no detectable modifications to the network after illumination (V_s = -0.3 V, I_t = 5 pA, 10 k, 20 nm x 20 nm).

On the other hand, the NDI molecules over Au(111) were subjected also to the same types of light illuminations (UV lamp 115-400 nm, UV LED 365 nm) for durations ranging between 3-15 hours. After these illuminations, no modifications were detected at all as presented in Figure V.11.c, the networks preserved the same structures intact with consistent periodicity akin to pre-illumination.

V.2.3 Supramolecular networks of TBB and TBPT on Au(111) and thermal annealing impact on both networks:

Each molecule was deposited on Au(111) substrate held at room temperature and then moved to the STM head to be monitored at room temperature, subsequently. As a result of diffusion (for submonolayer of molecules arrangement at room temperature), I had to arrange the molecule's deposition into a full monolayer on the surface to stabilize the supramolecular networks since we were working at room temperature. On Au(111) we find that molecular deposition at room temperature

results in an ordered, packed array of unreacted TBB and TBPT monomers. The network of assembled molecules with contrast is modulated in bright and dark stripes by the reconstructed underlying gold surface. Molecules can be resolved as trigonal features in an ordered arrangement. Figure V.12 showcases high-resolution STM images of the extended 2D supramolecular network formed by the self-assembly of TBB on Au(111), exhibiting a bow-tie shape. This supramolecular arrangement of the molecules is in total agreement with the observed network developed by Blunt et al.[25] The image reveal that the molecules organize into an ordered porous structure on the surface, with adjacent side-by-side molecules rotated by 180°. In the STM images, the bromine atoms appear brighter than the carbon skeleton of the molecules, each molecule displaying three bright spots at its edges. Based on the represented STM images analysis and geometric measurements, by associating the TBB molecule to the "Y shape" we build the corresponding supramolecular model for TBB/Au(111). The unit cell of the supramolecular network formed by the self-assembly of TBB molecular building blocks on Au(111) surface has a parallelogram shape. The parameters of this unit cell are measured as U_{TBB} = 2.02 ± 0.01 nm, V_{TBB} =1.69 ± 0.02 nm, with an enclosing angle of θ_{TBB} = 69°. The unit cell of the TBB supramolecular network comprises two TBB molecules within an area of 3.32 nm², corresponding to a molecular density of 0.6 molecules/ nm² for the TBB/Au(111) network. . Figure V.12.b illustrates the supramolecular model of TBB on the Au(111) surface, highlighting the distances between the Br-Br atoms about 0.52 nm falling in the range of halogen-halogen interactions pseudo type II (θ_1=98°, θ_2=161°, indicated in Figure V.12.b),[26] and the distance between the phenyl rings of adjacent TBB molecules ranging between 0.58-0.66 nm falling in the range of face-to-face π-π interactions. Consequently, the driving forces behind the supramolecular self-assembly of TBB on an Au(111) surface include intermolecular interactions (specifically halogen-halogen and π-π interactions), next to molecules-substrate Van der Waals interactions.

a)

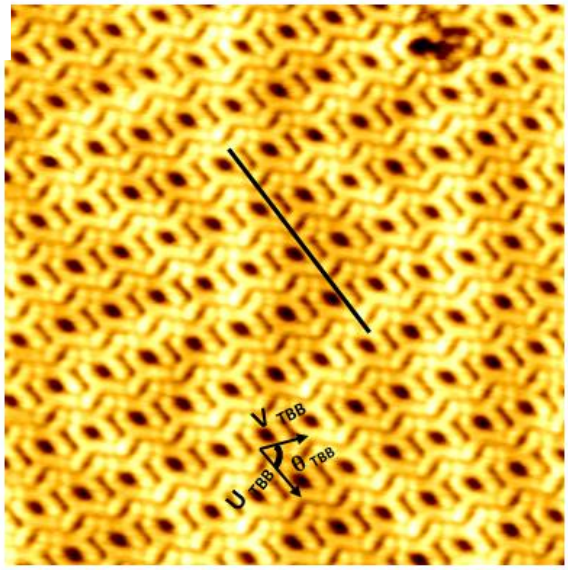

b)

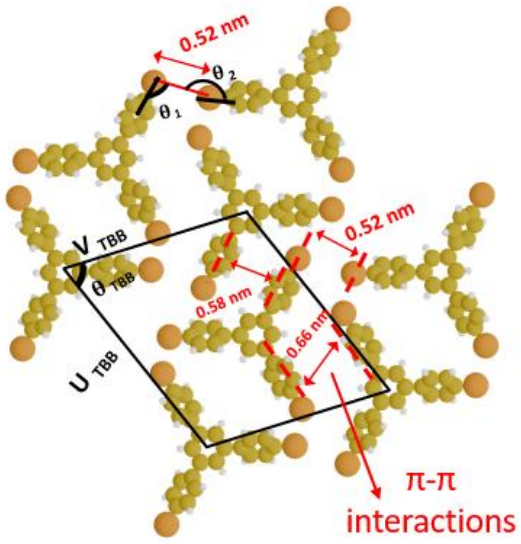

c)

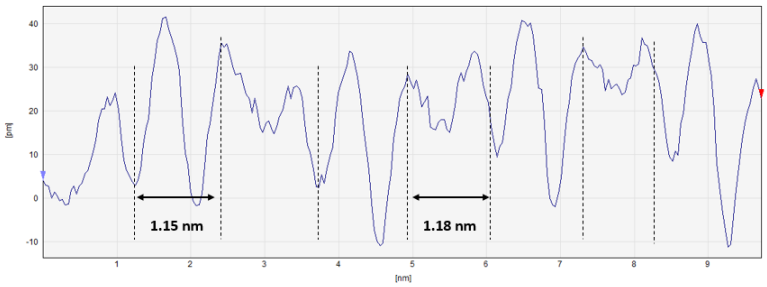

Figure V.12: a) STM image recorded at room temperature of the 2D-formed supramolecular network of TBB/Au(111), (V_s = -1 V, I_t = 15 pA, RT, 15 nm x 15 nm), showing the corresponding unit cell vectors (U_{TBB}= 2.02 ± 0.01 nm, V_{TBB} =1.69 ± 0.02 nm, θ_{TBB} = 65°), the repetitive unit pattern. b) The proposed model for the 2D supramolecular network of the TBB molecules on Au(111). c) Z-profile taken along the black line of (a) showing one arm of the molecules measuring between 1.15-1.18 nm.

In the case of TBPT on Au(111), depicted in Figure V.13, the deposition at room temperature led to the formation of a highly organized 2D supramolecular close-packed network. The STM image reveals that the molecules organize into an ordered structure on the surface, with adjacent molecules in the same row and column aligned all parallel to each other. This analysis is further detailed with a marked unit cell in Figure V.13.a. Based on the represented STM images analysis and geometric measurements the unit cell parameters are U_{TBPT} = 1.5 ± 0.08 nm and V_{TBPT} = 1.48 ± 0.02 nm, with an enclosing angle of θ_{TBPT} = 62°. The unit cell of the TBPT supramolecular network contains one TBPT molecule within an area of 1.48 nm², corresponding to a molecular density of 0.67 molecules/nm² for the TBPT/Au(111) network. Using the identification of the unit cell, we can construct a representative supramolecular model of the TBPT network. Figure V.13.b illustrates the supramolecular model of TBPT on the Au(111) surface, highlighting the distances between the bromine and nitrogen atoms about 0.616 ± 0.002 falling in the range of halogen bond interaction, this interaction is described due to the σ-hole region in bromine bending toward the electron rich area of nitrogen (lone pair of electrons).[24] Consequently, the driving forces behind the supramolecular self-assembly of TBPT on an Au(111) surface include intermolecular interactions, specifically Br-N interactions, next to molecules-substrate Van der Waals interactions.

a)

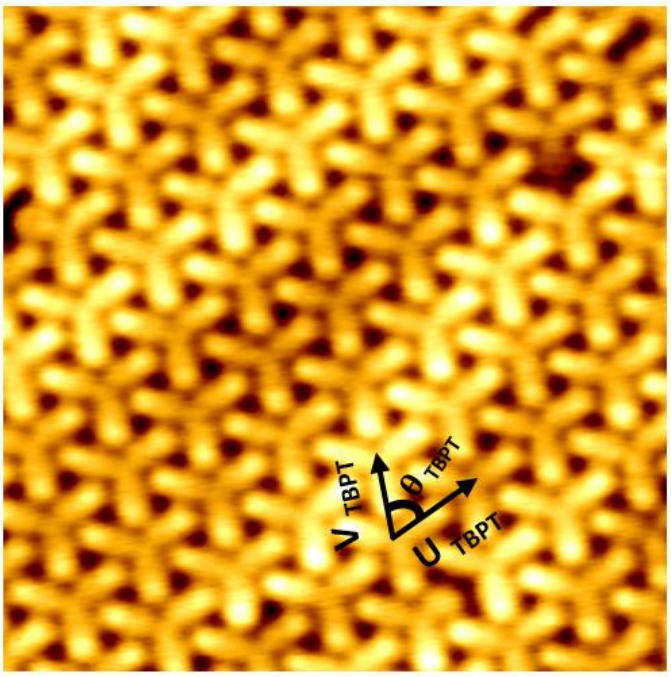

b)

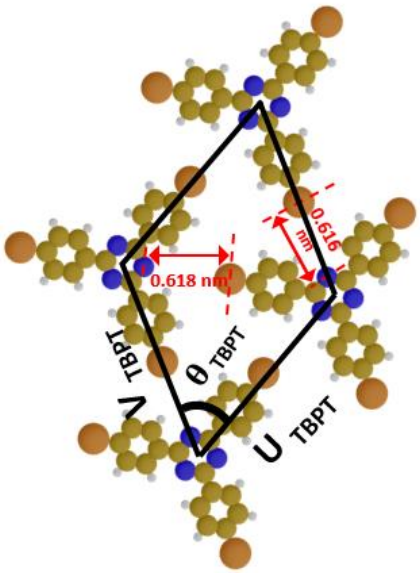

Figure V.13: a) STM image recorded at room temperature of the 2D-formed supramolecular network of TBPT/Au(111), (V_s = -1.4 V, I_t = 10 pA, RT, 10 nm x 10 nm), showing the corresponding unit cell vectors (U_{TBPT}= 1.5 ± 0.08 nm, V_{TBPT} =1.48 ± 0.02 nm, θ_{TBB} = 62°), the repetitive unit pattern. b) The proposed model for the 2D supramolecular network of the TBPT molecule. These include N-Br interactions within the neighboring molecules with a distance of 0.618 nm.

Annealing the supramolecular network of TBPT on Au(111) at 140°C for 30 minutes induces changes in the adsorbed molecular layers. STM image in Figure. V.14.a shows that a limited number of TBPT dimers are formed in localized regions close to step edges due to the cleaving of the C-Br bond on one side of the TBPT molecule. These dimer formations are close to the step edges of the Au(111) surface. The higher rate of dimer formation at step edges suggests that Au atoms with low coordination

numbers play a role in dimerization. The molecular dimers have a characteristic shape with a long axis corresponding to four phenyl groups which arises from the fusion of two of the trigonal lobes of the TBPT monomer following the catalytic cleavage of the C–Br bond with a length of about 1.45 nm which is consistent with its theoretical value of the chemical structure of the formed dimers. These features are consistent with the formation of a covalent bond through aryl-aryl coupling, which arises from the cleavage of C-Br bonds on neighboring molecules followed by the formation of a C-C bonding, which results in four bromophenyl groups are attached (two bromophenyl groups from each molecule). Further annealing at around 180°C, led to the cleavage of the C-Br bonds of all TBPT monomers on the surface, with no intact monomers present at this level of thermal annealing. The surface became a mixture of dimers, trimers, and oligomers as shown in Figure V.14.b. Annealing the surface at a higher temperature above 200°C led to the formation of an extended 2D covalent network (Figure V.14.c) consisting of areas of fully connected TBPT molecules which form a covalent nanoporous network consisting of polygons ranging between 5-8 edges. The TBPT molecules undergo further aryl-aryl coupling reactions to form multiply connected species which are the precursors of extended polymers. These two-dimensional covalent organic networks remained stable on the surface and retained their integrity until temperatures reached approximately 380°C. Beyond this temperature threshold, they began to disintegrate.

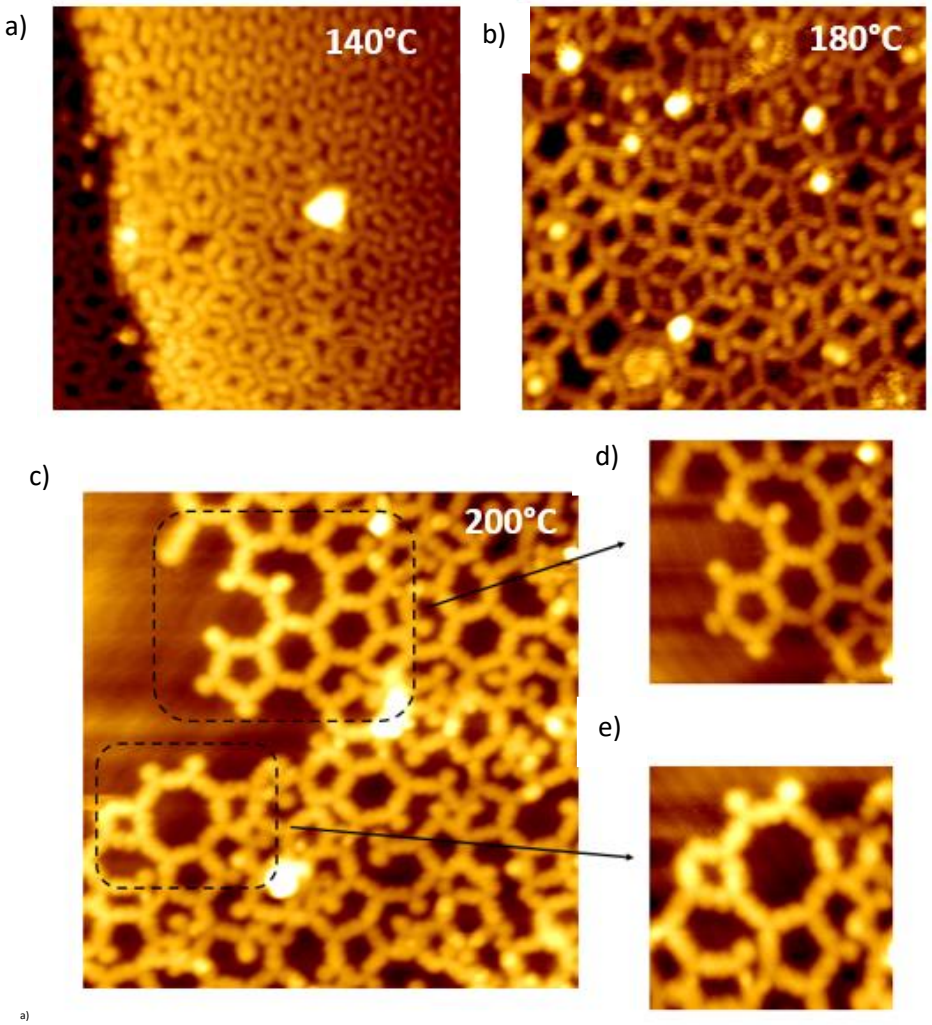

Figure V.14: STM images were recorded at room temperature after a series of annealing processes on the TBPT 2D supramolecular self-assembly on Au(111). a) STM image showing the dimerization of the TBPT molecules occurred near the Au step edges after the surface was annealed at 140°C. (V_s = -1.2 V, I_t = 10 pA, 18 nm x 18 nm). b) STM image showing the surface after annealing at 180°C. c) STM image showing the formation of the extended 2D porous covalent structure of TBPT

molecules after annealing at 200°C (V_s = -1.2 V, I_t = 10 pA, 20 nm x 20 nm). d) Zoomed STM image over three connected polygons each consisting of 5-6 edges (V_s = -1.2 V, I_t = 10 pA, 10 nm x 10 nm) e) Zoomed STM image over polygon consisting of 8 edges (V_s = -1.2 V, I_t = 10 pA, 8 nm x 8 nm).

On the other hand, the supramolecular network formed after the deposition of TBB on Au(111) depicted in Figure V.12 was also subjected to thermal annealing experiments. Annealing the supramolecular network at 130°C for 30 minutes induces changes in the adsorbed molecular layers. The STM image in Figure. V.15 shows the formation of TBB dimers and trimers after this level of annealing. The formed dimers have a "dumbbell shape "in Figure V.15.a, they are consistent with the formation of a covalent bond through aryl-aryl coupling, which arises from cleavage of C-Br bonds on neighboring molecules followed by the formation of a C-C, which results in a quaterphenyl backbone to which four bromophenyl groups are attached (two bromophenyl groups from each molecule). The molecular dimers have a characteristic shape with a long axis corresponding to four phenyl groups which arises from the fusion of two of the trigonal lobes of the TBB monomer following the catalytic cleavage of the C–Br bond with a length of about 1.53 nm which is consistent with its theoretical value (1.58 nm) of the chemical structure of the formed dimers. At this stage of annealing, the TBB molecules were also able to undergo additional aryl-aryl coupling reactions, resulting in the formation of multiply connected species that serve as precursors to extended polymers. In the upper part of Figure V.15.b, we observe several instances where several TBB molecules have combined to form an 2D extended polymers (highlighted by the black ellipses in figure V.15.b). Further thermal annealing at higher temperatures was not conducted. However, annealing at 130°C clearly demonstrates the influence of thermal annealing in cleaving the C-Br bonds in the TBB monomers, which leads to aryl-aryl coupling.

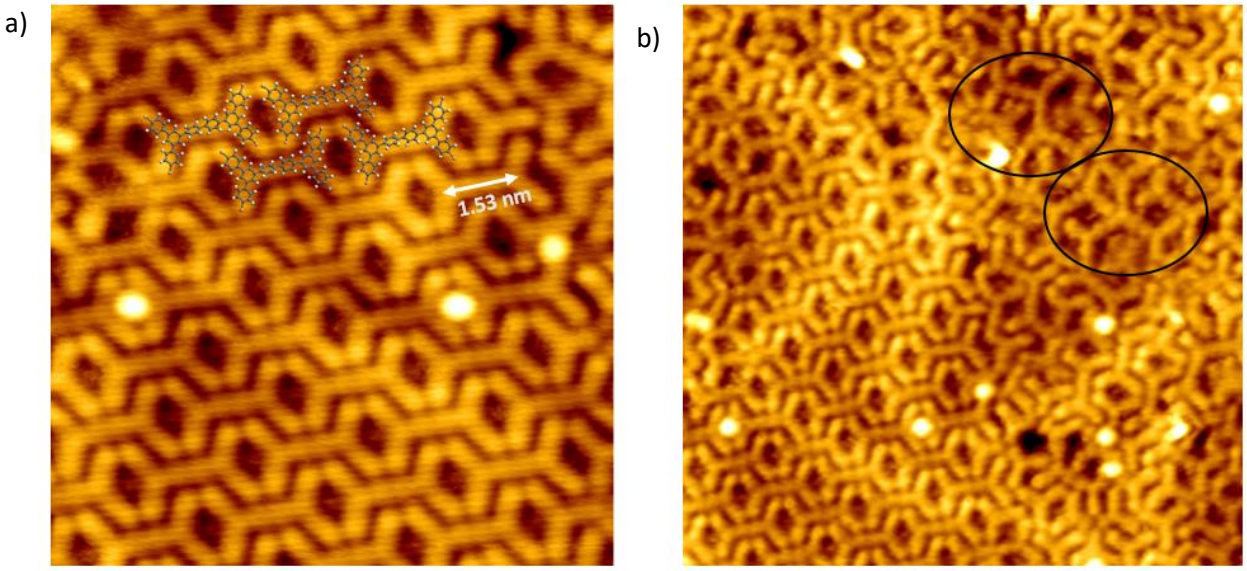

Figure V.15: STM images were recorded at room temperature after a annealing the TBB/Au(111) at 130°C. a) STM zoomed images over the TBB dimers with a "dumbbell shape ", (V_s = -1.2 V, I_t = 10 pA, 12 nm x 12 nm). b) STM image revealing the appearance of both dimers and 2D extended polymers (V_s = -1.2 V, I_t = 15 pA, 20 nm x 20 nm).

V.2.4 Light Illumination Impact on TBB and TBPT on Au(111):

In this section, we employed three varieties of lighting devices: a UV lamp emitting light in a range between 115-400 nm, a UV LED emitting light at 265 nm (Radiant power 100mW), and a UV LED emitting light at 275 nm (Radiant power 15.1 mW). The samples were exposed to these light sources within a UHV chamber through UV viewports, ensuring nearly perfect transmission. The samples were positioned approximately 10 cm from the light sources, and their temperature remained constant throughout the illumination period.

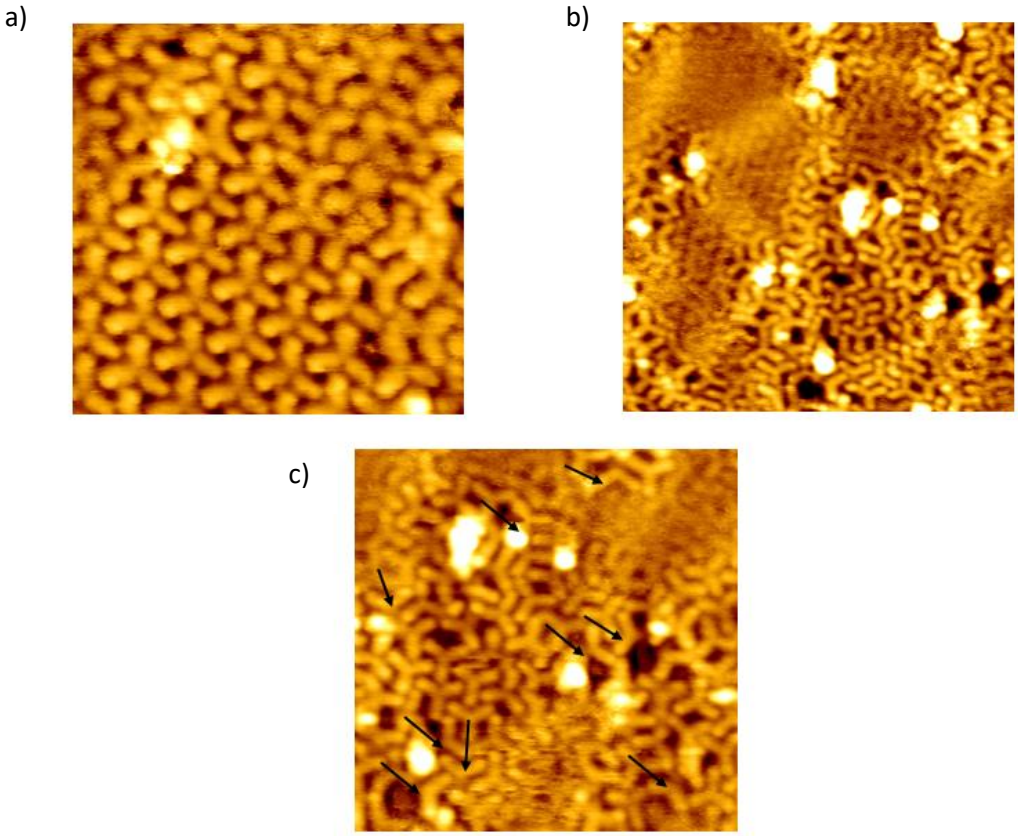

Figure V.16: STM images showing the surface of TPBT on Au(111) illumination with UV LED emitting light at 265 nm for 16 hours a) (V_s = -0.8 V, I_t = 5 pA, 15 nm x 15 nm) b) (V_s = -0.8 V, I_t = 5 pA, 10 nm x 10 nm) c) Black arrows highlighting the broken molecules with "V shape" (V_s = -0.8 V, I_t = 5 pA, 15 nm x 15 nm).

Each supramolecular network was then subjected to different light sources for durations ranging from 2 to 16 hours at room temperature. Illuminating the networks with a UV lamp emitting light in a range between 115-400 nm for 16 hours did not lead to any significant changes in either of the supramolecular networks. The assemblies formed by TBB and TBPT molecules remained intact, with all monomeric units remaining unaltered. No modifications were detected under this particular UV illumination, and the supramolecular self-assembled structures retained their original configurations as depicted in Figure V.12-13. Shining LED lights with wavelengths of 265 nm and 275 nm onto the surface at room temperature induced substantial alterations in the supramolecular network of TBPT and TBB molecules on Au(111). After illuminating for 15 hours the TBPT network on Au(111) at room temperature, there was a noticeable decrease in the number of TBPT molecules forming a full monolayer on the surface. Many molecules desorbed from the surface, and some were visibly broken, as indicated by the black arrows in Figure V.16.c, where only two legs of the molecule are visible showing a "V shape" instead of the "Y shape". The percentage of broken monomers (V shape) makes up around 17% of the total number of molecules present on the surface. Following the illuminations, the molecular arrangement on the surface became disordered, with intact monomers alongside broken ones, as illustrated in Figure V.16. This resulted in a noticeable decrease in the coverage density of the TBPT monolayer. Subsequent surface scanning proved challenging due to the increased mobility and diffusion of molecules across the surface, leading to significant tip fluctuations.

At room temperature, shining LED lights with wavelengths of 265 nm and 275 nm on the surface one at a time induced substantial alterations in the supramolecular network of TBB molecules on Au(111). We can see from Figure V.17 that the bromine substituents are readily split off and all TBB

intermediates over the surface are surrounded by spots corresponding to debromination due to the cleavage of the C-Br bonds after light illumination (using both LED lamps separately resulted in the same effect). The STM image (Figure V.17) shows that the bromine atoms positioned in two distinct locations within the network, labeled P1 and P2. In position P1, the bromine atom is situated between the two legs of two adjacent molecules that are oriented 180° relative to each other in the same row. In position P2 (as shown in Figure V.17), the bromine atom is found between two molecules aligned in the same column. It is noteworthy that the lengths of the three arms of the de-halogenated intermediates vary from roughly 0.752 to 0.825 nm, whereas initially, before illumination, these arms measured between 1-1.18 nm. This reduction in length further validates the cleavage of C-Br bonds from the three edges of the molecules. Additionally, it is important to note that after dehalogenation, the unit cell of the TBB network undergoes modification, resulting in a larger size. The parameters of the new unit cell are measured as U_{TBB} = 2.04 ± 0.02 nm and V_{TBB} = 1.76 ± 0.02 nm, with an enclosing angle of θ_{TBB} = 90°. This indicates that dehalogenation reduces steric hindrance between the molecules, leading to a change in intermolecular interactions. As a result, the dehalogenated intermediates adopt a more relaxed and expanded arrangement on the Au(111) surface. The exposure to both types of UV LED lights (265 nm and 275 nm) resulted in complete cleavage of the C-Br bonds of the TBB molecules on the surface after three hours of illumination, eliminating any remaining intact monomers. There were no traces of dimers, trimers, or polymers detected following the debromination process.

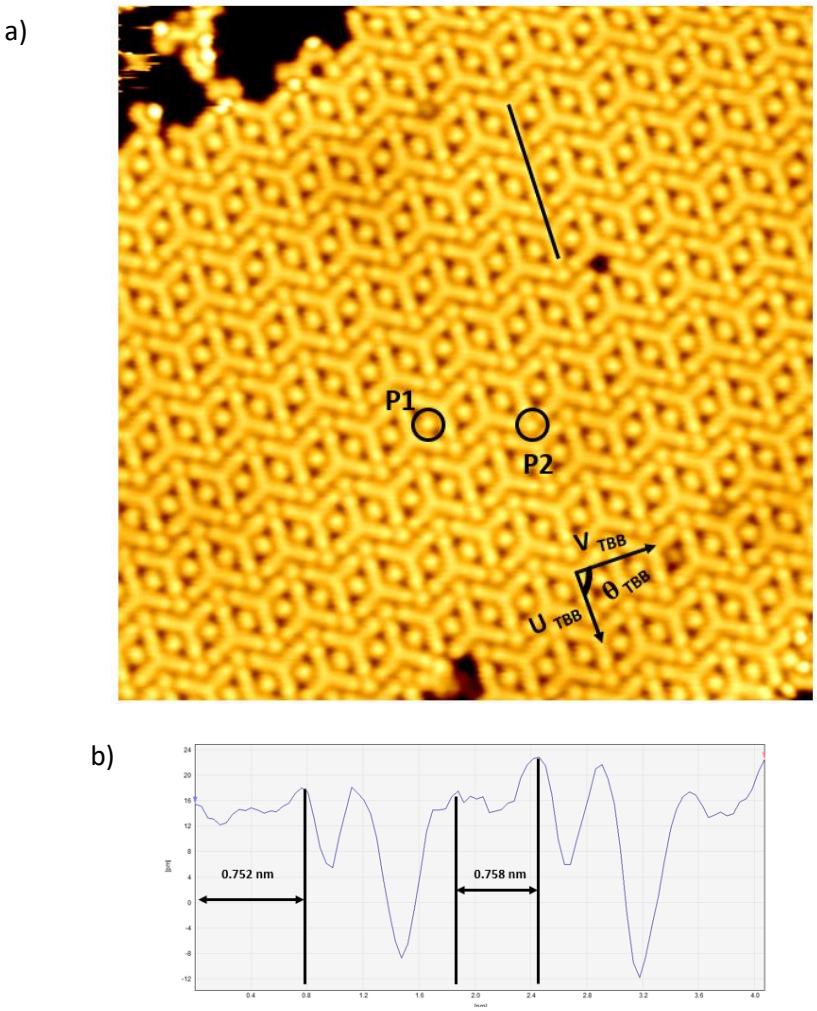

Figure V.17: STM images recorded at room temperature revealing the complete cleavage of the C-Br bonds of the TBB molecule after UV LEDS illuminations (265 nm and 275 nm each at a time) (V_s = 1.7 V, I_t = 2 pA, 10 K, 18 nm x 18 nm). b) Z-profile taken along the black line of (a).

V.3 Discussion and result analysis

Upon depositing the classical molecules NDB, NDI, TBB, and TBPT onto the Au(111) surface, well-established in the literature, they trigger the formation of 2D extended networks through intricate molecule-molecule and molecule-surface interactions. Subsequent annealing of these molecules on Au(111) resulted in the creation of 2D covalently bonded structures across the surface. Specifically, with NDB and NDI, our experiments demonstrated the emergence of interconnected covalently bonded molecules, forming dimers and trimers. Similarly, annealing TBB and TBPT also induced the development of covalent porous nanoarchitectures on Au(111). Notably, our investigations underscored the pivotal role of the Au(111) surface in facilitating the Ullmann coupling reaction in all four cases by cleaving the C-X (X=Br or I) and undergoing further coupling reactions. This catalytic assistance was instrumental in recognizing the formation of covalent bonds between the molecules. By carefully adjusting the annealing temperatures within the range of 120-150 °C, we initiated the polymerization process by cleaving the C-X bonds (where X= Br or I) and promoting the formation of dimers and trimers across the surface. Furthermore, as annealing temperatures were increased beyond this range, a transformation from dimers and trimers into extended 2D covalent nanostructures was observed caused by further aryl-aryl coupling reactions to form connected species. This temperature-dependent evolution highlights the intricate interplay between molecular reactivity, surface catalysis, and thermally induced transformations in the fabrication of tailored nanostructures on Au(111).

In our illumination experiments, we exposed NDB and NDI molecules to UV light using both a UV lamp (115-400 nm) and a UV LED lamp emitting light at wavelength of 365 nm (Radiant Power 1360 mW). This was guided by the absorption spectra we recorded, which showed that these molecules absorb photons at these particular wavelengths. Surprisingly, there were no substantial alterations observed in the supramolecular networks of either molecule following illumination. The periodicity and structure of the networks remained consistent with their pre-illumination states. However, localized disruptions were detected within the networks after subjecting NDB/Au(111) to UV light (115-400 nm) for 15 hours. These disruptions manifested as regions with disordered and random characteristics, lacking the discernible periodicity or order typically observed. This phenomenon is depicted in Figure V.11.

Meanwhile, when TBB and TBPT molecules were subjected to UV LED lamps emitting light at wavelengths of 275 nm and 265 nm each at a time, distinct effects were observed for each precursor. Illuminating TBB molecules over Au(111) with both LED lamps separately resulted in complete debromination of the molecules after three hours of exposure cleaving the C-Br bonds in the three edges of the molecules, as depicted in Figure V.17. Surprisingly, no polymer formation was detected, and the de-halogenated precursors remained isolated on the surface, surrounded by bromine atoms. The successful dehalogenation reaction of TBB molecules indicates that the initial step proceeds efficiently for cleaving the C-Br bonds without proceeding into the next step of aryl-aryl coupling. The subsequent polymerization or further reaction encounters kinetic barriers. For polymerization to occur, the de-halogenated molecules must form covalent bonds, necessitating specific molecular orientations. Steric effects may hinder these orientations, preventing efficient bond formation. Additionally, limitations in surface mobility can hinder the movement of intermediates, further obstructing polymerization. Overall, the absence of polymer formation despite successful dehalogenation suggests the presence of kinetic blockages. These barriers hinder the progression from de-halogenated intermediates to polymerized products, highlighting the importance of overcoming kinetic constraints in on-surface synthesis processes.

Aside from TBB, the behavior of the TBPT molecule on Au(111) after illumination with the LED lamps is completely different. A sharp decrease in the number of TBPT molecules that were forming a full monolayer on the surface was detected after illumination, next to the desorption from the surface, some molecules were visibly broken as shown in Figure V.16, where only two legs of the molecule are visible, and the molecular arrangement on the surface became disordered, with intact monomers alongside broken ones. The partial desorption of the TBPT on Au(111) after LED illuminations at room temperature can be attributed to the fact that the absorbed photons impart energy to the molecule, promoting vibrational and rotational motion that can exceed the binding energy between the molecule and the surface, weakening molecular interactions with the surface, facilitating desorption. In addition, the presence of broken molecules in the case of the TBPT molecule while this phenomenon didn't take place in the case of the TBB molecule indicates that changing the internal structure of the molecule by replacing the benzene central ring in the TBB molecule with triazine in the TBPT induces modification in the electronic structure (energy levels, electron density distribution, and potential reactivity) of the molecule which contribute to the presence of broken molecules on the surface after light illumination. TBPT has a nitrogen-rich core, which can influence the distribution of electron density upon excitation by light. Upon illumination, the triazine core may undergo electronic excitation that leads to a redistribution of electron density, facilitating the cleavage of the C-C bonds in the aromatic core, and potentially leading to highly reactive intermediates. Photochemical reactions triggered within the molecule may alter its chemical structure, affecting its affinity for the surface. The adsorption sites and interaction strength are different between the two molecules, TBB is a more stable molecule for interaction with light lacking the final step leading to polymerization.

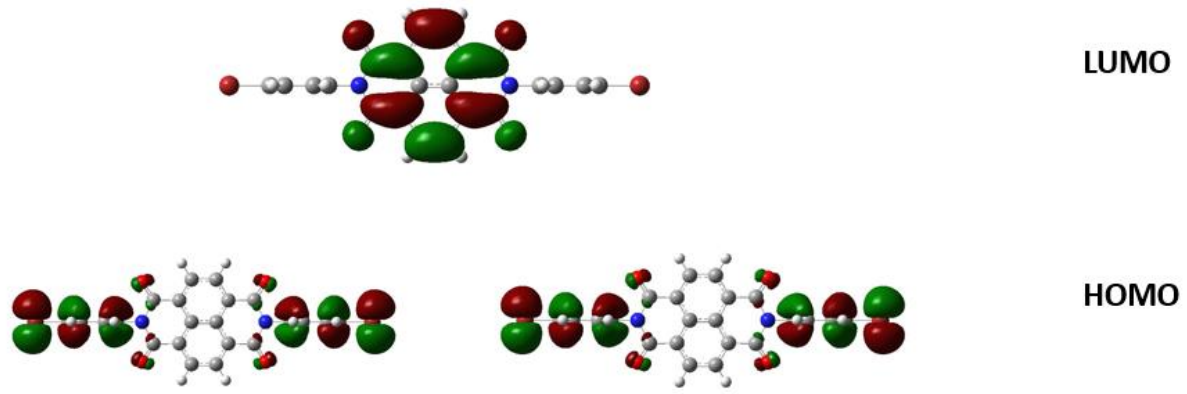

Figure 18: Molecular orbital states of NDB showing the Highest Occupied Molecular Orbital (HOMO) and the Lowest Unoccupied Molecular Orbital (LUMO) of the molecule in the vacuum state.

To provide an explanation for the various experimental observations, we decided to perform numerical simulations. To simplify these calculations, we considered isolated molecules in a vacuum, without an underlying surface. Density Functional Theory (DFT) calculations were performed with the Gaussian Software [27] to determine their molecular orbital states, specifically the Highest Occupied Molecular Orbital (HOMO) and the Lowest Unoccupied Molecular Orbital (LUMO). The basic set used is B3LYP/6-111++G(d,2p). By evaluating the HOMO and LUMO energy levels in the vacuum state as an initial DFT approach, basic insights into the molecule's electronic transitions are gained, providing a deeper understanding of their potential to absorb energy from light photons. The calculations revealed that, for NDB and NDI, the HOMO states are localized on the arms of the molecules (specifically on the bromophenyl and iodophenyl groups in NDB and NDI, respectively). Meanwhile, the LUMO states are concentrated at the core of the molecule, as illustrated in Figure V.18. Therefore, a light illumination

will induce a transition of the type π→π* from the HOMO (arms of NDB and NDI) to LUMO (core of the molecules) as well known in the literature. [28] In the case of TBB and TBPT molecules, their molecular orbitals showed a distinct localization of the HOMO and LUMO states. In the case of TBB, both the HOMO and LUMO states are distributed throughout the π-system molecule, as depicted in Figure V.19.b. If the photon energy is adequate to induce a π→π* transition, the antibonding states will become occupied by an electron. This can potentially lead to the cleavage of the C-Br bond in TBB, which is the weakest bond in the molecule. In TBPT, the molecule exhibits HOMO states that are dispersed across the bromophenyl rings and over the lone pair of the N atoms in the core of the molecule, as illustrated in Figure V.19.a. Conversely, the LUMO states are primarily concentrated on the C-C bonds present in both the central core and the lateral arms of the molecule. This configuration allows for two potential types of transitions. Therefore, for TBPT molecule, two transitions are possible: (i) the π→π* transition involving electron shifts from the HOMO to the LUMO states and (ii) n→π* transition results from the transition of the electron from a lone pair of the non-bonding orbitals localized on the nitrogen atoms in the core of the molecule to an unoccupied π* molecular orbital.[29] As a result of these two possible transitions, the transition between n→π* state would lead to the cleavage of the C-C bond between central triazine core and surrounding bromophenyl arms.

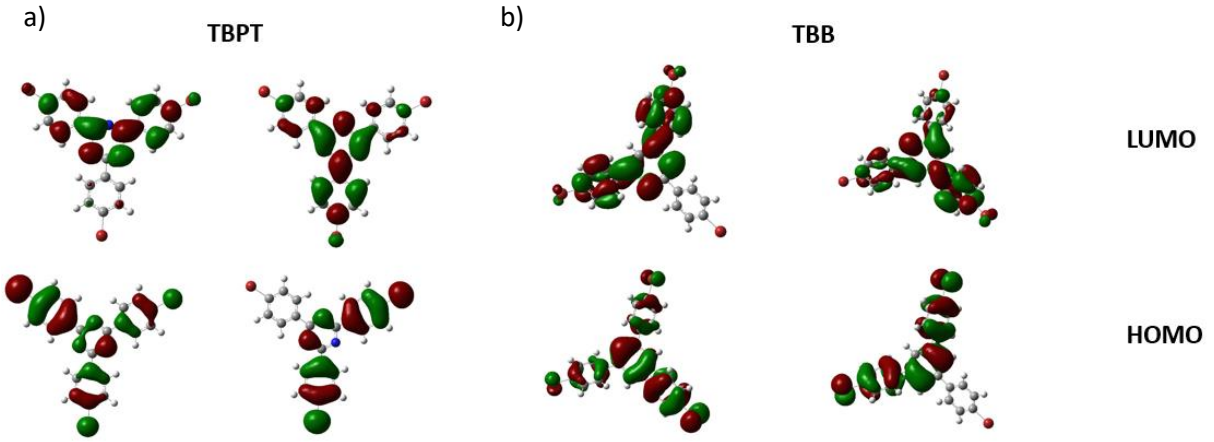

Figure 19: Molecular orbital states of TBPT and TBB showing the Highest Occupied Molecular Orbital (HOMO) and the Lowest Unoccupied Molecular Orbital (LUMO) of the molecules in the vacuum states.

V.4 Conclusion

In this chapter, we have proved that the thermally induced chemical reaction takes place via the conventional Ullmann coupling pathway in the four different molecules resulting in the formation of covalently bonded structures across the surface. By carefully controlling the thermal annealing temperatures, we have successfully initiated both the dehalogenation and polymerization processes, overcoming kinetic barriers that could hinder the reaction progression. In contrast, illumination experiments involving the NDI and NDB molecules did not result in any significant changes, the supramolecular networks on the surface maintained their structure with similar periodicity as observed before illumination. The remarkable difference in the case of TBB and TBPT after illumination suggests that the substitution of the benzene central ring with triazine alters the molecule's internal structure, leading to modifications in its electronic properties resulting in distinguished behaviors. This study demonstrates that TBB can undergo debromination through either thermal annealing or UV illumination. However, while the subsequent polymerization step occurs as expected with thermal annealing, it remains incomplete when triggered by illumination.

These experiments show the popularity of the thermal annealing method and rank it as the most adopted approach in on-surface synthesis in efficiently developing nanoarchitectures of molecular building blocks through thermal treatment. This technique is easy to implement given the availability of technological means that allow precise control of the temperature (heaters, thermocouples, pyrometers, etc.). The potential to utilize a different type of light, such as lasers, for NDI and NDB could be an option to induce changes in the supramolecular networks. However, currently, we are limited to the available light sources on hand. Understanding the behaviors of TBPT concerning the TBB requires advanced density functional theory calculations to know the preferred adsorption sites for photons at the level of each molecule when adsorbed at the surface beside the performed calculations for the molecules in the vacuum state.

References

[1] Joachim, C., Gimzewski, J. K., & Aviram, A. (2000). Electronics using hybrid-molecular and mono-molecular devices. Nature, 408(6812), 541–548, (2000).

[2] Gao, H.-J., & Gao, L. Scanning tunneling microscopy of functional nanostructures on solid surfaces: Manipulation, self-assembly, and applications. Progress in Surface Science, 85(1-4), 28–91, (2010).

[3] Park, J., Kim, K. Y., Chung, K.-H., Yoon, J. K., Kim, H., Han, S., & Kahng, S.-J. Interchain Interactions Mediated by Br Adsorbates in Arrays of Metal–Organic Hybrid Chains on Ag(111). The Journal of Physical Chemistry C, 115(30), 14834–14838, (2011).

[4] Wang, W., Shi, X., Wang, S., Van Hove, M. A., & Lin, N. Single-Molecule Resolution of an Organometallic Intermediate in a Surface-Supported Ullmann Coupling Reaction. Journal of the American Chemical Society, 133(34), 13264–13267, (2011).

[5] Bieri, M., Blankenburg, S., Kivala, M., Pignedoli, C. A., Ruffieux, P., Müllen, K., & Fasel, R. Surface-supported 2D heterotriangulene polymers. Chemical Communications, 47(37), 10239-10241, (2011).

[6] Eichhorn, J., Nieckarz, D., Ochs, O., Samanta, D., Schmittel, M., Szabelski, P. J., & Lackinger, M. On-Surface Ullmann Coupling: The Influence of Kinetic Reaction Parameters on the Morphology and Quality of Covalent Networks. ACS Nano, 8(8), 7880–7889, (2014).

[7] Fan, Q., Wang, C., Han, Y., Zhu, J., Kuttner, J., Hilt, G., & Gottfried, J. M. Surface-Assisted Formation, Assembly, and Dynamics of Planar Organometallic Macrocycles and Zigzag Shaped Polymer Chains with C–Cu–C Bonds. ACS Nano, 8(1), 709–718, (2013).

[8] Basagni, A., Sedona, F., Pignedoli, C. A., Cattelan, M., Nicolas, L., Casarin, M., & Sambi, M. Molecules–Oligomers–Nanowires–Graphene Nanoribbons: A Bottom-Up Stepwise On-Surface Covalent Synthesis Preserving Long-Range Order. Journal of the American Chemical Society, 137(5), 1802–1808, (2015).

[9] H. Y. Gao, D. Zhong, H. Monig, H. Wagner, P. A. Held, A. Timmer, A. Studer and H. Fuchs, J. Phys. Chem. C, 2014, 118, 6272–6277.

[10] Clair, S., & de Oteyza, D. G. Controlling a Chemical Coupling Reaction on a Surface: Tools and Strategies for On-Surface Synthesis. Chemical Reviews.119(7), 4717−4776, (2019).

[11] Palmino, F.; Loppacher, C.; & Chérioux, F. Photochemistry Highlights on On-Surface Synthesis. ChemPhysChem 20(18), 2271− 2280, (2019).

[12] Basagni, A., Colazzo, L., Sedona, F., DiMarino, M., Carofiglio, T., Lubian, E., Sambi, M. Stereoselective Photopolymerization of Tetraphenylporphyrin Derivatives on Ag(110) at the Sub-Monolayer Level. Chemistry - A European Journal, 20(44), 14296–14304, (2014).

[13] Nacci, C.; Schied, M.; Civita, D.; Magnano, E.; Nappini, S.; Píš, I.; Grill, L. Thermal- vs Light-Induced On-Surface Polymerization. The Journal of Physical Chemistry C, 125 (41), 22554-22561, (2021).

[14] Hla, S.W., Bartels, L., Meyer, G., & Rieder, K.-H. Inducing All Steps of a Chemical Reaction with the Scanning Tunneling Microscope Tip: Towards Single Molecule Engineering. Physical Review Letters, 85(13), 2777–2780, (2000).

[15] Shen, Q., He, J. H., Zhang, J. L., Wu, K., Xu, G. Q., Wee, A. T. S., & Chen, W. Self-assembled two-dimensional nanoporous molecular arrays and photoinduced polymerization of 4-bromo-4'-hydroxybiphenyl on Ag(111). The Journal of Chemical Physics, 142(10), 101902, (2015).

[16] Al Kobaisi, M., Bhosale, S. V., Latham, K., Raynor, A. M., & Bhosale, S. V. Functional Naphthalene Diimides: Synthesis, Properties, and Applications. Chemical Reviews, 116(19), 11685–11796, (2016).

[17] Kleiner-Shuhler, L., Brittain, R., Johnston, M. R., & Hipps, K. W. Scanning Tunneling Microscopy and Orbital-Mediated Tunneling Spectroscopy of N,N'-Dioctyl-1,8:4,5-naphthalenediimide Adsorbed on Highly Ordered Pyrolytic Graphite from Various Solvents and in Different Environments. The Journal of Physical Chemistry C, 112(38), 14907–14912, (2008).

[18] Russell, J. C., Blunt, M. O., Garfitt, J. M., Scurr, D. J., Alexander, M., Champness, N. R., & Beton, P. H. Dimerization of Tri(4-bromophenyl)benzene by Aryl−Aryl Coupling from Solution on a Gold Surface. Journal of the American Chemical Society, 133(12), 4220–4223, (2011).

[19] Gutzler, R., Walch, H., Eder, G., Kloft, S., Heckl, W. M., & Lackinger, M. Surface mediated synthesis of 2D covalent organic frameworks: 1,3,5-tris(4-bromophenyl)benzene on graphite(001), Cu(111), and Ag(110). Chemical Communications, (29), 4456-4458, (2009).

[20] Barnes, A.G.; Richy, N.; Amar, A.; Blanchard-Desce, M.; Boucekkine, A.; Mongin, O.; Paul, F. Electronic Absorption, Emission, and Two-Photon Absorption Properties of Some Extended 2,4,6-Triphenyl-1,3,5 Triazines. Photochem 2, 326–344, (2022).

[21] Bui, T. T. T., Dahaoui, S., Lecomte, C., Desiraju, G. R., & Espinosa, E. The Nature of Halogen···Halogen Interactions: A Model Derived from Experimental Charge-Density Analysis. Angewandte Chemie International Edition, 48(21), 3838–3841, (2009).

[22] Zhuang, W. R.; Wang Y.; Cui, P.F.; Xing, L.; Lee, J.; Kim, D.; Jiang, H. L.; Oh, Y. K. Applications of π-π stacking interactions in the design of drug-delivery systems. J. Control. Release, 294, 311-326, (2019).

[23] Duhm, S., Gerlach, A., Salzmann, I., Bröker, B., Johnson, R. L., Schreiber, F., & Koch, N. PTCDA on Au(111), Ag(111) and Cu(111): Correlation of interface charge transfer to bonding distance. Organic Electronics, 9(1), 111–118, (2008).

[24] Wang, Y.; Miao, X.; Deng, W. Halogen Bonds Fabricate 2D Molecular Self-Assembled Nanostructures by Scanning Tunneling Microscopy. Crystals, 10(11), 1057, (2020).

[25] Blunt, M. O., Russell, J. C., Champness, N. R., & Beton, P. H. Templating molecular adsorption using a covalent organic framework. Chemical Communications, 46(38), 7157, (2010).

[26] Gatti, R., MacLeod, J. M., Lipton-Duffin, J. A., Moiseev, A. G., Perepichka, D. F., & Rosei, F. Substrate, Molecular Structure, and Solvent Effects in 2D Self-Assembly via Hydrogen and Halogen Bonding. The Journal of Physical Chemistry C, 118(44), 25505–25516, (2014).

[27] Gaussian 09, Revision C.01, M. J. Frisch, G. W. Trucks, H. B. Schlegel, G. E. Scuseria, M. A. Robb, J. R. Cheeseman, G. Scalmani, V. Barone, G. A. Petersson, H. Nakatsuji, X. Li, M. Caricato, A. V. Marenich, J. Bloino, B. G. Janesko, R. Gomperts, B. Mennucci, H. P. Hratchian, J. V. Ortiz, A. F. Izmaylov, J. L. Sonnenberg, D. Williams-Young, F. Ding, F. Lipparini, F. Egidi, J. Goings, B. Peng, A. Petrone, T. Henderson, D. Ranasinghe, V. G. Zakrzewski, J. Gao, N. Rega, G. Zheng, W. Liang, M. Hada, M. Ehara, K. Toyota, R. Fukuda, J. Hasegawa, M. Ishida, T. Nakajima, Y. Honda, O. Kitao, H. Nakai, T. Vreven, K. Throssell, J. A. Montgomery, Jr., J. E. Peralta, F. Ogliaro, M. J. Bearpark, J. J. Heyd, E. N. Brothers, K. N. Kudin, V. N. Staroverov, T. A. Keith, R. Kobayashi, J. Normand, K. Raghavachari, A. P. Rendell, J. C.

Burant, S. S. Iyengar, J. Tomasi, M. Cossi, J. M. Millam, M. Klene, C. Adamo, R. Cammi, J. W. Ochterski, R. L. Martin, K. Morokuma, O. Farkas, J. B. Foresman, and D. J. Fox, Gaussian, Inc., Wallingford CT, (2009).

[28] Guha, S., Goodson, F. S., Roy, S., Corson, L. J., Gravenmier, C. A., & Saha, S. Electronically Regulated Thermally and Light-Gated Electron Transfer from Anions to Naphthalenediimides. Journal of the American Chemical Society, 133(39), 15256–15259, (2011).

[29] Liu, R., Shu, M., Hu, J., Zhu, S., Shi, H., & Zhu, H. Star-shaped D-π-A compounds with a 1,3,5-triazine core and N -aryl chromophore substituted fluorene arms: Synthesis, aggregation induced emission and two-photon absorption. Dyes and Pigments, 137, 174–181, (2017).

Chapter VI: Conclusion and Perspectives

The objectives of this thesis fall within the context of exploring unaddressed areas of surface science and on-surface synthesis and investigating their potential within the given context. The interplay between the well-defined geometric arrangement of the solid surface and its inherent chemical reactivity is important. This reactivity is dictated by both the intrinsic crystal structure and the elemental composition of the surface. The same importance is the design of the interacting molecular species. Their structure and functionality directly influence the reaction pathway and ultimately determine the desired products. These parameters are key factors to take control over the whole process reaching the desired outcome. All the performed experiments in this thesis were done under ultra-high vacuum (UHV) conditions and monitored by a variable temperature scanning tunneling microscope (VT-STM). The upcoming sections will provide a comprehensive overview of all the work conducted in the thesis, emphasizing key aspects of the experiments and offering insights into potential future directions.

VI.1 Dissociative chemisorption of inert N_2 molecules on a highly reactive Si(111)-7x7 and H atomic interaction with N-adsorbed compounds on the surface

The motivation behind the work in Chapter III stemmed from the desire to create a new, effective method for dissociating N_2 molecules under mild conditions and this could be pursued by on-surface synthesis on chemically reactive surfaces monitored by Scanning Tunneling Microscopy and X-ray photoelectron spectroscopy under UHV conditions to maintain the cleanliness and emphasis accurate investigation of reaction mechanism to fully understand N_2 activation. The choice of a highly reactive Si(111)- 7x7 surface plays a crucial role when seeking facile and direct dissociative adsorption of the impinging gas particles, in a way that intrinsic high surface reactivity requires less translational kinetic energy from the colliding gas sitting in the thermal range of energy distribution (Boltzmann-Maxwell) to be dissociated.

Fortunately, we demonstrated that the strong N_2 bond can be dissociated at low pressure and room temperature on a Si(111)-7x7 surface. N_2 gas was injected into the UHV chamber on a clean Si(111)-7x7 surface. For a partial pressure of N_2 gas above $2x10^{-6}$ mbar, a clear modification of the surface was detected experimentally by STM. The extinction of a number of silicon adatoms from the surface was observed approaching a limit value of 35% of the total surface adatoms after exposure to $1x10^{-5}$ mbar for 30 min. On the other hand, experimental analysis by X-ray photoemission spectroscopy of the modified surface indicated the presence of three different N-based components coexisting on the surface, confirming the dissociation of N_2 molecules. According to literature data, only one dominant component could be identified as Si_3N. The two other components were attributed to partially dissociated N_2 intermediate states bonded to the Si(111)-7x7 surface, especially since they transform in their totality into Si_3N upon thermal annealing at 800 K and no desorption was detected after this annealing.

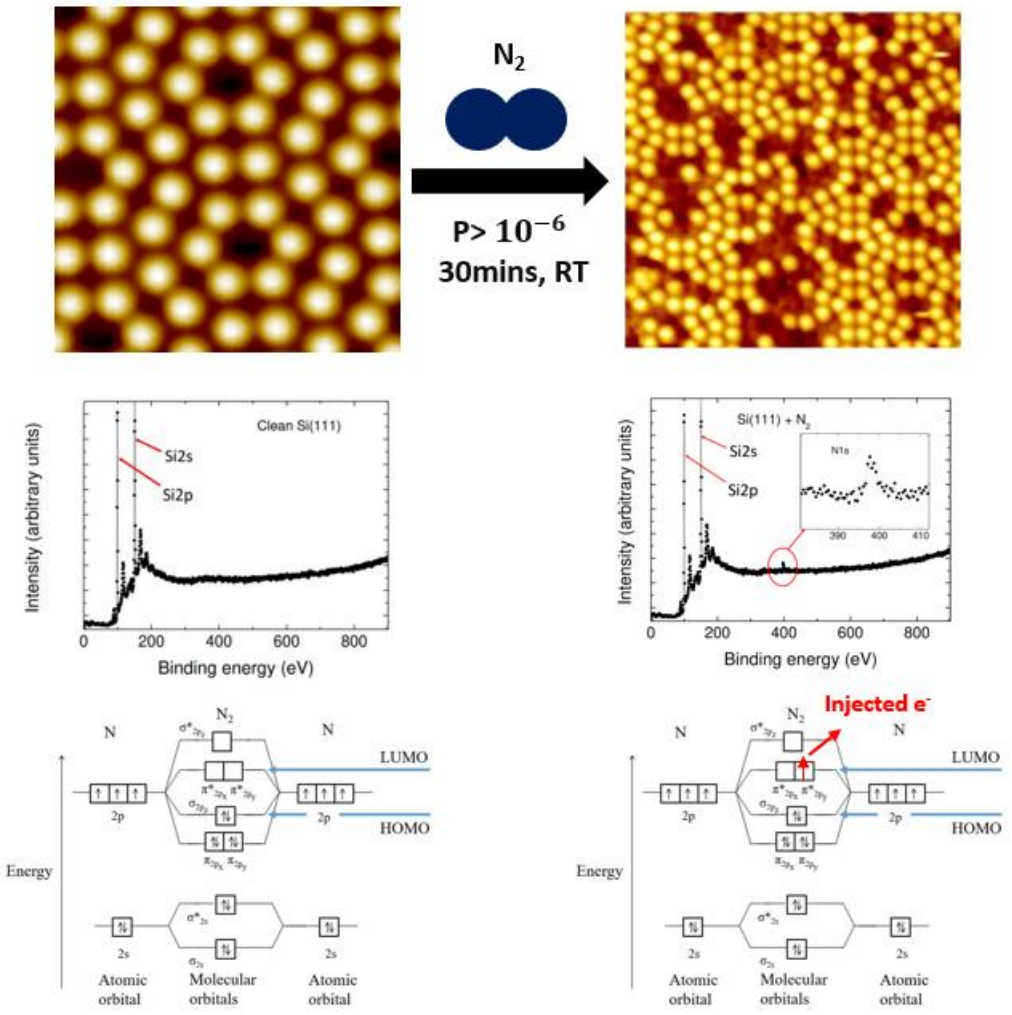

Figure VI.1: Summary diagram of the key findings concerning the study of collision-induced dissociation of N_2 inert molecules on a Si(111)-7x7 surface.

Density functional theory calculation revealed that the relatively low thermal energy of N_2 collision with the highly reactive surface facilitates the transfer of electrons from the Si(111)-7x7 surface to Π* antibonding orbitals of N_2, weakening the N_2 bond, leading to easy dissociation of the N_2 triple bond on the surface at room temperature and low gas pressure into several intermediates states. All the described key findings relative to this work are summarized in Figure VI.1.

The H atomic low exposure deposition over the N-adsorbed Si(111)-7x7 with the assistance of thermal annealing led to magnificent modification on the surface structure, synthesizing nitrogen-based chemicals in an energy-efficient manner. The appearance of the surface recovery and lowering of the number of dark spots according to the statistical calculations is attributed to the formation of N-species and its desorption from the surface.

This study highlights the reactive surface of Si(111)-7x7 as a potential candidate for the dissociation of inert molecules efficiently and easily. While acknowledging the challenge of identifying all adsorbed species on the surface, even with the XPS technique, it is evident that additional elemental analysis methods capable of operating in ultrahigh vacuum (UHV) are necessary for discrimination. Spectroscopic techniques like FTIR and Raman spectroscopy can provide valuable insights, aiding in the identification of observed species by local probe methods in UHV environments. The significant

influence of atomic hydrogen on nitrogen-adsorbed compounds on Si(111)-7x7, particularly when assisted by thermal annealing, holds great promise for synthesizing nitrogen-based chemicals in an energy-efficient manner and shedding light on the surface's capability to produce ammonia. However, further discrimination requires elemental analysis techniques operable in ultrahigh vacuum (UHV). Spectroscopic methods such as FTIR, Raman, XPS, and thermal desorption spectroscopy can provide valuable insights for identifying species observed by local probe methods under UHV conditions. Presently, these techniques are not fully developed for such conditions, but we anticipate future advancements in this area. Our forthcoming research will concentrate on exploring the feasibility of dissociating CO_2 gas similarly to our work with N_2.

VI.2 Toward Conformational Identification of Molecules in 2D and 3D Self-Assemblies

A significant challenge persisting in the realm of supramolecular self-assemblies involves transitioning from two-dimensional (2D) to three-dimensional (3D) nanostructures.[1,2] To address the paradigm shift from 2D to 3D self-assemblies and to determine the conformation of molecules within 2D (monolayer) and 3D (multilayered) supramolecular networks adsorbed onto a surface, we developed an efficient approach in Chapter IV combining STM under ultra-high vacuum, AFM, and AFM-IR under ambient conditions to deeply investigate the exploration of EsterOC18 molecule deposition into Highly Ordered Pyrolytic Graphite (HOPG).

Close examination of STM and AFM images reveals the consistent periodicity exhibited by the supramolecular networks formed after depositing EsterOC18 molecules onto a graphite surface, regardless of whether they take the form of 3D islands or 2D monolayers. Leveraging the high-resolution capabilities of STM images, we were able to observe the spatial arrangement of aliphatic chains surrounding the EsterOC18 molecules. The experimental periodicity (5.60 ± 0.1 nm) closely matches the length of EsterOC18 molecules (5.12 nm), suggesting the absence of lateral n-octadecyl chain interdigitation, since the nanorods are rotated at 120° between adjacent dark stripes we infer that EsterOC18 molecules align along the direction of the HOPG surface, forming a densely packed 2D lamellae of parallel-aligned, straight n-octadecyl chains, aligning with the Groszek model.

Furthermore, AFM-IR signatures provide additional insightful details compared to STM and AFM images. In the AFM-IR spectrum of a monolayer, the absence of C=C stretching peaks provides substantial evidence that the aromatic rings align parallel to the HOPG surface plane. This observation indicates that the aromatic rings within the monolayer adopt an in-plane orientation concerning the substrate. Another notable phenomenon observed in the monolayer pertains to the C=O stretching band, which exhibits a hypsochromic shift compared to the C=O stretching band observed in the FT-IR spectrum of the pure solid (bulk). This shift holds particular interest, as it signifies the absence of electronic conjugation between the C=O group and the surrounding phenyl ring. These collective findings provide compelling evidence that the C=O bond within the EsterOC18 monolayer is oriented out of the HOPG surface plane and distinct from the neighboring phenyl ring. In the case of multilayers, the band associated with C=C bond stretching is now observed, similar to the bulk. However, two bands related to C=O bond stretching are detected. One is identical to the bulk spectrum, while the second, with a weaker intensity, resembles the AFM-IR spectrum of the monolayer. Consequently, it can be inferred that two orientations or conformations of EsterOC18 molecules comprise the multilayered networks. The first layer, closest to the surface assumes the same conformation as the one constituting the monolayer, attributed to the molecule-surface interaction. In contrast, the conformation of EsterOC18 molecules in the upper layers of a multilayer system differs significantly, the phenyl rings rotate to enhance their conjugation with the C=O group, akin to the bulk.

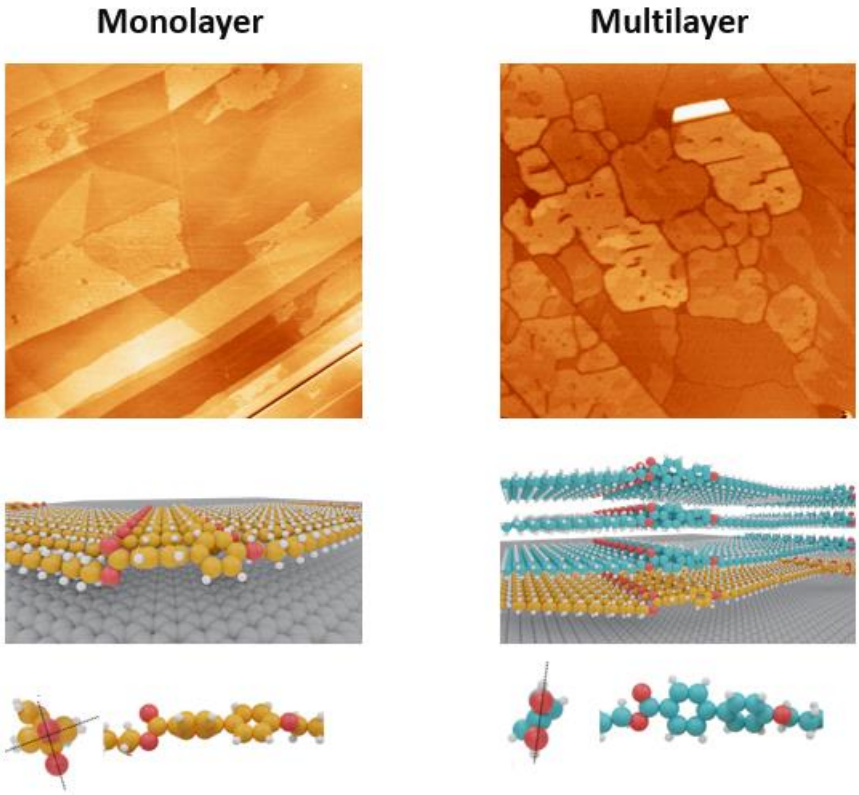

Figure VI.2: Summary diagram of the key findings concerning the study EsterOC18 exploration from monolayers to multilayers over HOPG.

Our research has highlighted the remarkable sensitivity and non-invasive nature of AFM-IR as a powerful tool for investigating molecular conformation within supramolecular networks. Through AFM-IR experiments, we have identified variations in the dihedral angle between the C=O group and the adjacent phenyl ring within 2D to 3D supramolecular networks adsorbed onto an HOPG surface under ambient conditions. Particularly noteworthy is the observation that in 3D supramolecular networks formed by stacked molecular layers, the molecular conformation varies between layers. The layer closest to the substrate reflects the conformation of the corresponding 2D monolayer, while others resemble the bulk conformation more closely. This study successfully demonstrates that combining STM, AFM, and AFM-IR not only reveals the orientation and arrangement of surface-adsorbed molecules but also discerns the molecular conformation across different layers of 3D multilayered supramolecular networks. Such an integrated analytical approach holds promise for unraveling the complexities of on-surface supramolecular self-assemblies universally.

While the progression from monolayers to bilayers and multilayers has opened up new avenues, it may explore an emerging topic in the foreseeable future: harnessing insights from these studies to fabricate real-space 3D perfect structures such as supramolecular single crystals and develop sandwich devices where the electron transfer is from up to down, vertical to the direction of the surface. Despite the considerable distance between assembled materials and practical applications, persistent efforts in this direction will undoubtedly unveil new avenues for exploring the architectures and properties of 3D supramolecular materials, benefitting numerous organic electronics and optoelectronic devices.

VI.3 Light vs thermal-induced on-surface Polymerization on Au(111)

A thorough comparative analysis of thermal and photochemical processes, spanning from the initial intact molecules to the final polymer formations, remains unexplored in depth. Investigating whether these processes follow parallel or divergent pathways is essential, as it will reveal whether they result in similar or distinct intermediate molecular arrangements and covalent structures. Therefore, understanding the mechanisms driving both thermal and light-induced approaches, their interactions, and their individual significance in on-surface synthesis is critical. Chapter V aims to explore and compare the on-surface polymerization processes triggered by thermal and photochemical methods on Au(111), employing four distinct molecular building blocks.

Depositing the classical molecules NDB, NDI, TBB, and TBPT onto the Au(111) surface at room temperature initiates the formation of 2D extended networks through complex molecule-molecule and molecule-surface interactions. Upon annealing, these molecules evolve into 2D covalently bonded structures on the Au(111) surface. Crucially, our investigations highlight the Au(111) surface's catalytic role in facilitating the Ullmann coupling reaction for all four molecules by cleaving the C-X bonds (X=Br or I) and promoting further coupling reactions. This catalytic process is key to forming covalent bonds between the molecules. By precisely adjusting the annealing temperatures between 120-150 °C, we triggered polymerization by cleaving the C-X bonds and encouraging the formation of dimers and trimers on the surface. As the annealing temperatures increased beyond this range, these dimers and trimers transformed into extended 2D covalent nanostructures due to additional aryl-aryl coupling reactions, demonstrating the intricate relationship between molecular reactivity, surface catalysis, and thermally induced transformations in creating tailored nanostructures on Au(111).

In our illumination experiments, we exposed NDB and NDI molecules to UV light using both a UV lamp (115-400 nm) and a UV LED lamp emitting at 365 nm, guided by the absorption spectra indicating photon absorption at these wavelengths. Surprisingly, the supramolecular networks of both molecules exhibited no significant changes post-illumination, maintaining their pre-illumination periodicity and structure. However, localized disruptions were observed in the NDB/Au(111) networks after 15 hours of exposure to UV light (115-400 nm). These disruptions appeared as regions with disordered and random characteristics, lacking the discernible periodicity or order typically observed.

Conversely, subjecting TBB and TBPT molecules to UV LED lamps emitting at 275 nm and 265 nm revealed distinct effects for each precursor. When TBB molecules were illuminated on Au(111) with both LED lamps, complete debromination occurred within three hours, cleaving the C-Br bonds at the three edges of the molecules. However, no polymer formation was observed; the de-halogenated precursors remained isolated on the surface, surrounded by bromine atoms. This successful dehalogenation indicates that the initial C-Br bond cleavage step proceeds efficiently, but without progressing to the subsequent aryl-aryl coupling. The lack of polymer formation, despite successful dehalogenation, suggests the presence of kinetic barriers that prevent the transition from de-halogenated intermediates to polymerized products. This highlights the significance of overcoming kinetic constraints in on-surface synthesis processes. In contrast to TBB, the behavior of TBPT molecules on Au(111) upon illumination with LED lamps was markedly different. After illumination, there was a notable decrease in the number of TBPT molecules forming a complete monolayer on the surface, accompanied by desorption and the appearance of broken molecules, characterized by a “V shape” instead of the original “Y shape.” The molecular arrangement became disordered, with intact monomers interspersed with broken ones. This partial desorption of TBPT at room temperature can be attributed to absorbed photons imparting sufficient energy to the molecules, enhancing vibrational and rotational motion that overcomes the binding energy between the molecule and the surface, thus

facilitating desorption. The occurrence of broken molecules in TBPT, unlike in TBB, suggests that altering the internal structure by replacing the benzene ring with a triazine ring in TBPT modifies its electronic structure. TBPT's nitrogen-rich core influences electron density distribution upon light excitation, potentially leading to C-C bond cleavage in the aromatic core and the formation of highly reactive intermediates.

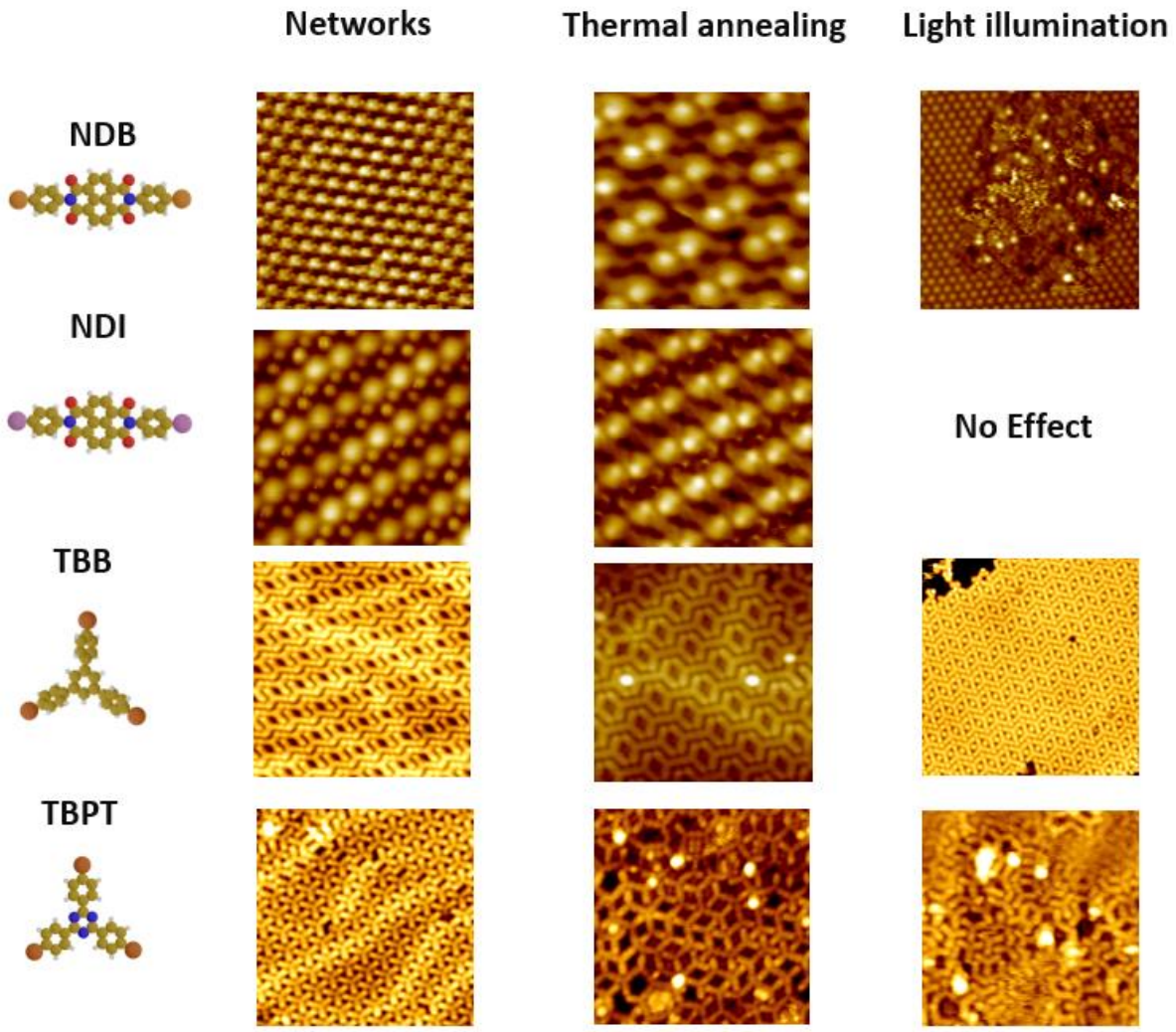

Figure VI.3: Summary diagram of the key findings concerning the study thermal and photochemical processes for the four used molecules, spanning from the initial intact molecules to the final compounds, showing a divergent pathway.

To provide an explanation for the various experimental observations, a numerical simulations using Density Functional Theory (DFT) calculations were performed to determine the molecular orbital states of the molecules (Highest Occupied Molecular Orbital (HOMO) and the Lowest Unoccupied Molecular Orbital (LUMO)) for the molecules isolated in vacuum. For NDB and NDI, the calculations revealed that one possible type of transition can be induced by light illumination, this transition of type $\pi \rightarrow \pi^*$ from the HOMO (arms of NDB and NDI) to LUMO (core of the molecules). In the case of TBB and TBPT molecules, their molecular orbitals showed a distinct localization of the HOMO and LUMO states. In the case of TBB, the photon energy is adequate to induce a $\pi \rightarrow \pi^*$ transition, the antibonding states will become occupied by an electron. This can potentially lead to the cleavage of the C-Br bond in TBB, which is the weakest bond in the molecule. In TBPT, two transitions are possible: (i) the $\pi \rightarrow \pi^*$ transition involving electron shifts from the HOMO to the LUMO states and (ii) $n \rightarrow \pi^*$ transition results from the transition of the electron from a lone pair of the non-bonding orbitals localized on the

nitrogen atoms in the core of the molecule to an unoccupied π* molecular orbital.[3] As a result of these two possible transitions, the transition between n→π* state would lead to the cleavage of the C-C bond between central triazine core and surrounding bromophenyl arms.

In this chapter, we have proved that the thermally induced chemical reaction takes place via the conventional Ullmann coupling pathway in the four different molecules resulting in the formation of covalently bonded structures across the surface. In contrast, illumination experiments involving the NDI and NDB molecules did not result in any significant changes, the supramolecular networks on the surface maintained their structure with similar periodicity as observed before illumination. The remarkable difference in the case of TBB and TBPT after illumination suggests that the substitution of the benzene central ring with triazine alters the molecule's internal structure, leading to modifications in its electronic properties resulting in distinguished behaviors. These experiments show the popularity of the thermal annealing method and rank it as the most adopted approach in on-surface synthesis in efficiently developing nanoarchitectures of molecular building blocks through thermal treatment. The potential to utilize a different type of light, such as lasers, for NDI and NDB could be an option to induce changes in the supramolecular networks. However, currently, we are limited to the available light sources on hand. Understanding the behaviors of TBPT concerning the TBB requires advanced density functional theory calculations to know the preferred absorption sites for photons at the level of each molecule when adsorbed at the surface beside the performed calculations for the molecules in the vacuum state.

References

[1] Koepf, M., Chérioux, F., Wytko, J. A., & Weiss, J. 1D and 3D surface-assisted self-organization. Coord. Chem. Rev. 256, 2872-2892 (2012).

[2] Xie, R., Hu, Y. & Lee, S.-L. A paradigm shift from 2D to 3D: surface supramolecular assemblies and their electronic properties explored by scanning tunneling microscopy and spectroscopy. Small 19, 2300413 (2023).

[3] Liu, R., Shu, M., Hu, J., Zhu, S., Shi, H., & Zhu, H. Star-shaped D-π-A compounds with a 1,3,5-triazine core and N -aryl chromophore substituted fluorene arms: Synthesis, aggregation induced emission and two-photon absorption. Dyes and Pigments, 137, 174–181, (2017).

école doctorale **sciences pour l'ingénieur et microtechniques** SPIM

Titre : Auto-assemblages supramoléculaires et réactions chimiques sur surface étudiés par microscopies à sonde locale

Mots clés : Auto-assemblage supramoléculaire, chimie sur surface, sciences des surfaces, microscopie à effet tunnel, microscopie à force atomique.

Résumé : Le travail présenté dans cette thèse est centré sur l'exploration des réseaux supramoléculaires et des réactions chimiques en surface sur diverses surfaces solides, en examinant des cas jusqu'alors inexplorés afin d'enrichir les connaissances dans ce domaine. La principale méthode utilisée pour étudier les phénomènes chimiques de surface est la microscopie à effet tunnel, réalisée sous ultra-haut-vide. Le premier chapitre fait un état de l'art en mettant en lumière les principes fondamentaux des réactions chimiques sur surface à travers quelques travaux illustratifs de la littérature. Le deuxième chapitre présente les techniques expérimentales et les équipements utilisés pour réaliser et surveiller les expériences sous UHV. De plus, je donne une brève présentation des surfaces utilisées et les différentes techniques de caractérisation employées pour mener nos expériences. La première partie du chapitre III se concentre sur l'utilisation de la surface Si(111)-7x7 sous UHV, pour promouvoir la dissociation des molécules inertes de N_2 par collision à température ambiante et à basse pression. La seconde partie décrira l'exposition de l'hydrogène atomique sur la surface Si(111)-7x7 sur laquelle des atomes d'azote sont adsorbés. Le chapitre IV se focalise sur l'expansion des monocouches en multicouches bien ordonnées pour améliorer la fonctionnalité et la complexité des auto-assemblages. Dans cette étude, nous présentons l'évolution de la conformation moléculaire des réseaux supramoléculaires en 2D à 3D adsorbés sur une surface de HOPG. Le cinquième chapitre s'intéresse à la comparaison des processus de polymérisation en surface induits par des méthodes thermiques et photochimiques sur Au(111) en utilisant quatre blocs de construction moléculaires distincts. Le dernier chapitre résume les résultats de l'ensemble des travaux de thèse et présente des perspectives pour des travaux futurs dans ce domaine.

UBFC UNIVERSITÉ BOURGOGNE FRANCHE-COMTÉ

Université Bourgogne Franche-Comté
32, avenue de l'Observatoire
25000 Besançon

école doctorale **sciences pour l'ingénieur et microtechniques** SPIM

Title: Supramolecular networks and on-surface chemical reactions

Investigated by scanning probe microscopies

Keywords: Supramolecular self-assembly, On-surface chemistry, UHV, STM, AFM, surface science, interface, bond dissociation

Abstract: The work in this thesis is focused on exploring supramolecular networks and on-surface chemical reactions on various solid surfaces, examining previously unstudied cases to enhance the field's knowledge base. The primary method employed to investigate surface chemical phenomena is scanning tunneling microscopy, conducted under ultra-high vacuum environment. The first chapter reviews the state-of-the-art by highlighting the basic keys of on-surface chemical reactions through some illustrative works from the literature. The second chapter represents the experimental techniques and equipment that are used for performing and monitoring experiments under UHV. As well, we give a brief presentation of used surfaces concerning their crystalline structures and the different used characterization techniques to conduct our experiments. Chapter III in the first part concentrates on the usage of highly reactive reconstructed Si(111)-7x7 surface, under UHV, to promote a facile dissociation of inert N_2 molecules upon soft collision at room temperature and low gas pressure. The second part will be depicted to promote the exposure of atomic hydrogen over the N-adsorbed Si(111)-7x7 surface. Chapter IV focuses on the expansion of monolayers to well-ordered multilayers to enhance the functionality and complexity of self-assemblies. In this study, we present the evolution of molecular conformation from 2D to 3D supramolecular networks adsorbed onto an HOPG surface. The fifth chapter will delve into comparing the on-surface polymerization processes induced by thermal and photochemical methods on Au(111) using four distinct molecular building blocks. The last chapter summarizes the results of the whole thesis work and presents perspectives for future related work.

UBFC UNIVERSITE BOURGOGNE FRANCHE-COMTE

Université Bourgogne Franche-Comté
32, avenue de l'Observatoire
25000 Besançon